INVESTIGATION OF DIELECTRIC AND MAGNETIC PROPERTIES OF COMPOSITES OF FERRITES AND 2D MATERIALS FOR ENERGY STORAGE

Thesis Submitted for the Award of the Degree of

DOCTOR OF PHILOSOPHY

in

Physics

By

MOHD ROUF KHAN

Registration Number: 12015311

Supervised By

Dr. Ajeet Kumar Srivastava (11459)

Department of Physics (Professor)

School of Computer Science and Engineering, Lovely Professional University

LOVELY PROFESSIONAL UNIVERSITY, PUNJAB

2025

DECLARATION

I hereby declared that the presented work in the thesis entitled **"Investigation of Dielectric and Magnetic Properties of Composites of Ferrites and 2D Materials for Energy Storage"** in fulfillment of degree of Doctor of Philosophy (Ph.D.) is outcome of research work carried out by me under the supervision of Dr. Ajeet Kumar Srivastava**,** working as Professor**,** in the Department of Physics, School of Computer Science and Engineering of Lovely Professional University, Punjab, India. In keeping with general practice of reporting scientific observations, due acknowledgements have been made whenever work described here has been based on findings of other investigators. This work has not been submitted in part or full to any other University or Institute for the award of any degree.

(Signature of Scholar)
Name of the Scholar: Mohd Rouf Khan
Registration No.: 12015311
Department of Physics, School of Chemical Engineering and Physical Sciences,
Lovely Professional University, Punjab, India-144411

CERTIFICATE

This is to certify that the work reported in the Ph.D. thesis entitled "**Investigation of Dielectric and Magnetic Properties of Composites of Ferrites and 2D Materials for Energy Storage**" submitted in fulfillment of the requirement for the award of the degree of Doctor of Philosophy in the Department of Physics, School of Chemical Engineering and Physical Sciences, is a research work carried out by Mohd Rouf Khan, 12015311, is bonafide record of his original work carried out under my supervision and that no part of thesis has been submitted for any other degree, diploma or equivalent course.

(Signature of Supervisor)
Name of supervisor: Dr. Ajeet Kumar Srivastava (11459)
Designation: Professor
Department/School: School of Computer Science and Engineering,
University: Lovely Professional University, Phagwara Punjab, India- 144411

Dedicated to my loving parents

and

beloved wife

Acknowledgment

I am deeply grateful and bow in reverence to ***Almighty Allah (SWT),*** the most merciful, the cherisher, and the supreme sustainer of the universe whose boundless generosity and enduring mercy have been the foundation of my journey to success, granting me the zeal, strength, and determination to complete this thesis.

The completion of any research work is a challenging endeavor, but it becomes a rewarding and enriching experience with the unwavering support and encouragement of many individuals. It is with immense gratitude that I take this opportunity to express my heartfelt appreciation to all those who contributed their guidance and assistance throughout this academic odyssey.

First and foremost, I feel privileged to express my deep sense of sincere gratitude and everlasting indebtedness to my esteemed supervisor, *Dr. Ajeet Kumar Srivastava (Professor),* whose invaluable guidance and excellent cooperation have been a beacon of limelight throughout this academic journey. His continuous encouragement, insightful advice, profound expertise, and unwavering belief in my potential have been instrumental in crafting this thesis. He guided me with his characteristic wisdom and patience, embracing all my limitations while honing my research skills with the utmost affection. He inculcated in me an unfathomable admiration for scholarly diligence and intellectual curiosity. Indeed, without his generous support and guidance, it would not have been possible for me to complete this work.

I wholeheartedly thank the Research Advisory Committee (RAC), especially *Dr. Mukesh Kumar,* for their thoughtful suggestions and constructive criticism, which significantly refined the direction and success of my research work. I also express special thanks to *Dr. Kailash Chandra Juglan (HOS)* for providing the necessary facilities to conduct this research. I would also like to thank all the faculty members of *the Department of Physics, School of Chemical Engineering and Physical Sciences, Lovely Professional University*. I feel highly privileged to have the honor to acknowledge D*r. Gaganpreet Kaur (Crdp, Lovely Professional University), Dr. Sachin Kumar Godara (Dept. of Chemistry, GNDU, Amritsar),* and *Dr. Basharat Ahmed Want (Dept. of Physics, University of Kashmir)* for providing their valuable characterization facilities.

I am profoundly grateful to my parents, *Mr. Gh Quadir Khan* and *Mrs. Fatima Begum,* for their invaluable support and blessings. Mere words can't fully express the depth of my extreme gratitude to my parents, whose unwavering love and sacrifices have been the cornerstone of my research journey. They have been my guiding light, lifting me during moments of doubt and celebrating every milestone with unmatched pride. Their trust in my abilities has been my greatest strength, propelling me forward despite challenges during this revolutionary progression. This accomplishment is a testament to their endless support and the invaluable lessons that have shaped my journey.

I owe immense gratitude to my esteemed siblings and sisters-in-law, *Mr. Zafar Ahmed Khan* and *Mrs. Zamrooda Begum; Mr. Reyees Ahmed Khan* and *Mrs. Bilkiss Jan* for their steady encouragement, timely support, unconditional love, and moral support, without whom I would never have enjoyed so many opportunities. To my cherished brother-in-law

and sister, *Mr. Masroor Ahmad Bhat* and *Mrs. Shaheena Akhter,* I extend my boundless thanks for their prayers, optimism, and the warmth they have infused into every step of this odyssey despite arduous days.

No words can sufficiently express my gratitude to my dearest wife, *Ms Bilkees Bano,* whose unwavering patience, sacrifices, care, and endless support have been my anchor. Her firm belief in me during exhaustion and self-doubt transformed challenges into triumphs. This milestone is as much hers as it is mine. I am equally indebted to my father-in-law, *Mr. Abdul Majeed Najar,* who deserves recognition for his wisdom and steadfast belief in my capabilities throughout my research odyssey, which inspired me to work tirelessly to accomplish this task.

A special mention goes to my beloved nieces/nephews *Mohsib Masoor Bhat, Farhan Ahmad Bhat, Zainab Zafar, Zeeyan Zafar Khan, Mehza Reyees, and Mohammad Milhaan Khan,* whose innocence, laughter, and boundless energy have been a source of pure joy and motivation throughout this journey. Their cheerful presence has lightened even the most stressful days, reminding me of the beauty of perseverance and the importance of cherishing every moment. This accomplishment is as much for them as it is for me.

I particularly thank my colleagues and friends *Dr. Latief Mohi Ud din, Dr. Aajaz Ahmad Teali, Dr. Azhar Yousuf Tantary, Dr. Hamnesh Mahajan, Dr. Gulzar Ahmad Lone, Dr Umer Mushtaq*, *and Zubair-Ul-Islam* for their camaraderie, stimulating discussions, and shared laughter. Their companionship turned arduous days into memorable experiences, and their constructive feedback often illuminated new perspectives.

Lastly, I acknowledge the countless researchers, authors, and mentors whose work laid the foundation for this thesis. Inspired by the legacy of brilliant intellects, I am humbled by the collective pursuit of knowledge that makes academic endeavors like this possible.

Dated: **Mohd Rouf Khan**

Reg. No. 12015311

Abstract

The rising global energy and environmental challenges, caused by rapid population expansion, demand the development of sophisticated energy storage technologies beyond traditional fuel cells and batteries. This study examines energy storage devices, notably supercapacitors (SCs), considering their unique blend of high-power density, extended cycle life, quick charge/discharge rates, and enhanced energy density, establishing them as a bridge between conventional capacitors and batteries. Despite its advantages, modern SCs encounter challenges concerning cost, manufacturability, stability, and environmental effects. Spinel ferrites provide affordability and magnetic separation capabilities, with metal-doped spinel ferrites further strengthening magnetic, electromagnetic, and chemical stability. Simultaneously, two-dimensional (2D) materials, notably reduced graphene oxide (rGO), are promising for their large surface area, conductivity, and mechanical robustness in energy storage. However, rGO alone sometimes falls short of the necessary power and energy capacity. To circumvent these restrictions, this thesis suggests an effective approach: fabricating nanocomposites of spinel ferrites and rGO. This technique exploits the complementary attributes of both materials to develop unique electrode compounds with outstanding charge storage capacity. The major goal is to develop high-performance, cost-effective SC electrodes employing rGO and mixed spinel ferrite nanoparticles, aiming for higher power and energy density, specific capacitance, and cycle stability using simple, industrially viable approaches. To validate this, rare-earth doped spinel ferrites, mixed spinel ferrite nanoparticles, rGO, and their nanocomposites were synthesized and electrochemically tested for their applicability as supercapacitor electrode materials.

This research work introduces lanthanum-doped copper-cobalt spinel ferrites ($Cu_{0.79}Co_{0.21}La_xFe_{2-x}O_4$), zinc-doped manganese-nickel spinel ferrite ($Zn_{0.1}Mn_{0.4}Ni_{0.5}Fe_2O_4$) nanoparticles, rGO, and $Zn_{0.1}Mn_{0.4}Ni_{0.5}Fe_2O_4$/rGO (ZMNFG) nanocomposite as cost-effective electrode materials designed to store energy and deliver power efficiently. The above $Cu_{0.79}Co_{0.21}La_xFe_{2-x}O_4$ and $Zn_{0.1}Mn_{0.4}Ni_{0.5}Fe_2O_4$ spinel ferrites prepared through sol-gel auto-combustion approach, rGO using modified hummers method, and the ZMNFG nanocomposite was created through a physical blending approach. The synthesized materials underwent extensive characterization via various techniques such as X-ray Diffraction (XRD) analysis, Vibrating Sample Magnetometry (VSM), Fourier Transform Infrared (FTIR) and Raman Spectroscopic analysis, Impedance Analyzer, Field Emission Scanning Electron (FESEM) Microscopy coupled with Energy Dispersive X-ray (EDX) analysis, Cyclic

voltammetric (CV) analysis, Electrochemical Impedance Spectroscopic (EIS) analysis, and Galvanostatic Charge-Discharge (GCD) analysis to determine their structural, magnetic, elemental, vibrational, dielectric, morphological, and electrochemical properties.

This research presents the successful synthesis of $Cu_{0.79}Co_{0.21}La_xFe_{2-x}O_4$ ($0.0 \leq x \leq 0.8$) nanoparticles via the sol-gel auto-combustion technique, with varying La^{3+} dopant concentrations. In this study, the estimated crystallite size (D) ranges from 27.92 nm to 40.90 nm. The microstructural parameter determination in XRD data was improved using Rietveld refinement. FTIR spectra exhibit two distinct metal stretching vibrational bands within (400 - 600) cm^{-1} range, a characteristic fingerprint region for all ferrites. FESEM analysis unveils that particle agglomeration occurs because of magnetic interactions, and non-uniform distribution of average particle sizes ranging from (1.06 - 1.87) μm. EDX validates the chemical composition's accuracy. Owing to the dilution effect resulting from the introduction of non-magnetic La^{3+} ions into the ferrite structure, there is a reduction in the saturation magnetization value, decreasing from 37.28 to 6.24 emu g^{-1} in the VSM study. Dielectric studies revealed that the dielectric constant's real part (ε') decreases with frequency and stabilizes beyond 1 MHz, demonstrating enhanced polarization with increased La^{3+} ion concentration. Likewise, the dielectric constant's imaginary part (ε'') showed high values at low frequencies, and dropped drastically as the frequency increased, indicating significant polarization mechanisms. At low frequencies, the loss tangent ($tan\ \delta$) reaches its maximum due to thermally activated charge carriers and structural defects, while higher frequencies reveal reduced losses attributed to charge hopping and dipole alignment mechanisms. AC conductivity was observed to rise with increasing frequency and La^{3+} ion incorporation, facilitated by enhanced polaron hopping and reduced grain boundary resistance, highlighting its potential for frequency-dependent applications. The electrochemical analysis showcases the impressive characteristics of newly synthesized ferrites, highlighting a significant specific capacitance (C_S) of 540.0 F g^{-1}. This finding suggests that lanthanum-doped copper-cobalt spinel ferrites have substantial potential for use in supercapacitor applications for energy storage.

Furthermore, another research work reports the synthesis of $Zn_{0.1}Mn_{0.4}Ni_{0.5}Fe_2O_4$ (ZMNF) nanoparticles via sol-gel auto-combustion method, rGO using modified hummers method, and $Zn_{0.1}Mn_{0.4}Ni_{0.5}Fe_2O_4$/rGO (ZMNFG) of ratio (1:3) nanocomposite via physical blending method. XRD analysis was conducted on GO, rGO, $Zn_{0.1}Mn_{0.4}Ni_{0.5}Fe_2O_4$ (ZMNF) nanoparticles, and the $Zn_{0.1}Mn_{0.4}Ni_{0.5}Fe_2O_4$/rGO (ZMNFG) nanocomposite to verify the

crystalline structure and ensure phase purity across all samples. GO exhibited two peaks, a sharp peak (001) and a less intense peak (100) at diffraction angles (2θ = 10.52˚) and (2θ = 42.36˚) respectively, that are indicative of oxygen functional groups. Likewise, in the case of rGO, two peaks (002) and (100) occurred at diffraction angles (2θ = 23.51˚) and (2θ = 43.14˚) respectively, demonstrating the successful reduction process through thermal treatment. The ZMNF nanoparticles showed intense peaks confirming a single-phase cubic structure with excellent crystallinity. The ZMNFG nanocomposite exhibited enhanced crystallite size (31.10 nm) compared to ZMNF nanoparticles (20.25 nm), suggesting strong interactions between ZMNF and rGO. Raman spectroscopy confirmed the successful reduction of graphene oxide (rGO), showing a D band at 1323.20 cm^{-1} and a G band at 1593.64 cm^{-1}. FTIR spectroscopy confirmed the vibration modes and chemical bonds in ZMNF nanoparticles, rGO, and the ZMNFG nanocomposite. The spectra revealed characteristic absorption bands indicative of metal-oxygen bonds in ZMNF, the restoration of graphitic structure in rGO, and combined peaks in the ZMNFG nanocomposite, verifying its successful synthesis and structural integration. FESEM analysis revealed unique morphologies of ZMNF nanoparticles, rGO, and ZMNFG nanocomposite while EDX analysis confirmed the elemental composition of ZMNFG nanocomposite. The ZMNFG nanocomposite exhibited a complex structure integrated with rGO and ZMNF nanoparticles, contributing to enhanced properties and high purity. VSM analysis showed that ZMNF nanoparticles and ZMNFG nanocomposite exhibit superparamagnetic behavior, with significant reductions in magnetic properties of ZMNFG nanocomposite compared to ZMNF nanoparticles due to the incorporation of non-magnetic rGO. Dielectric study of ZMNF nanoparticles, rGO, and ZMNFG nanocomposite exhibited frequency-dependent capacitance, real permittivity (ε'), and imaginary permittivity (ε'') characteristics. ZMNF nanoparticles demonstrated low capacitance and a simple dielectric response with a gradual decline in ε' as frequency increased, suggesting typical dielectric relaxation. In contrast, rGO and ZMNFG displayed negative permittivity at low frequencies, indicating unique polarization effects and resonance mechanisms. The imaginary permittivity (ε'') analysis showed that ZMNF nanoparticles, rGO, and ZMNFG nanocomposite exhibit varying dielectric loss behaviors, with significant energy dissipation at low frequencies and stabilization at high frequencies. Loss tangent ($tan\ \delta$) plots highlighted relaxation processes in rGO and ZMNFG nanocomposite, while ZMNF nanoparticles showed lower conduction losses. These findings reveal distinct dielectric behaviors and relaxation mechanisms across the materials. The analysis of AC conductivity for ZMNF nanoparticles, rGO, and ZMNFG

nanocomposite revealed low conductivity at low frequencies, with rGO and ZMNFG exhibiting negative conductivity at low frequencies before transitioning to positive conductivity at higher frequencies, indicative of complex microstructural effects and charge carrier dynamics. The CV study indicated that the ZMNFG nanocomposite possesses a notable C_S value (513.78 F g^{-1}, at 5 mV s^{-1}), outperforming ZMNF nanoparticles as well as rGO electrodes, attributable to its improved conductivity and porous morphology. GCD evaluation further demonstrated the excellent C_S value (311.25 F g^{-1}, at 1 A g^{-1}) and discharge performance of ZMNFG nanocomposite, underscoring its potential for advanced electrochemical supercapacitors. In the EIS study, it was found that the ZMNFG nanocomposite electrode displayed desirable electrochemical properties with minimal equivalent series resistance (R_s = 0.084 Ω) and charge transfer resistance (R_{ct} = 1.88 Ω), enhancing ion diffusion and confirming its potential for energy storage applications.

Table of Contents

List of Tables

List of Figures

List of Acronyms and Abbreviations

Acronym and Abbreviations	*Expansion*
AC	*Alternating current*
AR	*Analytical Reagent*
ATR	*Attenuated total reflectance*
CCD	*Charge-coupled device*
CE	*Counter electrode*
CFEGs	*Cold field emission guns*
CNT	*Carbon nanotubes*
CPE	*Constant phase element*
CSIRO	*Commonwealth Scientific and Industrial Research Organization*
CV	*Cyclic voltammetry*
DC	*Direct current*
DI	*Deionized*
DUT	*Device under test*
EDLCs	*Electric double-layer capacitors*
EDX	*Energy dispersive X-ray Analysis*
EIS	*Electrochemical impedance spectroscopy*
EMF	*Electromotive force*
EMI	*Electromagnetic Interference*
ESDs	*Energy storage devices*
ESR	*Equivalent series resistance*
FESEM	*Field emission scanning electron microscopy*
Fig.	*Figure*
FTIR	*Fourier transform infrared spectroscopy*
GC	*Gas chromatography*
GCD	*Galvanostatic charge-discharge*
GO	*Graphene oxide*

GoF	*Goodness of Fit*
HEVs	*Hybrid Electric Vehicles*
ICDD	*International Centre for Diffraction Data*
IEO	*International Energy Outlook*
IR	*Internal resistance*
JCPDS	*Joint Committee on Powder Diffraction Standards*
KBr	*Potassium Bromide*
KOH	*Potassium Hydroxide*
MD	*Multi-domain*
mins	*minutes*
MRI	*Magnetic resonance imaging*
MS	*Mass spectrometry*
NCC	*Nippon Chemi-Con*
NEC	*Nippon Electric Company*
NMP	*N-methyl-2-pyrrolidone*
PRI	*Pinnacle Research Institute*
PSD	*Pseudo-single domain*
PVDF	*Polyvinylidene fluoride*
pH	*Potential of hydrogen*
quads BTU	*Quadrillion British thermal units*
RE	*Reference electrode*
rGO	*Reduced graphene oxide*
SCs	*Supercapacitors*
SD	*Single domain*
SEM	*Scanning electron microscopy*
SFs	*Spinel ferrites*
SOHIO	*Standard Oil Company of Ohio*
TEM	*Transmission electron microscopy*
TMDs	*Transition metal dichalcogenides*

Viz.	*namely*
VOCs	*Volatile organic compounds*
VSM	*Vibrating sample magnetometer*
WE	*Working Electrode*
Wt.	*Weight*
XRD	*X-ray Diffraction*
ZMNF	*Zinc-doped manganese nickel spinel ferrite nanoparticles*
ZMNFG	*Zinc-doped manganese nickel spinel ferrite/rGO nanocomposite*
2D	*Two-dimensional*

List of Symbols

Symbols	*Expansion*
ε_0	*Absolute Permittivity of Free Space (Vacuum Permittivity)*
σ_{ac}	*AC conductivity*
ω	*Angular frequency*
K_1	*Anisotropy constant*
I_{pa}	*Anodic peak current*
E_{pa}	*Anodic peak voltage*
H	*Applied magnetic field*
N_A	*Avogadro's constant*
μ_B	*Bohr Magnetron*
θ	*Bragg's angle*
ρ_b	*Bulk density*
C	*Capacitance*
I_{pc}	*Cathodic peak current*
E_{pc}	*Cathodic peak voltage*
R_{ct}	*Charge transfer resistance*
χ^2	*Chi-squared*
H_c	*Coercivity*
A	*Cross-sectional area*
D	*Crystallite size*
I	*Current*
I_m	*Current density*
2θ	*Diffraction angle/Peak position*
Δt	*Discharging time*
δ	*Dislocation density*
E_{2g}	*Doubly Degenerate Vibrational Mode*
E_d	*Energy Density*

R_s	*Equivalent series resistance*
R_{exp}	*Expected R-factor*
f	*Frequency*
$I(\omega)$	*Frequency dependent current*
$V(\omega)$	*Frequency dependent voltage*
β	*Full width at half maximum*
h	*Height of pellet*
sp^2	*Hybridization of one s and two p orbitals*
j	*Imaginary number*
ε''	*Imaginary part of permittivity*
Z	*Impedance*
L	*Inductance*
d	*Interplanar spacing (XRD)*
a	*Lattice constant*
$\tan\delta$	*Loss tangent*
H_m	*Magnetic Field Value*
M-H curve	*Magnetic hysteresis curve*
χ	*Magnetic susceptibility*
M	*Magnetization*
m	*Mass of active electrode material (Loaded mass)*
m_p	*Mass of pellet*
M_{tetra}-O	*Metal-oxygen bond in tetrahedral coordination*
M_{octa}-O	*Metal-oxygen bond in octahedral coordination*
(hkl)	*Miller indices*
M	*Molecular weight*
B-site	*Octahedral site*
v_2	*Octahedral (Second Absorption) band*
n	*Order of diffraction*
%	*Percentage*

δ	*Phase difference (Dielectric)*
π	*Pi*
P (%)	*Porosity*
ΔV	*Potential window*
P_d	*Power Density*
R_p	*Profile R-factor*
r	*Radius of pellet*
X	*Reactance*
ε'	*Real part of permittivity*
ε	*Relative Dielectric constant (Dielectric)*
M_r	*Remnant magnetization*
R	*Resistance*
M_s	*Saturation magnetization*
υ	*Scan rate*
K	*Shape factor of crystallite*
dM/dH	*Slope of Magnetization Curve*
C_S	*Specific capacitance*
S	*Specific surface area*
R_{sq}	*Squareness ratio*
ε	*Strain (XRD)*
A-site	*Tetrahedral site*
d	*Thickness of Pellet (Dielectric)*
V	*Voltage*
V_{cell}	*Volume of unit cell*
Wt. %	*Weight percent*
R_{wp}	*Weighted Profile R-factor*
ρ_x	*X-ray density*
λ	*X-ray wavelength*

List of Units

Units	*Expansion*
A	*Ampere*
Å	*Angstrom*
cm	*Centimeter*
cc	*Cubic centimeter*
^{o}C	*Degree Celsius*
emu	*Electromagnetic unit*
eV	*Electron Volt*
erg	*Ergon*
F	*Farad*
g	*Gram*
Hz	*Hertz*
kg	*Kilogram*
KHz	*Kilohertz*
KJ	*Kilojoule*
KOe	*Kilo-Oersted*
MHz	*Megahertz*
MJ	*Megajoule*
m	*Meter*
μ_m	*Micrometer (Micron)*
mg	*Milligram*
ml	*Milliliter*
mV	*Millivolt*
nm	*Nanometer*
Oe	*Oersted*
Ω	*Ohm*
PJ	*Petajoule*

s	*Second*
V	*Volt*
W	*Watt*
Wh	*Watthour*

CHAPTER 1

Introduction

1.1 General Background

The introduction of this thesis begins with a brief overview of key areas such as energy storage devices (ESDs), spinel ferrites (SFs), two-dimensional (2D) materials especially reduced graphene oxide (rGO), and their composites. One of the most significant challenges in the 21st century is the growing demand for energy alternatives that are renewable and eco-friendly. Energy is often regarded as the cosmic spark that ignites the universe. It is at the heart of modern society as well as development. The alarming growth of the global population along with the ongoing energy crisis have intensified concerns about the generation and consumption of energy. According to the U.S. Energy Information Administration's International Energy Outlook 2017 (IEO2017), worldwide energy consumption is likely to rise by 28 % from 575 quadrillion British Thermal units (quads BTU) in 2015 up to 736 quads BTU by 2040 [1]. As per the statistical data, India has witnessed a robust increase in energy consumption, rising from 25,805 petajoules (PJ) in 2012–13 to 33,508 petajoules (PJ) in 2021–22. Despite a slight decrease in energy consumption to 30,354 PJ in 2020–21 from 32,729 PJ in 2019-20 due to the COVID-19 pandemic, which triggered negative growth across all the sectors, including industrial, agricultural, health, and others. Notably, the overall energy usage or consumption upsurges from 30,354 PJ in 2020–21 to 33,508 PJ in 2021–22, showing a substantial rise of 10.39 % [2]. The world's economic expansion, industrial revolution, and progressive lifestyle have all significantly relied on non-renewable fossil fuels [3]. However, the increasing depletion of these non-sustainable energy sources along with population growth, climate change, and environmental pollution collectively pose a severe threat to the global community [4]. Consequently, these factors demand an urgent need to think about alternate renewable energy remedies by developing energy storage devices using novel nanomaterials [5,6]. The fabrication of efficient as well as sustainable ESDs including capacitors, batteries, fuel cells, and supercapacitors (SCs) is essential for unlocking huge potential in renewable sources of energy, thereby addressing future energy needs [7,8]. Among these efficient ESDs, supercapacitors (SCs) have emerged as a potential choice that bridges the distance between batteries and traditional (conventional) capacitors [9].

The SCs deliver fast charging-discharging rates, enormous power density (P_d), cycling stability, and excellent protection as well, which makes them desirable for an extensive range of applications. The electrode material is the fundamental component that defines the performance of SCs. In the quest for novel materials, humongous research activities were focussed on enhancing the specific capacitance (C_S) and electrical conductivity of the electrode materials for promising applications in SCs. Furthermore, spinel ferrites and 2D materials, particularly rGO, gained considerable attention for serving as potential electrode materials for energy storage supercapacitors (SCs) owing to their unique attributes, including high specific surface area, good electrical conductivity, and structural stability [10].

This thesis explains how we prepare different spinel ferrites and rGO via sol-gel auto-combustion method and modified hummers method respectively and explore the behavior of these nanomaterials with various characterization techniques such as structural, magnetic, dielectric, and electrochemical. Furthermore, this thesis explores the fabrication of supercapacitor electrodes by the composites (insertion of rGO within the spinel ferrite matrix), which have shown encouraging results in boosting energy storage and power delivery capabilities.

1.2 Energy Storage Devices

In this era of modernization, energy storage devices (ESDs) are essential components for the generation, conversion, and storage of electrical energy to fulfill future necessities. ESDs hold significant importance in our daily lives. ESDs could retain energy in numerous aspects including electrochemical (using batteries, fuel cells, and SCs), thermal (using solar thermal power), hydrogen storage, mechanical (via kinetic and gravitational force), etc. As already stated in the general background section, ESDs are categorized into four main classes viz capacitors, batteries, fuel cells, and SCs. In conventional capacitors, energy is stored electrostatically between a pair of conducting plates that are separated via dielectric material. On the flip side, conventional capacitor storage mechanism occurs through a non-faradic process which means there is no transfer of electrons (charge) in between plates and dielectric medium. Besides, the small surface area in conventional capacitors provides a high level of P_d at the cost of relatively limited (low) energy density (E_d). Nonetheless, batteries store energy via chemical processes and are renowned for their high E_d, thereby corresponding to their long-term energy storage capabilities [11,12]. Moreover, fuel cells utilize

electrochemical reactions to transform chemical energy directly into electrical energy. They are renowned for their potential to deliver consistent power with high efficiency, effective emission control, and minimal pollution if fuel is supplied. This makes fuel cells ideal for applications such as transportation, backup power systems as well as stationary power generation [13,14]. Supercapacitors (SCs) often referred to as ultracapacitors or electric double-layer capacitors or electrochemical capacitors store energy due to the electrostatic separation of charges (electrostatic attractive or repulsive forces) at the electrode and electrolyte interface. This technique includes the development of an electrical double-layer where ions coming from the electrolyte get adsorbed by the electrode surface. This mechanism allows SCs to unite collaboratively the huge P_d of capacitors with the huge E_d of batteries, thus forming a hybrid device by integrating the properties of both devices (capacitors as well as batteries) [15].

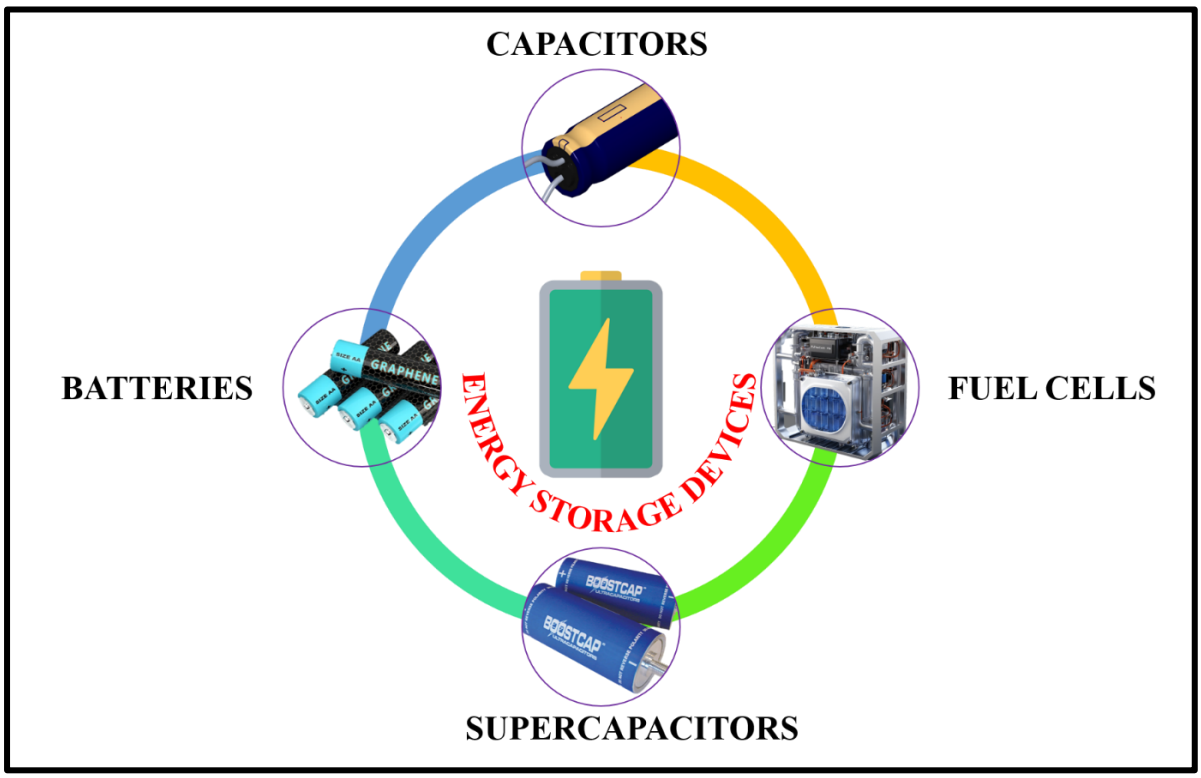

Fig. 1. 1: *Energy storages devices*

Compared to the above energy storage devices (ESDs) shown in Fig. 1.1, only three ESDs such as viz batteries, fuel cells, and SCs are extremely essential and advanced contributors in the realm of energy conversion and storage. Despite this, SCs and batteries attain respectable attention among researchers because of their extensive range of applications

and potential for groundbreaking future advancements. As mentioned in the general overview section, a supercapacitor (SC), an example of innovative technology is considered to be unique that fills the gap between batteries and traditional capacitors. Moreover, SCs are presently receiving enormous attention because of their exceptional characteristics which include high P_d, rapid charge/discharge rates, and long cyclic life [16–18]. A suitable and effective approach to evaluate and compare the operational characteristics of several ESDs such as capacitors, batteries, fuel cells, and SCs, by analyzing the plot of P_d against E_d, depicted in Fig. 1.2, known as Ragone plot [19]. It is obvious from the plot that SCs offer better E_d in contrast to traditional capacitors and higher P_d in comparison to batteries and fuel cells, thus occupying an intermediate position between these ESDs. However, due to the unique positioning and notable properties of SCs, they are suitable for diverse applications including hybrid electric vehicles, portable and wearable electronic devices, urban rail transit systems, smart grids in aircraft, industrial scale, defence, medical fields, etc [20–22].

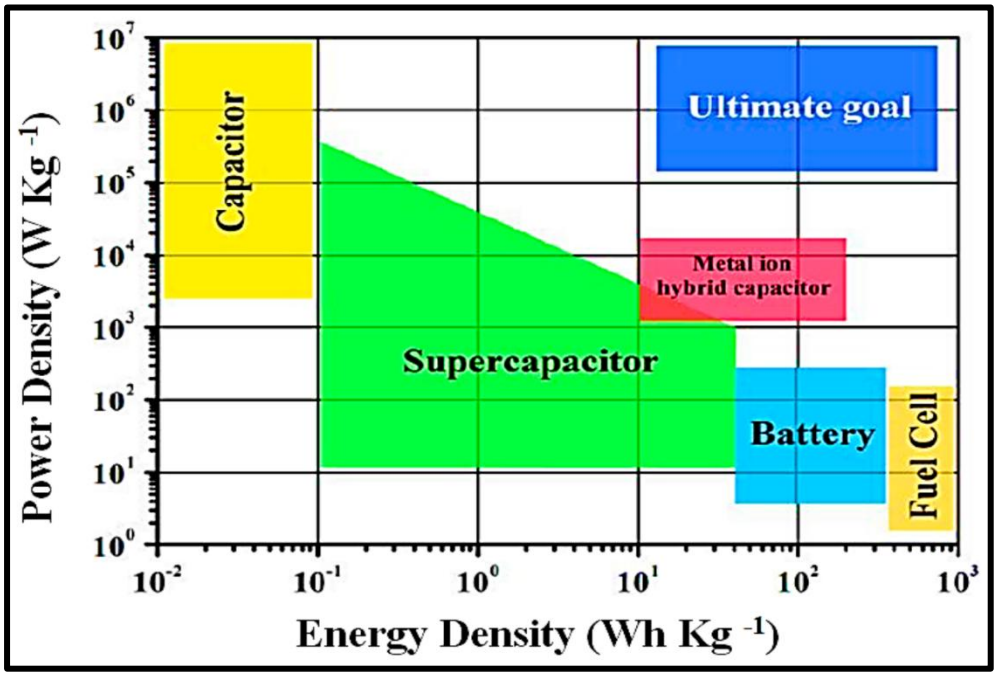

Fig. 1. 2: *Ragone plot illustrating power density as a function of energy density for several energy storage devices (ESDs)[19]*

1.3 Supercapacitors and their Classification

As mentioned in the general overview section, a supercapacitor (SC), an example of innovative technology is considered to be unique that bridges the gap between batteries and traditional capacitors. Moreover, SCs are presently receiving enormous attention because of their exceptional characteristics which include high P_d, rapid charge/discharge rates, and long cyclic life [16–18]. The compact-designed electrode layers of SCs have a large surface area, contributing to their much higher C_S values than traditional ones. Supercapacitors provide exceptional C_S values in contrast to traditional capacitors owing to their large surface area and densely packed electrode layers.

Based on charge storage mechanism and active electrode materials, SCs can be classified into three categories viz electric double layer capacitors (EDLCs), pseudo-capacitors, and hybrid capacitors [8] as shown in Fig. 1.3.

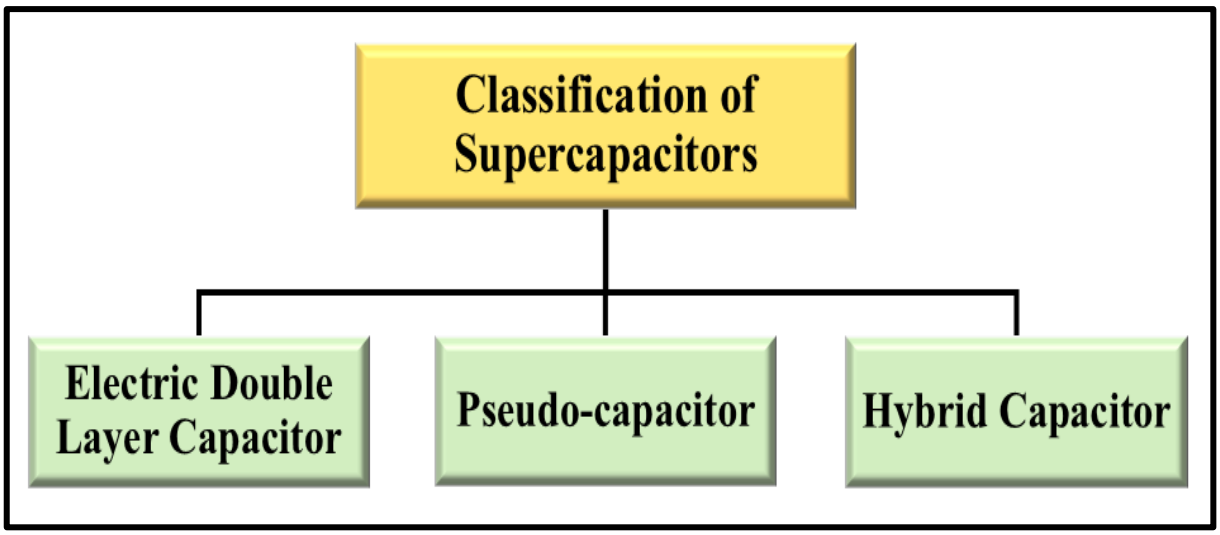

Fig. 1. 3: *Types of supercapacitors*

1.3.1 Electric Double-Layer Capacitor

The energy storage process in an electric double-layer capacitor (EDLC) resembles to the conventional capacitors. However, conventional capacitor normally uses a dielectric material sandwiched between two metallic plates to store charge, while the charge storage in EDLC happens electrostatically and is based on non-faradaic process. The charge storage mechanism in EDLC results from the build-up of a double layer at the electrode and electrolyte interface [23]. An EDLC structure comprises a pair of conducting electrodes having high surface area

and an electrolyte solution to offer a channel for the ions. Additionally, the inclusion of a dielectric layer (separator) between the electrodes lowers the possibility of contact between the two electrodes. In the context of an EDLC, the applied voltage induces the ion transition towards electrodes (the positive ions within the electrolytes shift toward the negatively charged electrode and vice versa). This process builds an additional layer of opposing charges at the corresponding surfaces of the aforementioned electrodes, without any chemical change [24]. Thus, an electric double-layer capacitor provides a quick response for charging and discharging cycles due to which energy is stored effectively within a short period and in a high-power density range, thus making an EDLC valuable in numerous applications concerning energy storage, particularly because of their high P_d compared to conventional capacitors [25]. Figure 1.4 demonstrates the working mechanism of charge storage in an EDLC.

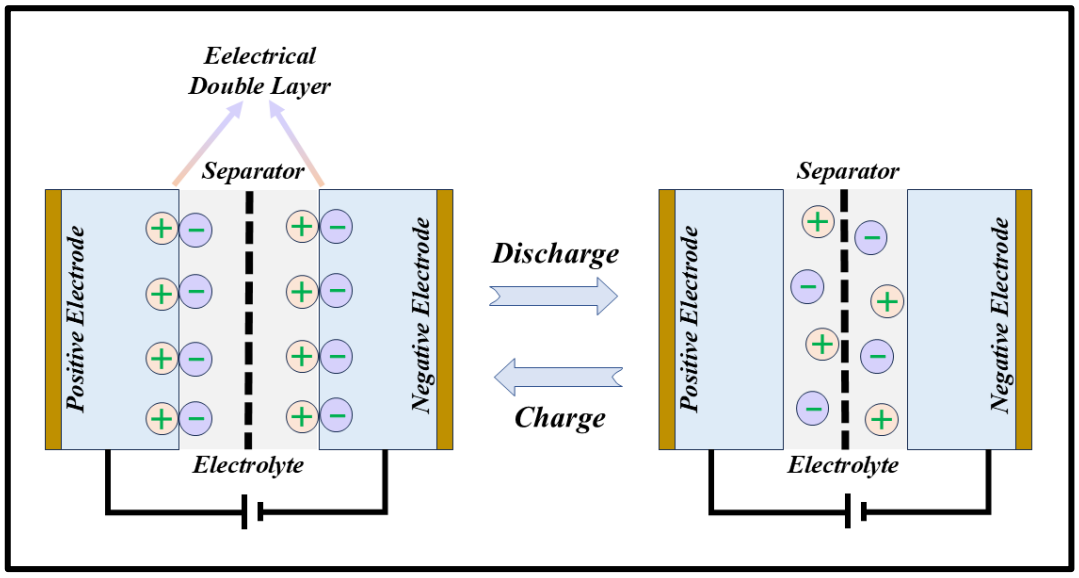

Fig. 1. 4: *Charge storage mechanism of electric double-layer capacitors (EDLC) [26]*

1.3.2 Pseudo-capacitor

Despite electric double-layer capacitors which rely solely on electrostatic attraction, pseudo-capacitors utilize fast, reversible redox reactions on the electrode surfaces to store additional charge via chemical reactions [27,28]. This process allows pseudo-capacitors to achieve higher energy densities compared to EDLCs, while still maintaining faster charge-discharge rates than batteries. The working of a pseudo-capacitor uses transition metal oxides together with conducting polymers as electrode materials to store electrical energy employing charge transfer between electrodes and electrolytes through a faradaic process [24] as depicted in Fig.1.5.

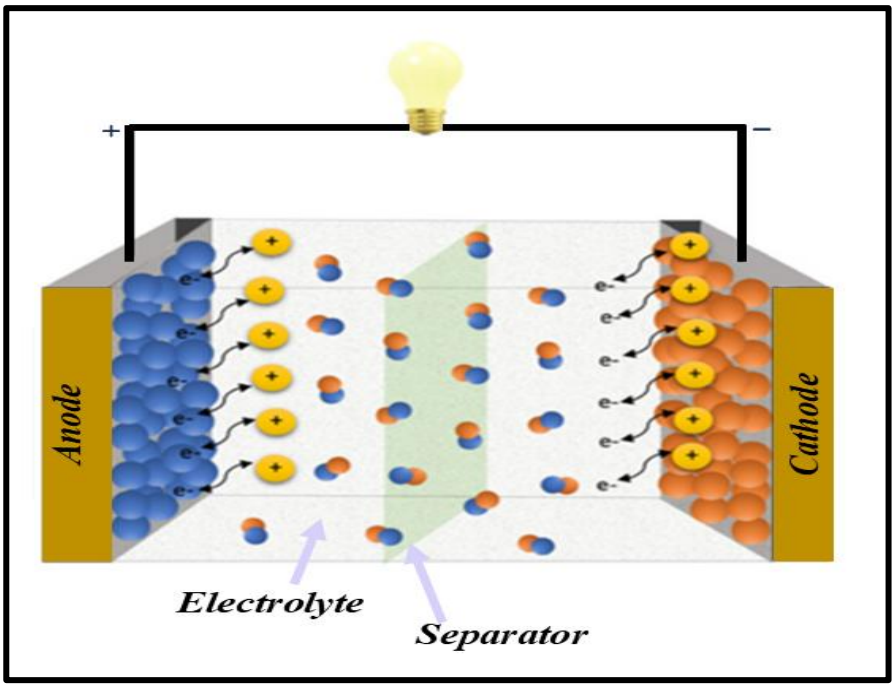

Fig. 1. 5: *Charge storage mechanism of pseudo-capacitor [29]*

Pseudo-capacitors are efficient energy materials with quick charge-discharge rates, and higher energy density and capacitance. However, they face a major drawback in mechanical and cycling stability with low P_d and degradation resulting from redox reactions, making it an important area of investigation to enhance such devices of energy storage [30].

1.3.3 Hybrid Capacitor

As an efficient alternative energy storage device, the high P_d together with E_d properties of hybrid capacitors are preferable over EDLCs and pseudo-capacitors [31]. The composite electrode of a hybrid capacitor is fashioned from two dissimilar electrodes made from different materials including metal oxides and carbon-based materials (see Fig.1.6). The main advantage of a hybrid capacitor is its charge storage mechanism that relies on both faradaic and non-faradaic processes [32]. Contrary to EDLCs and pseudo-capacitors, hybrid capacitors offer excellent cycling stability and durability [33].

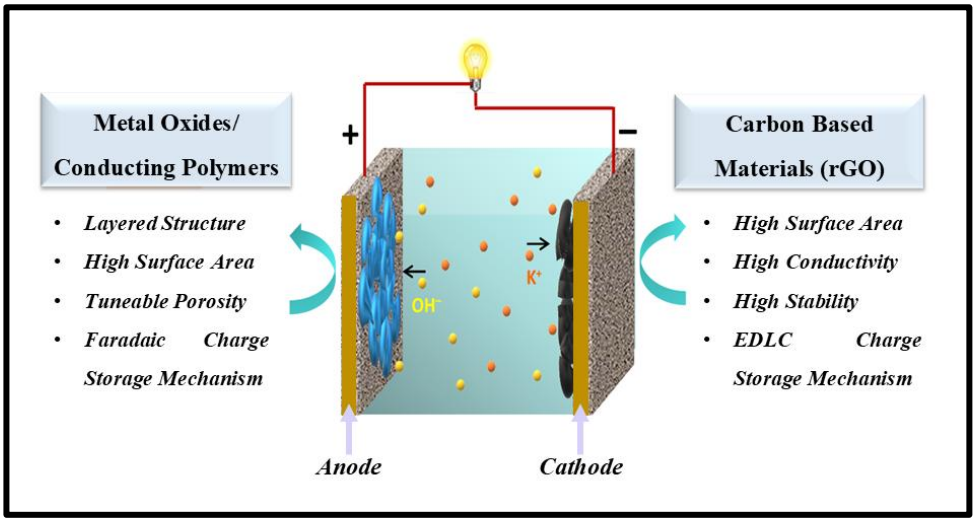

Fig. 1. 6: *Schematic representation of hybrid capacitors [34]*

In this thesis, we focus on different possible combinations of graphene-based electrode materials, metal oxide-based electrode materials, and electrolyte materials in quest of further enhancement of high E_d, P_d, and stability.

1.4 Electrode Materials for Supercapacitors

The SC's electrochemical capabilities mainly depend upon the choice of appropriate electrode materials. Various commercially available electrode materials, for instance, carbon and some forms of carbon like activated carbon, carbon black, carbon foams, carbon aerogels, graphene, reduced graphene oxide, carbon nanotubes, etc are utilized in electric double-layer capacitors, while electrode materials viz metal oxides, and conducting polymers are employed in pseudo-capacitors [16]. Some of the features of these materials are higher conductivity, thermal stability, corrosion resistance, surface area, and porosity in comparison with other materials at relatively low cost [27,35].

1.4.1 Carbon-Based Materials

Due to the widespread use of fuel energy extracted from fossil resources, the scientific community has focused its research on improving materials with better electrochemical performance. Among the electrode materials utilized in EDLCs, the major focus shifted towards carbon-based materials including carbon nanotubes, carbon aerogels, carbon foams,

activated carbon, graphene (GO, and rGO), due to their remarkable thermal, mechanical, and electrical properties [36]. Moreover, the large surface area and high storage capacity made these carbon-based materials quite apt for efficient energy storage supercapacitors. More specifically, high conductivity, good chemical stability, and lightweight together with high surface area of graphene make it an active electrode material in the fabricating process of supercapacitors. However, the graphene sheet restacking results in the supercapacitor electrodes experiencing a significant reduction in surface area, leading to minimal ion transport, storage capacity, and adsorption efficiency [37].

To overcome this problem several attempts have been made to develop the composites of graphene with transition metal oxides together with conducting polymers, carbon nanotubes, and others. These composites enhance the power density by providing a small channel for the diffusion of electrolytic ions, and at the same time improve their accessibility, preventing agglomeration within the graphene sheets, and gathering the advantages of individual components [38,39].

1.4.2 Conducting Polymers

Conducting polymers are frequently employed as potential electrode materials because they are endowed with excellent stability, adaptability in mechanical properties, and superior electronic conductivity. They undergo electrochemical charge-discharge processes based on the redox mechanism where the ions penetrate the conducting polymer during oxidation followed by their expelling back into the electrolyte solution during reduction. Conducting polymers offer higher specific capacitance than carbon-based materials, but their mechanical stability is a concern due to stress from redox cycling. Moreover, the low cyclic stability, swelling, and shrinking of conducting polymers can reduce their performance, which can be addressed by incorporating metal oxides or carbon-based materials [39–41].

1.4.3 Metal Oxides

Metal oxides are an exciting prospect for pseudo-capacitive electrodes due to their conductivity, electrochemical stability, high C_S, high cyclic stability, superior E_d, and several oxidation states compared to carbon-based EDLC electrodes and conducting polymer-based electrodes. This enables them to be an appropriate candidate in high-performance energy storage applications. The most frequently used metal oxides for supercapacitor electrodes include ZnO_2, RuO_2, Fe_2O_3, Co_2O_3, NiO, V_2O_5, Fe_3O_4, MnO_2, Co_3O_4, SnO_2, IrO_2, MoO, MoO_2,

CuO and Cu_2O, extensively explored for their capabilities in energy storage advancements [39,42,43]. Among all aforementioned metal oxides, extensive research efforts have been carried out initially on the electrode material of ruthenium dioxide (RuO_2) which was considered to be the most preferable due to its ability to undergo fast reversible redox processes, excellent conductivity, long cycle life, high specific capacitance, extremely low equivalent series resistance (ESR) value, and broad operating potential window compared to other metal oxides [44]. Despite the merits of ruthenium dioxide (RuO_2), it has certain limitations such as being highly toxic, expensive, and rarely available compared to other metal oxides [45]. These limitations restrict the commercialized utilization of ruthenium dioxide (RuO_2) in energy storage applications, thus encouraging researchers to explore new materials as an alternative to ruthenium dioxide [46–48]. The electrode materials such as iridium dioxide (IrO_2) and cobalt oxide (CoO) considered to be promising alternatives owing to their remarkable C_S together with cyclic stability, however, potential degradation and elevated prices of these electrode materials hamper their extensive utilization in commercial applications. Subsequently, nickel oxide (NiO) and manganese dioxide (MnO_2) were explored because of their impressive capacitance and reasonable cost. However, the applicability of nickel oxide (NiO) was indeed restricted by its limited electrical conductivity, along with its narrow potential window. This limitation hinders its performance in electrochemical devices where higher conductivity and a wider potential window are required for optimal performance. Thus, the research is focused on identifying cost-effective, high-specific capacitance materials suitable for commercial applications [42].

Manganese dioxide (MnO_2) on the other hand, was believed to be a potential electrode material compared to others because of its superior theoretical capacitance, large potential window, affordable cost, and eco-friendly nature [39]. Irrespective of these advantages of manganese dioxide (MnO_2), it has low conductivity, a low chemical stability, thereby limiting its performance in electrochemical applications. In order to overcome the poor electrical conductivity and chemical stability of manganese dioxide, it is crucial to improvise its surface area by synthesizing mesoporous nanostructures. Besides this, the merger of manganese dioxide with other metal oxides viz iron (Fe), copper (Cu), cobalt (Co), zinc (Zn), nickel (Ni), and others can further enhance its conductivity [49]. Iron-based electrode materials such as ferric oxide (Fe_2O_3), in particular, have been recognized as viable alternatives for supercapacitor applications because of their notable theoretical capacitance, widespread availability, and eco-friendly characteristics. Nevertheless, the single and binary transition metal oxides as electrode materials limit their conductivity and specific capacitance [43].

Research efforts have been made to address these issues by combining mixed transition metal oxides, thus facilitating quick redox responses along with higher specific capacitance than single and binary transition metal oxides. These mixed transition metal oxides, also called ternary metal oxides can exist in the form of perovskite structure and spinel structure.

Recently, the introduction of ferrites especially spinel ferrites such as manganese ferrite ($MnFe_2O_4$), zinc ferrite ($ZnFe_2O_4$), cobalt ferrite ($CoFe_2O_4$), nickel ferrite ($NiFe2O_4$), copper ferrite ($CuFe_2O_4$), nickel-copper ferrite ($Ni\text{-}CuFe_2O_4$), nickel-cobalt ferrite ($Ni\text{-}CoFe_2O_4$), and copper-cobalt ferrite ($Cu\text{-}CoFe_2O_4$) have gained immense interest as electrode materials due to their multiple oxidation states, electrical behavior, high stability and remarkable pseudocapacitive nature [43].

1.5 Ferrites

Ferrites, characterized by their dark grey or black color, are ceramic materials known for their hardness and brittleness. Their ferrimagnetic behavior categorizes them as magnetic materials, consisting primarily of ferric ions, hence the name "ferrite" derived from the Latin word "Ferrum". Ferrites can be produced in powder or thin-film form using various methodologies such as high-temperature solid-state reaction, coprecipitation, sol-gel synthesis, high-energy ball milling, pulsed laser deposition, and hydrothermal processes [50]. Ferrites exhibit insulating properties with moderate permittivity, high electrical resistivity, high magnetic permeability, low eddy currents, and minimal dielectric loss [51,52]. These diverse properties make them suitable for numerous applications across various disciplines [53]. Based on the properties of the magnetic field, ferrites can be categorized into soft and hard ferrites, while on a crystal structures basis, they are grouped into hexagonal ferrites, spinel ferrites, garnet ferrites, and ortho ferrites [54] as depicted in Fig 1.7.

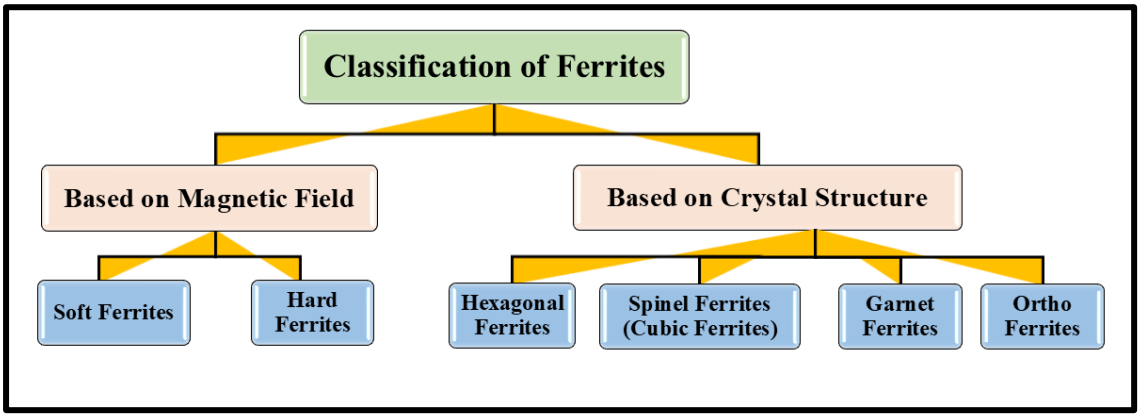

Fig. 1. 7: *Classification of ferrites*

Though all ferrites have magneto-dielectric characteristics, many researchers frequently employ spinel ferrites for applications involving energy storage due to the fact that they demonstrate outstanding magnetic and dielectric attributes over other ferrites. Moreover, SFs have moderate M_s, low H_c, high initial permeability, and remarkable stability, thereby making them befitting in diverse applications involving energy storage requirements [55].

1.5.1 Spinel Ferrites and their Crystal Structure

Spinel ferrites (SFs) belong to the class of metal oxides recognized for their remarkable magnetic characteristics and well-defined crystal structure. The structure of SFs is face-centered cubic with Fd3m as the space group, formed by the combination of iron oxide and various cations [56]. These cations can be either divalent, such as Cu^{2+}, Co^{2+}, Zn^{2+}, Cd^{2+}, Ni^{2+}, Mn^{2+}, Sr^{2+}, Ba^{2+}, Ca^{2+}, Mg^{2+} etc or trivalent, such as La^{3+}, Pr^{3+}, Ce^{3+}, Sm^{3+}, Eu^{3+}, Ho^{3+}, Dy^{3+}, Nd^{3+}, Gd^{3+}, Er^{3+} etc [57,58]. Chemical composition of SFs is expressed via AB_2O_4, where "A" and "B" symbolize cations involved in divalent and trivalent, respectively. The spinel structure is based on a close-packed arrangement of oxygen ions, with metal cations filling certain interstitial positions within this lattice [59,60].

The spinel structure comprises thirty-two closely packed oxygen anions to form a full structural unit cell. In this structure, there are two types of interstitial voids among these oxygen anions: tetrahedral voids or A-site and octahedral voids or B-site surrounded by four and six oxygen ions respectively. The cubic spinel ferrite unit cell consists of eight small cubes known as octants, and it possesses 64 tetrahedral sites, with 8 of them being occupied, and 32 octahedral sites, with 16 being occupied in it. All the ions are held in the octant body diagonal, and the octant on the privilege has a tetrahedral site in the middle, and four oxygen ions per octant, as shown in Fig. 1.8 [54,61]. The ions present in the tetrahedral position are called the “network formers” while the ions present at the octahedral position are also called the “network modifiers” [62].

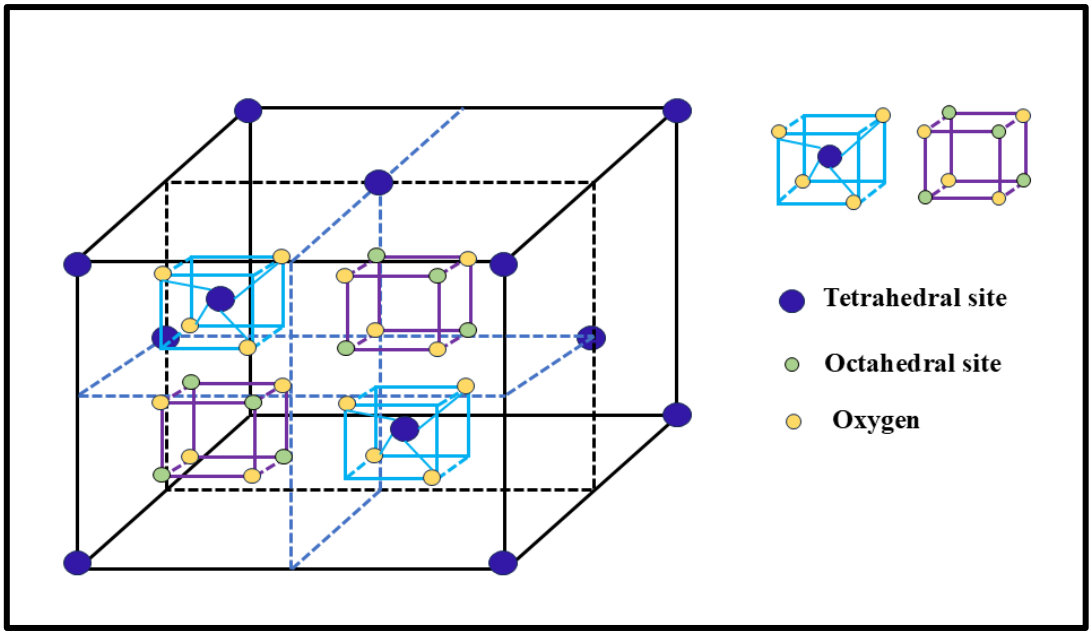

Fig. 1. 8: *Schematic representation of crystal structure of spinel ferrites representing tetrahedral and octahedral sites*

Spinel ferrites (SFs) follow the standard formula $M_x^{2+}Fe_{1-x}^{3+}[M_{1-x}^{2+}Fe_{1+x}^{3+}]O_4^{2-}$ [63]. In this structure, the cations positioned at tetrahedral sites are placed outside the brackets, while those at octahedral sites are inside the brackets. The degree of inversion, expressed by the variable "x" specifies the classification of SFs into three groups depending on the distribution of the metal cations within the unit cell such as normal SFs, inverse SFs, and mixed SFs, as depicted in Fig. 1.9 with detailed structural formulae [52,56]. In normal SFs, divalent (M^{2+}) cations occupy all tetrahedral sites, while trivalent (Fe^{3+}) cations occupy all octahedral sites. This specific cation distribution is exemplified by various materials, including zinc ferrite ($ZnFe_2O_4$) and cadmium ferrite ($CdFe_2O_4$) [64,65]. In inverse SFs, some trivalent (Fe^{3+}) cations migrate from the octahedral sites to occupy tetrahedral sites alongside divalent (M^{2+}) cations, with the remaining octahedral sites still occupied by trivalent (Fe^{3+}) cations. Some well-known examples of inverse SFs include magnetite (Fe_3O_4), nickel ferrite ($NiFe_2O_4$), copper ferrite ($CuFe_2O_4$), magnesium ferrite ($MgFe_2O_4$), and cobalt ferrite ($CoFe_2O_4$) [66]. However, mixed SFs exhibit a variable cation distribution (both divalent and trivalent) among tetrahedral and octahedral sites. Manganese ferrite ($MnFe_2O_4$) is one of the examples of mixed SFs [67,68]. These unique cation distributions and their characteristics impact the magnetic and electrochemical behavior of respective ferrites, resulting the exceptional capabilities in energy storage applications [54].

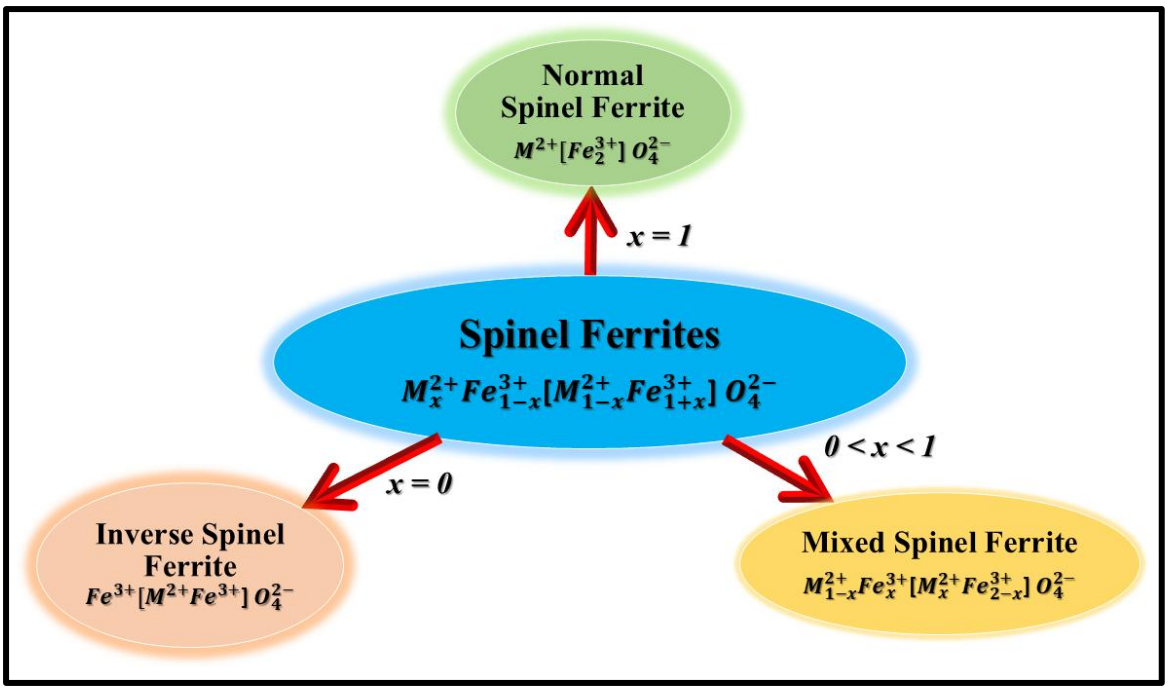

Fig. 1. 9: *Schematic representation of types of spinel ferrites*

1.6 Two-dimensional (2D) Materials

Two-dimensional materials emerge as a revolutionary class for supercapacitor electrodes because of their substantial electrochemical and physical properties. The two-dimensional (2D) materials, distinguished by their atomic-scale thickness exhibit exceptional electrical, optical, and mechanical properties. These unique features make them desirable for future applications in numerous fields such as electronics, sensing technologies, biomedical and drug delivery, photonics, energy storage and conversion, and optoelectronics. In particular, their advantages have made a profound impact on energy storage devices, making them more efficient and reliable. These 2D materials have grabbed substantial attention among researchers since the inception of graphene. Nowadays, for energy storage purposes, MXenes, black phosphorous, transition metal dichalcogenides (TMDs), and graphene oxide (GO), are extensively utilized [69,70].

Among the aforementioned 2D materials, reduced graphene oxide (rGO) stands out for its large surface area, high electrical conductivity, lightweight nature, and distinctive structure provide ultrathin layers and open frameworks for fast ion transport and charge storage, making them highly desirable for supercapacitor applications [71]. The usage of 2D materials especially rGO has drastically enhanced the efficacy of electric double-layer capacitors (EDLCs) and pseudo-capacitors, due to their flexibility and tuneable electrochemical

properties. Research efforts concentrate on optimizing these materials, either in their pure form or by amalgamation with other constituents, such as metal oxides, to enhance their overall power and energy densities [72].

1.6.1 Reduced Graphene Oxide

Graphene is among the most widely studied 2D materials which contains a monolayer of sp^2 hybridization of carbon configured in a honeycomb-like structure [73]. This material has received much attention for its excellent surface area, atomic-scale thickness, outstanding thermal and electrical conductivity, lightweight, and mechanical strength [74,75]. However, the synthesis of this material presents significant challenges, particularly when attempted on larger scales. Moreover, the tendency of graphene sheets to restack and agglomerate during cycling causes a reduction in surface area, limits ion transport, and severely influences the capacity to store energy. Consequently, researchers have explored alternate graphene derivatives like GO, and rGO, which are comparatively easier to yield in large scale [76].

GO, recognized as graphene's oxidized variant contains numerous oxygen-rich functional groups, which increase its solubility and processability compared to pristine graphene. However, the insulating or semi-insulating behavior of GO, affected by the existence of functional groups, limits its electrical conductivity and causes structural defects [77–79]. Moreover, graphene oxide has poor mechanical strength and a low carbon-to-oxygen ratio, which limits its use in various energy domains [80]. To solve these limitations, researchers have turned their emphasis toward rGO, a modified version of GO [81]. The conversion to GO and rGO from graphene was done using a modified hummers approach, in which oxidized functional groups are removed from graphene oxide through reduction, and the so obtained rGO is slightly different from undoped graphene due to certain imperfections and oxygen functional groups [82,83] as illustrated in Fig. 1.10.

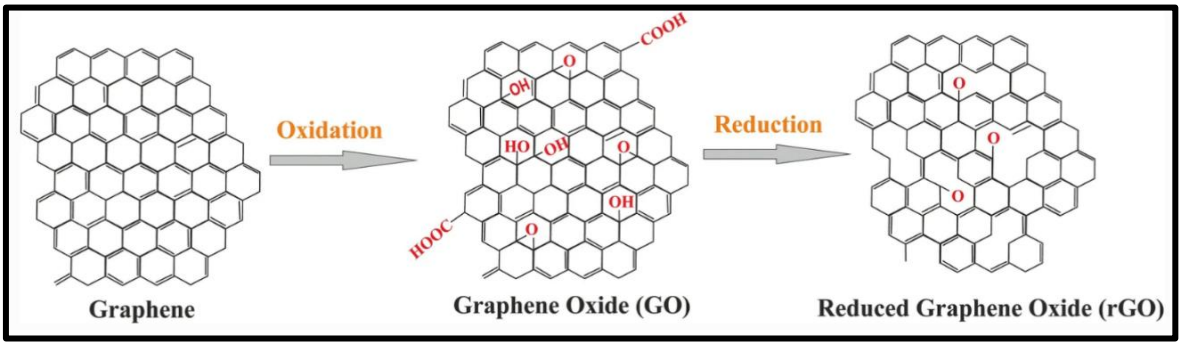

Fig. 1. 10: *Conversion of graphene oxide (GO) and reduced graphene oxide (rGO) [84]*

The creation of rGO via the thermal/chemical reduction of GO, restores most of the sp^2 hybridization of carbon atoms, considerably enhancing its conductivity while preserving a high surface area [85]. This positions rGO as a potential choice in diverse energy storage applications particularly when combined with other metal oxides, especially spinel ferrites. The extensive surface area of rGO facilitates more electrolytic ions to be adsorbed, while the spinel ferrites deliver pseudo-capacitance through fast redox reactions [86]. This combination not only overcomes the constraints of individual materials but also lays the foundation for producing high-performance supercapacitors that are cost-effective and efficient. Consequently, it enhances durability and cyclic stability, power efficiency/density, and energy storage capabilities/density, meeting the increasing need for sustainable energy storage solutions [87].

CHAPTER 2

Literature Review

2.1 Review of Supercapacitors

The history of supercapacitors (SCs) begins in 1745, with the invention of a Leyden jar also known as condenser by the German scientist and jurist Ewald Georg von Kleist [88]. In late 1745, he presented his invention to a group of German scientists, but his information about Leyden jar (condenser) somehow reached in muddled form to Leyden University, Netherlands. Later in 1746, the Dutch scientist Pieter van Musschenbroek along with his student Andreas Cunaeus at Leyden University succeeded in doing the same experiment with water [89]. In 1853, Hermann von Helmholtz presented the electric double-layer idea via his investigation of charge accumulation in capacitors, providing the groundwork for EDLCs. However, his model fell short of properly understanding the electrode/electrolyte interface structure [90]. In the early 90s, Guoy and Chapman refined Helmholtz's electric double-layer model by introducing a diffuse ion layer influenced by thermal motion. In 1924, Otto Stern combined this with Helmholtz's compact layer, forming the Stern model, which added the concept of adsorption and offered a more detailed structure of the electrode–electrolyte interface [90,91].

In the 1950s, H. Becker and engineers at General Electric pioneered the use of porous carbon electrodes, resulting in the first patent for a double-layer capacitor in 1957. This energy storage technique relies on porous carbon immersed in liquid electrolytes such as sulfuric acid (H_2SO_4) for effective charge accumulation. [92]. Despite its high specific capacitance due to the large electrode surface area, the 1957 patent lacked clarity on the energy storage mechanism, rendering it commercially unviable. In 1962, Robert A. Rightmire of Standard Oil Company, located in Ohio (SOHIO) proposed a refined electrochemical capacitor, patented in 1966, that stored energy via ionic adsorption at the interface of electron and ion conductors [93]. In 1970, SOHIO patented a carbon-based electrolytic capacitor with a high-capacitance double-layer interface. Nippon Electric Company (NEC) acquired the patent in 1971 and introduced the first commercial supercapacitor in 1975 [94].

Subsequently, in 1978, Panasonic came up with a supercapacitor known as the "Gold capacitor" for memory backup purposes [95]. In 1980, apart from porous carbon coin cells, new-generation high-performance supercapacitors were fabricated by using tantalum oxide

and ruthenium as high-capacitance electrode materials [96]. In the same year, 1980, SOHIO launched the "MaxCAP" double-layer capacitor, offering multiple farads at 5.5 V. The financial glitches of the SOHIO company led to its sale to NEC. NEC emerged as a global supercapacitor leader and popularized the term "Supercapacitor". By 1982, advancements in metal oxide electrodes led to low-resistance supercapacitors called the "PRI Ultracapacitor", developed by Pinnacle Research Institute (PRI) for military applications like missile guidance and laser weapons [97]. Researchers concentrated more on the utilization of supercapacitors in automobiles, particularly in the starters used in internal combustion engines, since early 1985 [89] ELNA began producing its double-layer capacitors under the name "Dynacap" in 1987. Meanwhile, heightened tensions during the Cold War and increased interest in space exploration prompted Russia to invest in supercapacitor technology [98]. In 1988, Russia's MP Pulsar (later ELIT) began producing advanced supercapacitors. By 1989, ELIT introduced the first asymmetric supercapacitors fabricated using nickel oxyhydroxide, activated carbon, and potassium hydroxide, designed to enhance battery performance for wheelchairs. In 1990, they developed symmetric supercapacitors with two activated carbon electrodes and the potassium hydroxide electrolyte [89,99]. Throughout these evolutionary stages, substantial research efforts were devoted to optimizing supercapacitor technology.

Until 1990, supercapacitors saw limited economic development due to low energy density, despite some applications in energy sectors. In 1991, "The Econd Corporation" in Moscow introduced supercapacitors suitable for trucks and hybrid vehicles, while NEC developed high-performance double-layer capacitors using activated carbon electrodes [100]. Besides this, the concept of pseudo-capacitance emerged in the same year (1991) from Conway's team by exploring RuO_2 with exceptional specific capacitance. Maxwell Technologies built its unique supercapacitors called "Boost Caps" in 1992 [101]. However, in the same year 1992, the U.S. Department of Energy endorsed the adoption of supercapacitors in hybrid electric vehicles through Maxwell Technologies [102]. This prompted Russia to establish ESMA in Troitsk in 1993, producing supercapacitor modules ranging from 20 kJ/14 V to 30 MJ/190 V with capacitances between 3000 and 100,000 Farads for heavy-duty transport. ESMA's activated carbon-based cells gained global recognition for their high-power efficiency, stable cycling, and cost-effectiveness, building on NEC Japan's Ni-Cd battery innovations for aircraft [89,100].

In 1994, a hybrid supercapacitor with a high pseudo-capacitance cathode composed of metal oxides combined with strong dielectric anode materials was introduced by Evans and

his team. In the same year, 1994, the Australian firm Commonwealth Scientific and Industrial Research Organization (CSIRO), headquartered at Clayton South, Victoria, formed a partnership with Plessey Ducon, a passive component manufacturer company. Subsequently, in two years, their researchers collaboratively developed carbon electrodes together with organic electrolyte-based spiral wound supercapacitors exhibiting 9 Wh/kg of total energy density with temporal constants on the scale of seconds to milliseconds [100]. Thus, during the year 1996, when the market race intensified all over the world, new supercapacitor models came forth, such as the FG-series, high-power FT-series, and FC-series, all under one trademark name "Tokin" by NEC. The first appearance of a supercapacitor on record was in 1997, when it was reported that supercapacitors achieved an energy density greater than 10 Wh kg^{-1} [89,99]. A Japanese company, so-called Nippon Chemi-Con (NCC), the world's largest manufacturer of aluminium electrolytic capacitors, came up with a supercapacitor product called "DLCAP". Moreover, in 1998, this company began the mass production of spiral-wound and prismatic cells, with a capacity of 3000F operating at 2.5V. In 1998, the South Korean Daewoo Group also created its initial supercapacitor product, called the "NessCap". During that period, these products were structured using organic electrolytes and a spiral-wound prismatic cell arrangement, which could offer capacitance ranging from a few farads to as high as 5000 F at 2.7 V [89,100].

Despite the hefty competition in the supercapacitor industry, the Japanese still occupied one of the leading positions in supercapacitor technology. In 1999, Panasonic introduced the "UpCap", a cost-effective, waterproof supercapacitor designed for hybrid electric vehicles (HEVs). With a capacity of 2000 F and 2.3 V, its sealed packaging minimized heat retention during charging cycles, making it ideal for regenerative braking and acceleration [103,104]. In the year 2001, another Japanese manufacturer, "Tokin", entered the supercapacitor market and introduced two distinct series, both using organic electrolytes, that include a spiral-wound series, a low-profile thin-format series. Later in 2002, the company rebranded from "Tokin" to "NEC-Tokin". In 2002, Dr. T. Morimoto of Asahi Glass Company outlined a novel asymmetric supercapacitor arrangement at the centennial gathering of the Electrochemical Society held in Japan. This design utilized two carbonaceous electrodes and an organic electrolyte containing lithium salt, achieving 16 Wh/L of volumetric energy density. As of now, this design is widely adopted by manufacturers for its higher 4.2 V output and improved energy density enabled by its asymmetric configuration [100].

In July 2002, Maxwell Technologies acquired Swiss supercapacitor firm Montena Components, introducing new design developments [105]. In 2005, its "Boostcap" ultracapacitor was selected by Diehl Luftfahrt Elektronik to power emergency actuation systems such as doors and evacuation slides on passenger aircraft, notably the Airbus A380 jumbo jet [106–108]. In 2006, Joel Schindall of MIT and his colleagues initiated a study on a "synthetic battery" based on nanotubes that would be better than existing capacitors or condensers [109]. In 2007, ESMA and American Electric Power developed a low-cost asymmetric supercapacitor using lead oxide, sulfuric acid, and activated carbon. Such supercapacitors, designed to store overnight grid energy, featured a 10-year lifespan, over 5000 cycles, and outperformed symmetric supercapacitors in energy density, though they remained below that of lead-acid batteries [100]. The next breakthrough came in the same year (2007), with the advent of lithium-ion capacitors into the market with high-power storage suitable for a multitude of applications [110]. Until 2007, significant advancement in the field of supercapacitors was observed. However, some issues such as low energy density, high manufacturing cost, and short cycle life remain unresolved. However, based on the developmental trend of supercapacitors since 2000, significant novel improvements have been noticed in energy density, high reliability, specific capacitance, power density, and safety aspects [111,112].

In 2004, the physics Nobel laureates, namely Andre K Geim and Konstantin S Novoselov, found the wonder material of the future, "Graphene" using a simple adhesive tape and a graphite sample at the University of Manchester, UK [113]. The pseudo-capacitive carbon-based electrodes, particularly graphene, became the focus of interest as they increased the energy density together with charge-discharge rate of SCs [114]. During the year 2010, Belle Dume presented supercapacitors made from curved graphene sheets. These flexible graphene-based sheets offer improved energy density with a specific charge density of 85.6 Wh kg^{-1} at room temperature and 136 Wh kg^{-1} at 80˚C. This technique was the turning point in the evolution of supercapacitors that are equivalent to nickel-metal hydride batteries [115]. Despite extensive global research attempts to boost C_S of graphene-based supercapacitor electrodes, the results show significant limitations in capacitance. These electrodes failed to achieve the theoretical C_S of 550 F g^{-1}, even though the single-layered graphene has a surface area of approximately 3000 m^2 g^{-1} [89,116]. Thus, to overcome this limitation the quality as well as the functioning of supercapacitors has been upgraded throughout the years. For example, activated carbons are extensively included in the main supercapacitors available in

the market because of their properties such as high cyclability, cheap cost, and corrosion resistance. However, carbon-based material offers C_S of 150 F g^{-1} at maximum, while the typical energy density is (3–5) Wh Kg^{-1} which is quite lower than lead-acid batteries (30–40) Wh Kg^{-1}. This abysmally low energy density limits their usage for certain energy-storage applications [117].

Nowadays, the fabrication of hybrid SCs via metal oxides, conducting polymers, together with graphene-based materials has been the focus of researchers to overcome these limitations by enhancing their energy as well as power density. Moreover, the integration of pseudocapacitive properties of metallic oxides into carbon-based materials, for instance, graphene or its reduced form, can potentially increase the double-layer capacitance. Furthermore, important achievements in the production of graphene supercapacitors have been observed by Sunvault Energy and Edison Power, by announcing the fabrication of the world's biggest graphene supercapacitor with a capacitance of 10,000 Farad. Supercapacitors attained worldwide acceptance since their inception, and the current market scenario is growing exponentially and is expected to flourish further in the near future.

2.2 Review of Electrode Materials

J. Kalidas et al. (2024) developed a core-shell manganese ferrite/reduced graphene oxide (CSMF/rGO) composite using a rapid two-step ultrasonication method. This study explained the synthesis of CSMF via an electrochemical method enhanced by ultrasound, resulting in a three-dimensional network integrated into a self-assembled graphene matrix. This hybrid structure effectively addresses volume expansion issues associated with magnetite, improving lithium-ion and electron mobility. The CSMF/rGO electrode achieved an impressive initial discharge capacity of (1512 mAh g^{-1} at 0.2 A g^{-1}) along with commendable reversible capacity of (492 mAh g^{-1} at 2.0 A g^{-1} after 500 cycles), with a coulombic efficiency greater than 99%. The findings of this research reveal that the CSMF/rGO hybrid electrode's potential has the possibility of becoming a choice for next-generation cost-effective high-capacitive anode for lithium-ion batteries to improve energy storage technologies [118].

S. Chai et al. (2024) synthesized $MnFe_2O_4$/rGO composite employing a single-step hydrothermal technique. In this study, the authors demonstrated an improvement in charge transfer due to the uniform dispersion of $MnFe_2O_4$ nanorods on rGO sheets, which further

improves interfacial interaction and reduces agglomeration. In addition, the authors claim that the optimized $MnFe_2O_4$/rGO composite electrode maintains a higher C_S of 195 F g^{-1} at current density (I_m) of 1 A g^{-1}, in contrast to individual electrode materials of $MnFe_2O_4$ and rGO both having respective capacitances of 77 F g^{-1} and 67 F g^{-1}. Moreover, the $MnFe_2O_4$/rGO composite exhibits excellent cycle stability having 75.22 % capacitive retention at the end of 4000 cycles at I_m of 2 A g^{-1}. This study further explains the ($MnFe_2O_4$/rGO/AC) based asymmetric supercapacitor (ASC) device reaches 16 W h kg^{-1} of energy density at 1280 W kg^{-1} of power density and demonstrates good cyclic stability with a total of 73.78 % capacitive retention after 5000 cycles at 1A g^{-1}, showcasing the potential for supercapacitor applications [119].

M. Ikram et al. (2024) showed the effectiveness of rGO which acts as a good electrode material in the fabrication of SCs mainly due to its flexibility, highly conductive nature, and improved surface redox reactivity. They had synthesized NiO/$CoFe_2O_4$/rGO composite electrodes via the sonication method. The findings of this study revealed that NiO/$CoFe_2O_4$/rGO composite electrode attained a high C_S of 911.25 F g^{-1} as well as low equivalent series resistance (ESR) of 0.29 Ω outperforming nickel oxide/cobalt ferrite (NiO/$CoFe_2O_4$), nickel oxide (NiO), and cobalt ferrite ($CoFe_2O_4$) electrode materials. This research reveals that the combined properties of both the superior conductivity of rGO and the good crystalline nature of metal oxides such as NiO and $CoFe_2O_4$, make NiO/$CoFe_2O_4$/rGO nanocomposite advantageous for supercapacitors [120].

Ahad et al. (2024) examined the role of manganese-substituted Ni-Mn-Cu-Zn spinel ferrites which were synthesized via the sol-gel auto-ignition approach. They also found that the average grain size and bulk density increases in these mixed spinel ferrites due to the incorporation of manganese (Mn) ions which act as grain growth accelerators. Moreover, they observed that the optimal composition of these mixed spinel ferrites exhibited high permeability along with saturation magnetization (M_s), low coercivity (H_c), and a broad operational frequency range of up to 10 MHz. These properties suggest that the synthesized mixed ferrites are promising for multifunctional electronic devices and medical applications such as cancer treatment [121].

T. Putjuso et al. (2023) synthesized cobalt-substituted zinc ferrite ($Co_xZn_{1-x}Fe_2O_4$) nanoparticles via the hydrothermal process. In this study, it was validated by XRD analysis that these synthesized nanoparticles possess a cubic structure, while the metal oxide vibrational modes were observed within the spinel structure which was confirmed through FTIR spectroscopy. It was observed that the substitution of cobalt (Co^{2+}) ions in cobalt-substituted zinc ferrite ($Co_xZn_{1-x}Fe_2O_4$) nanoparticles creates an impact in parameters like crystallite size, lattice constant, and average particle size, as these parameters decreased slightly with the varying cobalt (Co) concentrations. Moreover, they revealed the micrographs of SEM as well as TEM exhibit cuboidal-shaped evenly distributed nanoparticles, yielding a highly active electrode surface which in turn results in quick transport of ions and electrons, which was further confirmed by Brunauer-Emmett-Teller (BET) measurements. These researchers discussed that the cobalt ions not only impact the structural and morphological characteristics but also electrochemical properties. In addition, the cobalt-substituted zinc ferrite ($Co_xZn_{1-x}Fe_2O_4$) nanoparticles exhibit pseudo-capacitive behavior owing to their faradaic redox processes, particularly the nanoparticle at a specific concentration ($Co_{0.3}Zn_{0.7}Fe_2O_4$) attains a peak C_S of 855.33 F g^{-1} at I_m of 1 A g^{-1} together with impressive retention of 90.41 % after 1000 charge-discharge cycles, thereby solidifying its place as potential candidate in SC electrodes [122].

T. Hoang et al. (2023) explored the successful synthesis of spinel nickel-manganese cobaltite (s-NMC) using a hydrothermal/calcination technique, confirming its spinel structure and nanostructure through various characterization techniques. The electrochemical analysis of this study demonstrated that s-NMC exhibits pseudocapacitive behavior with a maximum C_S of 418.3 F g^{-1} at 10 mV s^{-1} of scan rate, and 216.2 F g^{-1} at I_m of 1 A g^{-1}, alongside impressive capacitive retention of approximately 95 % after 5000 cycles at I_m of 2 A g^{-1}. Furthermore, within this research work, the fabrication of an asymmetric SC device using s-NMC as the anode and activated carbon serving as the cathode achieved a peak energy density of 16.58 Wh kg^{-1} at 825 W kg^{-1} of power density and maintained approx. 97 % capacitive retention after 2000 cycles at I_m of 2 A g^{-1}, highlighting its place as an electrode material for SCs [123].

M. El-Masry et al. (2023) synthesized pristine cobalt ferrite ($CoFe_2O_4$) as well as copper- and zinc-doped cobalt nano-ferrites (Cu- and Zn-doped $CoFe_2O_4$) via the citrate auto combustion technique, examining these materials key attributes such as structural, thermal,

magnetic, and electrical. The authors noticed that all the synthesized samples were classified under the Fd3m space group, with crystallite sizes of 8 nm, 15 nm, and 14 nm for Cu-$CoFe_2O_4$, Zn-$CoFe_2O_4$, and $CoFe_2O_4$ respectively. Their study demonstrated that Cu^{2+} doping enhanced the elastic properties of cobalt nano ferrite ($CoFe_2O_4$), with increases in force constant (45%), elastic moduli (46%), and Poisson's ratio (66%) compared to pristine cobalt ($CoFe_2O_4$) and zinc-doped cobalt ferrite (Zn-$CoFe_2O_4$). While the pristine cobalt ferrite ($CoFe_2O_4$) exhibited the maximum saturation magnetization (56.1 emu g^{-1}), zinc-doped cobalt ferrite (Zn-$CoFe_2O_4$) demonstrated superior magnetic susceptibility (0.639). Furthermore, doping improved thermal characteristics, with copper-doped cobalt ferrite (Cu-$CoFe_2O_4$) achieving the peak thermal conductivity (0.95 Wm^{-1} K^{-1}) and diffusivity (0.75 m^2 s^{-1}), together with specific heat (0.85 MJ m^{-3} K^{-1}). These findings suggest that these comprehensive characterizations indicate the potential of doped cobalt ferrites for diverse electronic applications [124].

S. Habib et al. (2022) synthesized manganese ferrite ($MnFe_2O_4$), cobalt ferrite ($CoFe_2O_4$), and cobalt-manganese ferrite (Co-$MnFe_2O_4$) using a coprecipitation method. They developed composites of these ferrites with graphene at a 3:1 weight ratio (75 % ferrites, 25 % graphene). The experimental outputs validated the formation of single-phase nanoferrites having soft magnetic and semiconducting properties. Although the composites exhibited lower saturation magnetization and conductivity than pure ferrites, they retained similar behavior trends. This research highlights the potential improvements in materials for applications in supercapacitors and battery electrodes [125].

B. Mary et al. (2022) synthesized potential electrode materials, $CuFe_2O_4$, and $CuFe_2O_4$/rGO nanocomposite using a microwave combustion technique for supercapacitor applications. Their results showed $CuFe_2O_4$/rGO having a C_S of 800 F g^{-1} at I_m of 2 A g^{-1} in a 6M KOH electrolytic solution, outperforming pure $CuFe_2O_4$ at 712 F g^{-1}. This innovative synthesis achieved significant capacity at lower current densities, with the composite exhibiting 360 F g^{-1} at I_m of 1 A g^{-1}, a specific energy of 18.3 Wh kg^{-1}, with 455 W kg^{-1} of specific power, a 50 Ω resistance, and impressive stability, retaining 98% capacity after 3000 cycles. These findings suggest that $CuFe_2O_4$/rGO composite electrode is a viable eco-friendly option for high-performance energy storage solutions [126].

A. Aslam et al. (2021) synthesized La-doped Mg-Ni-Cu-Co spinel ferrites via a sol-gel auto-ignition route, confirming the cubic single-phase structure of these ferrites. They demonstrated that doping of Lanthanum (La^{3+}) ions into these ferrites causes fluctuations in certain parameters such as ionic radii, lattice constant, crystallite size, and X-ray density. FTIR and Raman analyses indicated La^{3+} ions preferentially occupy the octahedral site, while SEM revealed uniform morphology. EDS confirmed stoichiometry and UV-visible data showed a decline in energy band gap from (2.48−1.53) eV. Additionally, the activation energy decreased from (1.803−1.505) eV with La^{3+} ions doping, highlighting the influence of doping on the electronic and optical attributes of synthesized ferrites [127].

M. Roni et al. (2021) utilized a solid-state reaction approach to synthesize lanthanum-doped Mn-Zn ferrite nanoparticles, $Mn_{0.6}Zn_{0.4}La_xFe_{2-x}O_4$ with La^{3+} content (x) varied incrementally from 0.00 to 0.10. Their study revealed a cubic spinel structure through XRD analysis, predominantly oriented along the (311) plane, while microstructural parameters varied with La^{3+} content. FTIR identified key functional groups at 423 cm^{-1} and 529 cm^{-1}, and UV-visible absorption data revealed bandgaps of (1.23− 1.30) eV. Magnetic analysis showed that M_s decreased and H_c increased with La^{3+} ions doping. Additionally, this study showed that the dielectric properties attain higher values in undoped Mn-Zn ferrite compared to Lanthanum-doped samples [128].

M. A. Gabal et al. (2020) employed a sucrose-assisted auto-combustion technique to synthesize $Mg_{1-x}Zn_xFe_2O_4$ nanocrystalline ferrites with varying zinc (Zn) concentrations ranging between 0.0 to 1.0 for x. Their XRD analysis identified single phase structure up to Zn concentration (x = 0.2), with the formation of secondary phases ZnO and α-Fe_2O_3 emerging at higher Zn concentrations, alongside an increase in lattice parameters from (8.3937− 8.4454) Å ascribed to Zn^{2+} ions larger ionic radius than Mg^{2+} ions. The size of crystallites substantiated the nanocrystalline structure, while FTIR spectroscopy showed characteristic tetrahedral and octahedral ferrite bands. TEM imaging micrographs revealed spherical agglomerated particles consistent with XRD size measurements. In this study magnetic measurements unveiled that most of the samples exhibit soft ferromagnetic behavior, except for $ZnFe_2O_4$. The authors highlighted the influence of Zn substitution on magnetic parameters. They further demonstrated that all samples exhibited semiconducting behavior with AC conductivity showing temperature-dependent changes linked to a magnetic

transition from ferromagnetic to paramagnetic states around 500 K, corroborated by dielectric measurements [129].

L. Phor et al. (2020) examined synthesis of the magnetic nanoparticles with the composition $Mg_{1-x}Zn_xFe_2O_4$, where x varied from 0.3 to 0.7, using a coprecipitation route. Their XRD analysis indicated that the lattice parameter increased from (8.402−8.424) Å with higher Zn^{2+} content. Fourier transform infrared spectroscopy unveiled characteristic peaks at about 560 cm^{-1} and 430 cm^{-1}, confirming the structure of spinel ferrite nanoparticles. TEM micrographs indicated that the particle size increased from (18−24) nm with higher Zn^{2+} ion content. Magnetic studies via a vibrating sample magnetometer and electron paramagnetic resonance demonstrated superparamagnetic behavior, with magnetization peaking at 32.78 emu g^{-1} for x = 0.5 before decreasing. XPS was used to analyze the chemical composition and oxidation states [130].

R. Jasrotia et al. (2020) analyzed the influence of substituting Ag/Mn/Cr ions on nanosized Ni-Cu-Zn spinel ferrites, synthesized via the sol-gel auto-ignition approach. Their study revealed that increasing dopant concentration initially reduced the crystallite size with a subsequent rise at higher concentrations. The substitution of these dopant ions led to larger lattice parameters and an expanded unit cell volume, forming densely packed agglomerated cubic nanoparticles with a grain size of around 86 nm. FTIR results substantiated a single-phase spinel structure, and magnetic analysis showed a soft ferromagnetic character, with decreased saturation magnetization (M_s) and coercivity (H_c) at higher dopant concentrations. Furthermore, the authors concluded that resistivity measurements indicated semiconducting behavior, suggesting that these materials are viable in multi-layer chip inductors [131].

A. Rajeshwari et al. (2020) explored the successful synthesis of $MnLa_xFe_{2-x}O_4$ through the sol-gel auto-combustion technique. Such a structural study validated the cubic structure of spinel ferrites via XRD analysis, while the morphological FESEM study describes the spherical-shaped nano ferrites with little agglomeration. Moreover, the elemental composition validated by EDX confirms the presence of these substituted metal oxides (Mn, La, Fe, and O) in the intended proportions. UV diffuse reflectance spectroscopy revealed an inverse correlation between absorbance and energy band gap. In this study, the magnetic hysteresis loop demonstrated the soft ferromagnetic behavior of ferrites due to a decline in

M_s and an upsurge in H_c as the lanthanum ion concentration increases. The authors further discussed Mn^{2+} and Fe^{3+} ion's role in spinel lattice regarding ferromagnetism. Impedance spectra suggested grain boundary resistance increased with La^{3+} ions doping, while dielectric constant (ε) and tangent loss (tan δ) dropped with frequency, suggesting the synthesized ferrite's potential for enhanced radiation-absorption applications [132].

V. Verma et al. (2019) analyzed the effects of cobalt (Co^{2+}) and copper (Cu^{2+}) ion substitution on the properties of nanocrystalline ferrites ($Mn_{0.4}Co_{0.6-x}Cu_xFe_2O_4$) produced by the sol-gel approach. They found that varying the metal ion content in these ternary nano-ferrites significantly influenced the material's structural, magnetic, morphological, and optical attributes. The single-phase formation of nano-ferrites was confirmed through XRD, while SEM-EDX and TEM analysis exposed the surface area and surface morphology variations. The introduction of copper (Cu^{2+}) ions slightly increased magnetization, whereas cobalt (Co^{2+}) doping significantly enhanced it, attaining the M_s value up to 65.0 emu g^{-1} observed for $Mn_{0.4}Co_{0.4}Cu_{0.2}Fe_2O_4$ nano-ferrites. Furthermore, the optical investigations demonstrated a band gap reduction to 2.03 eV, with the lowest value in $Mn_{0.4}Co_{0.4}Cu_{0.2}Fe_2O_4$ nano-ferrites, highlighting the improved magnetic and optical properties compared to the undoped nano-ferrites. In light of these observations, ternary doping is shown to be of pivotal importance in an adjustment of $MnFe_2O_4$ properties for multifunctional uses [133].

S. Suresh et al. (2018) studied the electrochemical performance of nanocomposite hybrids of rGO/MFe_2O_4, where (M = Zn, Co, Fe, Ni) prepared through hydrothermal technique for supercapacitor electrode materials. Their findings validated the cubic spinel structure of ferrites and the successful reduction of GO, with ferrite nanoparticles well-distributed on rGO sheets. The study demonstrated that rGO significantly improved the charge storage capacity and efficiency of charging-discharging in 0.1 M of sodium sulfate (Na_2SO_4) electrolyte. The C_S values for pure ferrites were measured, showing respective values of 128 F g^{-1}, 117 F g^{-1}, 15.2 F g^{-1}, and 9.1 F g^{-1} for Fe_3O_4, $CoFe_2O_4$, $NiFe_2O_4$, and $ZnFe_2O_4$. In contrast, the rGO/ferrite nanocomposites achieved higher values of 233 F g^{-1}, 200 F g^{-1}, 25 F g^{-1}, and 66.8 F g^{-1} for rGO/Fe_3O_4, rGO/$CoFe_2O_4$, rGO/$NiFe_2O_4$, and rGO/$ZnFe_2O_4$, respectively. The study further found that not only the specific surface area, but the structural morphology also plays a crucial role in influencing how nanohybrids interact with electrolyte ions, thus ultimately leading to improved electrode performance [134].

N. Murali et al. (2017) analyzed the influence of aluminum substitution on the properties of $Co_{0.5}Zn_{0.5}Al_xFe_{2-x}O_4$, synthesized via the sol-gel route, yielding a single-phase cubic spinel structure with nanoscale crystallites. They observed that increasing the aluminum (Al^{3+}) ions concentration causes a drop in lattice constant from (8.385− 8.211) Å, which could be attributed to the small ionic radii of aluminum (Al^{3+}) ions than that of iron (Fe^{3+}) ions. Moreover, the reduction in M_s with increasing aluminum (Al^{3+}) concentrations was attributed to the aluminum's non-magnetic behavior. In contrast, the absence of hysteresis in the magnetization curves indicated nearly zero retentivity (M_r) and coercivity (H_c), suggesting the materials exhibit superparamagnetic behavior [135].

K. R. Babu et al. (2017) concluded that the auto-combustion sol-gel process successfully creates single-phase copper (Cu) substituted cobalt-zinc (Co-Zn) nanocrystalline ferrites with the absence of any secondary phase formation. They observed a linear reduction in lattice constant with the substitution of high-concentration copper (Cu^{2+}) ions, corroborating the solubility of these ions within the spinel structure. They further revealed that the substitution of copper (Cu^{2+}) ions not only influenced the density, particle size, and grain size but also influenced M_s, H_c, and M_r. Notably, the value of M_s for $Co_{0.5}Zn_{0.5}Fe_2O_4$ was found greater in comparison to other copper (Cu) substituted cobalt-zinc (Co-Zn) nano-ferrites, while the reduction in the value of M_s of Cu-substituted Co-Zn ferrites was because of the spin canting and cation redistribution between A and B sublattices. The findings of this study emphasize the potential of these nano-ferrites for magnetic recording applications [136].

R. Sharma et al. (2017) examined the successful synthesis of nickel-doped magnesium-zinc ferrites ($Mg_{0.5}Zn_{0.5-x}Ni_xFe_2O_4$) utilizing the co-precipitation method and analyzed through numerous techniques, including UV-Visible, XRD, VSM, FESEM, FTIR, and PL spectroscopy. They found a shift from (x = 0) which is superparamagnetic behavior to (x > 0) soft ferrimagnetism with increasing nickel (Ni^{2+}) content. They observed that the smaller size crystallites led to higher coercivity (H_c) but lower saturation magnetization (M_s), while the remanence ratio (M_r/M_s) increased with higher nickel (Ni^{2+}) content. The optical band gap estimated through Tauc plots, upsurges for a concentration (x = 0) from 4.50 eV to 5.60 eV up to concentration (x = 0.50). From the photoluminescence (PL) analysis, they observed that the band edge emission occurs at energies lower than the optical band gap, highlighting defect

states in the ferrites. The findings suggest that the ferrite's cation distribution, moderate coercivity (H_c), and saturation magnetization (M_s) showed promising potential in high-density information storage applications [137].

J. Wang et al. (2017) presented an innovative hydrothermal synthesis method to create composites of $CuFeO_2$/rGO and Cu/$CuFe_2O_4$/rGO for better-performing electrodes. They demonstrated that synergistic interaction between rGO and copper ferrites enhances storage capabilities by facilitating electron and ion transfer, providing structural stability, and offering a large surface area that mitigates volume expansion issues in copper ferrites. Notably, they revealed that the electrode material $CuFeO_2$/rGO achieved a reversible capacity of 587 mAh g^{-1} after 100 cycles at 200 mA g^{-1}. In contrast, hybrid Cu/$CuFe_2O_4$/rGO electrode material exhibited improved lithium storage performance, with a rate capability of 723 mAh g^{-1} at 800 mA g^{-1} and 560 mAh g^{-1} at 3200 mA g^{-1}, along with strong cycling stability at 1102 mAh g^{-1} after 250 cycles at 800 mA g^{-1}. Their findings revealed the structural design and electrochemical performances of these electrode materials make them suitable for stationary energy storage applications [138].

G. Chandra et al. (2017) examined how sintering temperature affects the properties of cobalt nanoferrites created using sol-gel route and characterized them using XRD, VSM, TEM, and Mossbauer spectroscopy. They found that higher sintering temperatures significantly enhance both particle size and saturation magnetization (M_s), with M_s values improved from (53−85) emu g^{-1} for the elevated temperature ranging from (300-900) ˚C. It was also observed that the retentivity (M_r) of nanoferrites upsurged, while the coercivity (H_c) experienced a slight reduction with temperature. Mossbauer analysis indicated a ferrimagnetic behavior of cobalt nanoferrites and a temperature-dependent cation distribution, with the stoichiometry determined as $(Co^{2+}_{x}Fe^{3+}_{1-x})[Co^{2+}_{1-x}Fe^{3+}_{1+x}]O_4$, indicating a transition from inverse to normal spinel structure with increased sintering temperature. The results of this study validated that the high saturation magnetization (M_s) of these nanomaterials holds significant potential for applications in high-density magnetic storage data and ferrofluid technologies [139].

M. A. Mousa et al. (2017) developed hybrid materials that consist of distinct ferrites (Fe_3O_4, $NiFe_2O_4$, $CoFe_2O_4$), polyaniline (PANI), and graphene, and they thoroughly performed an extensive characterization of their structural and electrochemical characteristics. Their

research demonstrated that ternary hybrid electrodes exhibited higher capacitance than those made from single or binary components. Notably, the hybrid $CoFe_2O_4$/graphene/PANI electrode achieved 1123 F g^{-1} of C_S, an energy density of 240 Wh kg^{-1}, together with a power density of 2680 W kg^{-1} at I_m of 1 A g^{-1}, while retaining 98.2 % of its capacitance with the culmination of 2000 cycles. This exceptional performance was attributed to the synergistic effects of these components, where PANI facilitated electron transport and nanoferrites restricted carbon sheet restacking, thereby increasing overall capacitance through faradaic processes. The findings of this research work pave the way for exploring innovative hybrid electrode materials for energy applications [140].

Q. Lin et al. (2015) performed an investigation on lanthanum-doped cobalt spinel ferrite $Cu_{0.5}Co_{0.5}Fe_{2-x}La_xO_4$, where La^{3+} ions concentration varied from 0 to 0.05 for x, synthesized through a sol-gel approach. Their findings revealed that a cubic single-phase structure was formed, while a reduction in lattice parameters and grain sizes was observed as La^{3+} dopant ions increased. Moreover, the nature of the spinel ferrite nanoparticles was confirmed through SEM, while Mossbauer spectroscopy revealed their ferrimagnetic properties. The investigation noted that M_s, M_r, and H_c initially increased before showing a decline with La^{3+} dopant ions addition [141].

R. Indhrajothi et al. (2015) synthesized pristine cobalt ferrite ($CoFe_2O_4$) and lanthanum-doped cobalt nanoferrites ($CoLa_{0.06}Fe_{1.94}O_4$) using citric acid, glycerol and urea-assisted combustion techniques. Their results demonstrated that larger radii of La^{3+} dopant ions than Fe^{3+} ions enhanced the $CoLa_{0.06}Fe_{1.94}O_4$ nanoferrites lattice parameter and lowered vibrational frequency, as validated by XRD and FTIR measurements. This study revealed that Lanthanum (La^{3+}) dopant ions substitution causes a decrease in electrical conductivity but improves the structural stability of undoped cobalt ferrites ($CoFe_2O_4$). The electrochemical findings of this research indicated the enhancement in oxidation processes of iron (Fe^{3+}) and cobalt (Co^{2+}) ions by substituting Lanthanum (La^{3+}) dopant ions, which helped to sustain lithium ions more efficiently during charge-discharge cycles, eventually boosting capacity retention over undoped cobalt ferrite ($CoFe_2O_4$) anodes [142].

Y. Wang et al. (2008) successfully produced $Ni_{0.6}Zn_{0.4}Cr_{0.5}La_xFe_{1.5-x}O_4$ nanoferrites using a rheological phase reaction approach, by examining the impact of La^{3+} ions in determining

their microstructural along with magnetic characteristics. XRD measurement showed the solubility limit of lanthanum (La^{3+}) ions within the spinel lattice. The results demonstrated that increasing Lanthanum (La^{3+}) dopant ion concentration lowered both the size of crystallites and saturation magnetization (M_s), while coercivity (H_c) increased. Their findings emphasize that these La-substituted ferrites showed potential as soft magnetic substances, with the possibility of improved microwave absorption properties by modifying the composition of ferrites [143] (Table 2.1).

***Table 2. 1**: Comparison of ferrite/rGO-based nanomaterials: synthesis methods, key findings, and applications*

Year	Authors	Material Synthesized	Synthesis Method	Key Findings	Applications
2024	S. Chai et al.	$MnFe_2O_4$/rGO composite	Hydrothermal	Capacitance: 195 F g^{-1}, 75.22% retention after 4000 cycles	Supercapacitors
2023	T. Putjuso et al.	$Co_xZn_{1-x}Fe_2O_4$ nanoparticles	Hydrothermal	Capacitance: 855.33 F g^{-1}, 90.41% retention after 1000 cycles	Supercapacitor electrodes
2022	B. Mary et al.	$CuFe_2O_4$/rGO nanocomposite	Microwave combustion	Capacitance: 800 F g^{-1}, 98% retention after 3000 cycles	Energy Storage
2021	M. Roni et al.	La-doped Mn-Zn ferrites	Solid-state reaction	Decreased Ms, increased Hc with La doping	Magnetic applications
2020	L. Phor et al.	$Mg_{1-x}Zn_xFe_2O_4$ nanoparticles	Coprecipitation	Superparamagnetic behavior, magnetization peak at 32.78 emu g^{-1}	Magnetic applications
2019	V. Verma et al.	$Mn_{0.4}Co_{0.6-x}Cu_xFe_2O_4$ nano-ferrites	Sol-gel	Ms up to 65.0 emu g^{-1}, band gap reduction to 2.03 eV	Multifunctional applications
2018	S. Suresh et al.	rGO/MFe_2O_4 (M = Zn, Co, Fe, Ni)	Hydrothermal	Enhanced capacitance (rGO/Fe_3O_4: 233 F g^{-1})	Supercapacitor electrodes
2017	M. A. Mousa et al.	$CoFe_2O_4$/graphene/PANI hybrid	Sol-gel auto combustion	Capacitance: 1123 F g^{-1}, 98.2% retention after 2000 cycles	Supercapacitors
2015	R. Indhrajothi et al.	La-doped $CoFe_2O_4$	Auto-Combustion	Improved capacity retention for lithium-ion batteries	Battery anodes

2.3 Motivation and Research Gap

The growing need for effective energy storage alternatives/solutions triggered our curiosity to explore innovative electrode materials that can greatly improve the energy storage efficacy in supercapacitor devices. Although SCs are well-established technologies, they still have plentiful obstacles particularly about attaining high power and energy density, which require advancements in electrode fabrication. This study intends to investigate the potential of electrode materials consisting of spinel ferrites, reduced graphene oxide, and their composites by examining their electrochemical characteristics including composition, surface area, morphology, and crystallinity. This study aims to determine the ideal combinations of electrode materials that may provide enhanced electrochemical performance, thereby fulfilling the escalating need for effective energy storage devices.

A comprehensive literature survey has been conducted on diverse studies, especially spinel ferrites, doped spinel ferrites, graphene-based electrode materials, and their respective nanocomposites. It was observed that most spinel ferrites are synthesized using approaches like co-precipitation, solid-state synthesis, as well as hydrothermal techniques. However, as far as our knowledge is concerned, there is a notable lack of research in synthesizing spinel ferrites from the sol-gel auto-combustion approach. Additionally, many existing studies focus on spinel ferrites containing only two divalent metal cations, while those incorporating more than two divalent cations for energy storage applications are rarely explored. The C_S, energy density, and power density of doped and undoped spinel ferrites are relatively low, indicating a need for improvement by incorporating other materials with spinel ferrites, to enhance their performance to be utilized in numerous applications. To overcome these problems, this research proposes to investigate various spinel ferrites, reduced graphene oxide, and their hybrid nanocomposites for energy storage applications.

2.4 Objectives of this work

A brief description of the core objectives of this thesis is given below:

I. To study the structural, magnetic, and dielectric properties of spinel ferrites.
II. To study the structural, magnetic, and dielectric properties of 2D material and spinel ferrites.

III. Investigation of electrochemical properties of composites for energy storage materials.

CHAPTER 3

Research Methodology and Characterization Techniques

3.1 Introduction

This chapter provides an overview of synthesis methods together with characterization techniques employed in the development of spinel ferrites (SFs), rGO, and their composites. The SFs were synthesized by utilising sol-gel auto-combustion approach, whereas rGO was made by a modified Hummers method. Composites were later made by the physical mixing of these components using a mortar and pestle. In addition to this, electrode fabrication based on these materials is discussed. Following the synthesis, several characterization approaches will be explored to understand the structural, morphological, magnetic, dielectric, and electrochemical features of the resulting materials.

3.2 Method of Synthesis

3.2.1 Sol-Gel Auto Combustion Approach

The sol-gel auto-combustion technique was employed for the synthesis of pristine and doped spinel ferrites. This wet chemical approach is extensively utilized in materials science and ceramic engineering, predominantly for synthesizing nanoparticles and metal oxides. The sol-gel approach has various benefits over other synthesis processes such as co-precipitation, solid-state synthesis, and hydrothermal methods. This method commences with the production of a sol, a colloidal mixture or solution consisting of small solid particles dispersed in a liquid, which is generated by mixing metal precursors with a suitable solvent (viz distilled or deionized water, ethylene glycol, alcohols, acetic acid, or glycerol) and stabilizing agent (citric acid). A network is formed during the ‘sol’ to ‘gel’ conversion, entrapping the metal ions or nitrates within. The gel is then dried or heated till auto-combustion or self-ignition occurs causing organic materials and metal precursors to react exothermically, evolve gases quickly, and produce porous crystalline powders. The sol-gel auto-combustion approach is a low-temperature technique for precise nanoparticle production, enabling control over particle characteristics such as size, morphology, porosity, and composition, while promoting uniform

dispersion. This technology is cost-effective and appropriate for large-scale manufacturing owing to its minimum energy and material needs [144]. The procedure for sample preparation using the sol-gel auto-combustion process is depicted in Fig. 3.1.

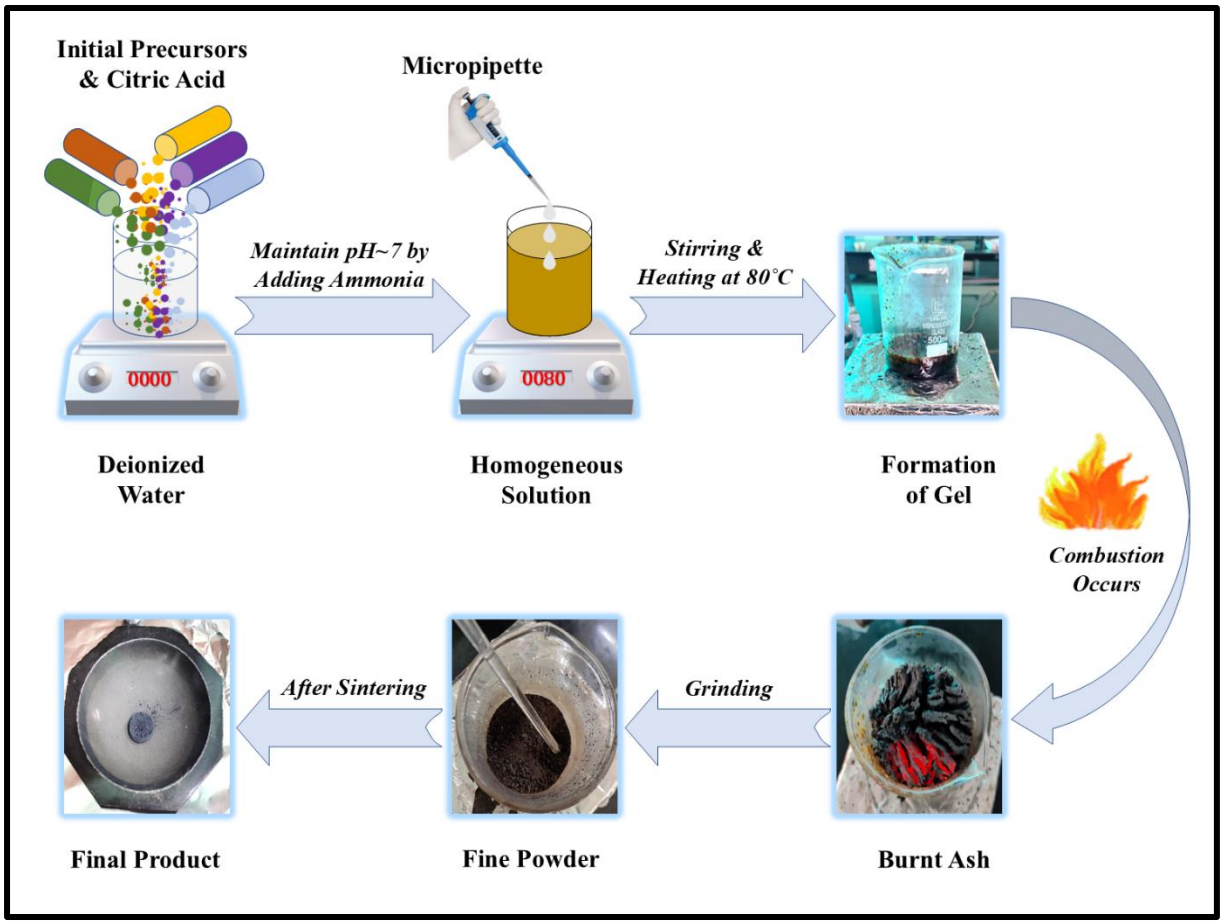

Fig. 3. 1: *Sol-gel auto-combustion method*

3.2.2 Modified Hummers Method

Modified Hummer's method is an extensively used chemical technique for oxidizing graphite to produce graphene oxide (GO). This method boosts the original Hummer's approach by incorporating modifications to improve yield, enhance oxidation, and reduce the risk of hazardous byproducts. The modified Hummer's method involves a combination of strong and powerful oxidizing agents, such as potassium permanganate ($KMnO_4$) and concentrated sulfuric acid (H_2SO_4), together with sodium nitrate ($NaNO_3$) to introduce oxygen-containing functional groups onto the graphite structure. This method starts by adding $KMnO_4$ and $NaNO_3$, along with graphite powder, to a sulfuric acid solution. An ice bath is used to control

the exothermic reaction by cooling the stirred mixture, allowing the graphite to be exfoliated into graphene oxide. Once the oxidation reaches its final stage, the reaction is ceased by quenching it with distilled water, followed by hydrogen peroxide (H_2O_2) which is used to eliminate leftover potassium permanganate ($KMnO_4$). Subsequent washing and filtration processes assist purify the solution by eliminating residual contaminants and acidic components yielding a dry storable graphene oxide powder for future use. The resultant GO comprises hydroxyl, epoxy, and carboxyl groups, which increase its dispersion in aqueous solutions and its suitability for further chemical modification or reduction to rGO. This modification not only boosts the quality of rGO generated, but also broadens its usefulness across sectors including electronics, materials science, sensors, and energy storage, where important qualities like surface area, conductivity, and reactivity are crucial for its functioning. In conclusion, the modified Hummer's method has received recognition for its scalability and ability to yield high-quality graphene oxide with regulated characteristics [83]. The synthesis process of the modified Hummer's method is clearly outlined in Fig. 3.2.

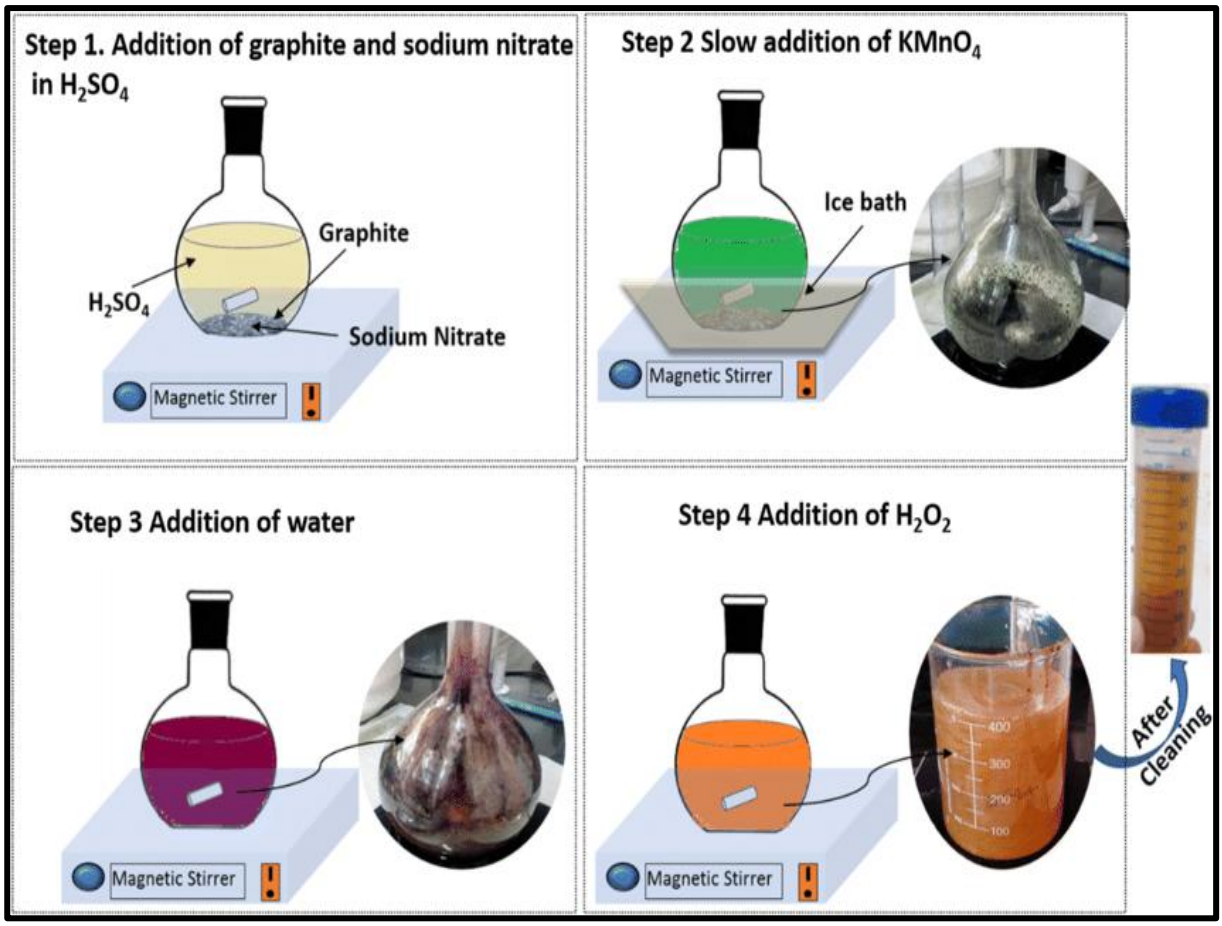

Fig. 3. 2*: Modified Hummers method [145]*

3.2.3 Physical Blending Method

The physical blending method, especially when utilizing a mortar and pestle, is an easy, efficient, cost-effective, and environment-friendly approach to yield nanocomposites of spinel ferrites and reduced graphene oxide (rGO). In this method, these two components are manually blended and pulverized to obtain homogeneous dispersion and mixing of the materials at the nanoscale. This method starts by carefully weighing the desired quantities of each component. In the case of spinel ferrites and rGO, the main purpose of the physical blending or mixing is to strengthen the interaction among ferrite nanoparticles and rGO sheets, thereby resulting in improved electrochemical and other properties for applications such as supercapacitors, sensors, and adsorption. The technique helps produce better dispersion of ferrite nanoparticles on the rGO surface, possibly enhancing conductivity, surface area, and overall performance of the resultant nanocomposites. This approach is typically applied as a pre-treatment step before additional processing such as calcination or sintering, which may increase the performance of the nanocomposite material for certain applications including energy storage and environmental remediation. Fig. 3.3. depicts a clear

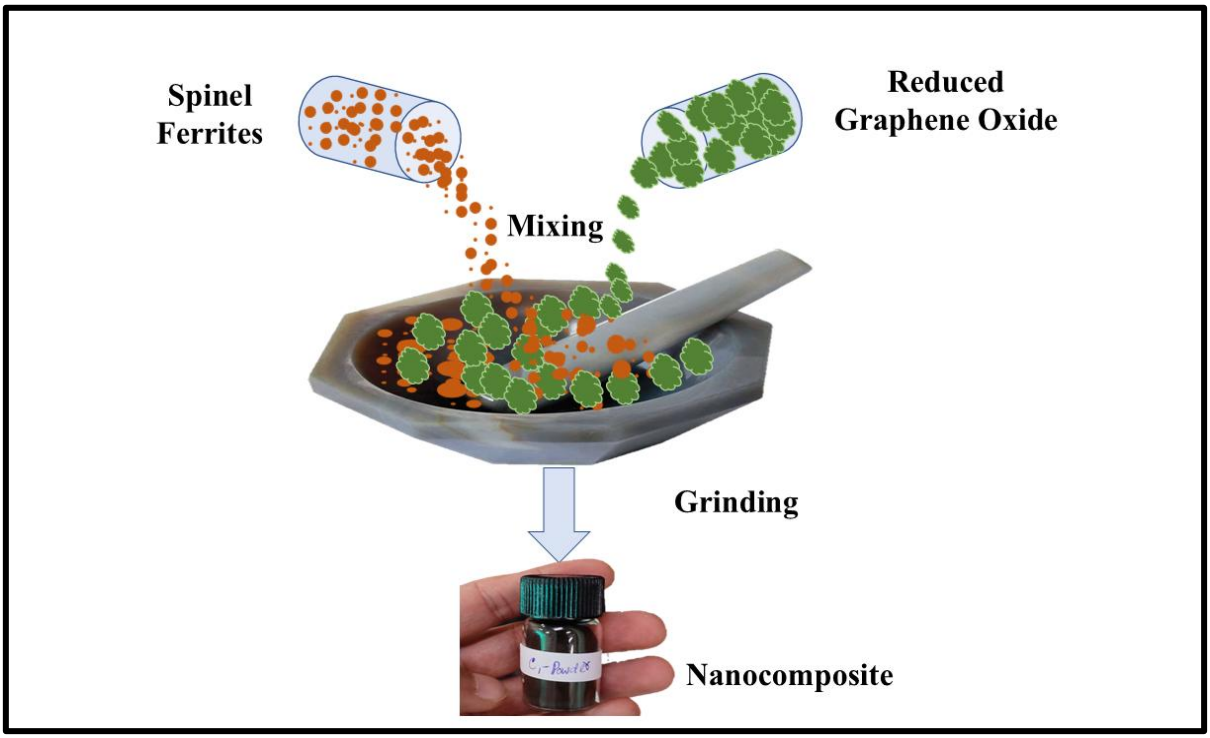

overview of the physical blending process for creating spinel ferrite/rGO nanocomposites.

Fig. 3. 3: *Physical blending method*

3.3 Experimental Synthesis

The experimental section includes the synthesis of specific spinel ferrites, two-dimensional reduced graphene oxide and their nanocomposites, along with the fabrication of electrodes.

3.3.1 Synthesis of Lanthanum-doped Cu-Co Spinel Ferrites

For the synthesis of $Cu_{0.79}Co_{0.21}La_xFe_{2-x}O_4$ ($0.0 \leq x \leq 0.8$) in increments or (steps) of 0.2, analytical grade chemicals were employed as shown in Fig. 3.4. The comprehensive procedures for preparing the spinel ferrites, along with the properties examined through various characterization techniques, are detailed in Table 3.1.

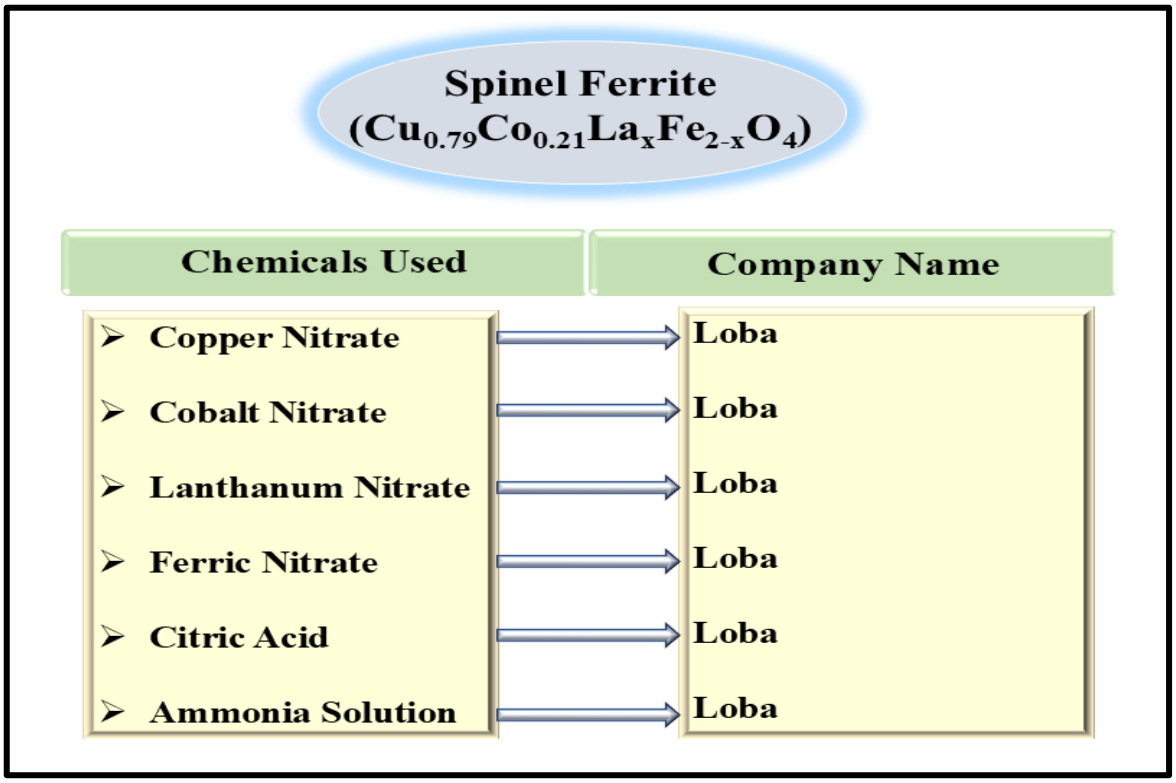

Fig. 3. 4: *Chemicals utilized for the preparation of $Cu_{0.79}Co_{0.21}La_xFe_{2-x}O_4$ spinel ferrites and their respective suppliers*

Table 3. 1: *Comprehensive procedure for synthesizing $Cu_{0.79}Co_{0.21}La_xFe_{2-x}O_4$ spinel ferrites*

<table>
<tr><td colspan="7">Material: Lanthanum doped Cu-Co spinel ferrites</td></tr>
<tr><td colspan="4">Chemical Formulae: $Cu_{0.79}Co_{0.21}La_xFe_{2-x}O_4$</td><td colspan="3">Doping Conc. (x): 0.0, 0.2, 0.4, 0.6, and 0.8</td></tr>
<tr><td colspan="4">Synthesis: Sol-gel auto-combustion approach</td><td colspan="3">Cations to Citric Acid Ratio: 1:1</td></tr>
<tr><td colspan="2">Chemicals Used</td><td>$Cu(NO_3)_2$</td><td>$Co(NO_3)_2$</td><td>$La(NO_3)_3$</td><td>$Fe(NO_3)_3$</td><td>Citric Acid</td></tr>
<tr><td colspan="2">Molecular Weight (in g)</td><td>241.60</td><td>291.03</td><td>433.02</td><td>404.00</td><td>192.13</td></tr>
<tr><td rowspan="5">Amount of Chemicals Used (in g)</td><td>x = 0.0</td><td>3.82</td><td>1.22</td><td>0.00</td><td>16.16</td><td>12.60</td></tr>
<tr><td>x = 0.2</td><td>3.82</td><td>1.22</td><td>1.73</td><td>14.54</td><td>12.60</td></tr>
<tr><td>x = 0.4</td><td>3.82</td><td>1.22</td><td>3.46</td><td>12.93</td><td>12.60</td></tr>
<tr><td>x = 0.6</td><td>3.82</td><td>1.22</td><td>5.20</td><td>11.31</td><td>12.60</td></tr>
<tr><td>x = 0.8</td><td>3.82</td><td>1.22</td><td>6.93</td><td>9.70</td><td>12.60</td></tr>
<tr><td colspan="7">Amount of distilled water utilized for combining nitrates and citric acid: 100 ml</td></tr>
<tr><td colspan="7">Duration for which the magnetic stirrer is operated to achieve a clear solution: 30 mins</td></tr>
<tr><td colspan="7">Gradual addition of ammonia until pH reaches 7</td></tr>
<tr><td colspan="7">Heated between 80 and 100˚C with continuous stirring to obtain a viscous gel: 4-5 hours</td></tr>
<tr><td colspan="7">For complete water removal from the gel, the temperature was raised to 300 ˚C or 350 ˚C till auto combustion occurred: 1-2 hours</td></tr>
<tr><td colspan="7">Further heating at 100 ˚C, the charred remnant produces a fluffy powder: 8-10 hours</td></tr>
<tr><td colspan="7">Using a muffle furnace, the fluffy powder was sintered at 1100 ˚C: 6 hours</td></tr>
<tr><td colspan="7">Pulverized the sintered material using a mortar and pestle to obtain: $Cu_{0.79}Co_{0.21}La_xFe_{2-x}O_4$ spinel ferrites</td></tr>
<tr><td colspan="7">Compressed the powder into 8 mm diameter and 1.5 mm thick cylindrical pellets using a hydraulic KBr press and KBr die set</td></tr>
<tr><td colspan="7">Properties studied: Structural (XRD and FTIR), Morphology (FESEM), Elemental (EDX), Magnetic (VSM), Dielectric (Impedance Analyzer), and Electrochemical (CV).</td></tr>
</table>

3.3.2 Synthesis of Zinc-doped Mn-Ni Spinel Ferrite

As illustrated in Fig. 3.5, $Zn_{0.1}Mn_{0.4}Ni_{0.5}Fe_2O_4$ (ZMNF) spinel ferrite nanoparticles were synthesised using purified AR grade chemicals. Table 3.2 summarizes the comprehensive synthesis route of spinel ferrite and the properties assessed by various characterization techniques.

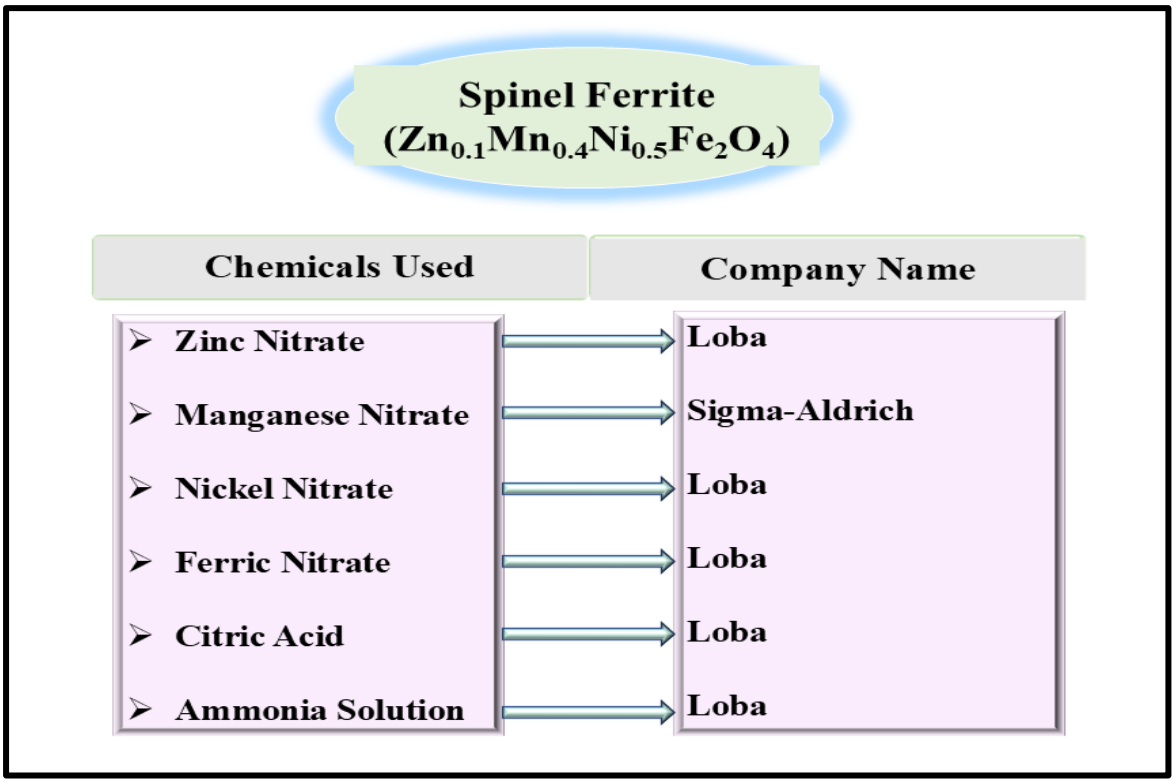

Fig. 3. 5: *Chemicals utilized for the preparation of $Zn_{0.1}Mn_{0.4}Ni_{0.5}Fe_2O_4$ spinel ferrite nanoparticles and their respective suppliers*

Table 3. 2: *Comprehensive procedure for synthesizing $Zn_{0.1}Mn_{0.4}Ni_{0.5}Fe_2O_4$ spinel ferrite nanoparticles*

Material: Zinc-doped Mn-Ni Spinel Ferrite (ZMNF) Nanoparticles					
Chemical Formulae: $Zn_{0.1}Mn_{0.4}Ni_{0.5}Fe_2O_4$			**Doping Conc. (x):** 0.0, 0.2, 0.4, 0.6, and 0.8		
Synthesis: Sol-gel auto-combustion approach			**Cations to Citric Acid Ratio:** 1:1		
Chemicals Used	*$Zn(NO_3)_2$*	*$Mn(NO_3)_2$*	*$Ni(NO_3)_3$*	*$Fe(NO_3)_3$*	*Citric Acid*
Molecular Weight (in g)	297.48	178.95	290.80	404.00	192.13
Amount of Chemicals Used (in g)	1.78	1.43	2.91	16.16	12.60
Amount of distilled water utilized for combining nitrates and citric acid: 100ml					
Duration for which the magnetic stirrer is operated to achieve a clear solution: 30 mins					
Gradual addition of ammonia until pH reaches 7					
Heated between 80 and 100˚C with continuous stirring to obtain a viscous gel: 4-5 hours					
For complete water removal from the gel, the temperature was raised to 300 ˚C or 350 ˚C till auto combustion occurred: 1-2 hours					
Further heating at 100 ˚C, the charred remnant produces a fluffy powder: 8-10 hours					
Using a muffle furnace, the fluffy powder was sintered at 1100 ˚C: 6 hours					
Pulverized the sintered material using a mortar and pestle to obtain: $Zn_{0.1}Mn_{0.4}Ni_{0.5}Fe_2O_4$ spinel ferrite nanoparticles					
Compressed the powder into 8 mm diameter and 1.5 mm thick cylindrical pellets using a hydraulic KBr press and KBr die set					
Properties studied: Structural (XRD and FTIR), Morphology (FESEM), Elemental (EDX), Magnetic (VSM), Dielectric (Impedance Analyzer), and Electrochemical (CV, GCD, EIS).					

3.3.3 Synthesis of Reduced Graphene Oxide (rGO)

For the synthesis of rGO, initial precursors such as graphite powder, sodium nitrate ($NaNO_3$), potassium permanganate ($KMnO_4$), sulfuric acid (H_2SO_4), hydrochloric acid (HCl), hydrogen peroxide (H_2O_2), and deionized water (DI water) were used. Modified Hummer's technique was employed to prepare graphene oxide from the graphite powder. 5 g of graphite powder and 2.5 g of $NaNO_3$ were taken in a beaker along with a magnetic stirrer. They were mixed together by adding 115 ml of concentrated sulfuric acid and stirred well to ensure uniform dispersion in an ice bath until the temperature reached below 5˚C. Subsequently, 15 g of $KMnO_4$ was very slowly included in the mixture under continuous stirring for 60 mins, and the reaction was carried out at a controlled temperature till $KMnO_4$ mixed properly with the solution. Gradually introduce 100 ml of deionized water while ensuring the temperature remains below 20˚C, and continue stirring for 10 to 15 minutes. The reaction was stirred at 90˚C on a magnetic stirrer for a predetermined time, followed by the removal of an ice bath and the addition of 250 mL of deionized water. To terminate the reaction, 12 ml of H_2O_2 was added to ensure the brownish color of the solution. The resulting solution is then washed several times with 150 ml of concentrated HCl (35%) and filtered with Whatman filter paper to remove impurities. Once the reaction reaches its final stage, the graphite turns into graphene oxide (GO). Finally, the dried GO powder was thermally reduced into rGO by heating at 200˚C for 10 mins on a hot plate covering the beaker with aluminium foil with punched pores on it, as illustrated in Fig. 3.6. We have taken small amount of GO to avoid spill out of the material.

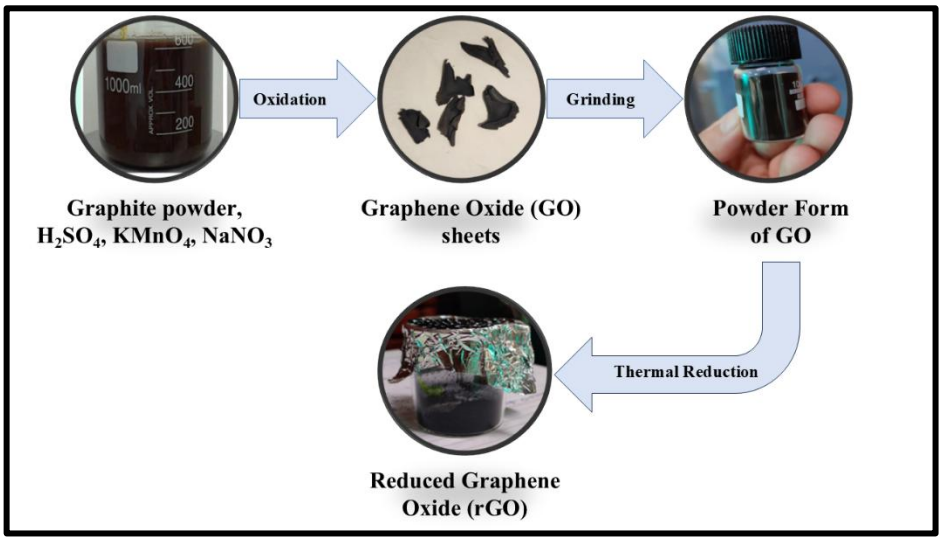

Fig. 3. 6: *Schematic representation of rGO synthesis from graphite, illustrating oxidation to GO followed by reduction to rGO*

3.3.4 Synthesis Approach of $Zn_{0.1}Mn_{0.4}Ni_{0.5}Fe_2O_4$/rGO (ZMNFG) Nanocomposite

The ZMNFG nanocomposite was prepared using a physical blending method. For this, a precise weight ratio of 1:3 was maintained between ZMNF nanoparticles (25 wt%) and reduced graphene oxide (rGO) (75 wt%), measured accurately using an analytical balance. The measured amounts of ZMNF nanoparticles and rGO were combined in an agate mortar. The mixture was then manually ground for 30 minutes using an agate pestle until a homogeneous blend of ZMNFG nanocomposite was achieved. The grinding procedure was executed with consistent pressure and in a circular motion to ensure uniform distribution of ZMNF nanoparticles within the rGO matrix. Finally, the obtained ZMNFG nanocomposite was collected and preserved in a sterile and moisture-free container for further characterization analysis and application investigations. Fig. 3.7. illustrates the physical blending method utilized for the preparation of ZMNFG nanocomposite.

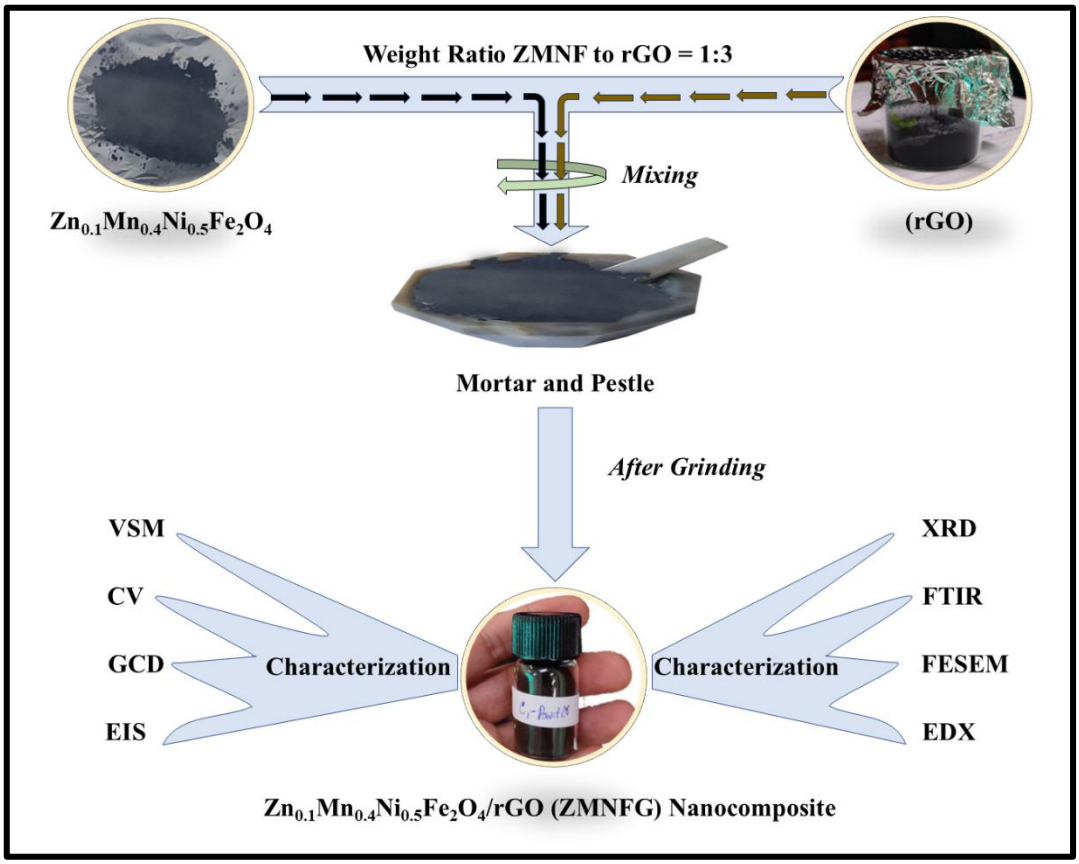

Fig. 3. 7: *Schematic representation of $Zn_{0.1}Mn_{0.4}Ni_{0.5}Fe_2O_4$/rGO (ZMNFG) nanocomposite preparation via physical blending method*

3.3.5 Fabrication of Electrochemical Electrodes

The fabrication of an effective electrochemical electrode is vital for several applications, including energy storage, conversion, and sensing technologies. Till now various categories of substrates such as carbon-based materials, metal foams, conductive polymers, etc have been investigated and utilized for the fabrication of electrodes, each having its own merits depending on the specific applications. Among them, nickel foam substrates are extensively used in electrode fabrication owing to their superior electrical conductivity, lightweight nature, high porosity, and structural durability, and hence boost the performance of these electrodes. These characteristics make nickel foam a good support for active materials in electrodes, allowing efficient ion transport and boosting overall electrochemical performance. In this section, we concentrate on the fabrication of ZMNF nanoparticles, reduced graphene oxide (rGO), and ZMNFG nanocomposite working electrodes on nickel foam substrates, as well as lanthanum-doped Cu-$CoFe_2O_4$ spinel ferrites electrodes. These materials are chosen for their promising electrochemical characteristics, which can greatly boost the efficiency and efficacy of energy-related applications. The subsequent subsections (a and b) discuss the comprehensive step-by-step techniques involved in the fabrication of these electrodes within a three-electrode system.

(a) Fabrication of ZMNF Nanoparticles, rGO, and ZMNFG Nanocomposite Working Electrodes:

For the fabrication of ZMNF nanoparticles, rGO, and ZMNFG composite electrodes, a nickel (Ni) foam substrate with dimensions of (1×1 cm^2) is used. Before utilization, the Ni-foam underwent a pre-treatment process to remove surface oxide layers and other surface impurities, improving its surface properties. This process involved immersing the Ni-foam in a concentrated HCl solution (37 wt.%) at 50˚C and exposing it to ultrasonic treatment for 30 minutes. Subsequently, the Ni-foam was carefully rinsed with deionized water and absolute ethanol for (5 to 10) minutes each to ensure a clean surface. The electrode preparation involved creating a homogeneous ink by combining the active material, consisting of ZMNFG nanocomposite, carbon black, and polyvinylidene fluoride (PVDF) in 8:1:1weight ratio. Specifically, 80 mg (80 wt.%) of ZMNFG nanocomposite, 10 mg (10 wt.%) of carbon black, and 10 mg (10 wt.%) of PVDF were mixed and dispersed in an appropriate amount of N-methyl-2-pyrrolidone (NMP) solvent to generate the ink. This ink was then drop-cast onto the pre-treated Ni-foam substrate. The coated Ni-foam was further dried under vacuum at 60˚C for 6 hours to ensure the comprehensive evaporation of the solvent and the proper

adhesion of active material onto its substrate, resulting in the final composite electrode. Fig. 3.8, shows the detailed steps involved in the fabrication process of ZMNFG nanocomposite working electrode. Similar methodologies were utilized to prepare the working electrodes for the comparative analysis of ZMNF nanoparticles and rGO. The three-electrode system used at room temperature during the electrochemical investigation included a working electrode composed of ink-loaded Ni-foam, silver/silver chloride (Ag/AgCl) reference electrode, and platinum wire counter electrode, with 3 M KOH solution as the electrolyte.

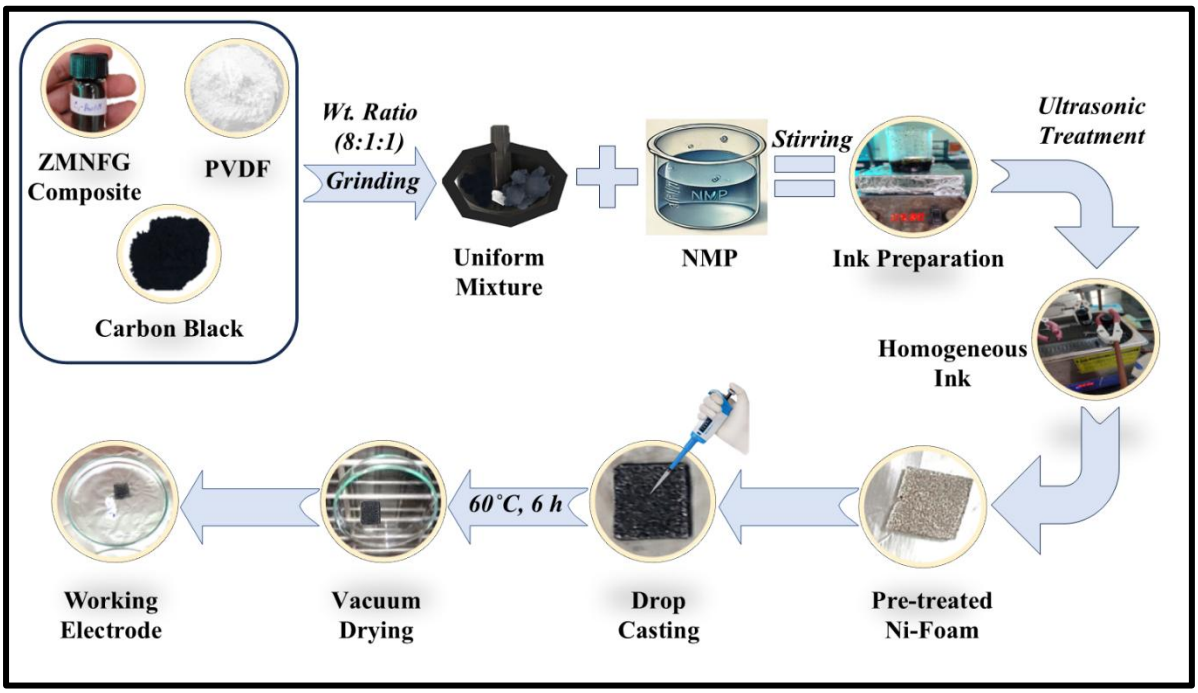

Fig. 3. 8: *Step-by-step fabrication process of $Zn_{0.1}Mn_{0.4}Ni_{0.5}Fe_2O_4$/rGO (ZMNFG) nanocomposite working*

(b) Fabrication of Lanthanum-doped Cu-$CoFe_2O_4$ spinel ferrites working electrode:

The three-electrode system consisted of a working electrode (ink-loaded nickel foam), a (Ag/AgCl) reference electrode, and a counter electrode (platinum wire), along with a 3 M KOH solution that served as the electrolyte. For the fabrication of $Cu_{0.79}Co_{0.21}La_xFe_{2-x}O_4$ spinel ferrite electrodes, the same procedure was followed as depicted in Fig. 3.8. The nickel foam (1x1 cm^2) working electrode was pretreated by sonication in 3 M HCl at 50˚C for 1 hour to remove the nickel oxide layer. After sonication, it was washed thoroughly with distilled water together with ethanol and then dried at 60˚C for 3 hours. The working electrode ink

was formulated using $Cu_{0.79}Co_{0.21}La_xFe_{2-x}O_4$ (70 wt.%), acetylene black (20 wt.%), and polyvinylidene fluoride (10 wt.%) in n-methyl-2-pyrrolidone (NMP) as the solvent. The nickel foam loaded with ink was dried at 60˚C for 12 hours. This procedure was repeated for all five distinct concentrations (x = 0.0, 0.2, 0.4, 0.6, 0.8) to ensure a relative study.

3.4 Characterization Techniques

3.4.1 X-ray Diffraction

X-ray diffraction (XRD) crystallography is a fundamental analytical technique used to determine the atomic and molecular structure of crystalline materials. The fundamental idea of XRD is based on the interaction between X-rays and the periodic arrangement of atoms in a crystal lattice [146]. A beam of monochromatic X-rays focused on a crystalline sample penetrates, the material and is scattered by the electron clouds of the atoms according to Bragg's law, formulated as

$$\boldsymbol{2dsin\,\theta\ =\ n\,\lambda}$$

Where n signifies the integer order of reflection, λ denotes the wavelength of the incident X-rays, d represents the interplanar distance, and θ indicates the angle of incidence [147]. Constructive interference occurs when the path length difference between waves scattered from distinct crystal planes satisfies specific criteria. This constructive interference produces intensified scattered X-rays at specific angles, forming a diffraction pattern indicative of the material's crystal structure Fig. 3.9. Through the analysis of these diffraction patterns, researchers can obtain essential information on the unit cell size, symmetry, and atomic configuration within the crystal. Determining these structural features is crucial for understanding the physical and chemical characteristics of materials since atomic structure influences material behavior under different circumstances [148].

An X-ray diffraction (XRD) apparatus consists of many basic components that work together to study crystalline materials. At its core is the X-ray source, often an X-ray tube that creates X-rays by striking a metal target (frequently copper or molybdenum) with high-energy electrons, creating X-rays through characteristic radiation. The X-rays are then collimated using a beam collimator to ensure a narrow, focused beam directed at the sample. The sample holder, which can hold powders, thin films, or single crystals, puts the material exactly in the direction of the X-ray beam. As the X-rays interact with the sample, they are scattered at

specified angles, which are captured by a detector, such as a scintillation counter or a CCD camera, that measures the intensity of the diffracted X-rays as a function of angle. A goniometer is used to spin the sample and the detector around a fixed axis, allowing for precise angle measurements [149]. The resultant data is represented as a diffractogram, where the intensity of the diffracted X-rays is displayed against the angle of diffraction. Each peak in the diffractogram corresponds to a distinct set of crystal planes, allowing researchers to extract information about the crystal structure, including lattice parameters, symmetry, and atomic locations. Furthermore, the study of these peaks can reveal insights into the crystallinity of the sample, phase identification, and even strain in the material. The flexibility of XRD makes it not only a potent instrument for structural determination but also a critical approach for exploring diverse material characteristics across several fields, including materials science, chemistry, geology, and biology.

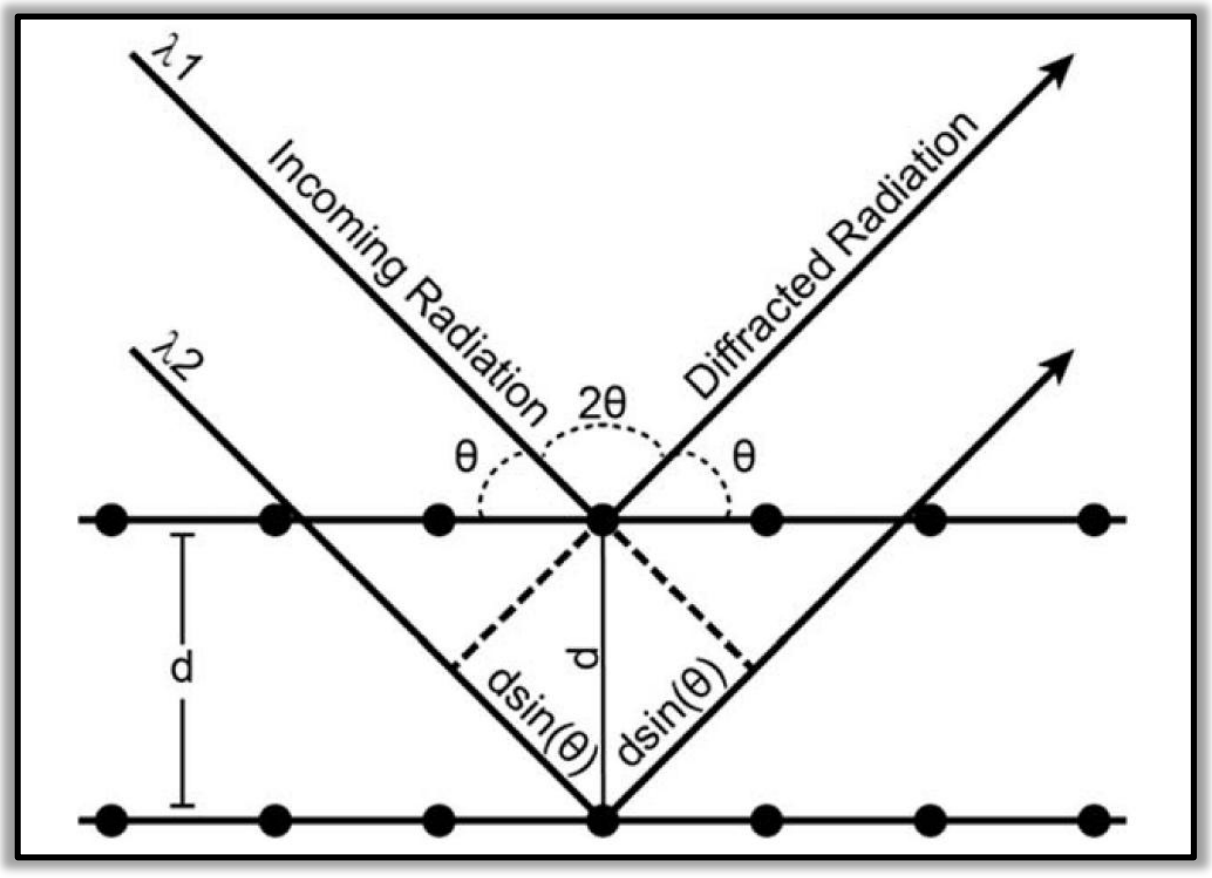

Fig. 3. 9: *Schematic representation of Bragg's law conditions [150]*

In the domain of materials research, XRD crystallography serves as a vital tool for characterizing novel materials, notably in the creation of improved ceramics, polymers, and composites. By giving extensive information on phase composition and crystallinity, XRD

assists in optimizing material qualities for specific applications, such as enhancing the mechanical strength of ceramics or improving the electrical conductivity of semiconductors. In the semiconductor sector, XRD is applied to examine the structural integrity of thin films and multilayers, which are critical for the functioning of electronic devices. The ability to monitor lattice parameters and identify phase transitions makes XRD a vital technique in the creation of novel materials tailored according to specific features. Furthermore, the approach may also be applied to explore the impact of processing conditions on the microstructure of materials, enabling researchers to link processing factors with subsequent material characteristics [146]. In the context of nanotechnology, XRD may be used to assess the crystallinity and size of nanoparticles, which are essential parameters determining their characteristics and applications in domains like as catalysis, drug delivery, and electronics. Moreover, the combination of XRD with complementary techniques, such as scanning electron microscopy (SEM) and transmission electron microscopy (TEM), provides a more thorough analysis of materials. This multimodal technique enables researchers to connect structural information derived from XRD with morphological and compositional data from electron microscopy, offering a complete perspective of material attributes. Such a multidisciplinary approach is increasingly crucial in current materials research because understanding the interplay between structure, composition, and characteristics is critical for generating breakthrough materials and technologies [151].

3.4.2 Fourier Transform Infrared (FTIR) Spectroscopy: A Comprehensive Analysis

FTIR spectroscopy is an efficient analytical technique that facilitates the characterization of molecular species via infrared light absorption. FTIR spectroscopy is fundamentally based on the concepts of vibrational spectroscopy, which involves molecular vibrations resulting from the stretching and bending of bonds within molecules. When infrared radiation is directed onto a sample material, certain wavelengths of light are absorbed, resulting in transitions between vibrational energy states. The absorption is intimately correlated with the molecular structure; various functional groups display unique absorption patterns which makes FTIR an essential instrument for the identification and analysis of materials spanning various fields of science. The operating mechanism of FTIR spectroscopy utilises an interferometer, often of the Michelson type, which is essential for obtaining data. In this configuration, the infrared beam is divided into two paths: one beam proceeds to a stationary mirror, while the other advances to a moving mirror. The two beams reflect and recombine at the beam splitter,

producing an interference pattern that varies with the motion of the movable mirror Fig. 3.10. The outcome is an interferogram, a time-domain signal encompassing all spectral information. The signal is subsequently converted into a frequency-domain spectrum by a Fourier transform algorithm. The benefit of this method is the simultaneous capture of all wavelengths of infrared light, which considerably boosts the speed of analysis compared to typical dispersive spectrometers [152,153].

The result of FTIR spectroscopy is a spectrum that illustrates absorbance or transmittance against wavenumber (cm^{-1}), with each peak corresponding to a distinct vibrational transition. The precise position of these peaks offers insight into the functional groups present in the sample, while their intensity could indicate the concentration of those groups. For instance, a wide peak at 3200-3600 cm^{-1} commonly implies the presence of hydroxyl (–OH) groups, while peaks in the range of 1700-1750 cm^{-1} are often linked with carbonyl (C=O) functional group. Moreover, the presence of peaks in the area (usually 600-1500 cm^{-1}) offers unique fingerprints for complex chemical substances, assisting in their identification [154,155].

One of the most significant developments in FTIR spectroscopy is the creation of Attenuated Total Reflectance (ATR) technology. ATR enables the study of solid, liquid, and even powdered materials with minimum pretreatment procedure, making the technique very flexible. In this approach, the infrared beam enters a crystal with a high refractive index, causing an evanescent wave that interacts with the sample brought in contact with the crystal surface. This interaction enables the collection of spectra from very small sample volumes, making it particularly helpful for examining valuable or rare materials, as well as for researching diverse samples [156].

FTIR spectroscopy has found uses in a wide array of fields, including chemistry, biology, materials science, and environmental research. In the pharmaceutical sector, FTIR is applied for quality control and to validate the identity of raw materials and final products. It assists in the identification of polymorphs, the investigation of drug formulation, and the monitoring of chemical reactions. In the domain of materials research, FTIR is applied to examine polymer compositions, coatings, and composites, offering insights into the interactions between diverse materials and their characteristics. Environmental applications of FTIR spectroscopy are also significant, notably in the monitoring of air and water quality. FTIR can be used to identify and quantify pollutants such as greenhouse gases (e.g., CO_2 and CH_4) and volatile organic compounds (VOCs) in the atmosphere. Additionally, in water

analysis, FTIR spectroscopy may detect toxins, simplifying environmental evaluations and the development of remediation solutions [157,158].

Despite its numerous advantages, FTIR spectroscopy does have some drawbacks. One problem is the overlap of absorption bands, especially in complex mixtures, which may impede the interpretation of spectra. To solve this issue, chemometric approaches, such as multivariate analysis and machine learning algorithms, are increasingly being applied to increase data interpretation and improve quantitative analysis. Furthermore, while FTIR is very effective for organic and inorganic materials, its sensitivity to certain low-abundance species might be restricted, necessitating the employment of complementing methods such as gas chromatography (GC) or mass spectrometry (MS) for thorough investigation [159].

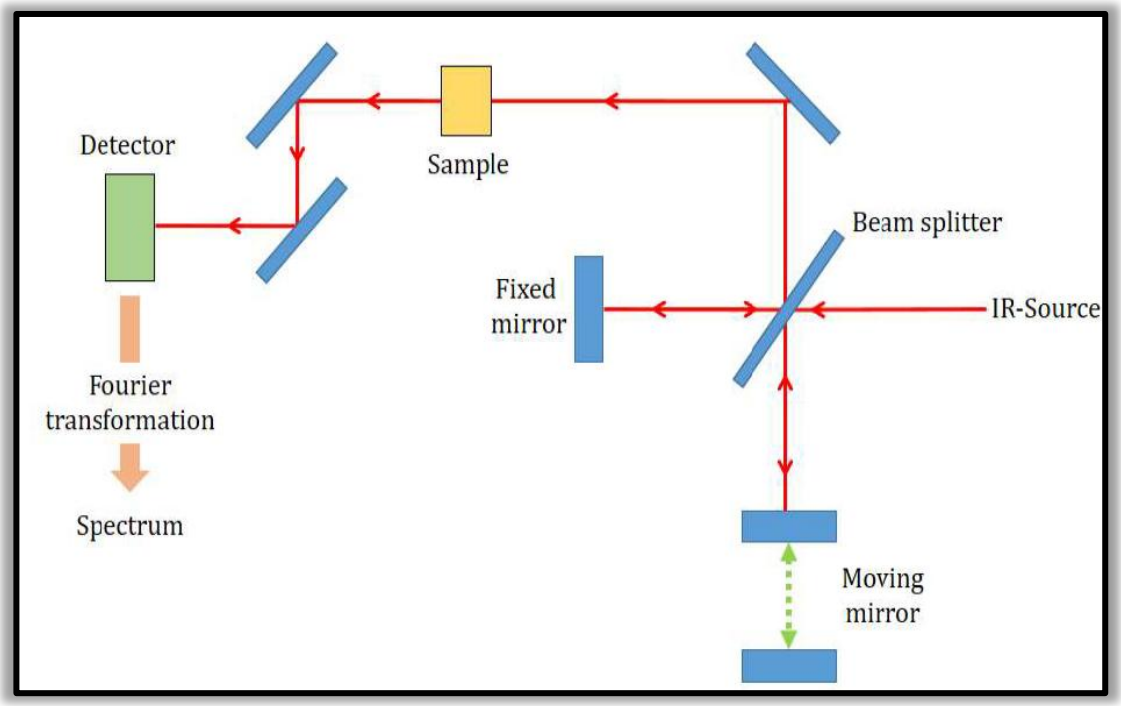

Fig. 3. 10: *Schematic representation of an FTIR spectroscopic device [160]*

The combination of quick data gathering, non-destructive analysis, and broad applicability makes FTIR a crucial tool in current scientific research and industrial applications. As improvements in technology continue to evolve, the possibilities for FTIR spectroscopy will expand, further reinforcing its position in investigating the complex realm of molecular interactions and material characteristics [161].

3.4.3 Raman Spectroscopy

Raman spectroscopy is a strong analytical method used to evaluate materials by studying their vibrational, rotational, and other low-frequency modes. In this spectroscopy, a laser or any other monochromatic light source is exposed to the sample to interact with it. The interaction between the incident photons and the sample molecules results in the occurrence of two distinct types of scattering such as elastic or Rayleigh scattering and inelastic or Raman scattering. As the incident light interacts with the sample, most photons scatter elastically, preserving their original energy resulting in Rayleigh scattering, while a small portion of scattered photons experience a shift (or change) in energy owing to vibrational or rotational energy levels of the molecules inside the sample resulting in Raman scattering [162] as seen in Fig. 3.11.

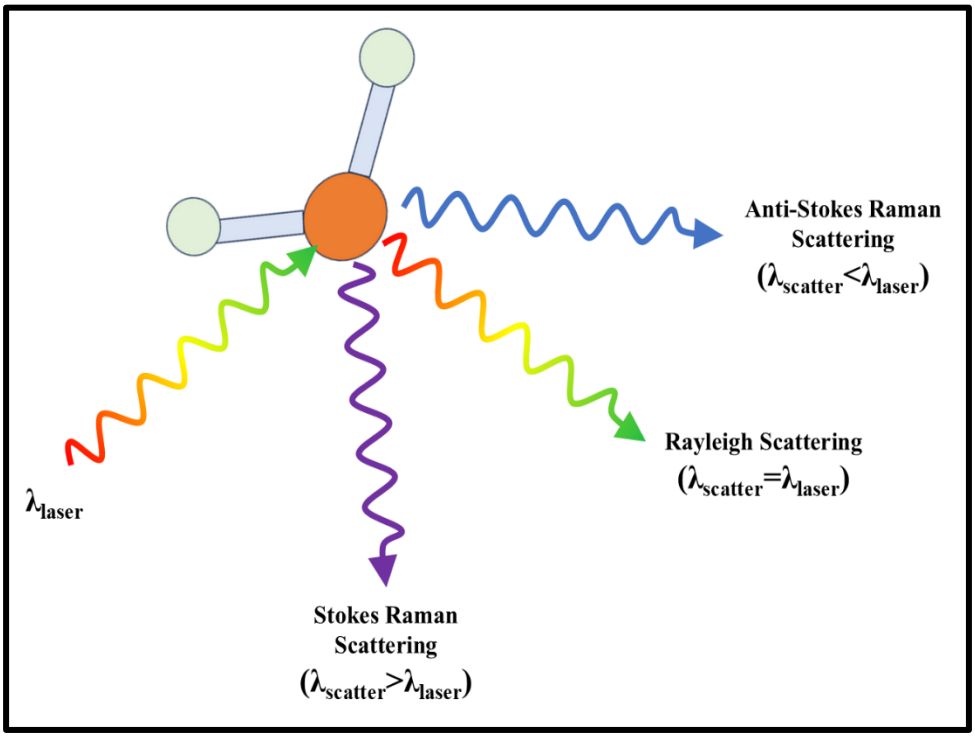

Fig. 3. 11: *Basic principle of Raman scattering*

Raman spectroscopy relies on inelastic scattering of monochromatic light, generally produced by a laser, where the scattered light offers a unique "fingerprint" of a material's molecular and crystal structure depending on their vibrational modes. A spectrometer is used to collect and analyze the light that gets scattered. This scattered light is then split (dispersed) into its component wavelengths or frequencies by diffraction grating or prism for comprehensive analysis. A Raman spectrum is produced using a detector that measures the

intensity of scattered light across different wavelengths. Variation in the energy between the incident and scattered photons is indicated by the Raman shift and is composed of Stokes and Anti-Stokes Raman scattering, which is normally represented in spectra form using intensity against shift. The characteristic peaks and bands of the vibrational and rotational modes of molecules in the samples are seen in the Raman spectrum. Later the spectrum is obtained on the display to assess the information. In Fig. 3.12, a schematic representation of a micro-Raman spectrometer illustrates the key components, and the arrangement of the optical system used in the analysis [163].

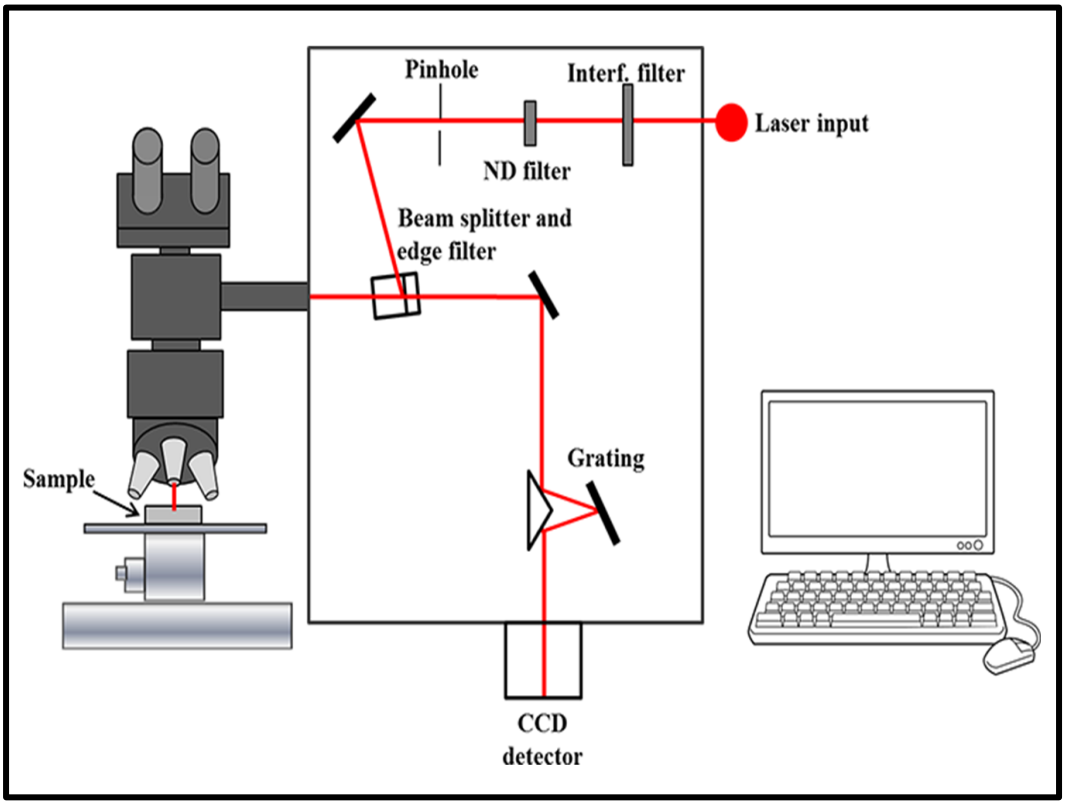

Fig. 3. 12: *Schematic representation of Raman Spectrometer [164]*

Raman spectroscopy is a non-destructive method which indicates that a sample can be analyzed without being modified or destroyed, hence appropriate for application in a broad variety of materials including biological ones. Raman spectroscopy is able to identify small concentrations of analytes, and as such it is particularly useful in areas such as in pharmacological analysis and environmental monitoring. The technique can be employed not only for solids and liquids, but also for gases and it has countless potential applications in chemistry, biology, materials science, and nanotechnology. In particular, it is an important

tool to unveil both the physical and chemical attributes of materials which makes it significant for numerous applications in fundamental and industrial research [165,166].

3.4.4 Field Emission Scanning Electron Microscopy (FESEM) coupled with EDX

Field Emission Scanning Electron Microscopy (FESEM) is an advanced imaging method that utilizes a precisely focused electron beam to generate high-resolution pictures of a sample's surface at the nanoscale. The fundamental principle of FESEM is based on the interaction between an electron beam and the specimen's atoms, producing distinct signals that can be detected and analyzed. In contrast to traditional SEM, which relies on thermionic emission sources (usually tungsten filaments), FESEM utilizes field emission sources, such as cold field emission guns (CFEGs) or Schottky emitters. These sources function by using a strong electric field on a sharp metallic tip, facilitating the extraction of electrons from the surface without requiring high thermal energy. This technique produces a highly collimated electron beam with a tiny diameter, often between 1 and 10 nanometres, which is crucial for attaining the high spatial resolution typical of FESEM [167].

The operational mechanism of FESEM consists of several essential stages: electron production, beam focussing, specimen contact, and signal detection. Electrons are initially emitted from the field emission source and subsequently accelerated towards the sample by an anode at high voltage, generally ranging from 1 kV to 30 kV. The released electrons produce a beam that travels through a series of electromagnetic lenses designed to concentrate the beam onto the specimen surface. These lenses comprise condenser lenses that regulate the beam width and objective lenses that deliver the ultimate focus. The focused electron beam is subsequently raster-scanned over the specimen's surface. As the beam interacts with the material, it creates numerous signals, including secondary electrons, backscattered electrons, and X-rays. Secondary electrons, which are released from the outer shells of atoms, offer topographical information about the surface, whereas backscattered electrons, which are reflected from deeper inside the material, yield compositional contrast. X-ray emissions can be studied for elemental composition by energy-dispersive X-ray spectroscopy (EDX), allowing for simultaneous imaging and analysis [168]. The working principle of FESEM is illustrated in Figure 3.13, highlighting the essential components and operational mechanisms involved in the imaging process.

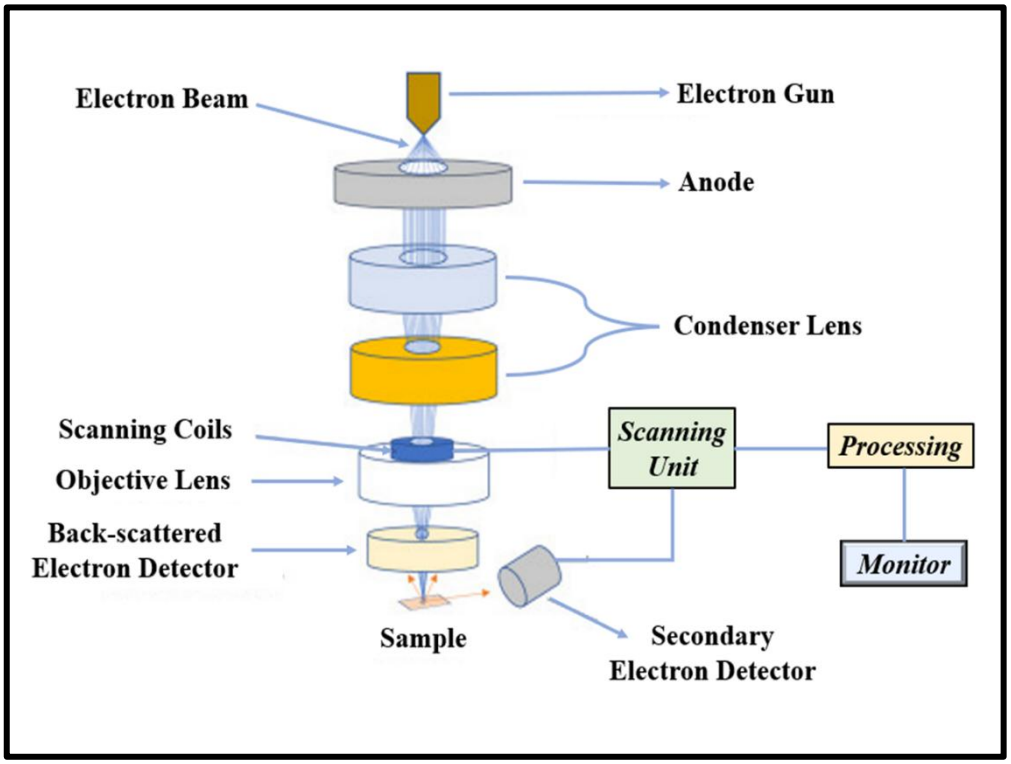

Fig. 3. 13: *Schematic representation of working principle of FESEM [169]*

The science underpinning each phase in the FESEM process is anchored in fundamental principles of physics and materials science. The initial electron emission is regulated by the Fowler-Nordheim equation, which explains the relationship between the electric field intensity and the current density of emitted electrons [170]. This enables precise control of electron beam properties. The focusing of an electron beam depends on the laws of electromagnetism, where magnetic fields created by the lenses control the course of the electrons to reach a desired focus on the sample surface. During the interaction between the electron beam and the specimen, numerous scattering mechanisms occur. Elastic scattering results in backscattered electrons, while inelastic scattering leads to the creation of secondary electrons and X-rays. The detection of these signals is aided by specialized detectors, such as scintillation counters or semiconductor detectors, which transform the emitted signals into electrical signals that may be processed to generate pictures. The resultant pictures give extensive insights into the sample's surface morphology, composition, and crystallography, making FESEM a useful tool in research and industrial applications spanning numerous domains, including materials science, biology, and nanotechnology.

FESEM has become a vital tool in several scientific areas due to its capacity to give high-resolution pictures and extensive information on material characteristics. In materials

research, FESEM is extensively utilized to explore the microstructural characteristics of metals, ceramics, polymers, and composites. For example, researchers can investigate the fracture surfaces of materials to determine failure causes, explore grain boundaries and phase distributions in alloys, or define the surface morphology of coatings and thin films. The capability to view nanostructured materials, such as nanoparticles and nanowires, enables the analysis of their shape, size, and distribution, which are crucial for modifying their properties for applications in catalysis, drug delivery, and electronics. Furthermore, the ability to work at low accelerating voltages minimizes sample damage, making FESEM particularly ideal for studying delicate materials and biological specimens. In the biological sciences, FESEM plays a significant role and is vital for analyzing the ultrastructure of cells, tissues, and biomaterials. The approach enables a comprehensive investigation of cellular components, including membranes, organelles, and extracellular matrices, offering insights into biological processes and interactions at the nanoscale. For instance, researchers can use FESEM to analyze the morphology of bacteria, monitor the attachment of cells to biomaterials, or explore the surface features of implants. The great resolution and depth of field achieved through FESEM enable scientists to view the fine features of biological structures, promoting a deeper understanding of cellular activities and interactions. Additionally, FESEM may be applied in drug delivery studies to examine the interaction between nanoparticles and biological systems, giving significant information on the efficacy and safety of nanocarriers [171].

Looking ahead, the integration of machine learning and artificial intelligence in image processing is likely to transform the interpretation of FESEM data. These technologies can permit faster and more accurate identification of characteristics and patterns within complex datasets, considerably boosting the efficiency of data processing. The continued advancement of FESEM technology promises to expand our understanding of the nanoscale environment, paving the path for novel solutions to challenging problems in science and engineering [172].

3.4.5 Vibrating Sample Magnetometry (VSM)

Vibrating Sample Magnetometry is a complex and extremely sensitive technique adopted for the characterization of magnetic materials, offering crucial insights into their magnetic characteristics through precise determination of magnetization in response to an applied magnetic field. At the core of VSM is the principle of electromagnetic induction, stated by Faraday's law, which says that a changing magnetic field generates an electromotive force

(EMF) in a conductive circuit. In a basic VSM arrangement, a tiny sample often in the form of a powder, thin film, or bulk material is placed in a uniform magnetic field generated by an electromagnet. The sample is then exposed to sinusoidal vibration at a given frequency, generally a few hertz. As the sample moves through the magnetic field, it induces variations in magnetic flux within surrounding pickup coils Fig. 3.14. This action creates an EMF that is directly proportional to the magnetic moment of the sample. By measuring this induced voltage across a range of applied magnetic fields, a full magnetization curve for the sample can be obtained, revealing critical magnetic characteristics such as saturation magnetization (M_s), coercivity (H_c), remanence (M_r), and magnetic anisotropy [173].

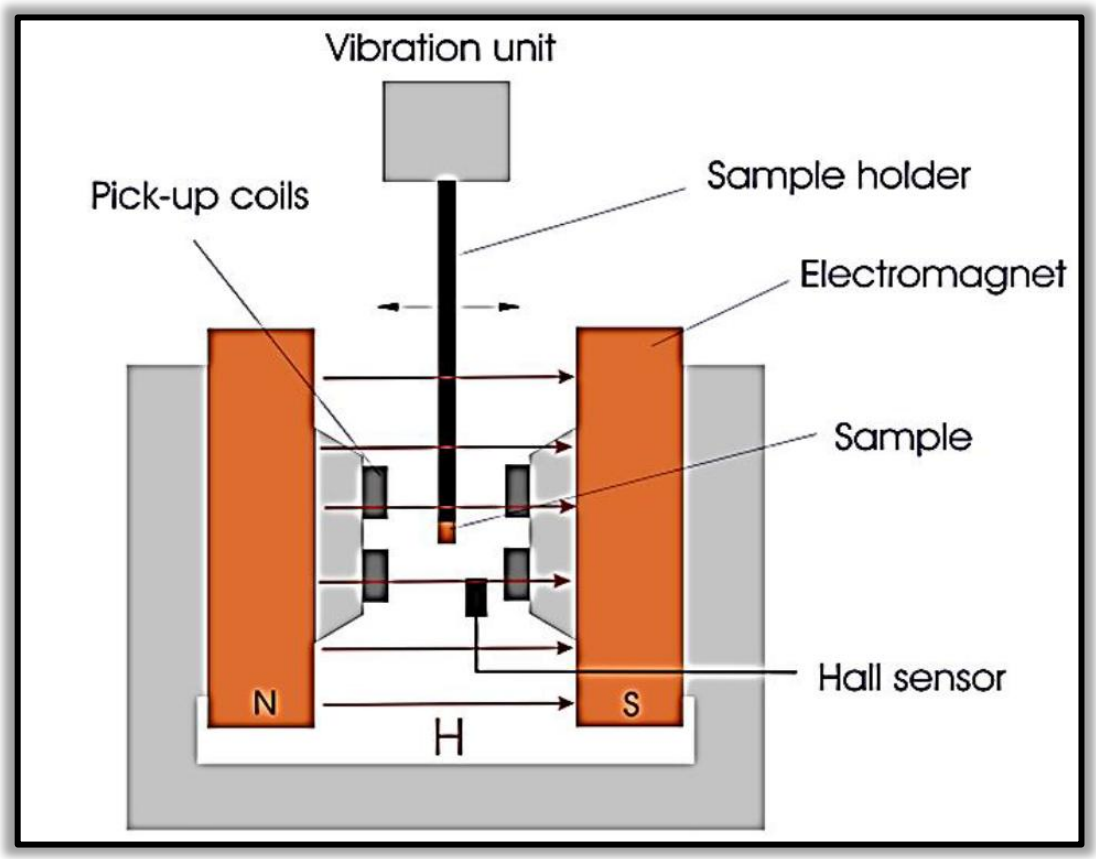

Fig. 3. 14: *Schematic diagram of a vibrating sample magnetometer [175]*

The adaptability of VSM allows it to be applied across a large range of scientific fields, including materials science, condensed matter physics, and engineering applications. One of the primary benefits of VSM is its ability to characterize a wide variety of magnetic materials, including ferromagnetic, antiferromagnetic, and paramagnetic compounds, as well as thin films and nanostructures. The approach is useful for the fundamental study of magnetism, enabling insights into critical phenomena like phase transitions, magnetic

ordering, and the impact of temperature and pressure on magnetic behavior. It is also crucial in the development of innovative materials for technical applications, such as magnetic storage devices, magnetic sensors, and permanent magnets. By enabling the accurate assessment of magnetic characteristics, VSM contributes to the optimization and tailoring of materials for specific applications, enhancing their performance and utility [174].

Modern VSM systems are equipped with sophisticated features that increase their capabilities and allow for a more comprehensive investigation of magnetic materials. For instance, several VSM devices may be linked with cryostats to provide temperature-dependent measurements, enabling research of magnetic characteristics over a wide temperature range, from cryogenic temperatures to ambient temperatures. This capability is vital for understanding how variations in temperature impact magnetic behavior, particularly in materials that display complex magnetic interactions. Additionally, certain VSM installations feature the capability to apply external pressure, allowing researchers to explore the impact of mechanical stress on magnetic characteristics. This is particularly significant in the research of materials developed for high-performance applications, where both magnetic and mechanical characteristics are crucial. The data collected from VSM studies may be examined using several models of magnetic behavior, which give a theoretical foundation for explaining the observed magnetization curves. For example, the Stoner-Wohlfarth model may be employed to understand the hysteresis loops of single-domain ferromagnets, whereas the Neel model is typically utilized for antiferromagnetic materials. These models aid in elucidating the mechanisms behind magnetism, such as domain growth, magnetic anisotropy, and exchange interactions [176,177].

VSM also contributes significantly to the expanding field of nanotechnology, where magnetic nanoparticles and nanostructures are of considerable interest owing to their unique magnetic characteristics and potential uses in biomedicine, data storage, and environmental remediation. The capacity of VSM to describe tiny sample volumes with great sensitivity makes it a promising method for exploring the magnetic characteristics of nanoparticles, which generally display distinct behavior compared to their bulk counterparts. For instance, phenomena like as Superparamagnetism, which occurs in nanoscale ferromagnetic materials, may be efficiently investigated via VSM, supporting the development of new applications such as modified drug delivery systems and hyperthermia treatment in cancer therapy [178,179].

Thus, Vibrating Sample Magnetometry (VSM) is a crucial and versatile technique for the characterisation of magnetic materials, providing researchers with an effective means for analysing the magnetic characteristics of a wide range of substances. The technique's ability to collect precise and comprehensive magnetization data, along with its capability for temperature and pressure control, puts VSM as a cornerstone in both basic research and practical applications. As developments in VSM technology continue to evolve, the potential for such a technique will expand, offering deeper insights into the complex world of magnetism and promoting innovation across multiple fields of science and technology [180,181].

3.4.6 Impedance Analyzer

An impedance analyzer is a sophisticated electronic device designed for the accurate determination of the impedance of components and circuits over a wide frequency range, varying from a few hertz to several megahertz or even gigahertz in some circumstances. The main purpose of an impedance analyzer is to apply an alternating current (AC) signal to the device under test (DUT) and then measuring the voltage (V) across it and the current (I) flowing through the DUT, using high-precision voltage and current sensors. This allows the analyzer to calculate impedance (Z), which in actuality is a complex number; with the real part being resistance (R) and the imaginary part being reactance (X), usually represented as:

$$\boldsymbol{Z = R + jX}$$

The analyzer measures the phase angle between voltage and current to separate these components and could perform frequency sweeps to examine how impedance fluctuates over a range of frequencies. The measurements obtained can give a valuable information about electrical properties of materials and components like capacitors, inductors and resistors and their variation with operating conditions, as well as reveal resonant behaviours, losses, and other frequency-dependent phenomena that are essential in applications like RF circuit design, filter design, and signal integrity analysis. Moreover, the impedance analyzer processes the collected data and presents it in graphical forms such as Nyquist and Bode plots. Such visualizations let users assess the performance of DUT efficiently. Furthermore, the dielectric parameters including dielectric constant (ε'), dielectric loss (ε''), tangent loss (tan δ), and ac conductivity (σ_{ac}), could be determined using the values of impedance (Z), capacitance (C), and angle (θ) obtained from the impedance analyzer [182].

Like all measuring instruments, impedance analyzers are equipped with features that improve their operation. Many of these systems can incorporate automated testing capacity so that many samples or various conditions can be tested in a short duration of time without the need for assistance. Data logging options allow recording measurements over a time to support and conduct long-term investigations and quality control processes. Many modern analyzers also allow for software integration, making it possible to perform more complex data analysis and presentation of advanced data.

In the field of research and development, impedance analyzers are used in material characterization to examine the dielectric properties of materials required for other applications such as in electronics, telecommunications, and biomedical engineering among others. For instance, in biomedical applications, impedance analysis can be employed in the examination of biological tissues to realize their state and condition [183,184].

3.4.7 Electrochemical Characterization Techniques (CV, GCD, EIS)

Electrochemical characterization techniques are valuable tools to determine the properties and performance of materials used in energy storage applications. A trio of distinct electrochemical characterization methods is predominantly used to assess electrode's supercapacitor performance viz Cyclic Voltammetry (CV), Galvanostatic Charge Discharge (GCD), and Electrochemical Impedance Spectroscopy (EIS). In our research, we utilize a three-electrode setup integrated with an electrochemical workstation to conduct all these tests (CV, GCD, and EIS), for comprehensive electrochemical measurements. This setup is made up of three dissimilar electrodes which include the working electrode (WE), the counter electrode (CE), and the reference electrode (RE). All electrodes are dipped in an electrolyte solution. A schematic representation of a three-electrode system is provided in Fig. 3.15.

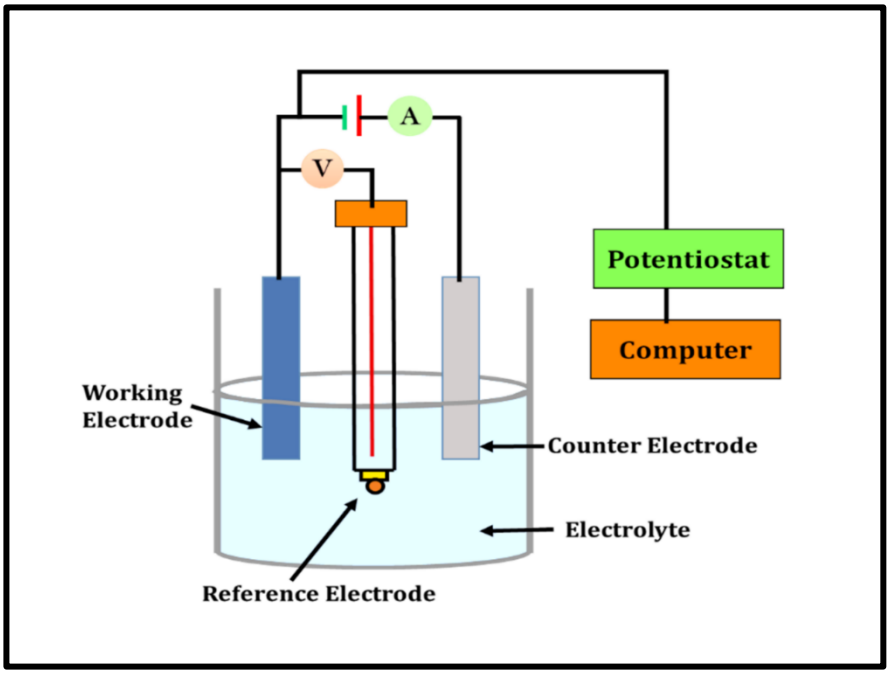

Fig. 3. 15: *Schematic diagram of three-electrode system [185]*

This configuration provides fine control of voltage (potential) given to WE while minimizing the influence of current on the RE. The current passing through the counter and working electrodes is determined by analyzing the potential difference between the WE and RE. The resultant current, proportionate to the voltage produced between the WE and RE is recorded by a data-collecting device, ensuring reliable electrochemical measurements. Furthermore, the electrochemical workstation adjusts and monitors the applied potential or current while measuring the subsequent response, allowing extensive insights into the electrochemical behavior of the system under investigation [186]. The detailed description of characterization techniques like CV, GCD, and EIS are as follows:

(a) Cyclic Voltammetry (CV)

CV is an important technique that offers useful data regarding the electrochemical performance of materials owing to redox reactions under varying applied voltage (or potential). In a CV test, a three-electrode configuration is utilized, where a triangular potential waveform is supplied to the WE and scanned with respect to RE. The resulting current generated by redox reactions at the surface of the WE is recorded through the CE in an unstirred analyte solution. CV operates by sweeping the voltage linearly back and forth between two set points (or limits) in an electrochemical cell while recording the current

response [185]. A duck-shaped cyclic voltammogram is obtained by plotting the current versus the applied voltage, as shown in Fig. 3.16.

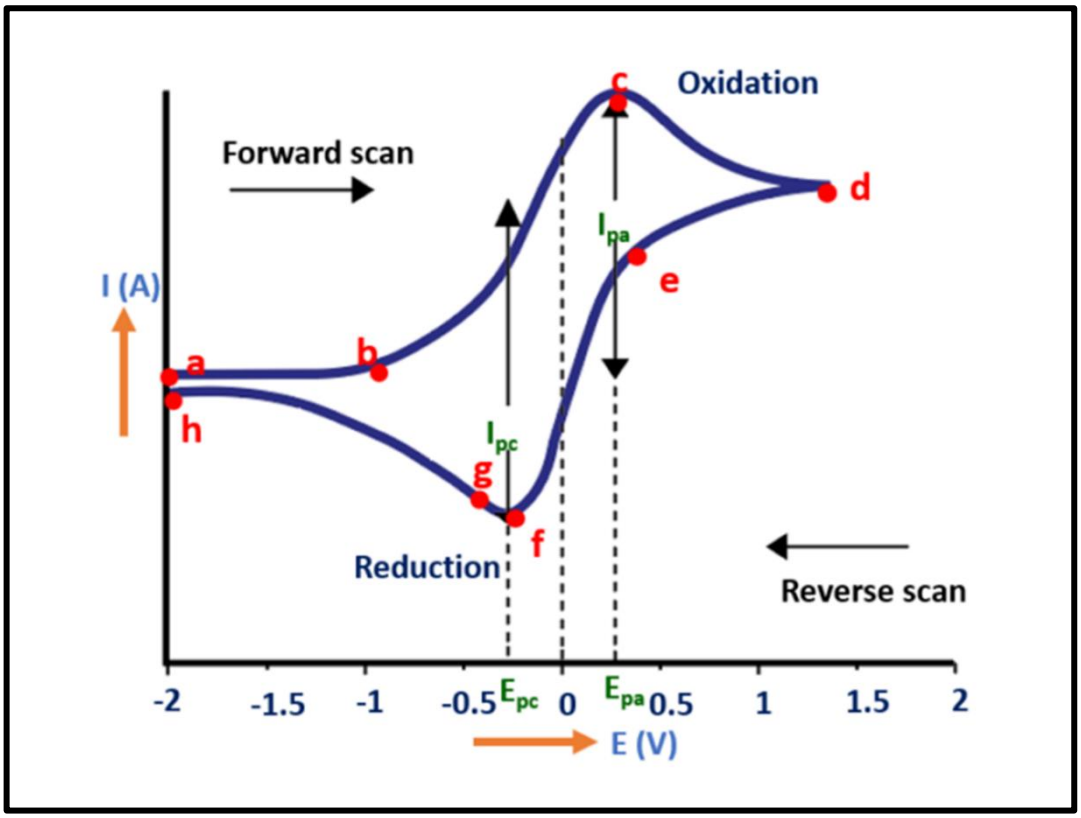

Fig. 3. 16: *Schematic representation of cyclic voltammogram obtained from CV measurements [187]*

The voltammogram shown in Fig.3.16 clearly displays two distinct peaks that are indicative of oxidation and reduction processes. During the anodic forward sweep (or scan), the current increases as the potential is swept in a positive direction, causing the analyte to oxidize. This results in the peak that signifies the maximum oxidation current. When the potential is reversed, the current decreases due to which a reduction peak appears that signifies the restoration of the oxidized species to its original state. The peak potential difference (ΔV) is the difference in potential between both oxidation and reduction peaks, which could offer information about the kinetics of redox processes and the reversibility of the reactions [188].

The more specific and focussed description of cyclic voltammogram involves various phases starting from “a” to “h” as shown in Fig. 3.16. To start with, the oxidation process is initiated from “a” (the initial potential) to “d” (the switching potential). In this region, potential is scanned in a positive direction to induce oxidation. The current that is produced in this process is known as the anodic current (I_{pa}). At point “c”, the anodic peak potential

(E_{pa}) is observed when the entire substrate adjacent to the surface of the working electrode has undergone oxidation. Once the switching potential is attained "d", the potential is then scanned in the negative direction from "d" to "h". As such it gives rise to cathodic current (I_{pc}) and the occurrence of reduction. At point "f", the cathodic peak potential (E_{pc}) is obtained when the whole substrate on the electrode surface has undergone reduction [189].

Moreover, the area under the CV curve can be quantitatively calculated to achieve the C_S value of electrode material based on a three-electrode system as follows [190]:

$$\boldsymbol{C_S = \left(\frac{1}{mv\Delta V}\right) \int_{V_i}^{V_f} I(V)dV}$$

Where $"m"$ corresponds to the mass of active electrode material, $"I(V)"$ signifies current corresponding to peak response, $"\upsilon"$ denotes the scan rate, $"\Delta V"$ represents the potential window over which the measurement is taken, and the area under the CV curve is denoted by the integral "$\int_{V_i}^{V_f} I(V)dV$".

Such information revealed from the cyclic voltammogram plot, and the mathematical calculations mentioned above elucidates the mechanism of oxidation and reduction potentials, the specific capacitance of the material, the number of electrons that take part in redox processes, and the kinetics of the reactions [191].

(b) Galvanostatic Charge Discharge (GCD)

The GCD approach is widely used in the supercapacitor domain because of its scalability from laboratory experiments to industrial applications. It is a prevalent method for determining C_S, cyclability, internal resistance (IR) drop, E_d, and P_d of a material at constant current mode. In contrast to the CV technique which controls the voltage (or potential), the GCD approach evaluates the system's response to a constant current by measuring the voltage over the charging or discharging time. The IR drop sometimes referred to as equivalent series resistance (ESR) refers to the voltage (or potential) drop caused by internal resistance which takes place at the initial stage of the discharge as indicated by a vertical line in the discharge curve [192] shown in Fig. 3.17.

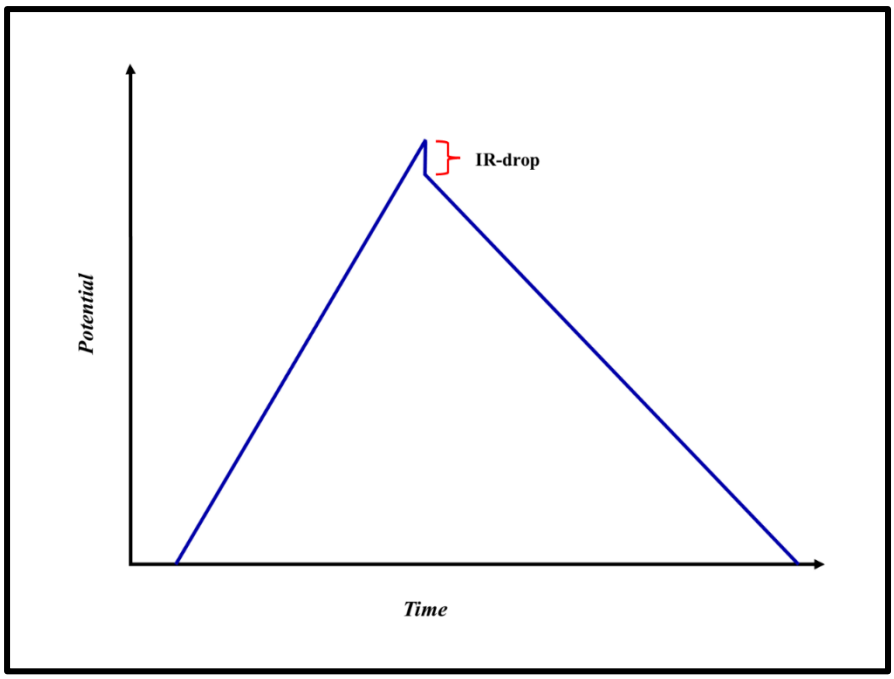

Fig. 3. 17: *Schematic representation of GCD curve at constant current, depicting IR-drop [193]*

In the GCD approach, a constant current passes through the working electrode during the charge-discharge processes, to measure the potential changes over time against a reference electrode. At first, the potential varies abruptly owing to internal resistance (IR) drop, followed by a steady fluctuation as overpotential builds up across the electrodes, which happens when the reactant concentration diminishes at the electrode surface. While charging, the energy is stored in a material resulting an increase in voltage till it hits the preset cut-off voltage. However, during discharging the energy stored in material is released at a steady current until it reaches the lower cut-off voltage.

The C_S value of electrode materials can be derived from the discharge curve of GCD as follows [190]:

$$\boldsymbol{C_S = \left(\frac{I_m \Delta t}{\Delta V}\right)}$$

Where "$Im = \frac{I}{m}$" represents the current density; "Δt" is the discharging time; and "ΔV" denotes the applied potential window.

In addition, the E_d and P_d of the supercapacitor electrode materials can be calculated by utilizing the appropriate formulae [190]:

$$\boldsymbol{E_d = \left(\frac{1}{2}\right) C_s \Delta V^2,}$$

and

$$P_d = \frac{E_d}{\Delta t}$$

The above parameters of E_d and P_d have their usual meanings as discussed earlier.

Specifically, GCD is advantageous for measuring the cycle stability and rate capacity of ESDs. When several charge-discharge cycles are performed, for instance, the capacity retention and degradation of the material can be investigated. This approach is vital for establishing the practical usability of materials in real-world energy storage systems, since it replicates realistic operating circumstances [194].

(c) Electrochemical Impedance Spectroscopy (EIS)

EIS is a sophisticated technology that can deliver detailed investigations of the electrochemical processes such as mass transfer from bulk solution to electrode surface, charge transfer at the electrode-electrolyte interface, adsorption of electroactive species, and electrolyte resistance, taking place within energy storage systems. It effectively examines the behavior of electrode materials and the correlation between capacitive characteristics and both electronic and ionic resistance of electrodes. The complexity of EIS can be explained more effectively by expressing the foundational concept of resistance (R) from Ohm's law, which gives a relationship between voltage (V) and current (I)as follows[195]:

$$R = \frac{V}{I}$$

This frequency independent Ohmic equation is advantageous only in case of direct current (dc) systems. However, in case of alternating current (ac) systems, the measure of resistance in a circuit is given by impedance (Z) and the equation of impedance is analogous to Ohm's law as follows [195]:

$$Z = \frac{V(\omega)}{I(\omega)}$$

Where the impedance is proportional to frequency-dependent voltage $V(\omega)$ and current $I(\omega)$ with "ω" being the angular frequency of oscillating sinusoidal waves. By applying a small amplitude ac signal to the system and measuring the resulting current response over a wide range of frequencies, the EIS spectra can be visualized by Nyquist plot with equivalent circuits, as depicted in Fig. 3.18.

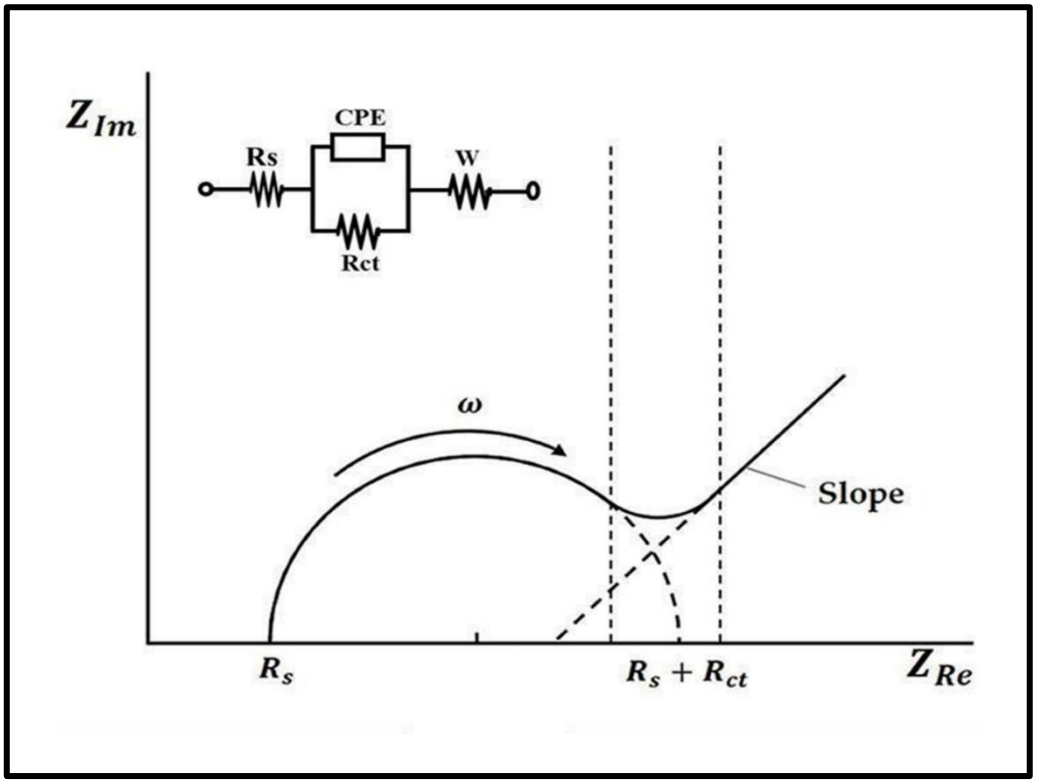

Fig. 3. 18: *Nyquist plot of EIS spectra with an electrical equivalent circuit [186]*

The equivalent circuit shown in Fig. 3.18 consists of four elements: Ohmic resistance (R_s), constant phase element (CPE), charge transfer resistance (R_{ct}), and Warburg impedance (W). To describe complex electrochemical reactions adjacent to the electrode-electrolyte interface, equivalent circuit models based on common electrical circuit components like capacitors and resistors are used. Table 3.3 displays the components of these equivalent circuits along with equations that describe their current-voltage relationships [196] .

Table 3. 3: *Electrical components with their mathematical relations*

Component	***Voltage (V) and Current (I) relation***	***Impedance***
Resistor	$E = IR$	$Z = R$
Inductor	$E = L\frac{d(I)}{dt}$	$Z = j\omega L$
Capacitor	$I = C\frac{d(E)}{dt}$	$Z = \frac{1}{j\omega C}$

Electrolytic solution resistance is a crucial element in the impedance of an electrochemical cell. This resistance is controlled by temperature, the concentration and type

of ions present, and the shape of the region through which the electric current flows. Since the resistor is independent of frequency and does not have any imaginary components, while the inductor and capacitor include imaginary elements in their impedance The Nyquist plot given in Fig. 3. 18 demonstrates both the imaginary and real components of impedance. The imaginary component is displayed on the Y-axis, while the real component is illustrated on the X-axis. An inset diagram depicts a fitted equivalent circuit matching to the Nyquist plot, where the semi-circular loop illustrates the charge transfer resistance (R_{ct}) and the slant line reveals the diffusion process. The ionic diffusion may lead to a phenomenon known as Warburg impedance, which is represented by a diagonal line with a 45° angle, indicating the mass transfer of ions. Warburg impedance lowers at higher frequencies while increases at lower frequencies due to the diffusion of reactants over shorter and longer distances respectively [197].

Moreover, in the medium-frequency range, the physical and morphological properties of the electro-active material considerably impact the capacitance value and behave as a mixture of resistors and capacitors. Unlike capacitors, the interpretation of non-ideal electrochemical behavior is given by CPE which is an essential component in EIS to analyze the deviations caused by factors such as surface roughness, inhomogeneities, or distributed time. The Nyquist plot analysis underscores the importance of EIS in understanding and quantifying key parameters such as charge transfer resistance and ion diffusion behavior, which are essential for optimizing electrochemical systems in practical applications, including corrosion, semiconducting electrodes, coatings, batteries and fuel cells, electrochemical kinetics and mechanisms, biomedical and biological systems, and solid-state systems [183].

CHAPTER 4

Results and Discussion

4.1 La-Doped Cu-$CoFe_2O_4$ Spinel Ferrites

4.1.1 Characterization

The synthesized pristine and lanthanum-doped Cu-Co spinel ferrites underwent extensive characterization to determine the structural, morphological, magnetic, and electrochemical properties. XRD study was done for evaluating the crystalline structure and phase of synthesized samples for which powdered samples were scanned using an X-ray diffractometer (Bruker D8 Advance) equipped with a Cu Kα radiation source (λ = 1.5406 Å) having a range of 20˚ to 70˚, in steps of $0.02^{\circ}s^{-1}$ (generator power, sealed tube: 3kW - IμS: 50 W - TXS/TXS-HE: 6 kW). Using a (Perkin-Elmer) infrared spectrophotometer (resolution 0.5 cm^{-1}), the produced sample's FTIR spectra were obtained within wavenumber range (400 cm^{-1} to 4000 cm^{-1}), to detect active vibrational modes. Surface morphology, as well as elemental composition analysis, were conducted on the synthesized samples through FESEM, JSM-7610F-Plus, [SEI resolution: 1.0nm (15kV), 1.3nm (1kV); during analysis: 3.0 nm, 15 kV; probe current: 5 nA] with an integrated EDX system. A thin fine layer of gold (Au) was applied to the samples before imaging. Magnetic measurements within the field range of ±20 kOe, were conducted at ambient temperature via VSM (VSM-EZ9). A hydraulic KBr press was used to prepare pellets by compressing the powdered samples and then perform dielectric measurements within the frequency range of 100 Hz and 120 MHz, via Impedance Analyzer (WK 6500B). Cyclic voltammetry (CV) was performed by utilizing (METROHM) electrochemical workstation (potential resolution: 3 μV) to examine the fabricated electrode's electrochemical performance for supercapacitor applications.

4.1.2 XRD Analysis

XRD spectra of $Cu_{0.79}Co_{0.21}La_xFe_{2-x}O_4$ with varying concentrations of lanthanum ($0.0 \leq x \leq 0.8$ in steps of 0.2) are presented in Fig. 4.1. The XRD spectra indicate strong and well-defined diffraction peaks of the synthesized samples having a high degree of crystallinity with some additional peaks of lanthanum-doped Cu-Co samples. This information provides significant insights into the composition and crystalline structure of samples. XRD analysis of

lanthanum-doped Cu-Co samples confirmed the presence of finely indexed diffracted peaks, specifically (220), (311), (222), (400), (422), (511), and (440), indicating the formation of cubic spinel structure classified within (Fd3m) space group. These peaks matched with the standard (ICDD # 34-0425) and (ICDD # 22-1086) of (Cu - ferrite) and (Co - ferrite) respectively, as reported in references [58,198]. Furthermore, the XRD spectra show several specific peaks annotated with an asterisk (*) that verify the presence of lanthanum doping along with the emergence of an orthorhombic ($LaFeO_3$) secondary phase within (Pbnm) space group, consistent with standard (ICDD # 74-2203) [199]. Fig. 4.1 demonstrates a direct correlation between the La^{3+} ion concentration and the peak intensity of $LaFeO_3$ phase, indicating that the peak's intensity rises with an increase in La^{3+} ion concentration. Conversely, by increasing the amount of La^{3+} ions, several intensity peaks associated with the spinel ferrite phase were dampened, distorting the crystal lattice. These findings suggest that the solubility of La^{3+} ions within the spinel lattice is limited [200]. Furthermore, the identification of a dual-phase structure in lanthanum-doped Cu-Co ferrites has a significant impact on their potential applications, particularly in high-performance permanent magnets. These materials could be employed in various technologies, including electric motors, magnetic sensors, and magnetic resonance imaging (MRI) devices. Moreover, the dual-phase ferrite offers opportunities for designing multifunctional sensors capable of detecting both magnetic and dielectric signals simultaneously, with potential applications in navigation systems, robotics, and medical devices. Additionally, the unique dual-phase structure may provide synergistic effects, making it suitable for energy-related catalytic processes such as energy storage supercapacitors, fuel cells, or gas conversion reactions. Furthermore, this dual-phase material holds promise for applications in the multilayer chip inductor [201], microwave frequency devices [202], and biomedical fields such as cell manipulation, tumour therapy, and targeted drug delivery [203]. The microstructural parameters listed in Table 4.1 were determined using established equations and analysis of XRD data, with a particular focus on the dominant peak corresponding to the (311) crystallographic plane. The equations used for finding various microstructural parameters are as follows [128,204,205]:

$$\boldsymbol{a = d\sqrt{(h^2 + k^2 + l^2)}} \quad \textbf{(4.1)}$$

$$\boldsymbol{D = K\lambda/\beta Cos\theta} \quad \textbf{(4.2)}$$

$$\boldsymbol{\delta = 1/D^2} \quad \textbf{(4.3)}$$

$$\boldsymbol{\varepsilon = \beta/4tan\theta} \quad \textbf{(4.4)}$$

$$\rho_x = 8M/(N_A a^3) \quad (4.5)$$

$$\rho_b = m_p/(\pi r^2 h) \quad (4.6)$$

$$P(\%) = ((\rho_x - \rho_b)/\rho_x) \times 100 \quad (4.7)$$

$$S = 6000/(D\rho_x) \quad (4.8)$$

The variables used to calculate these parameters are outlined as follows: The symbols 'a' and 'd' signify the lattice constant and inter-planar spacing respectively; 'h, k, and l' are Miller indices; 'D' signifies the size of crystallite; 'k = 0.94' is dimensionless shape factor (Scherrer's constant); 'λ' represents wavelength of X-rays; 'β' is used to denote the full-width at half-maximum (FWHM) of diffraction line; Angle 'θ' is associated with Bragg's law. Dislocation density and strain are represented by 'δ' and 'ε' respectively. Also, 'M' implies the sample's molecular weight; 'N_A' represents Avogadro's constant; Pellet's mass, height, and radius are represented by 'm_p', 'h', and 'r' respectively. The symbols 'ρ_x' and 'ρ_b' indicate the X-ray and bulk density respectively. The sample's porosity is denoted by 'P (%)'; and 'S' represents the specific surface area.

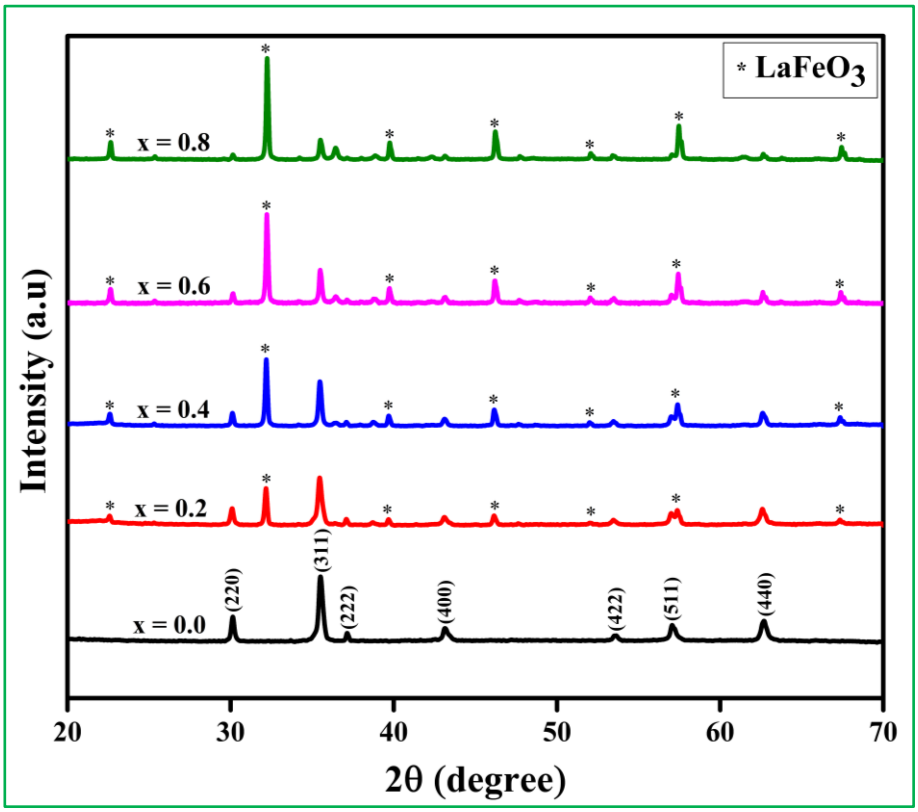

Fig. 4. 1: *XRD patterns of* $Cu_{0.79}Co_{0.21}La_xFe_{2-x}O_4$

Table 4. 1: *Reliability factors (R_p, R_{wp}, R_{exp}), peak position (2θ), FWHM (β), Inter-planar spacing (d), XRD and refined lattice parameters (a and V_{cell}), (D_{311}), (δ), (ε), (ρ_x), (ρ_b), P(%), (S), chi-square (χ^2) and good of fit (GoF) of $Cu_{0.79}Co_{0.21}Fe_{2-x}La_xO_4$*

Parameters	**x = 0.0**	**x = 0.2**	**x = 0.4**	**x = 0.6**	**x = 0.8**
R_p **(%)**	17.6	21.9	18.2	19.8	21.1
R_{wp} **(%)**	17.0	20.9	17.8	21.0	25.8
R_{exp} **(%)**	13.9	17.3	15.9	16.5	8.45
2θ(°)	35.51	35.46	35.47	35.49	35.50
β (°)	0.301	0.312	0.218	0.213	0.215
d (Å)	2.526	2.529	2.529	2.527	2.527
a (Å)	8.378	8.389	8.387	8.382	8.380
V_{cell} (Å^3)	588.022	590.433	589.950	588.985	588.503
a (Å) (Rietveld)	8.376279	8.381635	8.379889	8.383554	8.377952
V_{cell} ***(Å^3) (Rietveld)***	587.697(0.05)	588.825(0.27)	588.457(0.25)	589.230(0.04)	588.049(0.07)
D_{311} (nm)	28.94	27.92	39.96	40.90	40.52
$(\delta * 10^{-3})$ (nm^{-2})	1.19	1.28	0.63	0.60	0.61
$(\varepsilon * 10^{-3})$	4.10	4.26	2.97	2.90	2.93
ρ_x $\left(\frac{g}{cm^3}\right)$	5.382	5.734	6.111	6.498	6.878
ρ_b $\left(\frac{g}{cm^3}\right)$	2.464	4.084	4.115	2.834	4.469
P (%)	54.22	28.77	32.67	56.38	35.02
$(S * 10^7)$ (cm^2/g)	38.513	37.477	24.568	22.577	21.528
χ^2	1.487	1.460	1.264	1.614	9.290
GoF	1.2	1.2	1.1	1.3	3.0
Bragg R-factor (%)	8.91	21.3	6.38	8.18	16.2

Table 4.1 displays a variation in the evaluated lattice constant 'a', ranging between 8.378 Å and 8.389 Å for varying La^{3+} ions concentrations. Initially, the lattice constant increased until the La^{3+} ion concentration reached x = 0.2. Subsequently, it gradually decreased with further substitution of La^{3+} dopant ions. The observed increase in 'a' is likely because of the disparity in ionic radii; the larger radius (1.06 Å) of La^{3+} ions than Fe^{3+} ions (0.67 Å), results in expansion of crystal structure. However, incorporating more La^{3+} ions restricts the expansion of crystal structure growth due to $LaFeO_3$ phase formation, causing a reduction in lattice constant [143,199,206]. The Debye-Scherrer equation, expressed in eqn. (4.2), was employed to compute the crystallite size 'D_{311}' of samples, yielding an estimated size range of (27.92 - 40.90) nm. Equations (4.3) and (4.4) were employed to calculate dislocation density 'δ' and strain 'ε' respectively. The concentration of La^{3+} ions significantly influenced the size of the crystallites 'D_{311}', 'δ', and 'ε' as illustrated in Table 4.1. The undoped (pristine) sample had a 'D_{311}' of 28.94 nm, a 'δ' of 1.19 nm^{-2}, and a 'ε' of 4.10. As the concentration of La^{3+} ions increased, the crystallite size 'D_{311}' initially decreased to 27.92 nm, accompanied by an elevation in both dislocation density 'δ' and strain 'ε' to 1.28 nm^{-2} and 4.26 respectively, until reaching a concentration of x = 0.2. This trend resulted in a decrease in the degree of crystallinity, as depicted in Fig. 4.2.

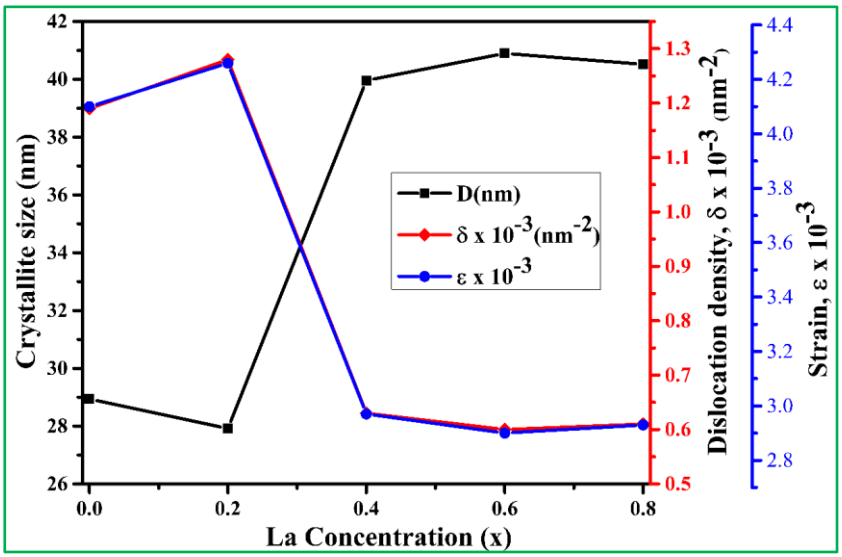

Fig. 4. 2: *Variation in 'D_{311}', 'δ', and 'ε' with La^{3+} ions concentration for $Cu_{0.79}Co_{0.21}La_xFe_{2-x}O_4$*

Subsequently, for concentrations x = 0.4 and 0.6, the crystallite size 'D_{311}' increased to 39.96 nm and 40.90 nm, while dislocation density 'δ' decreased to 0.63 nm^{-2} and 0.60 nm^{-2}, and strain 'ε' decreased to 2.97 and 2.90 respectively. The decrease in both 'δ' and 'ε'

indicates a lower concentration of imperfections (defects) in lattice and the formation of high-quality synthesized samples [207]. Furthermore, the crystallite size 'D_{311}' slightly decreased to 40.52 nm, resulting in a slight increase in both dislocation density 'δ' and strain 'ε' to 0.61 nm^{-2} and 2.93 respectively, until the concentration reached x = 0.8. Data analysis revealed a fluctuating trend in the sample's crystallite size 'D_{311}' as the La^{3+} ions doping concentration increased. The reduction in crystallite size 'D_{311}' initially resulted from differences in ionic radii between La^{3+} and Fe^{3+} ions, making the substitution of La^{3+} ions challenging. This resulted in La^{3+} ions occupying interstitial sites, imposing additional stress that hindered the crystallization of synthesized samples [201,208]. Nonetheless, the growth in crystallite size 'D_{311}' resulted from the larger ionic radius of La^{3+} ions, fostering grain growth [128,199].

The outcomes of 'ρ_x', 'ρ_b', and 'P (%)' as obtained from equations (4.5), (4.6), and (4.7) are reported in Table 4.1. The graph depicted in Fig. (4.3) illustrates the variations in these parameters as the dopant La^{3+} ion concentration changes. The increasing amount of La^{3+} ions doping leads to a corresponding rise in X-ray density 'ρ_x', possibly due to the higher molar weight of La^{3+} ion than Fe^{3+} ion. Moreover, the increase in molar weight surpasses the expansion in the unit cell volume, leading to a linear upsurge in X-ray density 'ρ_x' [209]. On the other hand, the bulk density 'ρ_b' exhibits a non-linear trend, possibly because of the occurrence of certain unavoidable voids formed throughout the sintering and synthesis process of the bulk samples [127]. The porosity 'P (%)' of synthesized samples, ranging from 28.77 % to 56.38 % as shown in Table 4.1, demonstrates a noteworthy improvement compared to previous studies on $Mg_{0.25}Ni_{0.25}Cu_{0.5-x}Co_xFe_{1.97}La_{0.03}O_4$ [58] and $Zn_{0.5}Co_{0.25}Cu_{0.25}Fe_{2-x}La_xO_4$ [198]. The existence of these pores could potentially benefit energy storage applications by enabling convenient electrolyte access to electrodes.

Table 4.1 summarizes the specific surface area 'S' values for synthesized samples, obtained through calculations using equation (4.8). As observed from the data in Table 4.1, an apparent correspondence between the substitution of La^{3+} dopant ions and the increasing crystallite size 'D_{311}', which subsequently leads to a significant decline in 'S'. The reduction in 'S' can be attributed to formation of larger crystal domains and utilization of a high calcination temperature during the synthesis process [210].

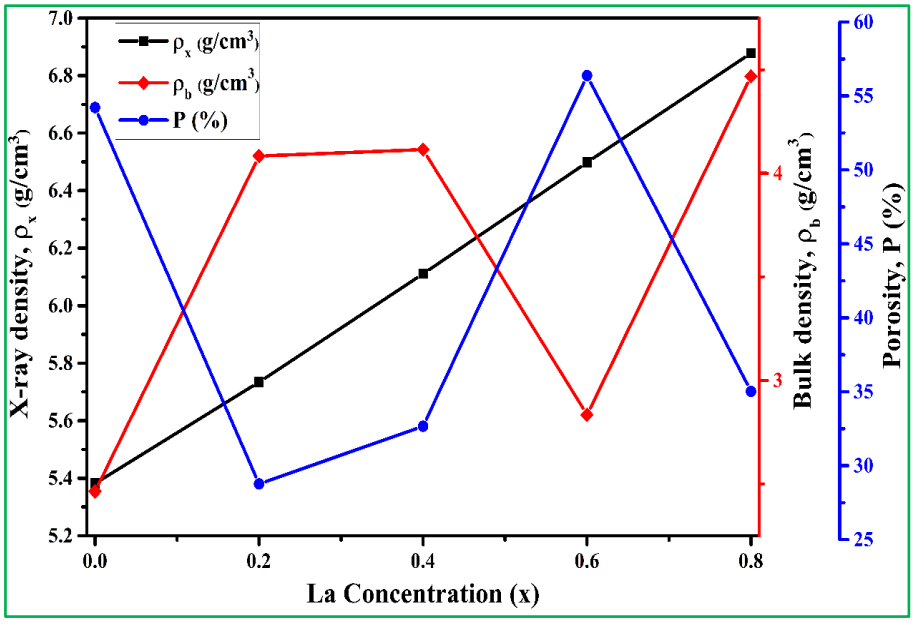

***Fig. 4. 3**: Variation in X-ray density (ρ_x), bulk density (ρ_b), and porosity (P) with La^{3+} ions concentration for $Cu_{0.79}Co_{0.21}La_xFe_{2-x}O_4$*

To verify the phase structure of synthesized samples, Rietveld refinement analysis was conducted on the raw data of a pristine cubic ferrite sample and lanthanum (La^{3+}) doped samples, exhibiting a dual phase of cubic and orthorhombic structures. The Full-Prof Suite program was used to carry out the refining procedure. Fig. 4.4 illustrates the Rietveld fitted diffractograms, highlighting variations in intensity between the empirical (observed) data and computed data. Several R-factors (R_p, R_{wp}, R_{exp}), chi-square (χ^2) and goodness of fit (GoF = $\frac{R_{wp}}{R_{exp}}$), were employed to assess the dependability of the structural analysis [211,212]. Table 4.1 displays the refined parameters obtained through Rietveld fitted refinement process. A lower value of chi-square (χ^2) and goodness-of-fit (GoF) signifies a better alignment (fit) to the desired crystalline phase. The fitted refinement process was iteratively carried out until the value of chi-square (χ^2) and goodness of fit (GoF) approached ≈ 1, except for the last dopant concentration (x = 0.8) which signifies the least fit for the desired crystalline phase [198].

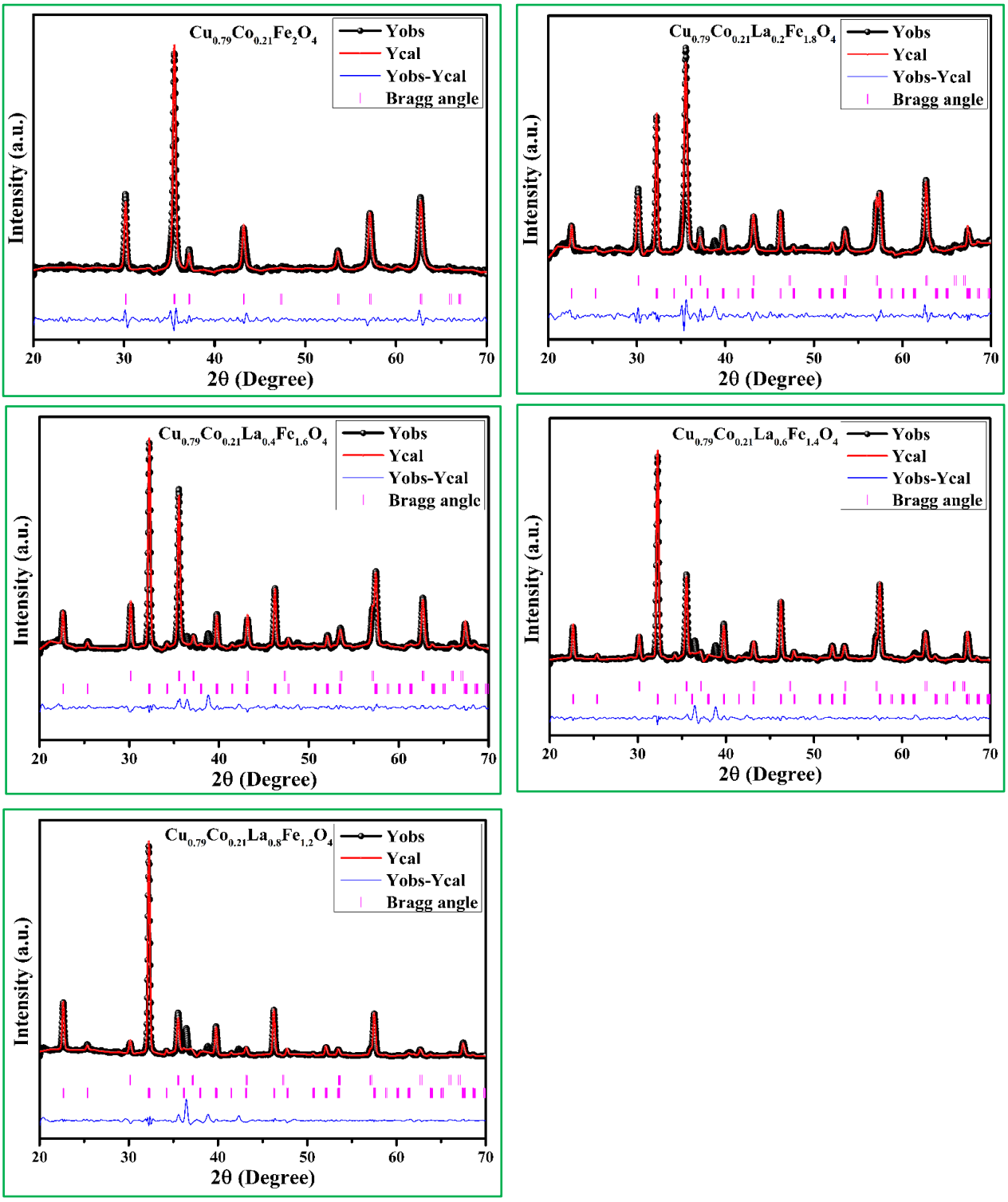

Fig. 4. 4: *Rietveld Refinement of* $Cu_{0.79}Co_{0.21}La_xFe_{2-x}O_4$

4.1.3 FTIR Spectroscopic Analysis

FTIR spectroscopy serves as a valuable tool for examining sample quality, identifying chemical bonds along with functional groups, confirming the presence of spinel structure, and elucidating variations in ferrite systems caused by rare-earth dopant ion substitution [137]. The FTIR spectra were obtained at ambient temperature, ranging from 400 to 4000 cm^{-1}, revealing discrete vibrational bands that are essential for determining the molecular structure for both pristine and lanthanum-doped Cu-Co spinel ferrite samples with varying concentrations of La^{3+} dopant ions. Fig. 4.5 displays the FTIR results for all synthesized samples, prominently unveiling two key vibrational bands (υ_1 and υ_2) located within (400 – 600) cm^{-1} range. In this study, the initial (highest) vibrational band (υ_1) detected in the 524 - 531 cm^{-1} range is linked to intrinsic metal stretching vibrations at a tetrahedral site (M_{tetra}-O). While a subsequent (lower) vibrational band (υ_2) detected in the (461 – 465) cm^{-1} range, relates to octahedral stretching of metal (M_{octa}-O). These findings validate the presence of spinel structure in all produced samples [211,213]. The bands observed at (1733 and 1089) cm^{-1} ascribed to the stretching vibration of the C=O bond, providing insights into the occurrence of certain functional groups within the samples. Additionally, the band that occurred at 955 cm^{-1} is related to the deformation of Fe-O-H groups, providing further understanding of the ferrite's chemical composition. Furthermore, a broad absorption band, indicating stretching vibrations of O-H bonds was identified at a wavenumber of 3276 cm^{-1}. This observation highlights the presence of hydroxyl groups within the synthesized samples, further enriching our understanding of their molecular structure [214]. Furthermore, Fig. 4.5 illustrates that with an increase in the lanthanum content within the nanoparticles, a slight shift in the frequency band is observed, potentially attributed to variations in grain size and lattice parameters. The stretching vibrations of Fe^{3+}- O^{2-} bonds result from alterations in the lattice constant, consequently leading to a displacement in the band position. Moreover, upon comparing five data sets ($0.0 \leq x \leq 0.8$), it was evident that higher La^{3+} ion concentration correlates with an increased intensity of the υ_2 absorption band, while the υ_1 absorption band shows no significant change in intensity. [215–217].

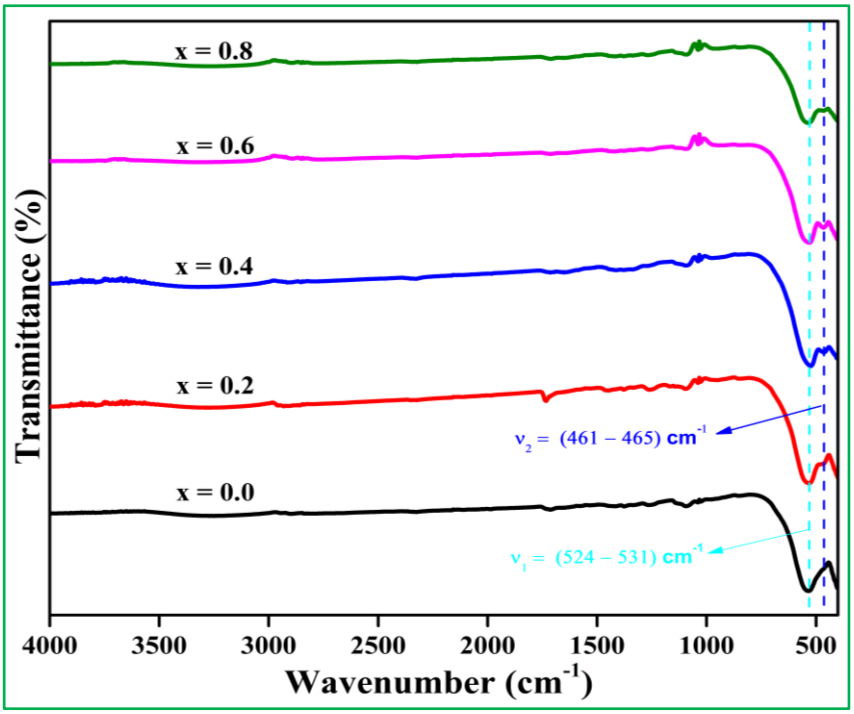

Fig. 4. 5: *FTIR spectra of* $Cu_{0.79}Co_{0.21}La_xFe_{2-x}O_4$

Upon analyzing the IR spectra alongside the data presented in Table 4.2, a compelling correlation emerges. Variations and shifts in the specific positions of vibrational bands υ_1 and υ_2 are noted, attributable to varying concentrations of La^{3+} dopant ions within the lattice sites. These fluctuations in iron-oxygen bond length indicate a significant impact of dopant concentration on the structural characteristics of synthesized ferrite samples [218].

Table 4. 2: *FTIR absorption bands of* $Cu_{0.79}Co_{0.21}La_xFe_{2-x}O_4$

Absorption bands	**x = 0.0**	**x = 0.2**	**x = 0.4**	**x = 0.6**	**x = 0.8**
$\boldsymbol{\upsilon_1\ (cm^{-1})}$	531	530	524	526	531
$\boldsymbol{\upsilon_2\ (cm^{-1})}$	462	465	461	465	464

To sum up, the thorough examination of FTIR spectra not only confirms the existence of the spinel structure but also unveils significant evidence about the structural details and complex molecular composition of synthesized Cu-Co spinel ferrite samples, enhancing our comprehension of their properties and potential applications [219].

4.1.4 Morphological (FESEM) Analysis

Figure 4.6 presents FESEM micrographs showing the surface morphology, along with a corresponding histogram depicting the particle size distribution of $Cu_{0.79}Co_{0.21}La_xFe_{2-x}O_4$ samples with varying concentrations (x = 0.0, 0.2, 0.4, 0.6, and 0.8) of lanthanum (La^{3+}) ions. The micrographs clearly demonstrate the existence of particles with irregular shapes and varying sizes, along with a noticeable degree of agglomeration in all $Cu_{0.79}Co_{0.21}La_xFe_{2-x}O_4$ ferrite samples. The porosity detected in all the samples will find its potential in gas sensing and energy storage applications. The observed agglomeration is consistent with previous studies [220], indicating that it occurs due to magnetic interactions and process-related factors such as precursor concentration, mixing conditions, crystallite size, and calcination process [128,221]. Furthermore, the histogram displays the particle size distribution, which is determined by analyzing FESEM micrographs using ImageJ software. The experimental results reveal the non-uniform size distribution of particles, varying between 1.06 µm and 1.87 µm, as the concentration of La^{3+} ion increases. The observed variations in particle size of lanthanum-doped Cu-Co ferrite samples can be attributed to factors such as non-uniform nucleation, heterogeneous growth rates, as well as existence of oxygen vacancies and voids along grain boundaries during the synthesis process [222–224].

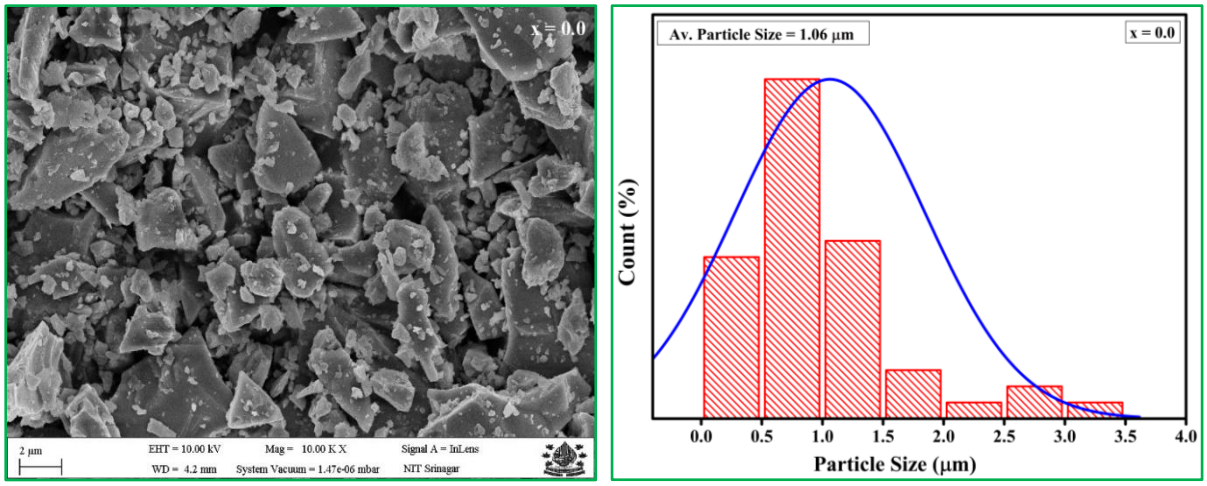

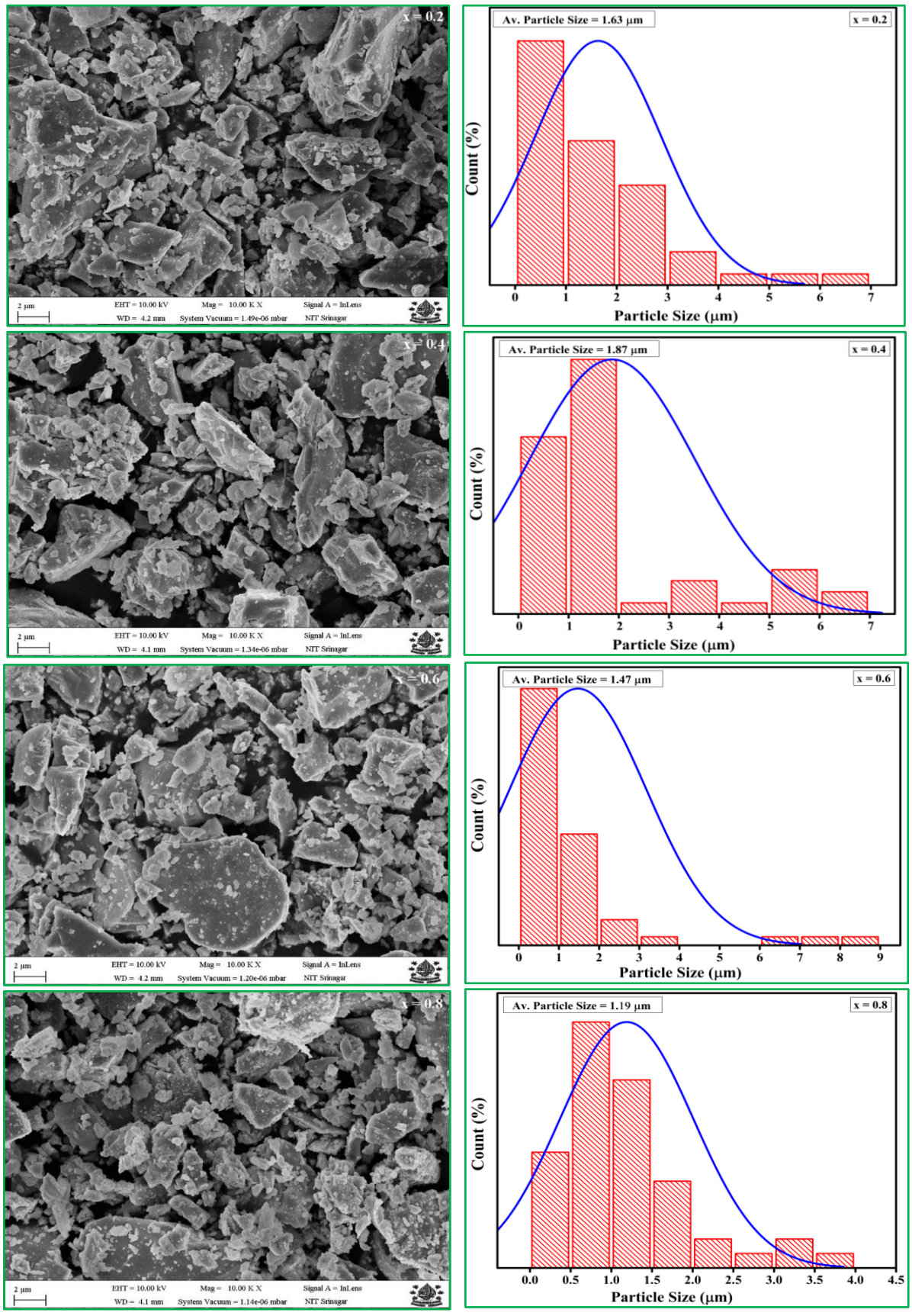

Fig. 4. 6: *FESEM micrographs and particle size distribution of* $Cu_{0.79}Co_{0.21}La_xFe_{2-x}O_4$

4.1.5 Elemental (EDX) Analysis

The elemental composition of $Cu_{0.79}Co_{0.21}La_xFe_{2-x}O_4$ ($0.0 \leq x \leq 0.8$) ferrite samples was investigated using EDX, an analytical method for identifying and quantifying elements in materials. The EDX spectrum in Fig. 4.7 shows clear and distinct peaks corresponding to lanthanum (La), copper (Cu), iron (Fe), cobalt (Co), and oxygen (O), indicating their presence in accurate stoichiometric ratios across all synthesized ferrite samples. The rise in intensity of the lanthanum peak, coupled with a concurrent decrease in the intensity of the iron peak at higher doping concentrations, indicates the effective replacement of Fe^{3+} ions by La^{3+} ions in the doped ferrite samples. Elemental mapping images visually display the spatial distribution of these elements within the samples. Also, the detection of peaks corresponding to gold and carbon in all samples is attributed to the utilization of gold sputter coating and carbon taping respectively, which are essential preparatory steps for conducting accurate EDX measurements [199,225]. Furthermore, the observed ratios of elements closely match the chemical formula for the specific compositions. Consequently, the employed synthesis technique has proven to be highly effective in producing mixed ferrites that exhibit exceptional stoichiometry and a commendable degree of purity.

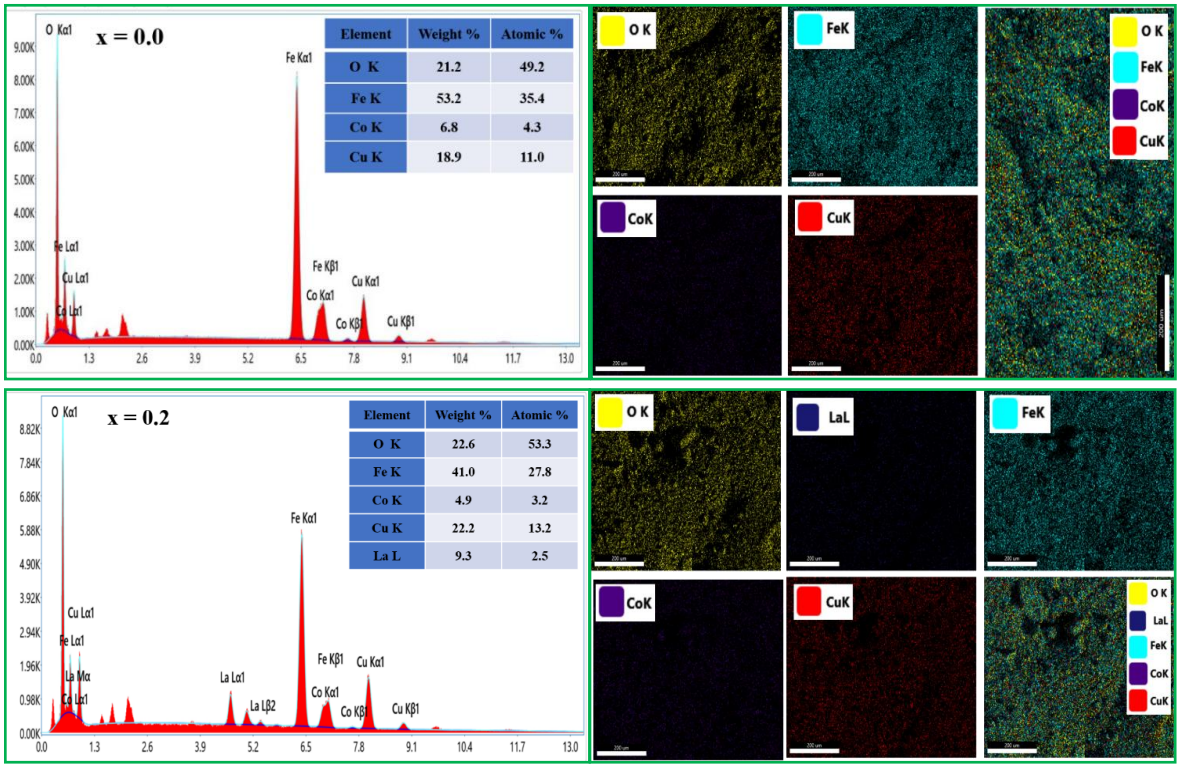

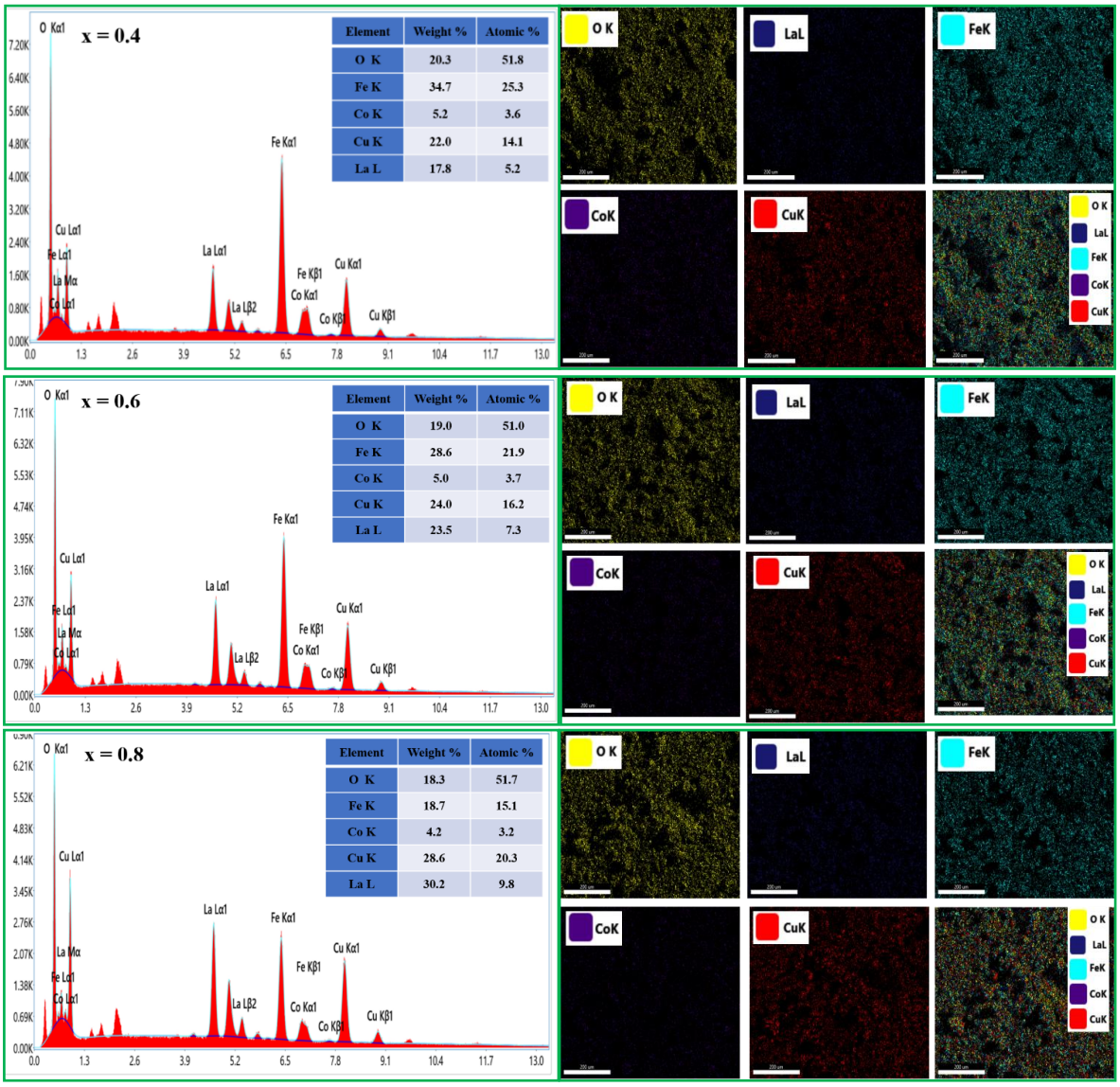

Fig. 4. 7: *EDX spectrum and mapping of* $Cu_{0.79}Co_{0.21}La_xFe_{2-x}O_4$

4.1.6 Magnetic (VSM) Measurements

In this study, the magnetic properties of $Cu_{0.79}Co_{0.21}La_xFe_{2-x}O_4$ ferrite samples were systematically analyzed at room temperature via a VSM technique. This investigation aimed to understand the magnetic behavior of samples as a function of lanthanum (La^{3+}) ion doping, which was varied within the range of 0.0 to 0.8, with step intervals of 0.2 as depicted in Fig. 4.8. The study primarily focused on six key magnetic parameters: saturation magnetization (M_s), retentivity (M_r), coercivity (H_c), magnetic moment (n_B), squareness ratio (R_{sq}), and anisotropy constant (K_1). The saturation magnetization (M_s) values for the $Cu_{0.79}Co_{0.21}La_xFe_{2-}$

$_xO_4$ ferrite samples were observed to decrease as the concentration of La^{3+} ion increased. Specifically, the M_s values were found to be 37.28 emu g^{-1}, 24.95 emu g^{-1}, 21.84 emu g^{-1}, 6.24 emu g^{-1}, and 10.40 emu g^{-1} for La^{3+} ion concentrations of x = 0.0, 0.2, 0.4, 0.6, and 0.8, respectively. The decline in M_s with increasing La^{3+} ion concentration (Fig. 4.9) can be attributed to the dilution effect caused by the incorporation of non-magnetic La^{3+} ions into the ferrite structure. As the La^{3+} ion content rises, the number of magnetic Fe^{3+} ions decreases, thus leading to a reduction in an overall magnetic moment [226]. Similarly, the retentivity (M_r) of the ferrite samples was also observed to decrease with increasing La^{3+} ion concentration shown in Fig. 4.9. The values of M_r were found to be 20.13 emu g^{-1}, 13.46 emu g^{-1}, 9.6 emu g^{-1}, 2.52 emu g^{-1}, and 2.85 emu g^{-1} for La^{3+} ion concentrations of x = 0.0, 0.2, 0.4, 0.6, and 0.8, respectively. This decrease in M_r can be attributed to the decreasing M_s, as M_r is dependent on M_s. When the saturation magnetization decreases, the material's ability to sustain magnetization without an external magnetic field also decreases.

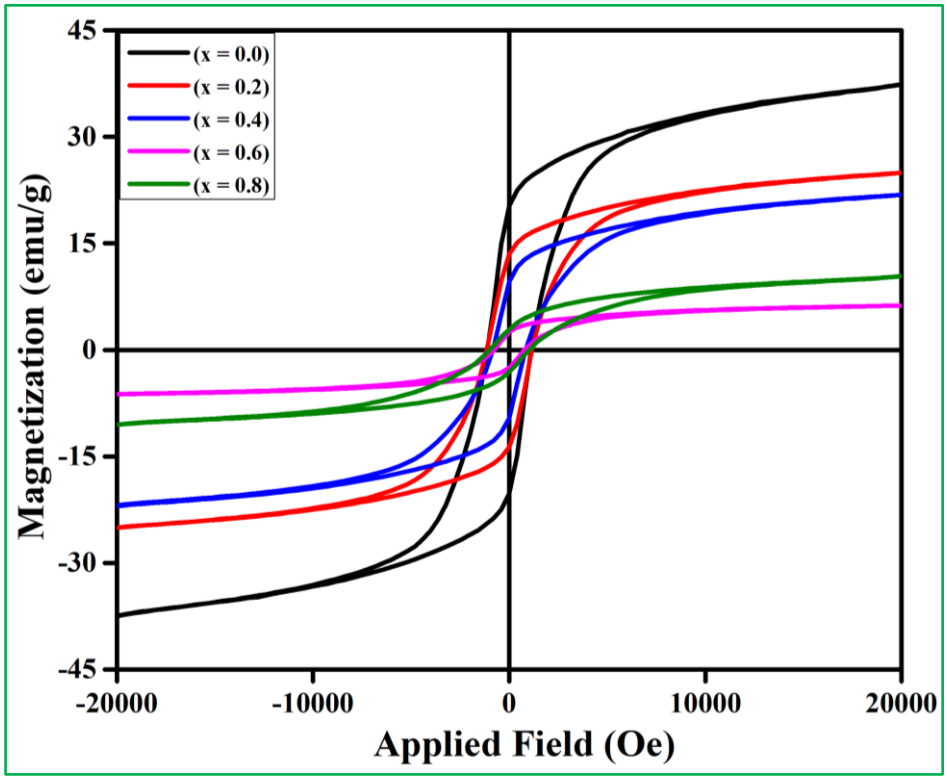

Fig. 4. 8: *M-H curve of* $Cu_{0.79}Co_{0.21}La_xFe_{2-x}O_4$

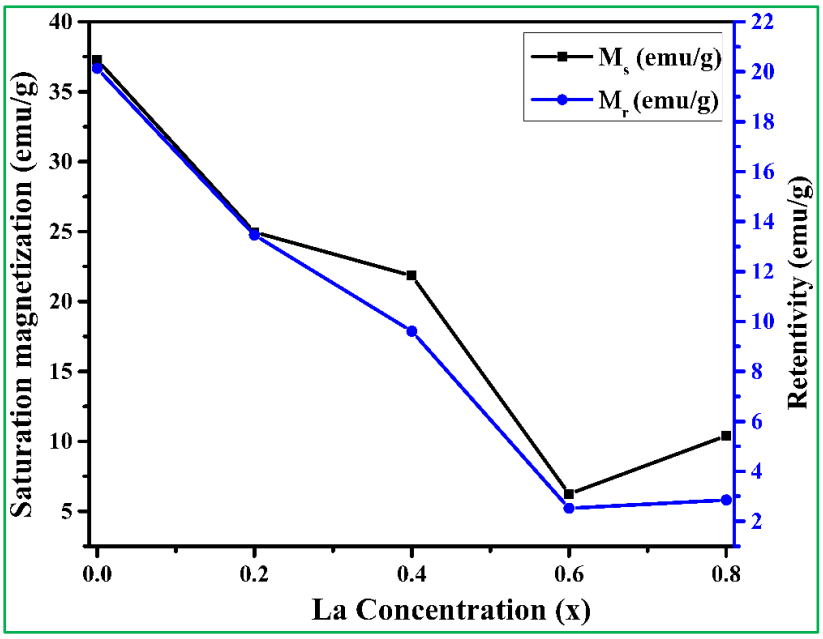

Fig. 4. 9: *Variation in saturation magnetization (M_s), and retentivity (M_r) with La^{3+} ions concentration for $Cu_{0.79}Co_{0.21}La_xFe_{2-x}O_4$*

The coercivity (H_c) of the samples was calculated using the formula:

$$H_c = \frac{0.96 * K_1}{M_s} \qquad (4.9)$$

Here K_1 is the anisotropy constant. It was observed that H_c exhibited an irregular trend with increasing La^{3+} ion concentration. The coercivity values were 1118.98 Oe, 1147.38 Oe, 826.84 Oe, 754.92 Oe, and 978.25 Oe for La^{3+} ion concentrations of x = 0.0, 0.2, 0.4, 0.6, and 0.8, respectively. This irregular trend in coercivity can be attributed to the complex interplay of magnetic interactions in the ferrite structure, which is influenced by the changing composition of the addition of La^{3+} ion. The competition between exchange interactions and anisotropy effects can lead to this non-linear behavior. The irregular trend in coercivity, which reflects the complex interplay of magnetic interactions, suggests potential use in magnetic recording media, where precise control of coercivity is essential for data storage [227]. The magnetic moment (n_B) for the prepared samples was calculated using the formula:

$$n_B = \frac{M_s * MW}{5585} \qquad (4.10)$$

Here M_s is the saturation magnetization, and MW is the molecular weight. The magnetic moment values were found to decrease with increasing La^{3+} ion concentration and

were 1.59 μB, 1.14 μB, 1.06 μB, 0.32 μB, and 0.57 μB for La^{3+} ion concentrations of x = 0.0, 0.2, 0.4, 0.6, and 0.8, respectively. This decrease in magnetic moment is a direct consequence of the reduction in M_s. As previously mentioned, the incorporation of non-magnetic La^{3+} ions into the ferrite lattice reduces the number of magnetic ions, resulting in a smaller magnetic moment [228]. The squareness ratio (R_{sq}) was evaluated by the formula:

$$\boldsymbol{R_{sq} = \frac{M_r}{M_s}} \qquad \textbf{(4.11)}$$

For all the prepared samples R_{sq} value was found to be less than 1, indicating superparamagnetic behavior. This behavior suggests that the magnetic moments within the samples are not aligned and exhibit rapid and random switching under the influence of an external magnetic field. Superparamagnetism is commonly observed in nanoscale materials, and the small particle size and compositional variations in the ferrite samples likely contribute to this behavior [229]. The superparamagnetic behavior makes these materials suitable for applications in magnetic nanoparticles for targeted drug delivery, where the rapid and random switching of magnetic moments can enable the controlled release of therapeutic agents in response to an external magnetic field. Additionally, these spinel ferrites may find applications in magnetic sensors for detecting weak magnetic fields due to their superparamagnetic behavior, making them valuable in geophysical exploration and non-destructive testing. The anisotropy constant (K_1) values were found to decrease with increasing La^{3+} ion concentration. The K_1 values were 42566.91 erg/cc, 29211.36 erg/cc, 18426.72 erg/cc, 4806.84 erg/cc, and 10381.43 erg/cc for La^{3+} ion concentrations of x = 0.0, 0.2, 0.4, 0.6, and 0.8, respectively. The decrease in K_1 can be attributed to the changing structural and compositional features of the ferrite samples as the La^{3+} ion is incorporated. Anisotropy in magnetic materials is influenced by factors such as crystallographic orientation and domain structure. The variation in La^{3+} ion concentration may lead to changes in these factors, resulting in the observed decrease in K_1. The observed magnetic behavior can have implications in designing efficient microwave absorbers for electromagnetic interference (EMI) shielding, as the variation in anisotropy constant (K_1) can impact the absorption characteristics, making them suitable for EMI protection in electronics and telecommunication equipment. Overall, the tuneable magnetic properties of these spinel ferrite materials offer versatility for applications in diverse technological domains [230].

Table 4. 3: *Magnetic parameters of* $Cu_{0.79}Co_{0.21}La_xFe_{2-x}O_4$

Conc. (x)	M_s	M_r	H_c	n_B	R_{sq}	K_1	H_m	dM/dH	
								H →	
								0	H_m
	(emu/g)	(emu/g)	(Oe)	(μ_B)		(erg/cc)	(Oe)	(emu/gOe) * 10^{-3}	
0.0	37.28	20.13	1118.98	1.59	0.54	42566.91	822.21	9.36	20.40
0.2	24.95	13.46	1147.38	1.14	0.54	29211.36	815.10	6.28	13.74
0.4	21.84	9.61	826.84	1.06	0.44	18426.72	403.99	8.37	11.65
0.6	6.24	2.52	754.92	0.32	0.40	4806.84	412.30	2.37	3.35
0.8	10.40	2.85	978.25	0.57	0.27	10381.43	480.60	2.49	3.10

Further, magnetic susceptibility (χ) of a material can be described in terms of dM/dH. Owing to the magnitude's relationship to the switching or inversion field distribution (SFD), magnetic susceptibility (dM/dH) is frequently estimated to assess the magnetic interaction in various systems. The dM/dH curve is a useful tool for assessing the behavior of grains in prepared samples, particularly in distinguishing between single-domain (SD)/pseudo-single domain (PSD) and multi-domain (MD) behavior. Certain magnetic values viz. H_m, dM/dH at $H\rightarrow0$ and $H\rightarrow H_m$ are presented in Table 3. In the case of an ideal single-domain particle with a square-shaped M-H loop, the χ is significantly high at the coercive field (H_c) and drops to zero as $H\rightarrow0$. According to Table 4.3, it is notable that there are finite χ values at $H\rightarrow0$, specifically 9.36, 6.28, 8.37, 2.37, and 2.49 in 10^{-3} emu g^{-1} Oe units for x = 0.0, 0.2, 0.4, 0.6, and 0.8 samples, respectively. This observation further supports the presence of single domain/pseudo-single domain and multi-domain grains in the samples under investigation. The peaks observed in the data are evenly spaced at $2H_m$ and symmetric around $H\rightarrow0$. Examining Figure 4.10, we notice that the peak height of χ at H_m is 20.40, 13.74, 11.65, 3.35, and 3.10 in 10^{-3} emu g^{-1} Oe units for x = 0.0, 0.2, 0.4, 0.6, and 0.8 samples, respectively. These peak heights are higher than the χ at $H\rightarrow0$, as confirmed by Table 4.3. The increasing separation between peaks at H_m, along with the higher peak height of χ = dM/dH indicates a magnetically stable state and a well-crystallized cubic matrix in all the samples. In contrast, the narrow peak separations and small peak heights observed in the nano ferrites can be attributed to the presence of large, unstable superparamagnetic domains. As evidenced by

Table 4.3, the values of H_m are consistently lower than H_c, suggesting the absence of a switching field distribution, which is often observed in nanoparticles with disordered shell structures [228,229,231].

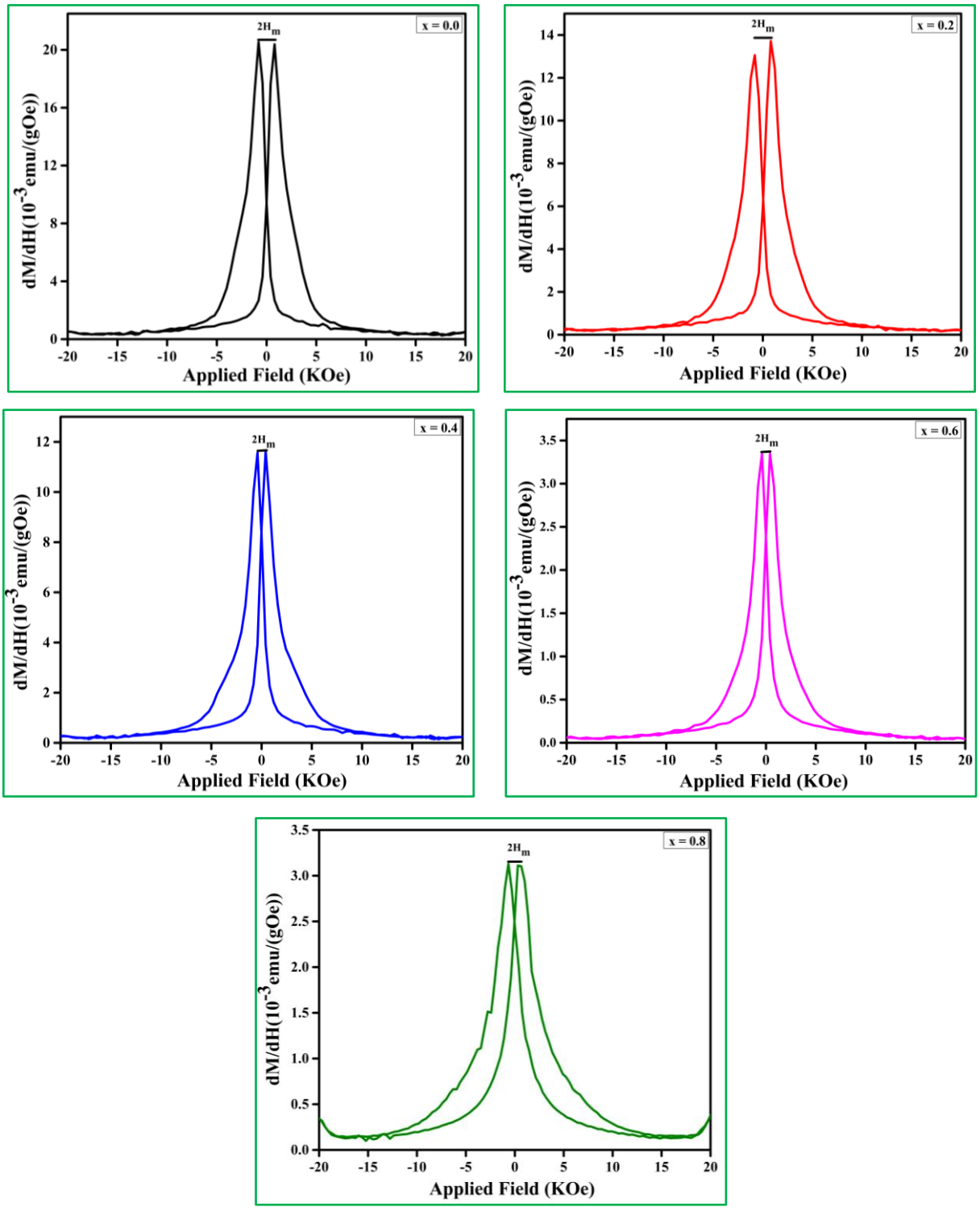

Fig. 4. 10: *dM/dH plot of* $Cu_{0.79}Co_{0.21}La_xFe_{2-x}O_4$

4.1.7 Dielectric Studies

The dielectric studies of $Cu_{0.79}Co_{0.21}La_xFe_{2-x}O_4$ ferrite samples at five different concentrations (x = 0.0, 0.2, 0.4, 0.6, 0.8) were analyzed using an impedance analyzer. This investigation aimed to understand the room temperature dielectric behavior of the samples within the logarithmic frequency range of 100 Hz - 120 MHz. The dielectric characteristics of a material are influenced by ionic, dipolar, electronic, and space-charge polarization processes, each contributing variably over distinct frequency ranges. The dielectric behavior of a material is often characterized by the relative dielectric constant (ε) represented in the form of a complex quantity as follows [232]:

$$\boldsymbol{\varepsilon = \varepsilon' + i\varepsilon''} \quad \textbf{(4.12)}$$

The above equation (4.12) includes real (ε') and imaginary (ε'') components of dielectric constant, in which the former signifies the material's ability to store energy in a dielectric material via polarization, while the latter denotes the energy dissipated (loss) as heat when subjected to an applied field.

In addition, the correlations between the real part (ε'), imaginary part (ε''), and tangent loss or dissipation factor ($tan\ \delta$) was calculated using the following relations [233,234] :

$$\boldsymbol{\varepsilon' = \frac{Cd}{\varepsilon_0 A}} \quad \textbf{(4.13)}$$

$$\boldsymbol{\varepsilon'' = \varepsilon' * tan\ \delta} \quad \textbf{(4.14)}$$

Where 'C' signifies the capacitance measured by the impedance analyzer, 'd' represents the thickness of pellets (1.4 mm < d < 1.8 mm), 'A' corresponds to the area of the cross-section of pellets, $(\varepsilon_0 = 8.85 * 10^{-12})F\ m^{-1}$ denotes the absolute permittivity of vacuum, and 'δ' represents the phase difference that exists between the induced current and the applied field.

The variation of frequency-dependent dielectric constant's real part (ε'), dielectric constant's imaginary part (ε''), and loss tangent ($tan\ \delta$) of $Cu_{0.79}Co_{0.21}La_xFe_{2-x}O_4$ are presented in Fig. 4.11, Fig. 4.12, and Fig. 4.13, respectively.

As observed in Fig. 4.11, the frequency-dependent behavior of ε' displays dispersion. For all pristine and La-doped Cu-Co ferrites, the ε' values decrease with an increase in frequency (up to 1MHz) and stabilize to nearly constant values for frequencies above 1MHz. At low frequencies, the ε' displays high values across all La^{3+} ion compositions (x) of $Cu_{0.79}Co_{0.21}La_xFe_{2-x}O_4$ ferrites, primarily due to interfacial polarization arising from surface charges at the grain boundaries and the influence of space charge polarization that prevails in

materials with heterogeneous structures. The induced field at this low frequency allows ample (or sufficient) time for dipoles to align completely, resulting in a noticeable dielectric response [235,236]. In addition, as frequency increases, the value of (ε') drops drastically for compositions (x = 0.4, 0.6, and 0.8) and slightly for compositions (x = 0.0 and 0.2) of $Cu_{0.79}Co_{0.21}La_xFe_{2-x}O_4$. This phenomenon arises as the induced dipoles struggle to follow the rapidly oscillating field at elevated frequencies, resulting in reduced polarization [67,68]. Furthermore, the value of (ε') increases with higher concentration (x) in $Cu_{0.79}Co_{0.21}La_xFe_{2-x}O_4$, demonstrating that higher lanthanum (La^{3+}) ions doping enhances polarization processes. This tendency may be ascribed to structural changes or an increased charge carrier density. It is also observed from the plot that the maximum value of (ε') is achieved at a concentration of (x = 0.8), indicating that the substitution of La^{3+} ions considerably affects the material's polarizability [221]. These studies suggest that lanthanum (La^{3+}) ion doping enhances polarization, dielectric properties, and magnetic behavior in various materials, making them viable for applications in radiation absorption, data recording, and photocatalysis [132].

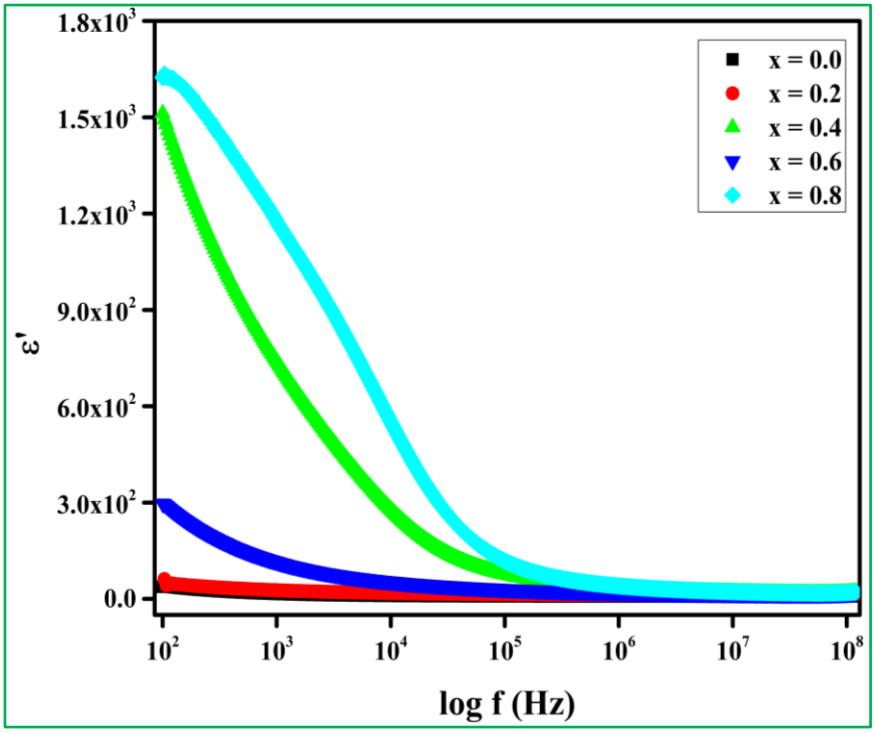

Fig. 4. 11: *Room-temperature variation of dielectric constant's real part (ε') with frequency of $Cu_{0.79}Co_{0.21}La_xFe_{2-x}O_4$*

To examine the conduction characteristics, the frequency-dependent imaginary part of dielectric constant (ε'') for varying La^{3+} ions concentrations (x) in $Cu_{0.79}Co_{0.21}La_xFe_{2-x}O_4$ ferrites is portrayed in Fig. 4.12. At low frequencies, the dielectric loss or imaginary part of dielectric constant (ε'') exhibits high values across all compositions (x) of $Cu_{0.79}Co_{0.21}La_xFe_{2-x}O_4$ ferrites due to interfacial polarization and then declines sharply as the frequency escalates due to the misorientation of dipoles in response to the varying electric field. Such dispersion behavior in $Cu_{0.79}Co_{0.21}La_xFe_{2-x}O_4$ ferrites can be described using Maxwell Wagner-type interfacial polarization in compliance with Koop's phenomenological theory [239–241]. As observed clearly in Fig. 4.12, the dielectric loss (ε'') reaches maximum values at lower frequencies for specific concentrations of lanthanum (La^{3+}) ions (x = 0.4 and 0.8), attributed to enhanced polarization mechanisms and structural modifications caused by La^{3+} ion substitution. Furthermore, this substitution modifies the ionic conductivity and facilitates enhanced $Fe^{2+} \leftrightarrow Fe^{3+}$ hopping processes within the material. Consequently, these alterations lead to a notable increase in the dielectric losses observed in these compositions [128]. Finally, at high frequencies (above 100 KHz), the imaginary part of dielectric constant (ε'') stabilizes and approaches nearly zero, indicating that electronic polarization dominates, while ionic and orientational polarization mechanisms contribute insignificantly to dielectric loss at these frequencies [242].

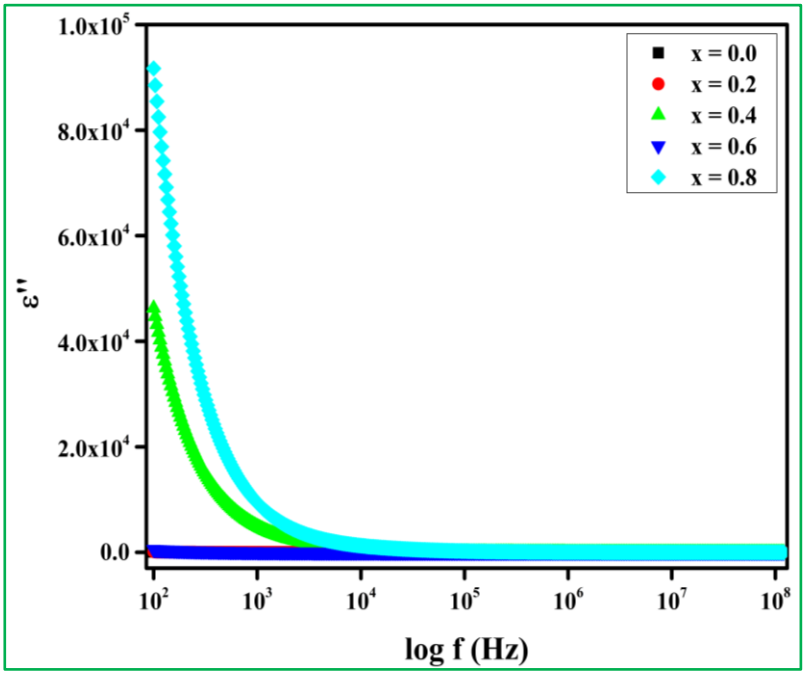

Fig. 4. 12: *Room-temperature variation of dielectric constant's imaginary part (ε'') with frequency of $Cu_{0.79}Co_{0.21}La_xFe_{2-x}O_4$*

The loss tangent ($tan\ \delta$) is a key contributor to the core loss of $Cu_{0.79}Co_{0.21}La_xFe_{2-x}O_4$ ferrites. Its magnitude is influenced by structural uniformity, the presence of Fe^{2+} ions, and the synthesis conditions such as sintering temperature and time [243]. The frequency-dependent loss tangent ($tan\ \delta$) for varying La^{3+} ions concentrations (x) in $Cu_{0.79}Co_{0.21}La_xFe_{2-x}O_4$ ferrites is depicted in Fig. 4.13. At low frequencies (around 100 Hz), the value of "$tan\ \delta$" attains its maxima across all compositions (x) of $Cu_{0.79}Co_{0.21}La_xFe_{2-x}O_4$ ferrites, which may be ascribed to thermally excited (or activated) charge carriers and the presence of structural defects within the material. As frequency increases, there is a noticeable drop in "tan δ" up to a certain frequency threshold of around 1MHz. The observed decrease in "tan δ" is mainly attributed to the inability of charge carriers to follow the quick oscillations of the electric field, along with charge hopping process between Fe^{2+} and Fe^{3+} ions, and dipole orientation towards the direction of electric field. In the high-frequency range, low resistivity allows grains to dominate conduction, requiring less energy for electrons to shift between ions, resulting in minimal tangent loss [244]. Beyond 1 MHz of frequency, the "($tan\ \delta$)" reaches a steady (or constant) lower value which indicates the intrinsic dielectric loss of the material caused by ionic as well as electronic polarization mechanisms. Moreover, it is observed from the plot that an increasing La^{3+} ions doping concentration shifts the "($tan\ \delta$)" curves upward, indicating enhanced dielectric losses possibly due to the lattice distortions and defects that generate localized charge carriers. These observations correspond well with Koop's hypothesis, which emphasizes the interaction between high-resistance grain borders and low-resistance grains in determining dielectric properties [241,242] .

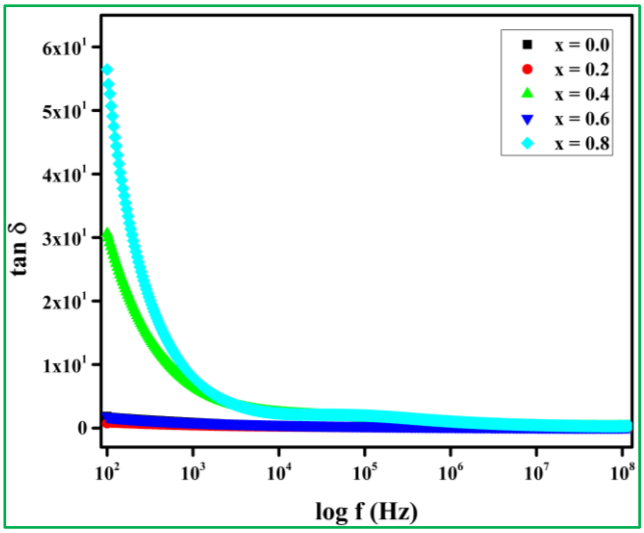

Fig. 4. 13: *Room-temperature variation of the tangent loss ($tan\ \delta$) with frequency of $Cu_{0.79}Co_{0.21}La_xFe_{2-x}O_4$*

4.1.8 AC Conductivity

The frequency-dependent AC conductivity (σ_{ac}) is an important electrical characteristic. The variation of AC conductivity (σ_{ac}) across all concentrations (x) of La^{3+} ion in $Cu_{0.79}Co_{0.21}La_xFe_{2-x}O_4$ ferrites shown in Fig. 4.14, was analyzed within the frequency range of 100 Hz - 120 MHz using the following relation [243]:

$$\sigma_{ac} = \omega \varepsilon_0 \varepsilon' \tan \delta \qquad (4.15)$$

where ($\omega = 2\pi f$) signifies the angular frequency.

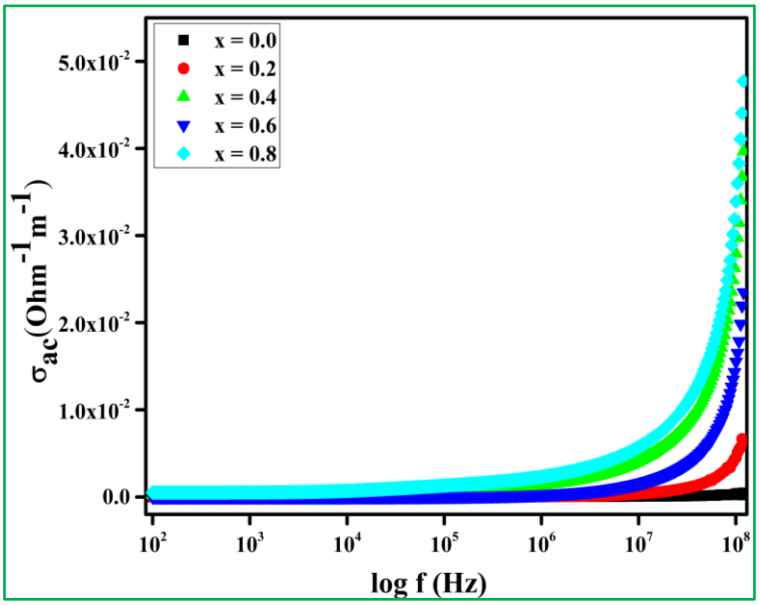

Fig. 4. 14: *Room-temperature variation of AC conductivity (σ_{ac}) with frequency of $Cu_{0.79}Co_{0.21}La_xFe_{2-x}O_4$*

As observed in Fig. 4.14, at lower frequencies, (σ_{ac}) stays largely invariant (or constant) across all concentrations of La^{3+} ions up to 1 MHz. This results from the predominance of localized charge carriers at the grain boundaries and the infrequent hopping activities between Fe^{2+} and Fe^{3+} ions [245]. As the frequency increases, the AC conductivity (σ_{ac}) progressively rises owing to grain conductivity and enhanced polaron hopping within the $Cu_{0.79}Co_{0.21}La_xFe_{2-x}O_4$ ferrites [237]. However, at elevated frequencies especially (beyond 10 MHz), the AC conductivity (σ_{ac}) exhibits an exponential increase, a characteristic feature of ferrites, and is caused by the enhanced mobility of charge carriers at higher energy levels. It is noticed from the plot that the σ_{ac} of $Cu_{0.79}Co_{0.21}La_xFe_{2-x}O_4$ ferrites increases significantly with higher doping concentrations (x) of La^{3+} ions. This enhancement results from structural modifications that promote the hopping of electrons among Fe^{2+} and Fe^{3+} ions and reduce

grain boundary resistance, thereby facilitating better charge transport [246,247]. These findings offer useful insights into the electrical characteristics and conduction processes of $Cu_{0.79}Co_{0.21}La_xFe_{2-x}O_4$ ferrites, which may be employed to enhance their performance for specific frequency-dependent applications.

4.1.9 CV Study

This study investigates the electrochemical behavior of $Cu_{0.79}Co_{0.21}La_xFe_{2-x}O_4$ spinel ferrite samples at five different concentrations (x = 0.0, 0.2, 0.4, 0.6, 0.8) as potential materials for supercapacitors. Cyclic Voltammetry (CV) was conducted to understand the electrochemical properties of these samples at room temperature using a three-electrode system.

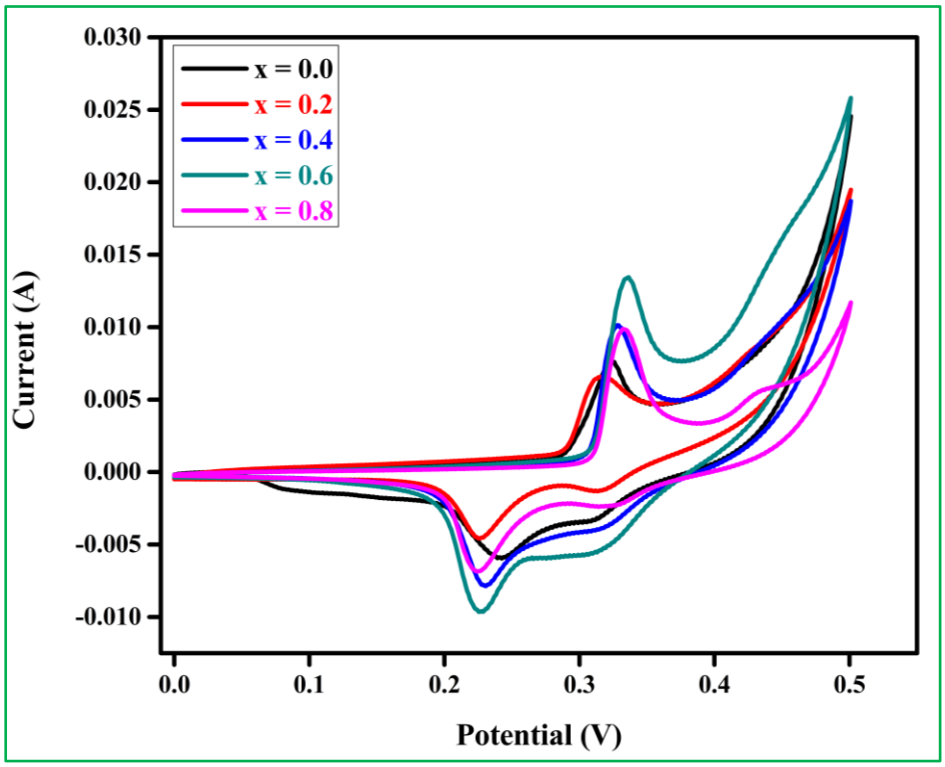

Fig. 4. 15: *CV curve of $Cu_{0.79}Co_{0.21}La_xFe_{2-x}O_4$*

CV experiments were performed at a scan rate of 10 mV s^{-1} within a potential window of 0-0.5 V for all samples. The CV curves shown in Fig. 4.15 displayed characteristic redox peaks, indicative of faradic (battery-like) behavior. The cyclic behavior in CV is ascribed to the reversible redox reactions within the electrode material. During forward and reverse scans, oxidation and reduction processes occur, resulting in the characteristic redox peaks. The specific capacitance (C_S) was determined using the formula [205]:

$$C_S = \frac{1}{mv\Delta V}\int_{V_i}^{V_f} I(V)\, dV \qquad (4.16)$$

Here, 'm' represents the loaded mass, 'υ' denotes the scan rate, 'ΔV' corresponds to the potential window, and the integral signifies the area under the CV curve. As known, capacitance is directly proportional to the area of the CV curve. The specific capacitance values for x = 0.0, 0.2, 0.4, 0.6, and 0.8 were calculated as 372.0 F g^{-1}, 270.8 F g^{-1}, 395.6 F g^{-1}, 540.0 F g^{-1}, and 292.8 F g^{-1} respectively (see Table 4.4). The highest specific capacitance was observed for x = 0.6, reaching 540.0 F g^{-1}. The augmentation in C_S at x = 0.6 can be attributed to the increased porosity level at this composition, a finding that is corroborated by the XRD analysis detailed in Table 4.1.

Table 4. 4: *Electrochemical parameters from CV curve of* $Cu_{0.79}Co_{0.21}La_xFe_{2-x}O_4$

Conc. (x)	Area	Scan rate	Scan rate	Potential window	Mass	Mass	C_s
	(AV)	(mV s^{-1})	(V s^{-1})	(V)	(mg)	(g)	(F g^{-1})
0.0	0.00186	10	0.01	0.5	1	0.001	372.0
0.2	0.001354	10	0.01	0.5	1	0.001	270.8
0.4	0.001978	10	0.01	0.5	1	0.001	395.6
0.6	0.0027	10	0.01	0.5	1	0.001	540.0
0.8	0.001464	10	0.01	0.5	1	0.001	292.8

The superior specific capacitance observed at x = 0.6 can be attributed to several factors:

- **a.** Optimal Composition: The composition of $Cu_{0.79}Co_{0.21}La_xFe_{2-x}O_4$ at x = 0.6 may have a balanced ratio of active sites, allowing for increased charge storage capacity.
- **b.** Crystal Structure: The crystal structure at x = 0.6 may facilitate faster ion diffusion and better charge transport, enhancing capacitance.
- **c.** Surface Area: The specific surface area at x = 0.6 might be more favorable for electrolyte-electrode interactions, promoting higher capacitance.

The C_S of 540.0 F g^{-1} was achieved for x = 0.6 surpasses the values reported in previous studies, such as Cu-$CoFe_2O_4$ (221 F g^{-1} at 5 mV s^{-1}), Ni-$CoFe_2O_4$ (60 F g^{-1} at 5 mV s^{-1}), Ni-$CuFe_2O_4$ (16.9 F g^{-1} at 5 mV s^{-1}) [248] $MnFe_2O_4$ (25.21 F g^{-1} at 50 mV s^{-1}) [249],

$NiFe_2O_4$ (79.04 F g^{-1} at 2 mV s^{-1}), $Ni_{0.75}Mg_{0.25}Fe_2O_4$ (65.27 F g^{-1} at 2 mV s^{-1}), $Ni_{0.50}Mg_{0.50}Fe_2O_4$ (82.45 F g^{-1} at 2 mV s^{-1}), $Ni_{0.25}Mg_{0.75}Fe_2O_4$ (149.88 F g^{-1} at 2 mV s^{-1}), $MgFe_2O_4$ (178.34 F g^{-1} at 2 mV s^{-1}) [250].

To further enhance the C_S of these spinel ferrites, future research can focus on the innovative preparation of composites with 2D materials like rGO, MXene, and Polyaniline. These composites are expected to exhibit improved electrochemical performance. The ultimate goal of this research is to develop efficient supercapacitors, which can find wide applications in various sectors, contributing to sustainable development goals and benefiting society at large. The higher specific capacitance values acquired in this study represent a significant step towards achieving this objective.

4.2 $Zn_{0.1}Mn_{0.4}Ni_{0.5}Fe_2O_4$ (ZMNF) Nanoparticles, Reduced Graphene Oxide (rGO), and $Zn_{0.1}Mn_{0.4}Ni_{0.5}Fe_2O_4$/rGO (ZMNFG) Nanocomposite

4.2.1 Physical and Electrochemical Characterization

The comprehensive characterization of synthesized ZMNF nanoparticles, rGO, ZMNFG composite, and their corresponding electrodes utilized in this research were thoroughly analyzed to evaluate their physical and electrochemical properties. The XRD patterns of synthesized materials were analyzed using a (BRUKER D8 ADVANCE) X-ray diffractometer (generator power, sealed tube: 3kW - IμS: 50 W - TXS/TXS-HE: 6 kW), with Cu Kα radiation (wavelength, λ = 1.5406 Å) as the X-ray source. The scanning range was set from 10˚ to 70˚ with a step size of $0.02^{\circ}s^{-1}$ to determine the crystalline structure and phase of the samples. Raman spectroscopic analysis was performed solely on rGO using the Raman spectrophotometer (BRUKER RFS 27 FT) to investigate their structural and vibrational properties, offering essential insights into the quality and structure of graphene. The (PERKIN–ELMER) FTIR spectroscopy (resolution: 0.5 cm^{-1}), revealed the presence of functional groups and chemical bonding within the wavenumber range of 400 – 4000 cm^{-1}. The visualization of surface morphology and identification of the elemental composition of samples were analyzed by FESEM (model JSM–7610F–PLUS), [SEI resolution: 1.0nm (15kV), 1.3nm (1kV); during analysis: 3.0 nm, 15 kV; probe current: 5 nA] equipped with EDX spectroscopy. The VSM (model VSM–EZ9) was utilized to evaluate the magnetic properties of samples within the applied field range of ±15 kOe. Furthermore, electrochemical characterization techniques such as CV, GCD, and EIS were employed to assess the energy storage performance and charge transfer kinetics of fabricated ZMNF nanoparticles, rGO, and ZMNFG composite electrodes in an electrochemical workstation, METROHM, (potential resolution: 3 μV). These electrochemical studies are vital for assessing their feasibility for supercapacitor applications.

4.2.2 XRD analysis of ZMNF nanoparticles, rGO, and ZMNFG nanocomposite

XRD analysis was performed on GO, rGO, $Zn_{0.1}Mn_{0.4}Ni_{0.5}Fe_2O_4$ (ZMNF) nanoparticles as well as the nanocomposite $Zn_{0.1}Mn_{0.4}Ni_{0.5}Fe_2O_4$/rGO **(**ZMNFG), to examine the crystal structure and phase purity of all samples. Figures (4.16 and 4.17) depict the XRD patterns of

GO, rGO, ZMNF nanoparticles, and the nanocomposite (ZMNFG). The XRD pattern of the synthesized GO, as depicted in Figure (4.16a) exhibits a sharp and prominent peak (001) at 2θ = 10.52˚ and a weaker peak (100) at 2θ = 42.36˚ with interplanar spacings of 8.4 Å and 2.1 Å, respectively. These peaks are indicative of the formation of oxygen functional groups within the GO layers, thereby confirming the successful synthesis of GO [251–253]. Figure (4.16b) presents the XRD patterns of rGO after thermal treatment. The broader diffraction peak observed at approximately 2θ = 23.51˚ corresponds to the (002) plane is due to the presence of the graphitic (graphite-like) structure with an interplanar spacing of 3.7 Å. Furthermore, the XRD pattern of rGO displays an extra diffraction peak (100) at 2θ = 43.14˚ characterized by an interplanar spacing of 2.0 Å. This weak diffraction peak likely arises due to the restacking of the graphene sheets in their reduced state. Consequently, the observed reduction in interplanar spacing of rGO in comparison to GO is possibly ascribed to the absence of certain oxygen-based functional groups on the basal plane [254]. This observation suggests the successful reduction of GO during the reduction process. These findings highlight the effectiveness of thermal treatment in reducing GO and restoring its graphitic structure. The observed restacking of the reduced graphene sheets suggests the potential for further optimization of the thermal treatment process to achieve improved structural properties and boosted performance in numerous applications such as energy storage supercapacitors, batteries, electronics, and biomedical applications.

Likewise, the XRD pattern of pristine ZMNF nanoparticles (Fig. 4.17a) exhibits intense peaks, ensuring an excellent crystallinity of the obtained $Zn_{0.1}Mn_{0.4}Ni_{0.5}Fe_2O_4$ nanoparticles. The detected reflections or diffraction peaks of ZMNF nanoparticles with various hkl values: (111), (220), (311), (222), (400), (422), (511), and (440) were identified at values of (2θ =18.24˚, 30.02˚, 35.35˚, 36.98˚, 42.97˚, 53.30˚, 56.83˚ and 62.38˚) respectively. These findings demonstrate the formation of ZMNF nanoparticles with a single-phase cubic structure, specifically belonging to the Fd3m space group, without any detectable impurities. The quality of the synthesized cubic-structured ZMNF nanoparticles is in good agreement with the XRD standard file of (ICDD: 08-0234) [121,255]. Furthermore, the XRD pattern of ZMNFG nanocomposite reveals prominently strong and sharp peaks corresponding to both ZMNF nanoparticles and rGO without any other (extraneous) undesired peaks. The ZMNFG nanocomposite (Fig. 4.17b) displays all the crystalline peaks of pristine ZMNF as well as rGO. The increase in peak intensity of both ZMNF and rGO in the ZMNFG nanocomposite may be due to a combination of reasons, including the insertion of rGO within

the ZMNF matrix, enhanced crystallinity, and reduced defects [256]. This observation indicates the successful synthesis of a highly pure ZMNFG nanocomposite. The peak position of ZMNF nanoparticles remains unchanged, while the peak position of rGO situated at 2θ = 26.42˚ shown in (Fig. 4.17b) shifts towards a higher angle in ZMNFG nanocomposite compared to pure rGO shown in (Fig. 4.16b). This shift may be possibly due to the intercalation or interaction between rGO and ZMNF nanoparticles, potentially affecting the lattice parameters and introducing lattice strain [134,257].

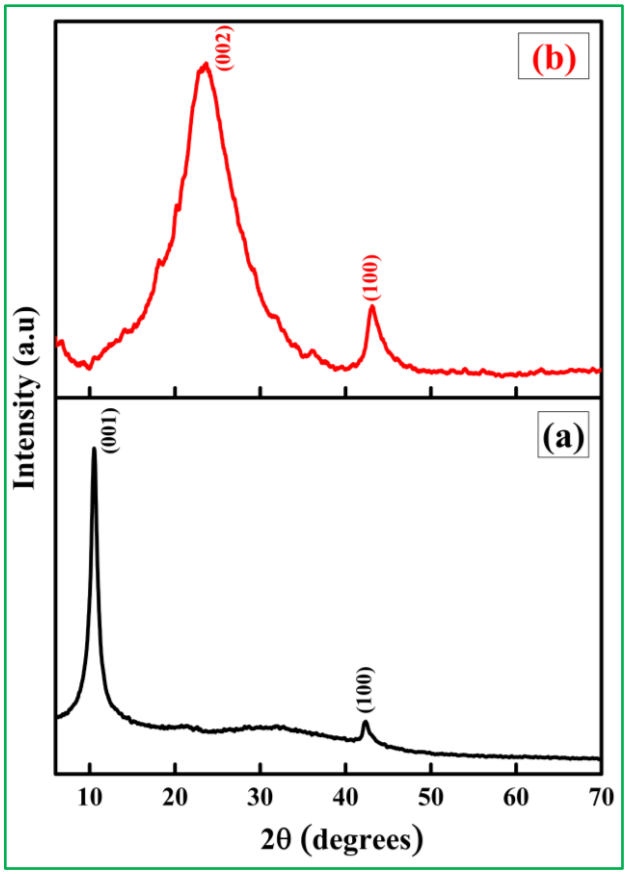

Fig. 4. 17: *Xrd plot of (a) graphene oxide (GO); and (b) reduced graphene oxide (rGO)*

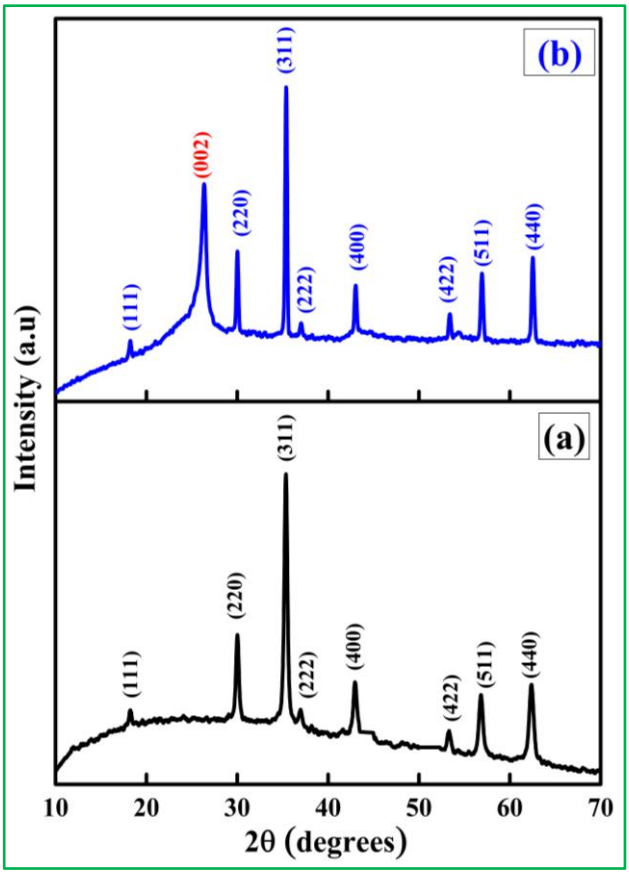

Fig. 4. 17: *Xrd plot of (a) ZMNF nanoparticles; and (b) ZMNFG nanocomposite*

Moreover, Table 4.5 presents the calculated values of certain structural parameters viz crystallite size (D), lattice constant (a), inter-planar spacing (d), and the strain (ε) corresponding to the high-intensity peak (311) of both ZMNFG nanocomposite and ZMNF nanoparticles. The Scherer equation ($D = k\lambda/\beta Cos\theta$) was applied to ZMNFG nanocomposite and ZMNF nanoparticles, yielding an estimated crystallite size of approximately 31.10 nm and 20.25 nm respectively. The lattice constant was obtained by applying the formula ($a = d\sqrt{(h^2 + k^2 + l^2)}$), resulting in an estimated value of around

8.408 Å for ZMNFG nanocomposite and 8.415 Å for ZMNF nanoparticles. Using Bragg's equation ($n\lambda = 2dSin\theta$), distance between the planes (d-spacing) was found to be 2.535 Å for ZMNFG nanocomposite and 2.537 Å ZMNF nanoparticles. The equation ($\varepsilon = \beta/4tan\theta$) was employed to determine the lattice strain of ZMNFG nanocomposite and ZMNF nanoparticles, resulting in values of 0.0038 and 0.0059 respectively. The observed increase in crystallite size (D) of ZMNFG nanocomposite compared to ZMNF nanoparticles occurs due to the interaction between ZMNF nanoparticles and rGO, which induces structural changes in ZMNF nanoparticles [258]. This validates that the expansion of pre-existing crystallite size leads to a rise in the size of crystallites in comparison to pristine ZMNF nanoparticles. This outcome indicates that larger crystallites may be linked to improved performance in specific applications. Nonetheless, comprehending the underlying mechanisms is crucial for designing and optimizing nanomaterials to meet the specific needs of each application.

Table 4. 5: *Structural parameters of (a) ZMNF nanoparticles; and (b) ZMNFG nanocomposite*

Sample code	Peak Position	hkl Values	FWHM	Interplanar Spacing	Lattice Constant	Crystallite Size	Lattice Strain
	2θ (deg)		β (deg)	d (Å)	a (Å)	D (nm)	
(a)	35.35	311	0.43	2.537	8.415	20.25	0.0059
(b)	35.38	311	0.28	2.535	8.408	31.10	0.0038

4.2.3 Raman Analysis of rGO

To further confirm the formation of rGO, Raman spectroscopic investigations were conducted on the sample (material) to analyze the structure and characteristics of rGO as depicted in Fig. 4.18. The Raman spectra of rGO typically display two main peaks within the wavenumber range of 1000 – 3000 cm^{-1}, known as D and G bands of graphene sheets. The D band observed at around 1323.20 cm^{-1}, reflects the defects and disorders within the graphene structure [259]. On the flip side, the G band observed at approximately 1593.64 cm^{-1}, corresponds to the first–order E_{2g} mode of sp^2-hybridized carbon atoms, indicating the presence of graphitic domains in the material [260]. The intensity ratio (I_D/I_G) of D and G bands is typically utilized to

determine the degree of disorder in rGO. In this study, the (I_D/I_G) ratio in rGO was determined to be 0.830, higher than the intensity ratio (I_D/I_G) of 0.109 reported for graphene oxide (GO) in the literature [261,262]. This higher value of (I_D/I_G) ratio confirms the successful formation of rGO sheets with reduced defects compared to GO [263].

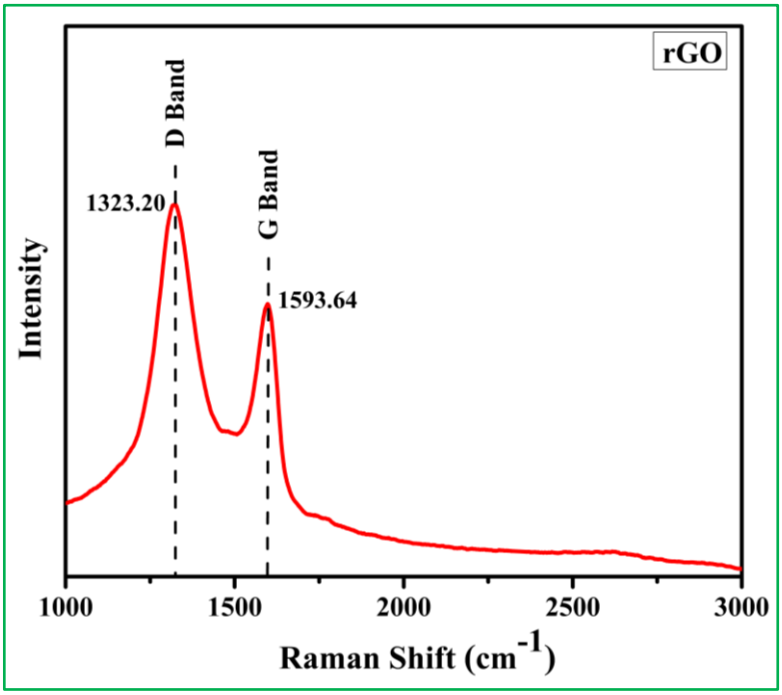

Fig. 4. 18: *Raman spectra of reduced graphene oxide (rGO)*

4.2.4 FTIR Analysis

FTIR spectroscopy is a powerful analytical technique utilized to ascertain the vibration modes of the functional groups and chemical bonds that exist in ZMNF nanoparticles, rGO, and ZMNFG nanocomposite. Figure 4.19 illustrates the FTIR spectra of all samples within the wave number range of 400 – 4000 cm^{-1}. Based on Waldron's findings, spinel ferrites often exhibit two absorption bands υ_1 and υ_2 within the frequency range of 550 – 650 cm^{-1} and 350 – 450 cm^{-1} respectively [264]. In this study, FTIR spectra of ZMNF nanoparticles (Fig. 4.19(a)) exhibited a strong higher frequency absorption band υ_1 at around 531.76 cm^{-1}, which corresponds to the stretching vibrations of metal-oxygen (M–O) and/or (Fe–O) bond, thus confirms the presence of spinel ferrite phase [265]. Irrespective of this, no significant absorption band υ_2 is noticed in a lower frequency range (350 – 450) cm^{-1}, which might be below the detection limit of sensitive FTIR instruments [254,266]. Moreover, the spectrum of rGO (Fig. 4.19(b)) shows three highly prominent absorption bands at 1193.41 cm^{-1},

1555.76 cm^{-1}, and 1726.12 cm^{-1} which are ascribed to the stretching vibrations of C–O of alkoxy groups, C=C of aromatic carbon-carbon double bonds, and C=O of carboxyl or carbonyl groups respectively [251,267,268]. The intense absorption band observed at 1555.76 cm^{-1} provides evidence for the successful restoration of sp^2 unoxidized graphene sheets, thereby demonstrating the successful reduction of GO [269,270]. These findings are in complete compliance with the outcomes achieved from Raman analysis. Similarly, the FTIR spectra of ZMNFG nanocomposite displayed a combination of characteristic peaks (bands) of both ZMNF nanoparticles (522.35 cm^{-1}) and rGO (1015.53 cm^{-1}, 1532.24 cm^{-1}, and 1712.94 cm^{-1}). In addition to this, an absorption band detected at 3739.30 cm^{-1} corresponds to the stretching vibration of the O–H bond in hydroxyl (alcohol) functional groups or water molecules [253]. Compared to rGO, slight shifting and decrease in peak intensities of absorption bands were observed in the ZMNFG nanocomposite, as depicted in Fig. 4.19(c). Moreover, the integration of rGO into ZMNF nanoparticles leads to a decrease in infrared peak intensities of absorption bands due to the strong rGO adsorption capacity and alterations in crystal structure, thus corroborates the successful formation of ZMNFG nanocomposite [258].

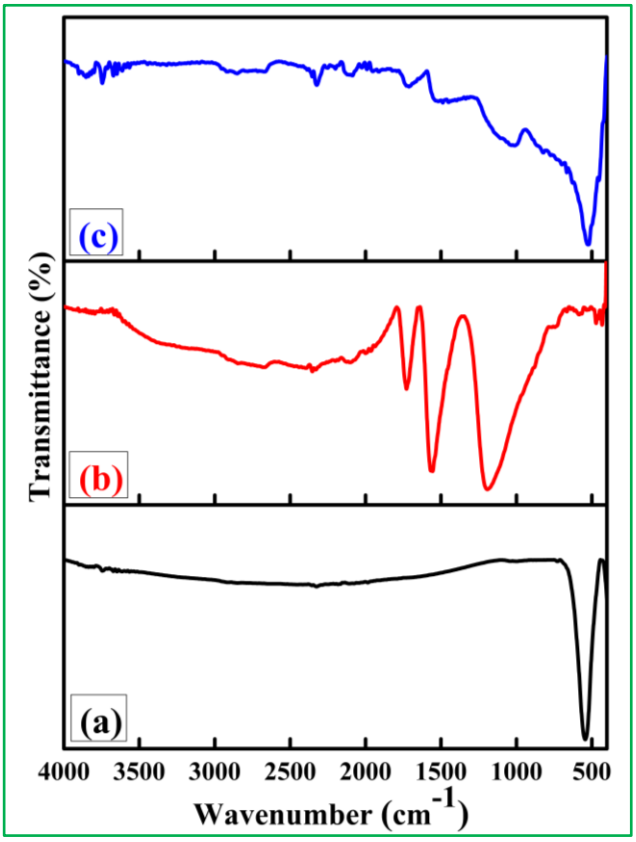

Fig. 4. 19: *FTIR spectra of (a) ZMNF nanoparticles, (b) rGO, and (c) ZMNFG nanocomposite*

4.2.5 FESEM/EDX Analysis

FESEM micrographs reveal unique morphological characteristics of ZMNF nanoparticles, rGO, and ZMNFG nanocomposite along with EDX elemental composition of ZMNFG nanocomposite as depicted in Fig. 4.20. The FESEM micrograph of ZMNF nanoparticles depicted in Fig. 4.20 (a) reveals an asymmetrical distribution of grains with an average size of 0.29 μm. The micrograph exhibits an agglomerated morphology, possibly due to magnetic interactions and a porous morphology, which may result from gas emissions during combustion [261,271]. Additionally, the morphology of pristine rGO material as shown in Fig. 4.20 (b) exhibits a wrinkled and partially folded sheet-like structure, which is in good agreement with findings reported in previous studies [272–274]. Furthermore, the FESEM micrograph of ZMNFG nanocomposite shown in Fig. 4.20 (c) depicts a complex structure characterized by layered formations of graphene sheets interspersed with granular ZMNF nanoparticles, thus illustrating a robust connection between ZMNF nanoparticles and rGO matrix [268]. The unique porous morphology of ZMNFG nanocomposite is expected to contribute to the enhanced physical and electrochemical attributes, positioning it well-suited for various uses, such as energy storage, catalysis, and sensing devices [275–277]**.**

Moreover, the elemental composition and elemental mapping of ZMNFG nanocomposite were examined via EDX analysis, as displayed in Fig. 4.20 (d) and Fig. 4.21, respectively. The EDX spectra of ZMNFG nanocomposite show the presence of peaks that correspond to zinc (Zn), manganese (Mn), nickel (Ni), iron (Fe), oxygen (O), and carbon (C) with certain weight percent (wt %) ratios as mentioned in Fig. 4.16 (d). Nonetheless, a strong carbon (C) peak with 82.02 wt % is observed in the spectrum, confirming the existence of a good amount of rGO in ZMNFG nanocomposite matrix. Notably, a small intensity peak is detected in the spectrum, possibly due to carbon tape coating applied on samples before EDX testing [199]. Furthermore, the absence of extra peaks associated with impurities indicates the high purity of ZMNFG nanocomposite. As seen in Fig. 4.21, the elemental mapping results reveal that the elements: carbon (C) and oxygen (O) are primarily concentrated within the graphene sheets, whereas the elements zinc (Zn), manganese (Mn), nickel (Ni), and iron (Fe) are dispersed throughout the nanocomposite, thereby demonstrating the successful integration of ZMNF nanoparticles into the rGO matrix. This thorough research offers critical insights

regarding the elemental composition and distribution of ZMNFG nanocomposite, further confirming its potential for numerous applications.

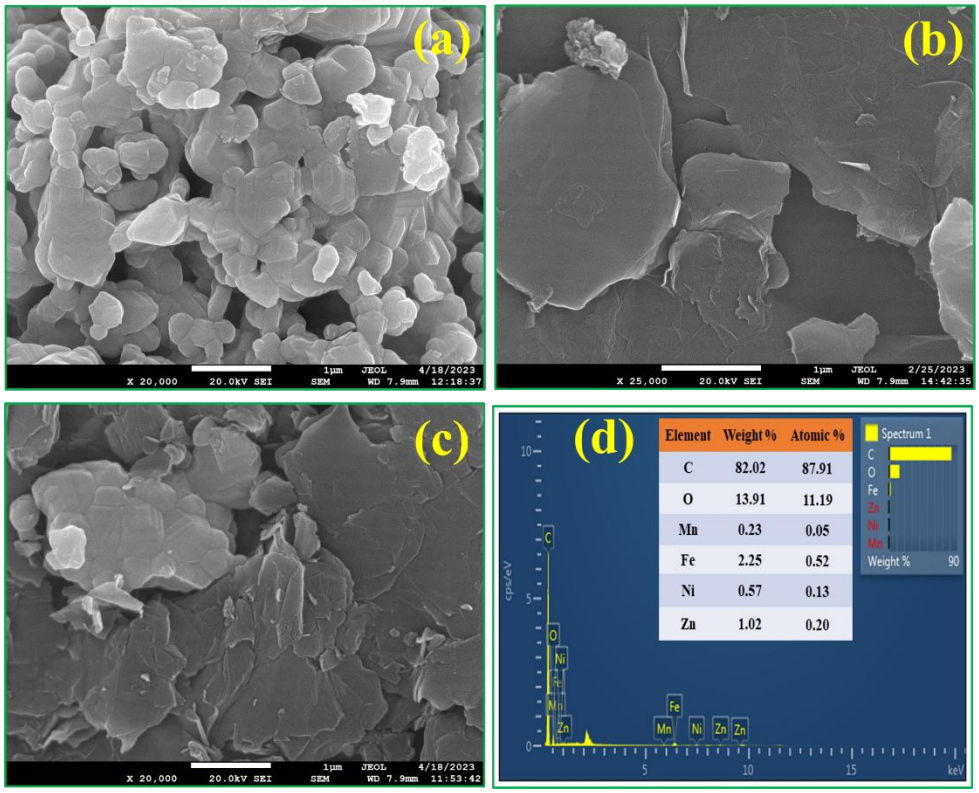

Fig. 4. 20: *FESEM micrographs of (a) ZMNF nanoparticles, (b) rGO, (c) ZMNFG nanocomposite, and (d) EDX of ZMNFG nanocomposite*

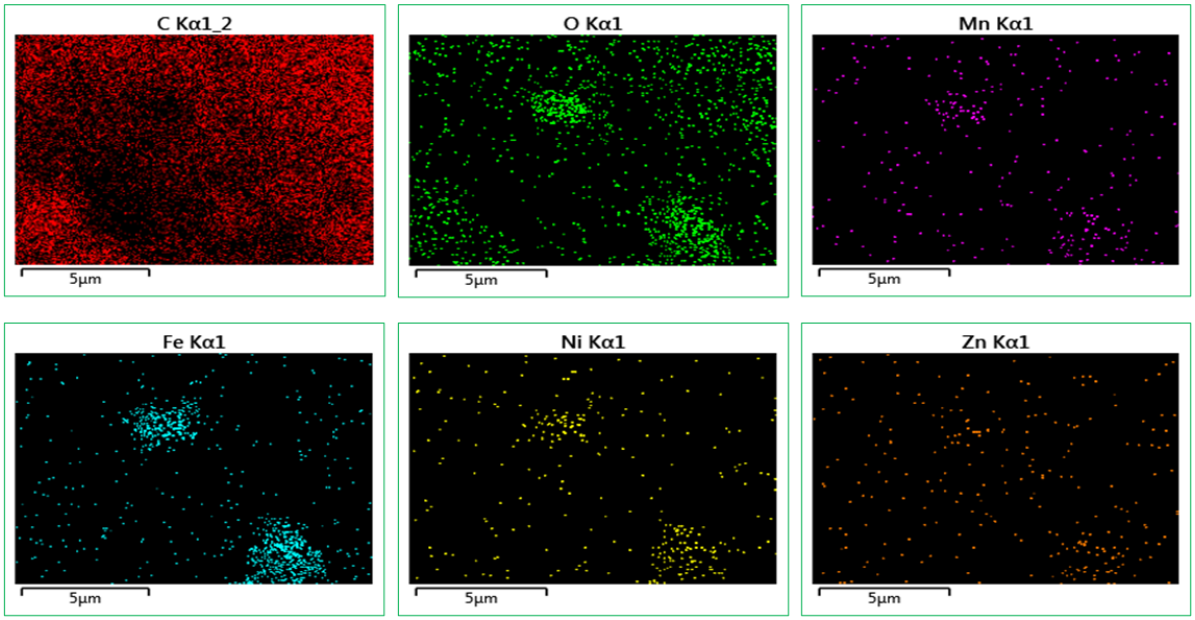

Fig. 4. 21: *Elemental mapping of ZMNFG nanocomposite*

4.2.6 Magnetic Study

The room temperature magnetic responses of ZMNF nanoparticles, rGO, and ZMNFG nanocomposite were meticulously recorded by utilizing a VSM in the presence of magnetic field oscillating within ± 15 kOe as illustrated in Fig. 4.22. The magnetic (M-H) hysteresis loops of ZMNF nanoparticles and ZMNFG nanocomposite exhibited an S-shaped curve unlike rGO as shown in Fig. 4.22 (a-c). The essential magnetic parameters like M_s, M_r, H_c, R_{sq}, and K_1 were evaluated and compared between ZMNF nanoparticles, rGO, and ZMNFG nanocomposite and are presented in Table 4.6. Meanwhile, rGO behaves linearly along the applied field (Fig. 4.22 (b)), due to its non-magnetic behavior as reported in previous studies [278–280]. The M_s, M_r, and H_c values of ZMNFG nanocomposite are 22.61 emu g^{-1}, 0.83 emu g^{-1}, and 20.70 Oe respectively. In contrast, the M_s, M_r, and H_c values of ZMNF nanoparticles are 103.45 emu g^{-1}, 4.05 emu g^{-1}, and 20.47 Oe respectively, as observed in Table 4.6. Compared to ZMNF nanoparticles, the M_s of ZMNFG nanocomposite reduced by 78.14 % and the M_r reduced by 71.56 % which is due to the non-magnetic behavior of rGO [265,281,282] and smaller crystallite size of ZMNF nanoparticles [283]. The variations observed in M_s and M_r values between ZMNF nanoparticles and ZMNFG nanocomposite exhibit a similar decreasing trend as shown in Table 4.6. Additionally, the dependence of M_r is mainly influenced by two factors: the change in M_s and the overall alignment of magnetization inside the grains, which is controlled by super-exchange interactions among the magnetic nanoparticles as reported in the literature [284]. This significant reduction in magnetic properties of ZMNFG nanocomposite occurs possibly due to the addition of rGO (75 wt.%), which is three times more than ZMNF nanoparticles, thereby leading to the dominant non-magnetic behavior of rGO into ZMNFG nanocomposite matrix.

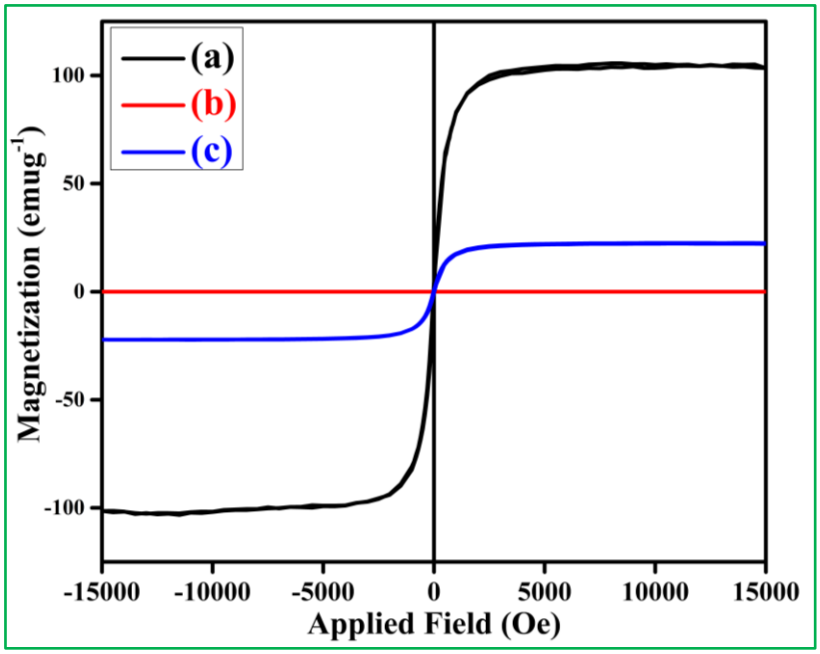

Fig. 4. 22: *VSM plot (M-H) curve of (a) ZMNF nanoparticles, (b) rGO, and (c) ZMNFG nanocomposite*

Moreover, the H_c values of ZMNFG nanocomposite and ZMNF nanoparticles show minimal change with the insertion of rGO on the intrinsic magnetic properties of ZMNF nanoparticles. The coercivity (H_c) and crystallite size (D) demonstrate an inverse correlation in multi-domain regions and a direct correlation in single-domain region [285]. The relationship between these two parameters (H_c and D) can be mathematically described using an established equation [286]: ($H_c = e + f/D$) where e and f are constants. In this study, the coercivity (H_c) value decreases from 20.70 Oe (for ZMNF nanoparticles) to 20.47 Oe (for ZMNFG nanocomposite), whereas the crystallite size (D) value increases from 20.25 nm (ZMNF nanoparticles) to 31.10 nm (ZMNFG nanocomposite). This inverse relationship between H_c and D confirms the presence of multi-domain behavior [257]. Furthermore, as discussed earlier, the differences in crystallite size, morphology, and microstructure between the ZMNFG nanocomposite and ZMNF nanoparticles, with the incorporation of rGO, may also contribute to the observed changes in the magnetic properties.

Table 4. 6: *Magnetic parameters of (a) ZMNF nanoparticles, (b) rGO, and (c) ZMNFG nanocomposite*

Sample code	M_s	M_r	H_c	R_{sq}	K_1
	(emu g^{-1})	(emu g^{-1})	(Oe)		(erg cm^{-3})
(a)	103.45	4.05	20.70	0.039	2185.12
(b)	0	0	0	0	0
(c)	22.61	0.83	20.47	0.036	472.27

The squareness ratio ($R_{sq} = M_r/M_s$), also known as the remanence ratio is a fundamental parameter that describes the material's magnetic domain regime and is influenced by its anisotropy. It illustrates the rapid and effortless reorientation of magnetization towards the nearest easy axis after the removal of the magnetic field. The Stoner-Wohlfarth (S-W) theory predicts R_{sq} values around 0.50 for the non-interacting random distribution of nanoparticles with uniaxial anisotropy, and around 0.831 for those with cubic anisotropy [284,287]. Moreover, the value of the squareness ratio ($R_{sq} \geq 0.5$) suggested that the nanoparticles are in a single magnetic domain, whereas the value of the squareness ratio ($R_{sq} < 0.5$) confirms the formation of multi-domain structure [288]. The squareness ratio (R_{sq}) values for ZMNF nanoparticles and ZMNFG nanocomposite were computed and are presented in Table 4.6. As evident from data in Table 4.6, R_{sq} of ZMNF nanoparticles and ZMNFG nanocomposite were found to be 0.039 and 0.036 respectively. These R_{sq} values are significantly lower than 0.5, which may be ascribed to the influence of surface spin disorder effects. Additionally, the observed R_{sq} values of ZMNF nanoparticles (0.039) and ZMNFG nanocomposite (0.036), which are less than 0.5 further summarize the multi-domain magnetic structure with uniaxial anisotropy. The R_{sq} values of ZMNF nanoparticles and ZMNFG nanocomposite align well with the inverse relationship between H_c and D revealing a multi-domain regime. Thus, smaller R_{sq} values of ZMNF nanoparticles and ZMNFG nanocomposite are often used in applications where easy magnetization reversal is desirable, such as in soft magnetic cores for transformers, inductors, electromagnetic shielding, inkjet printing, and ferrofluid applications [289,290].

The anisotropy constant (K_1) defines how strongly a material prefers to have its magnetic moments aligned in a specific direction. The values of the anisotropy constant (K_1)

were evaluated using Brown's relation ($H_c = 0.96 * \frac{K_1}{M_s}$). On comparing Table 4.5 and Table 4.6, it is observed in Fig. 4.23, that the value of K_1 directly correlates with H_c, while H_c has an inverse relationship with D, leading to an inverse dependence of K_1 on D which is in good agreement with the obtained results [121,280].

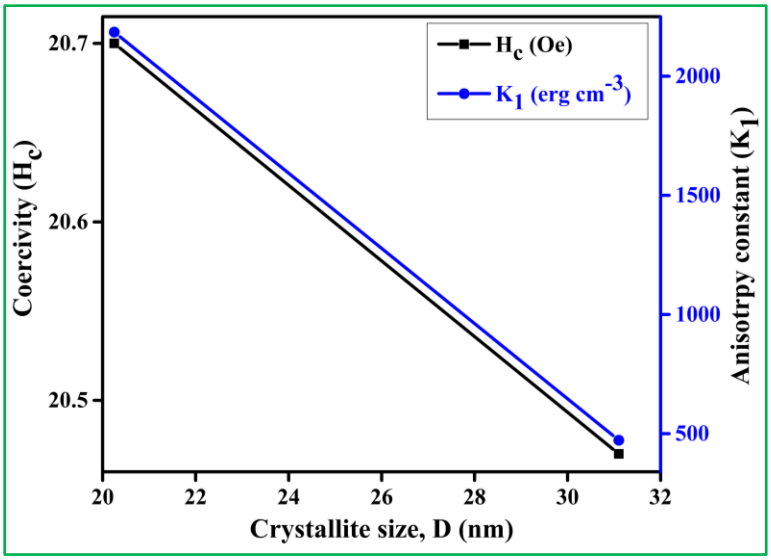

Fig. 4. 23: *Crystallite size (D) dependence of coercive field (H_c) and anisotropy constant (K_1) of ZMNF nanoparticles and ZMNFG nanocomposite*

This observation suggests a strong decrement in ZMNFG nanocomposite (472.27 erg cm^{-3}) compared to ZMNF nanoparticles (2185.12 erg cm^{-3}). The decrease in K_1 of ZMNFG nanocomposite may also be likely due to the strong incorporation of rGO [285,291]. As reported in the literature, materials with crystallite size (D) less than around 30 nm exhibit superparamagnetic behavior, characterized by randomly oriented magnetic dipoles that can easily flip direction due to thermal fluctuations [292]. Another study revealed that $MnFe_2O_4$ and $MnFe_2O_4$/G demonstrated superparamagnetic behavior at ambient temperature, with a notable M_s value of 57.56 emu g^{-1} for $MnFe_2O_4$. However, the presence of GO layers in $MnFe_2O_4$/G resulted in a considerable reduction of M_s value to 41.39 emu g^{-1}, as reported by Chella et al [293]. It is also reported in the literature that small coercivity values in the material occur due to thermal agitations, identifying them as soft magnetic materials that exhibit superparamagnetic behavior [252,294]. Consequently, our findings align well with the literature, demonstrating that ZMNF nanoparticles and ZMNFG nanocomposite exhibit superparamagnetic behavior.

4.2.7 Dielectric Analysis

Three distinct samples of ZMNF nanoparticles, rGO, and ZMNFG nanocomposite designated as (a), (b), and (c) respectively are displayed in different colors in the given Fig. 4.24, which shows the fluctuation of capacitance (F) with the logarithmic frequency ($log\ f, in\ Hz$). In material studies, it is usual practice to analyze such frequency-dependent capacitance data to comprehend dielectric characteristics, charge storage behavior, and relaxation processes of different materials [295]. Different capacitance values are displayed in each sample in the low-frequency spectrum. The capacitance of ZMNF nanoparticles is the lowest and drops off rapidly, whereas rGO and ZMNFG nanocomposite have larger initial capacitance values that fluctuate. The capacitance of all samples noticeably decreases as the frequency rises, indicating that the material's polarization response decreases with frequency. The presence of interfacial or dipolar polarization is indicated by the peaks and fluctuations seen in rGO and ZMNFG nanocomposite, which may result from charge accumulation at interfaces or within grain boundaries [296]. All samples achieve a stable capacitance at high frequencies; ZMNF nanoparticles have a low value that is almost constant, but rGO and ZMNFG nanocomposite attain saturation at various capacitance levels. Effective polarization decreases because of this trend, which suggests that the dipoles or charge carriers are less able to align with the quickly shifting field.

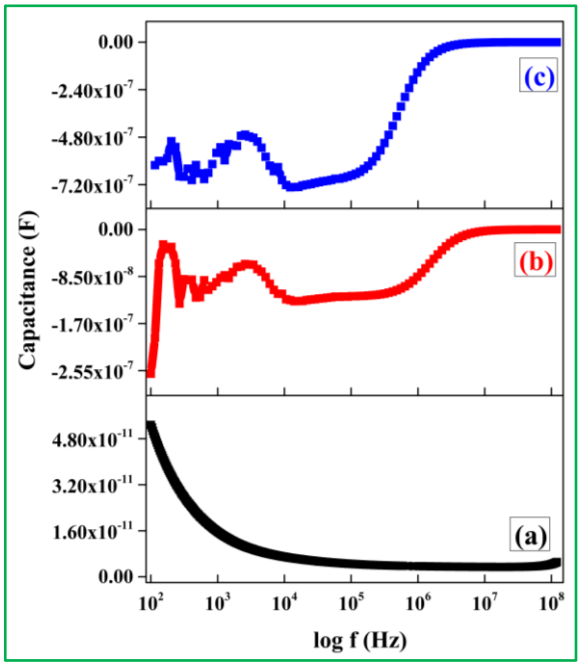

Fig. 4. 24: *Variation of capacitance versus frequency of (a) ZMNF nanoparticles, (b) rGO, and (c) ZMNFG nanocomposite*

Fig. 4.25 shows three plots of the real part of permittivity (ε') as a function of logarithmic frequency ($log\ f$) of ZMNF nanoparticles, rGO, and ZMNFG nanocomposite samples, labeled (a), (b), and (c), and color-coded in black, red, and blue, respectively. In Fig. 4.25 (a) ZMNF nanoparticles, the permittivity begins at a reasonably high value of roughly 110 Hz at low frequencies and gradually declines as frequency increases. This behavior is consistent with conventional dielectric relaxation, which occurs when low-frequency permittivity is high due to interfacial polarization or ionic motions [183]. The absence of large fluctuations or a plateau suggests that the material has a simple dielectric response, with no strong resonance or dipolar relaxation in this frequency range. Fig. 4.25 (b) rGO, depicts a negative permittivity at low frequencies, which varies before asymptotically increasing toward zero as the frequency increases [297]. Negative permittivity at low frequencies is unusual and can arise in materials with peculiar dispersion or in metamaterials that display effective medium behavior, which is frequently caused by resonance events. This curve indicates that the material may have localized resonance mechanisms or interactions that result in unique polarization effects, particularly at lower frequencies. Fig. 4.25 (c) ZMNFG nanocomposite, like Fig. 4.25 (b) rGO, has negative permittivity values at low frequencies, which fluctuate and then increase to zero as frequency increases. Compared to rGO, this curve appears to have a less negative permittivity impact because ZMNFG nanocomposite is a composite of ferrite and 2D materials, influencing its dispersion properties [298]. The shift in behavior to higher frequencies, followed by flattening, could indicate a secondary relaxation mechanism or structural effect influencing permittivity at these frequencies.

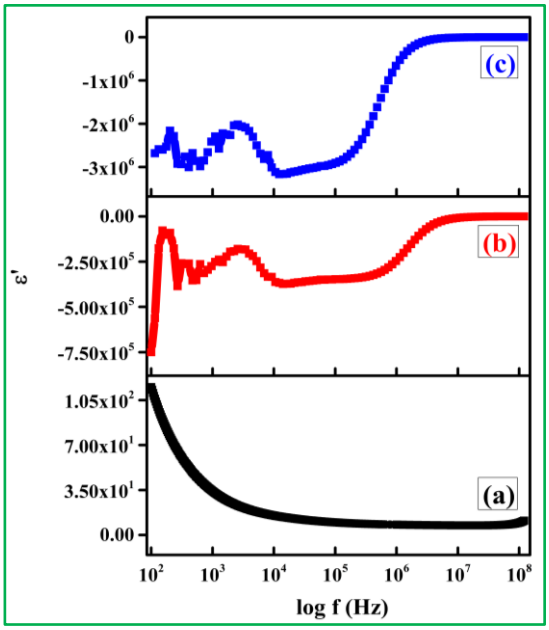

Fig. 4. 25: *Variation of the real part of permittivity (ε') versus frequency of (a) ZMNF nanoparticles, (b) rGO, and (c) ZMNFG nanocomposite*

Fig. 4.26 shows three plots of the imaginary component of permittivity (ε'') vs the logarithmic frequency ($log\ f$) for three samples of ZMNF nanoparticles, rGO, and ZMNFG nanocomposite labeled as (a), (b), and (c) respectively. When exposed to an alternating electric field, a material's energy dissipation is indicated by its imaginary permittivity, also known as dielectric loss (ε'') [299]. The black curve (a) ZMNF nanoparticles, indicates a high ε'' value at low frequencies, which declines dramatically as frequency increases. This behavior is typical of materials dominated by ionic or charge carrier conduction at low frequencies. The decrease shows that charge carriers at higher frequencies are unable to follow field fluctuations, resulting in less energy dissipation. Such behavior is frequently observed in dielectric or insulating materials with some ionic mobility, which leads to energy loss at lower frequencies. The red curve (b) rGO, begins with a high negative ε'' values at low frequencies and gradually rises to zero as the frequency increases, eventually plateauing. Negative values of ε'' indicate a complicated dielectric response, possibly due to resonance or specific interactions within the material structure, which could result in inductive effects at low frequencies [300]. The progressive increase and levelling off suggest that energy dissipation systems are more active at lower frequencies and less effective at higher frequencies. The blue curve (c) ZMNFG nanocomposite, like the red curve (b) rGO, also begins with high negative ε'' values and gradually increases to zero at higher frequencies. This response indicates that the ZMNFG nanocomposite has a similar or even stronger low-frequency dielectric loss mechanism, most likely due to a specific phase that generates inductive effects. At high frequencies, the ε'' plateau indicates stability where energy dissipation is minimal. This could be due to polarization saturation or the material's charge carrier's inability to keep up with field variations.

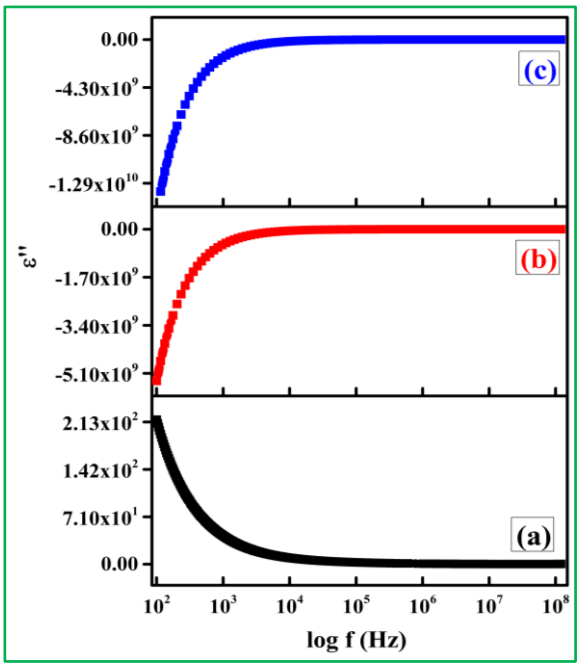

Fig. 4. 26: *Variation of the imaginary part of permittivity (ε'') versus frequency of (a) ZMNF nanoparticles, (b) rGO, and (c) ZMNFG nanocomposite*

For ZMNF nanoparticles, rGO, and ZMNFG nanocomposite samples or materials, the provided Fig. 4.27 displays three plots of the loss tangent ($tan\ \delta$) against the logarithmic frequency ($log\ f$). These plots are labeled as (a), (b), and (c), and are colored black, red, and blue, respectively. In Fig. 4.27 (a) ZMNF nanoparticles as frequency increases, the $tan\ \delta$ values gradually drop from their initial relatively high level. This behavior is common in materials where ion mobility or interfacial polarization may cause large conduction losses at lower frequencies [301]. The lack of a clear peak indicates that there is little dielectric relaxation in the frequency range that is being measured, which suggests that the sample may mostly show conductive losses instead of dipolar relaxation. Fig. 4.27 (b) rGO, has a prominent peak at 160 Hz in the lower frequency range. This peak is typical of a dielectric relaxation process, such as dipolar relaxation or Maxwell-Wagner interfacial polarization. After the peak, $tan\ \delta$ rapidly declines, indicating that beyond the relaxation frequency, the material's dipoles or charge carriers cannot keep up with the alternating field, resulting in decreased energy dissipation. Fig. 4.27 (c) ZMNFG nanocomposite sample also has a peak, though at a lower intensity than the rGO. This could indicate a weaker relaxation process, possibly due to a relaxation mechanism of lower strength [302]. Like the other curves, $tan\ \delta$ reduces as frequency increases, demonstrating a general tendency of lower losses at higher frequencies.

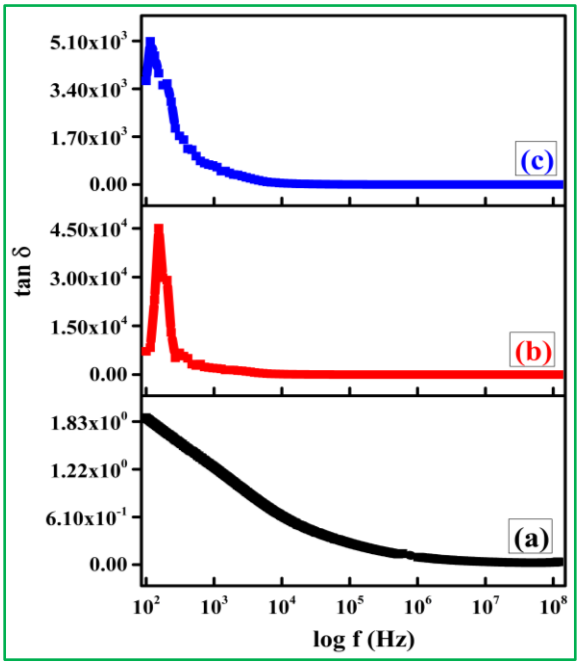

Fig. 4. 27: *Variation of the tangent loss* $(\tan \delta)$ *versus frequency of (a) ZMNF nanoparticles, (b) rGO, and (c) ZMNFG nanocomposite*

4.2.8 AC Conductivity

The graphic in Fig. 4.28 illustrates three plots of AC conductivity (σ_{ac}) as a function of logarithmic frequency ($log\ f$) for ZMNF nanoparticles, rGO, and ZMNF nanocomposite samples. They are labeled as (a), (b), and (c), and color-coded as black, red, and blue, respectively. The conductivity is initially low in Fig. 4.28 (a) ZMNF nanoparticles, virtually constant at low frequencies, and then increases considerably at high frequencies. This is typical of a dielectric material with low DC conductivity and increasing AC conductivity at higher frequencies due to charge carrier hopping or ion mobility. The little increase at low frequencies indicates minimal DC conduction, whereas the dramatic spike at high frequencies may imply greater polarization or hopping conduction [303]. Fig. 4.28 (b) rGO, shows negative conductivity values at low frequencies, which steadily increase and eventually approach zero before shifting to positive conductivity at higher frequencies. Negative conductivity at low frequencies is unusual and can suggest an inductive-like response in complex systems. It has been reported in materials with localized resonance phenomena as well as metamaterials. The dramatic rise in positive conductivity at higher frequencies is characteristic of materials in which higher frequency fields activate more conductive channels or facilitate charge carrier hopping [304]. Fig. 4.28 (c) ZMNFG nanocomposite sample, like

Fig. 4.28 (b) rGO sample, also shows negative conductivity values at low frequencies before progressively transitioning to positive values as the frequency increases. The curve's shape shows that the sample may have complicated microstructural or compositional features that produce inductive or resonance effects at low frequencies, possibly because of interactions between phases or components. At high frequencies, the curve continually rises, showing normal behavior as charge carriers accumulate enough energy to contribute to AC conduction.

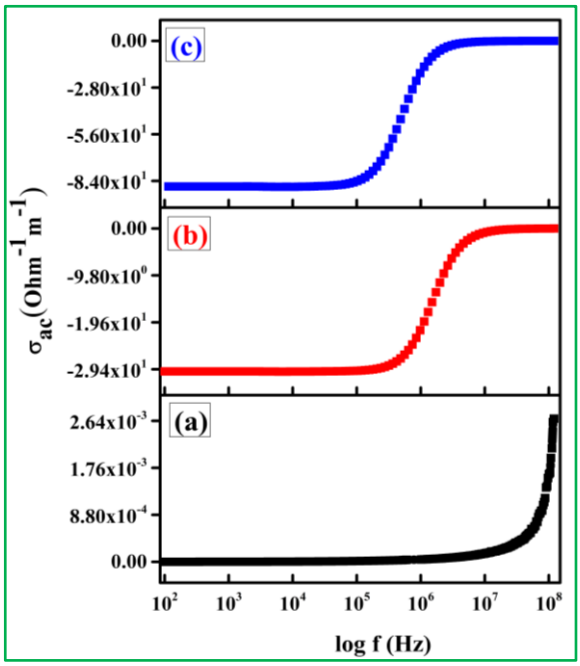

Fig. 4. 28: *Variation of AC conductivity (σ_{ac}) versus frequency of (a) ZMNF nanoparticles, (b) rGO, and (c) ZMNFG nanocomposite*

4.2.9 Electrochemical Investigation

To assess the potential of ZMNFG nanocomposite electrodes as a promising material for SCs, we analyzed the electrochemical characteristics of pristine ZMNF nanoparticles, pristine rGO, and ZMNFG nanocomposite electrodes using CV, GCD, and EIS tests with three-electrode configuration setup. In this analysis, a 3 M KOH aqueous solution was chosen as the electrolyte because of its high ionic concentration and low resistance. The selection of electrolytes greatly influences the performance of SCs [305].

4.2.9 (I) Cyclic Voltammetry (CV) Analysis

The CV measurements were performed at varying scan rates of (5 – 80) mV s^{-1}, with the potential window set between 0 and 0.5 V, as depicted in Fig. 4.29. The CV curves present in Fig. 4.29 (I) compare the electrochemical performance of ZMNF nanoparticles, rGO, and ZMNFG nanocomposite electrodes, obtained at a scan rate of 5 mV s^{-1} exemplified distinctive redox peaks. The presence of these redox peaks (cathodic as well as anodic) suggests that the ZMNF nanoparticles, rGO, and ZMNFG nanocomposite exhibit pseudo-capacitive behavior [123,268]. In cyclic voltammetry (CV) curves, the area under the CV curve of ZMNFG nanocomposite electrode is outstandingly high compared to that of ZMNF nanoparticles and rGO electrodes, thereby confirming a comparatively high specific capacitance (C_S) of ZMNFG nanocomposite electrode, as summarized in Table 4.7, which demonstrates that the incorporation of rGO in ZMNF nanoparticles improves the electrochemical performance of ZMNFG nanocomposite electrodes [306,307].

Furthermore, CV curves of the ZMNFG nanocomposite electrode shown in Fig. 4.29 (II) were recorded at scan rates of 5, 10, 20, 40, and 80 mV s^{-1}, using 3 M KOH aqueous electrolyte. It is obvious from Fig. 4.29 (II), that the peak current response in CV curves increases with corresponding scan rate. The CV curves of ZMNFG nanocomposite at different scan rates do not show symmetrical potential for the reduction (cathodic) and oxidation (anodic) peaks. With the variation in scan rate from 5 – 80 mV s^{-1}, cathodic peaks in CV curves exhibit a slight shift towards lower potentials, whereas anodic peaks shifted towards higher potentials. The observed change in the peak potentials can be ascribed to the strong electric polarization. This polarization effect becomes increasingly prominent at higher scan rates, suggesting the occurrence of irreversible faradaic reactions under such conditions [268]. At various scan rates, the C_S values of ZMNF nanoparticles, rGO, and ZMNFG nanocomposite electrodes were calculated by applying the equation: $C_S = \left(\frac{1}{mv\Delta V}\right)\int_{V_i}^{V_f} I(V)dV$. The parameters represented in the equation are as follows: 'm' is the mass of active materials loaded on Ni-foam, 'υ' signifies the applied scan rate, '$\Delta V = Vf - Vi$' corresponds to the difference in the potential window of CV curve, and the integral $\int_{V_i}^{V_f} I(V)dV$ denotes the area under the CV curve [271]. These C_S values are listed in Table 4.7.

Table 4. 7: *CV parameters of (a) ZMNF nanoparticles, (b) rGO, and (c) ZMNFG nanocomposite*

Sample code	Area	Scan rate (υ)	Potential window (ΔV)	Mass (m)	Specific Capacitance (C_S)
	(AV)	(mV s^{-1})	(V)	(mg)	(F g^{-1})
(a)	0.00060434	05	0.5	1	**241.74**
	0.00080518	10	0.5	1	161.04
	0.00152551	20	0.5	1	152.55
	0.00293832	40	0.5	1	146.92
	0.00455568	80	0.5	1	113.89
(b)	0.00112693	05	0.5	1	**450.77**
	0.00172131	10	0.5	1	344.26
	0.00326224	20	0.5	1	326.24
	0.00520721	40	0.5	1	260.36
	0.00797213	80	0.5	1	199.30
(c)	0.00128444	05	0.5	1	**513.78**
	0.00194605	10	0.5	1	389.21
	0.00364361	20	0.5	1	364.36
	0.00577948	40	0.5	1	288.97
	0.00848658	80	0.5	1	212.16

The data provided in Table 4.7 demonstrates that the respective C_S values of ZMNF nanoparticles, rGO, and ZMNFG nanocomposite electrodes, when tested at 5 mV s^{-1} are 241.74 F g^{-1}, 450.77 F g^{-1}, and 513.78 F g^{-1}. These results validate the enhanced electrochemical performance of ZMNFG nanocomposite compared to ZMNF nanoparticles and rGO electrodes. The observed C_S (513.78 F g^{-1}) at 5 mV s^{-1} of ZMNFG nanocomposite surpasses previously reported values such as $NiFe_2O_4$ (30 F g^{-1} at 1mV s^{-1}), graphene (223 F g^{-1} at 1mV s^{-1}), graphene/$NiFe_2O_4$ (81 F g^{-1} at 1mV s^{-1}) [140]; rGO (218 F g^{-1} at 10 mV s^{-1}) [308]; GO (125 F g^{-1} at 10 mV s^{-1}), rGO (170 F g^{-1} at 10 mV s^{-1}), nitrogen doped graphene (247 F g^{-1} at 10 mV s^{-1}) [309]; rGO/ZnO (312 F g^{-1} at 5 mV s^{-1}) [306]; rGO/$MnFe_2O_4$ (147 F g^{-1} at 5 mV s^{-1}) [310]. The higher C_s values of ZMNFG nanocomposite may be ascribed to the insertion of rGO into ZMNF nanoparticles. As seen in Fig. 4.29 (I), the ZMNFG

nanocomposite displays a higher current response compared to individual ZMNFG nanoparticles and rGO alone, demonstrating the addition of rGO improves the conductivity of electrode material. The improved electrical conductivity facilitates rapid ion diffusion and effective transport of electrons between electrode and electrolyte solution. As reported in previous studies, the C_S of an electrode relies primarily on the efficiency of charge transfer within the electrode material, diffusion of ions within the electrolyte, and ion adsorption on the surface of the electrode material [311–313].

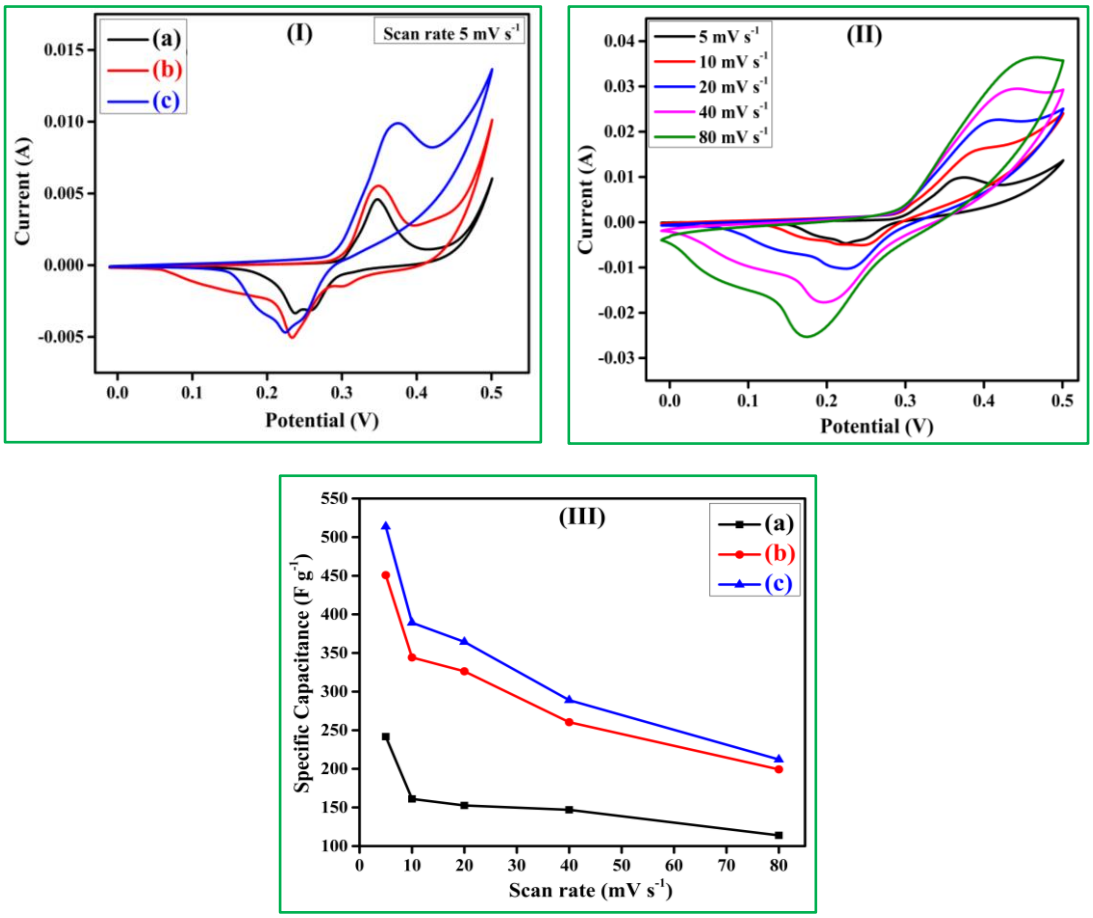

Fig. 4. 29: (I) *Comparison curves of (a) ZMNF nanoparticles, (b) rGO, and (c) ZMNFG nanocomposite at 5 mV s^{-1};* ***(II)*** *CV curves of ZMNFG nanocomposite at distinct scan rates; and* ***(III)*** *Specific capacitance of (a) ZMNF nanoparticles, (b) rGO, and (c) ZMNFG nanocomposite as a function of scan rate*

The relationship between the C_S and the scan rate is depicted in Fig. 4.29 (III) for ZMNF nanoparticles, rGO, and ZMNFG nanocomposite. At a comparatively low scan rate, the ions in the electrolyte have adequate time to diffuse within the porous structure of the electrode material. Consequently, the electrodes exhibit higher specific capacitance (C_S)

values due to the effective utilization of electrode materials. Conversely, at higher scan rates, the charge-transfer reactions occur too rapidly for complete ion diffusion to take place. This resulted in the minimal utilization of the electrode surface area, leading to lower C_S values [123]. Moreover, as evident in Fig. 4.29 (III), the ZMNFG nanocomposite electrode exhibits superior C_S values compared to both ZMNF nanoparticles and rGO electrodes across all scan rates (5 - 80 mV s^{-1}). The enhanced C_S values of the ZMNFG nanocomposite may be attributed to its porous morphology. Additionally, the intercalation of ZMNF nanoparticles on rGO nanosheets further improves the electrochemical process, facilitating the movement of electrolyte ions at the interface between the electrode and electrolyte [306,309]. These findings are further supported by the corresponding FESEM analysis.

4.2.9 (II) Galvanostatic Charge Discharge (GCD) Analysis

GCD testing is a precise technique for evaluating the electrochemical performance of pseudo-supercapacitors [314]. GCD measurements were performed across a spectrum of current densities, ranging from (1 – 5) A g^{-1}, within a potential window of (0 to 0.4) V, as shown in Fig. 4.30. At a current density of 1 A g^{-1}, the comparison of GCD curves of ZMNF nanoparticles, rGO, and ZMNFG nanocomposite electrodes are shown in Fig. 4.30 (I). It is obvious, that ZMNFG nanocomposite outperformed both rGO and ZMNF nanoparticles in discharge time rate, as indicated by the data in Table 4.8. Additionally, the GCD curves of ZMNFG nanocomposite electrode were investigated at varying current densities, ranging from (1 – 5) A g^{-1}, as depicted in Fig. 4.30 (II). Moreover, the asymmetrical GCD curves shown in Fig. 4.30 (I and II) exhibit non-linear shapes due to their pseudocapacitive nature, which is in good agreement with CV analysis. At lower current density (1 A g^{-1}), the observed GCD patterns of ZMNF nanoparticles, rGO, and ZMNFG nanocomposite electrodes exhibit longer discharging time duration, ultimately leading to a larger value of specific capacitance. This phenomenon may be ascribed to the slower charging and discharging rates associated with lower currents, leading to longer durations for both charging as well as discharging processes [315]. The C_S at varying current densities for ZMNF nanoparticles, rGO, and ZMNFG nanocomposite electrodes was determined from their GCD profiles using the equation: $C_S = \left(\frac{I_m \Delta t}{\Delta V}\right)$; where '$Im = \frac{I}{m}$' represents the current density; 'Δt' is the discharging time; and 'ΔV' denotes the applied potential window [316]. Moreover, the equations: $E_d = C_s(\Delta V)^2/2$ and $P_d = E_d/\Delta t$ were utilized to calculate respective energy density (E_d) and

power density (P_d) values for ZMNF nanoparticles, rGO, and ZMNFG nanocomposite electrodes at a specific current density (1 A g^{-1}).

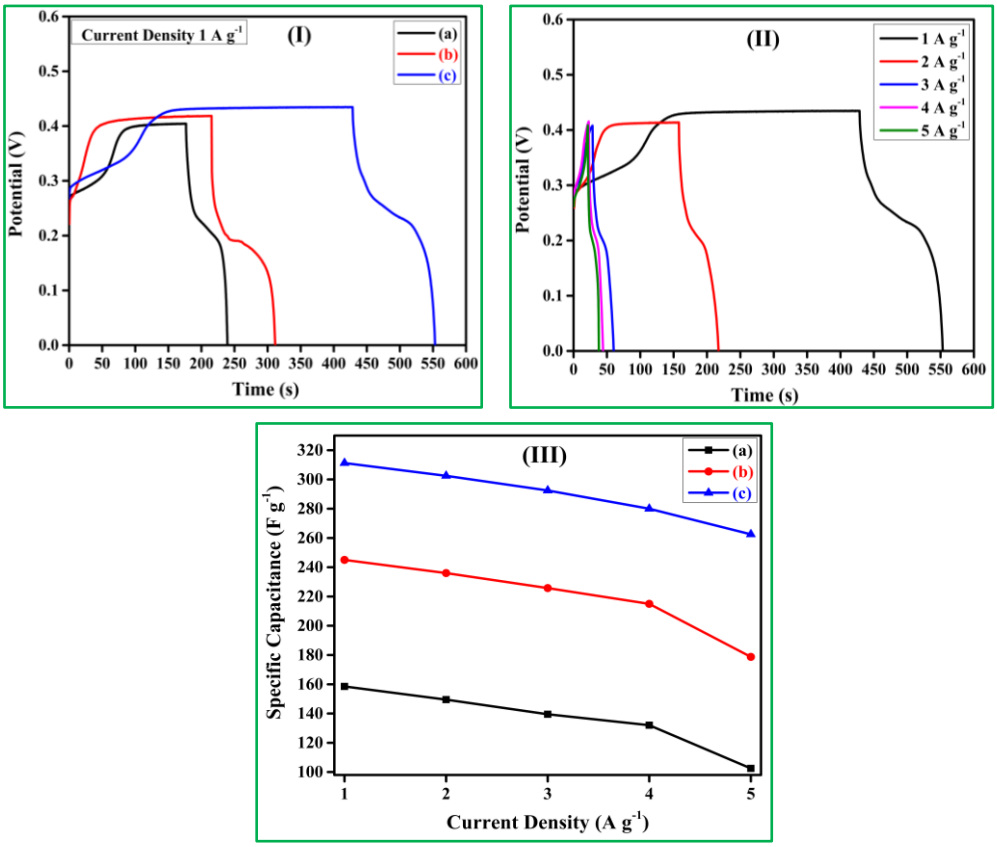

Fig. 4. 30: (I) *Comparison plots of (a) ZMNF nanoparticles, (b) rGO, and (c) ZMNFG nanocomposite at 1 A g^{-1} current density;* ***(II)*** *GCD plots of ZMNFG nanocomposite at various current densities; and* ***(III)*** *Specific capacitance of (a) ZMNF nanoparticles, (b) rGO, and (c) ZMNFG nanocomposite as a function of current density*

Table 4.8 exhibits the calculated specific capacitance (C_S) values of ZMNF nanoparticles, rGO, and ZMNFG nanocomposite electrodes at varying current densities. The C_S values reported in Fig. 4.31 clearly show that the ZMNFG nanocomposite electrode possesses a maximum C_S value of 311.25 F g^{-1} at 1 A g^{-1}, compared to their counterparts i.e., ZMNF nanoparticles (158.5 F g^{-1}) and rGO (245 F g^{-1}). Capacitance retention data recorded between current densities of 1 and 5 A g^{-1} indicate that ZMNFG nanocomposite retained approximately 84.33% of its initial capacitance, outperforming rGO and ZMNF nanoparticles, which showed retention values of 72.96% and 64.67%, respectively. These results underscore the superior rate capability of ZMNFG nanocomposite and reinforce its

suitability for high-performance supercapacitor applications. In addition, the superior energy density (E_d = 24.9 Wh kg^{-1}) and power density (P_d = 830 W kg^{-1}) values were achieved for ZMNFG nanocomposite than rGO (E_d = 19.6 Wh kg^{-1}, P_d = 653.33 W kg^{-1}) and ZMNF nanoparticles (E_d = 12.6 Wh kg^{-1}, P_d = 630 W kg^{-1}). Furthermore, the obtained C_S value of ZMNFG nanocomposite outperforms the previously reported C_S values such as $ZnFe_2O_4$ microspheres (131 F g^{-1} at 0.1 A g^{-1}) [317]; $NiFe_2O_4$ (50 F g^{-1} at 0.5 A g^{-1}), rGO-$NiFe_2O_4$ (215.7 F g^{-1} at 0.5 A g^{-1}) [318]; $Ni_{0.8}Zn_{0.2}Fe_2O_4$ (12 F g^{-1} at 1 A g^{-1}), $Ni_{0.8}Zn_{0.2}Fe_2O_4$/rGO (127.94 F g^{-1} at 1 A g^{-1}) [319]; $MnFe_2O_4$ (245 F g^{-1} at 1 A g^{-1}) [320]; GO/$MnFe_2O_4$ (60 F g^{-1} at 10 A g^{-1}) [321]; $MnFe_2O_4$/rGO (195 F g^{-1} at 1 A g^{-1}), $MnFe_2O_4$ (77 F g^{-1} at 1 A g^{-1}), rGO (67 F g^{-1} at 10 A g^{-1}) [119].

Table 4. 8: *GCD parameters of (a) ZMNF nanoparticles, (b) rGO, and (c) ZMNFG nanocomposite*

Sample code	**Current Density (I_m)**	**Discharging time (Δt)**	**Potential (ΔV)**	**Specific Capacitance (C_S)**
	(A g^{-1})	**(s)**	**(V)**	**(F g^{-1})**
(a)	1	63.4	0.4	**158.5**
	2	29.9	0.4	149.5
	3	18.6	0.4	139.5
	4	13.2	0.4	132
	5	8.2	0.4	102.5
(b)	1	98	0.4	**245**
	2	47.2	0.4	236
	3	30.1	0.4	225.75
	4	21.5	0.4	215
	5	14.3	0.4	178.75
(c)	1	124.5	0.4	**311.25**
	2	60.5	0.4	302.5
	3	39	0.4	292.5
	4	28	0.4	280
	5	21	0.4	262.5

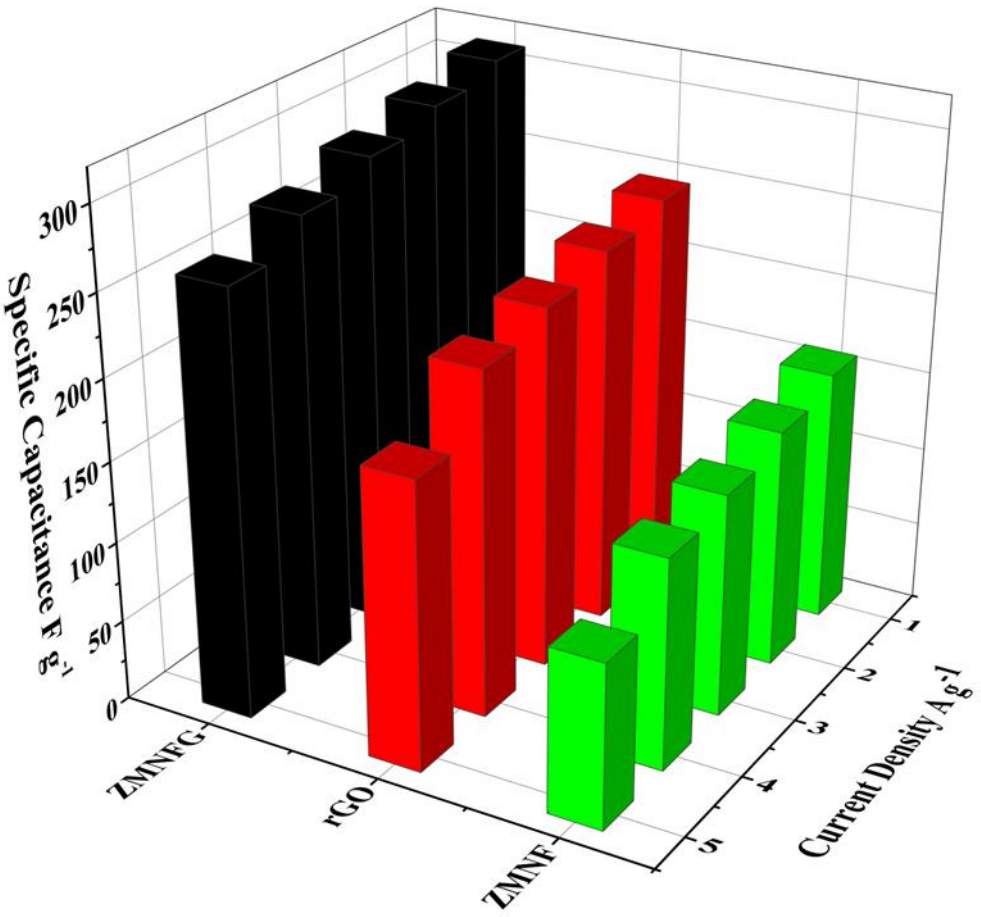

***Fig. 4. 31**: Specific capacitance variation of ZMNF nanoparticles, rGO, and ZMNFG nanocomposite with current density*

The C_S values of ZMNF nanoparticles, rGO, and ZMNFG nanocomposite electrodes derived from GCD tests as a function of current densities are shown in Fig. 4.30 (III). As illustrated in Fig. 4.30 (III), specific capacitance (C_S) exhibits an inverse relation with current density, which is likely attributed to the increasing potential drop at higher current density [306]. The decline in C_S with rising current density can be explained by the rapid arrival of electrolyte ions at the electrode surface. These ions do not penetrate the inner pores of active material due to swift changes in potential. Additionally, the rate at which the electrochemical reaction occurs among active material and electrolyte ions cannot accommodate the increased flow of ions at higher current densities [123]. Conclusively, the inclusion of rGO in ZMNFG nanocomposite leads to improved electron conductivity, due to its porous nature and significant surface area. This improvement results in a notable increase in specific capacitance (C_S), energy density (E_d), and power density (P_d) values of ZMNFG nanocomposite, making it a prominent choice for high-performance supercapacitors [315].

4.2.9 (III) Electrochemical Impedance Spectroscopy (EIS) Analysis

EIS was performed at an applied potential of 5 mV to analyze the electrical response of embedded sample electrodes within a frequency range of 100 kHz-10 MHz. Fig. 4.32 illustrates the Nyquist plots for ZMNF nanoparticles, rGO, and ZMNFG nanocomposite electrodes, which consist of two distinct regions. The x-axis represents the real part of impedance (Z′), which is associated with series resistance (R_s) and charge transfer resistance (R_{ct}), while the y-axis denotes the imaginary part of impedance (Z″), related to the capacitive and diffusive behavior of ZMNF nanoparticles, rGO, and ZMNFG nanocomposite electrode material. The high-frequency region displays a semicircle, which is ascribed to charge transfer resistance (R_{ct}) at the interface between the electrode and electrolyte. Conversely, the linear response observed in the low-frequency region signifies ion diffusion in the electrolyte, known as Warburg impedance. These characteristics are associated with the pseudocapacitive behavior of materials such as ZMNF nanoparticles, rGO, and ZMNFG nanocomposite electrodes. It is evident from Fig. 4.32 that the equivalent series resistance (R_s) for ZMNF nanoparticles, rGO, and ZMNFG nanocomposite electrodes were analyzed using the semi-circle intercept along the real axis in high-frequency region, yielding values of 0.31, 0.17, and 0.084 Ω, respectively. The ZMNFG nanocomposite electrode has a smaller value of equivalent series resistance (R_s = 0.084 Ω) than their counterparts ZMNF nanoparticles (R_s = 0.31 Ω) and rGO (R_s = 0.17 Ω) electrodes, facilitating more rapid ion transfer [195,322]. Moreover, the R_{ct} attributed to the ions at the electrode-electrolyte interface was ascertained by measuring the semicircle's diameter along the real axis. For ZMNF nanoparticles, rGO, and ZMNFG nanocomposite electrodes, the R_{ct} values were 7.63, 4.07, and 1.88 Ω, respectively, as depicted in the inset of Fig. 4.32. Due to the smaller diameter of the semicircle, the lowest value of (R_{ct} = 1.88 Ω) was evidenced for the ZMNG nanocomposite electrode compared to ZMNF nanoparticles (R_{ct} = 7.63 Ω) and rGO (R_{ct} = 4.07 Ω) electrodes. This minimal R_{ct} value for the ZMNFG nanocomposite electrode signifies enhanced ion diffusion at the interface of an electrode and electrolyte [323]. At low-frequency region, the slope observed in the Nyquist plot for ZMNF nanoparticles, rGO, and ZMNFG nanocomposite electrodes is due to the Warburg impedance, which reflects the diffusion of OH^- ions inside these materials [322]. The inset of Fig. 4.32 shows that the slope varies among all the samples. The ZMNF nanoparticle electrode has the least slope, indicating limited ion diffusion, while the slope of rGO electrode is steeper than the ZMNF nanoparticle electrode. However, the ZMNFG nanocomposite electrode also shows a steeper 45˚ slope, suggesting

enhanced ion diffusion. This improvement may be ascribed to porous structure of rGO, which facilitates electrolyte access to active sites more effectively [309]. These observed experimental results are consistent with CV and GCD findings and suggest that the ZMNFG nanocomposite electrode is a potential choice for energy storage applications like supercapacitors [268].

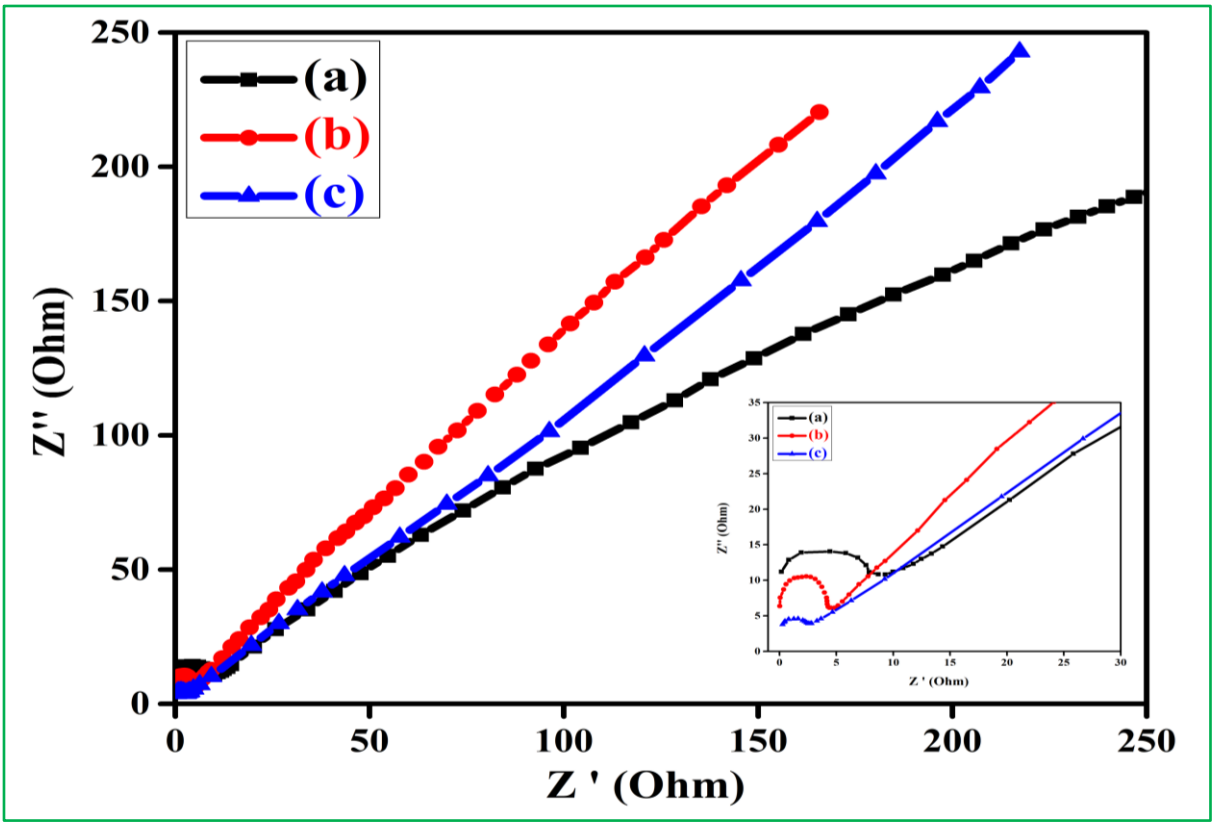

Fig. 4. 32: *EIS comparison plots of (a) ZMNF nanoparticles, (b) rGO, and (c) ZMNFG nanocomposite*

CHAPTER 5

Summary and Conclusion

This thesis primarily aims to investigate the structural, magnetic, dielectric, and electrochemical properties while also designing an enhanced supercapacitor electrode material using a straightforward and simple method for practical applications in the energy sector. The first chapter (i.e; introduction) of this this began with an overview of the importance of renewable and environmentally sustainable energy solutions, emphasizing the growing worldwide energy demand and the constraints associated with non-renewable fossil fuels. The introduction further addressed the essential areas such as energy storage devices, spinel ferrites, and two-dimensional (2D) materials especially reduced graphene oxide, with a particular emphasis on spinel ferrite/rGO nanocomposites.

The second chapter of this thesis provides a thorough review of existing literature in the context of history and evolution of supercapacitors outlining important breakthroughs and significant milestones in the field of supercapacitors. This chapter not only discusses the historical aspects of supercapacitors but also provides a detailed elucidation of different electrode materials, demonstrating important research findings and advancements. The motivation behind this research work comes from a vigorous literature survey wherein numerous researchers emphasize the need for effective energy storage solutions and the exploration of novel electrode materials. Furthermore, a thorough review of existing studies on spinel ferrites, rGO, and their composites is also presented, setting the foundation for experimental work conducted in this study.

The third chapter of this thesis discusses the research methodology and characterization techniques. This chapter of the thesis explains how we prepare different spinel ferrites, rGO, and nanocomposites via sol-gel auto-combustion method, modified hummers method, and physical blending method respectively. This thesis explores the behavior of these nanomaterials with various characterization techniques such as XRD, FTIR, Raman, FESEM, EDX, VSM, Impedance Analyzer, and Electrochemical Workstation. The electrochemical performance of the electrodes was assessed using CV, GCD, and EIS techniques within a three-electrode system. Furthermore, this thesis explores the fabrication of various supercapacitor electrodes such as $Cu_{0.79}Co_{0.21}Fe_{2-x}La_xO_4$ spinel ferrites, $Zn_{0.1}Mn_{0.4}Ni_{0.5}Fe_2O_4$ (ZMNF) spinel ferrite nanoparticles, reduced graphene oxide (rGO),

and $Zn_{0.1}Mn_{0.4}Ni_{0.5}Fe_2O_4$/rGO (ZMNFG) nanocomposite which have shown encouraging results in boosting energy storage and power delivery capabilities.

The fourth chapter of this thesis presents a comprehensive analysis of results and discussions, divided into two main sections. The first section (4.1) focuses on La-Doped Cu-$CoFe_2O_4$ Spinel Ferrites:

This section deals with $Cu_{0.79}Co_{0.21}Fe_{2-x}La_xO_4$ (spinel ferrite) nanoparticles with varying stoichiometric ratios were effectively synthesized by the sol-gel auto-combustion technique. The increase in lattice constant with increasing La^{3+} ion content, ranging between 8.378 Å and 8.389 Å for varying concentrations of La^{3+} ions, can be attributed to the larger ionic radius of La^{3+} ions (1.06 Å) compared to Fe^{3+} ions (0.67 Å). Rietveld analysis showed that all our prepared samples align well with the desired crystalline phase, as indicated by the lower chi-square (χ^2) and goodness-of-fit (GoF) values. Analysis of the FTIR spectra revealed shifts and variations in vibrational bands (υ_1 and υ_2) in response to different concentrations of La^{3+} dopant ions, suggesting a significant influence on the structural characteristics of our prepared samples. Notably, the vibrational bands υ_1 and υ_2 were observed at (524 - 531) cm^{-1} and (461 - 465) cm^{-1} respectively, confirming the presence of the spinel structure and providing insights into the molecular composition of the synthesized ferrite samples. The porous morphology observed in FESEM micrographs makes these materials promising for applications in gas sensing and energy storage supercapacitors. EDX spectra confirmed that the atomic and weight percent values align with the chemical formula for each composition, affirming the quality of our synthesized samples. The superparamagnetic behavior of our materials, indicated by $R_{sq} < 1$, makes them suitable for use in magnetic nanoparticles for targeted drug delivery. Furthermore, our magnetic susceptibility (χ) data showed that the values of H_m were consistently lower than Hc, suggesting the absence of a switching field distribution typically seen in nanoparticles with disordered shell structures. Additionally, the retentivity (M_r) values displayed a decreasing trend, ranging from 20.13 emu g^{-1} to 2.85 emu g^{-1} for x = 0.0 to 0.8 samples, while as, the coercivity (H_c) values exhibited variations with increasing La^{3+} ion concentration, ranging from 754.92 Oe to 1147.38 Oe for the same concentration range. The irregular trend in coercivity observed in VSM reflects the complex magnetic interactions, making these materials potentially valuable for magnetic recording media where precise coercivity control is essential for data storage. The dielectric constant's real part (ε') exhibited a strong dispersion, decreasing with increasing frequency and stabilizing at higher frequencies, influenced by interfacial polarization and space charge

effects. Higher La^{3+} doping concentrations enhanced polarization, demonstrating the significant effect of La^{3+} ions on dielectric properties. Likewise, the dielectric constant's imaginary part (ε'') showed high values at low frequencies due to interfacial polarization and dropped sharply with increasing frequency, stabilizing at higher frequencies where electronic polarization dominates. The loss tangent ($tan\ \delta$) was highest at low frequencies, decreasing with increasing frequency due to reduced charge carrier mobility, and stabilized at higher frequencies. The AC conductivity (σ_{ac}) analysis highlighted an exponential increase at higher frequencies due to enhanced polaron hopping and reduced grain boundary resistance with increasing La^{3+} content. The characteristic redox peaks in the CV curves for all samples indicate a faradic (battery-like) behavior. Specific capacitance values ranged from 270.8 F g^{-1} to 540.0 F g^{-1} for x = 0.0 to 0.8 samples, with the highest observed at x = 0.6. These findings suggest that La^{3+} doping not only improves the dielectric and conduction properties but also tailors the magnetic and electrochemical behavior, making $Cu_{0.79}Co_{0.21}La_xFe_{2-x}O_4$ ferrites promising candidates for applications in energy storage, radiation absorption, data recording, and photocatalysis.

Considering the promising specific capacitance of La-doped Cu-$CoFe_2O_4$ spinel ferrites, we synthesized various mixed spinel ferrites, such as $Zn_{0.1}Mn_{0.4}Ni_{0.5}Fe_2O_4$ and a 2D material like rGO. We then created $Zn_{0.1}Mn_{0.4}Ni_{0.5}Fe_2O_4$/rGO nanocomposite to look for further enhancement of the specific capacitance of these nanomaterials.

The second section (4.2) of this chapter reports on $Zn_{0.1}Mn_{0.4}Ni_{0.5}Fe_2O_4$ (ZMNF) nanoparticles, reduced graphene oxide (rGO), and $Zn_{0.1}Mn_{0.4}Ni_{0.5}Fe_2O_4$/rGO (ZMNFG) nanocomposite. This section confirmed the successful synthesis and phase purity of GO, rGO, ZMNF nanoparticles, and the ZMNFG nanocomposite by XRD analysis. The GO showed distinct peaks indicative of oxygen functional groups, while rGO exhibited reduced interplanar spacing due to the removal of oxygen groups, restoring its graphitic structure. The ZMNF nanoparticles displayed sharp peaks corresponding to a cubic spinel structure with excellent crystallinity (ICDD: 08-0234). In the ZMNFG nanocomposite, enhanced peak intensities and slight shifts in the diffraction peak of rGO suggest strong interactions between ZMNF nanoparticles and rGO, influencing lattice strain and crystallite size. Structural parameter calculations revealed larger crystallite size and reduced lattice strain in the nanocomposite, indicating structural optimization for potential application in energy storage devices. The results of Raman spectroscopy also affirmed the formation of rGO, with an (I_D/I_G) ratio of 0.830 depicting reduced defects and an improved graphitic structure. FTIR

spectroscopic analysis verified the spinel ferrite phase in ZMNF nanoparticles revealing a strong and noticeable absorption band at 531.76 cm^{-1}. The spectra of rGO showed significant bands, confirming the successful reduction, which is consistent with Raman analysis. The ZMNFG nanocomposite had distinct peaks corresponding to ZMNF and rGO, proving its effective formation and structural integration. The FESEM analysis revealed that ZMNF nanoparticles exhibit an agglomerated morphology with an average grain size of 0.29 μm, while pristine rGO displays a wrinkled, sheet-like structure. In the ZMNFG nanocomposite, FESEM images showed a layered configuration of graphene sheets interspersed with granular ZMNF nanoparticles, indicating the successful integration of ZMNF nanoparticles into the rGO matrix. EDX analysis showed Zn, Mn, Ni, Fe, O, and a high amount of C, confirming the composition and purity of the ZMNFG nanocomposite. VSM analysis demonstrated that ZMNF nanoparticles and ZMNFG nanocomposite exhibit superparamagnetic behavior, while rGO remains non-magnetic. The ZMNFG nanocomposite showed reduced saturation magnetization (M_s) and retentivity (M_r) compared to ZMNF nanoparticles due to the non-magnetic nature of rGO. The coercivity (H_c) displayed minimal change with rGO addition, confirming multi-domain behavior. The lower squareness ratio (R_{sq}) values indicate the multi-domain structure, suitable for applications requiring easy magnetization reversal, such as soft magnetic cores and electromagnetic shielding. The dielectric analysis revealed that the capacitance of ZMNFG nanocomposite and rGO show higher initial values and interfacial polarization effects compared to ZMNF nanoparticles, which display a rapid drop. The real (ε') and imaginary (ε'') parts of permittivity indicated unique polarization and energy dissipation characteristics, with ZMNFG nanocomposite and rGO exhibiting negative permittivity at low frequencies. The loss tangent ($tan\ \delta$) analysis highlighted significant dielectric relaxation in rGO and ZMNFG nanocomposite, suggesting their potential for applications requiring frequency-dependent dielectric properties. The AC conductivity (σ_{ac}) indicated that the ZMNFG nanocomposite and rGO display negative conductivity values at low frequencies, shifting to positive values at elevated frequencies, implying complex inductive or resonance phenomena. Meanwhile, ZMNF nanoparticles exhibited typical dielectric behavior with poor DC conductivity and enhanced AC conductivity (σ_{ac}), attributed to charge carrier hopping and ion mobility at higher frequencies. These results underscore the distinctive electrical properties of these materials, which are influenced by their microstructural attributes and compositional characteristics. CV study revealed the enhanced electrochemical performance of ZMNFG nanocomposite electrode and exhibits a

higher C_S value of 513.78 F g^{-1} at 5 mV s^{-1} compared to pristine ZMNF nanoparticles and rGO electrodes. The enhancement is due to increased electrical conductivity, efficient ion diffusion, and the porous structure of the ZMNFG nanocomposite, facilitating effective charge transfer and ion adsorption. GCD analysis showed that ZMNFG nanocomposite electrodes exhibit higher specific capacitance (C_S) and longer discharge times than ZMNF nanoparticles and rGO electrodes. The ZMNFG nanocomposite demonstrated a maximum C_S value of 311.25 F g^{-1} at 1 A g^{-1}, outperforming its counterparts due to improved electron conductivity and porous morphology. EIS analysis reveals that the ZMNFG nanocomposite electrode exhibits the lowest equivalent series resistance (R_s = 0.084 Ω) and charge transfer resistance (R_{ct} = 1.88 Ω) compared to ZMNF nanoparticles and rGO electrodes, ensuring enhanced ion transfer and diffusion at the electrode-electrolyte interface. The comprehensive results from CV, GCD, and EIS studies collectively reveal that the ZMNFG nanocomposite electrode is an auspicious material for advanced supercapacitor applications.

Future Scope

The following points explain possible future avenues and areas for development that can be investigated based on the results of this research:

- **Optimization of Synthesis Conditions:** By optimizing synthesis conditions, unique hybrid nanostructures of spinel ferrites with improved surface area and porosity can be developed, enhancing their electrochemical performance. These materials may be scaled through partnerships with energy companies for mass production of high-performance supercapacitors.
- **Tailored Ferrite Compositions:** Novel spinel ferrites can be synthesized by incorporating one or two transition metal ions within the ferrite lattice, enabling deeper investigation of their electrochemical behavior. Collaborations with battery manufacturers and academic labs could accelerate the translation from lab-scale discovery to commercial prototypes.
- **2D Materials Integration for Ternary Composites:** By integrating 2D materials such as rGO, MXene, and polyaniline with ternary or quaternary metal oxides, we can develop distinctive ternary composites. This unique approach offers the potential to boost the specific capacitance of these composites. These composites have potential in next-

generation electronics and could benefit from joint development with semiconductor firms and supercapacitor startups.

- **Nanobot Applications in Biomedicine:** Ternary composites of spinel ferrites and 2D materials present promising opportunities for the development of nanobots, which can significantly boost advanced biomedical technologies by providing exceptional control and efficiency. Potential collaborations with healthcare innovators and biotech companies could lead to breakthroughs in targeted drug delivery and biosensing platforms.
- **Advanced Electrode Materials:** The investigation of various electrode materials, such as activated carbon, carbon black, carbon aerogels, and carbon nanotubes (CNT), presents an opportunity to enhance electrical conductivity and improve supercapacitor performance. This could be pursued in collaboration with companies developing flexible electronics, grid storage devices, and fast-charging systems.
- **Metal Oxides and Conducting Polymers:** Although activated carbons remain the predominant electrode materials, the consistent development of metal oxides and conducting polymers offers a promising direction. Industrial co-development of pseudocapacitive materials could pave the way for compact and powerful energy storage modules for EVs and aerospace systems.

This research offers a novel pathway to design and fabricate advanced energy storage devices, especially for hybrid electric vehicles (HEVs) and power grid applications. These future developments are essential for fabricating effective supercapacitors with extensive applications, thereby facilitating sustainable development goals and industrial demands. The ternary composites developed from various spinel ferrites and two-dimensional (2D) materials may also find promising applications across multiple domains, such as electromagnetic interference shielding, energy harvesting technologies, and advanced sensor systems. Additionally, these materials show promise for biological applications, including drug delivery systems, tissue engineering scaffolds, electrochemical biosensors, magnetic hyperthermia for cancer therapy, and antimicrobial surfaces for medical equipment. The adaptability of these ternary composite systems highlights their importance in energy storage and a wider range of technological applications.

Bibliography

[1] US Energy Information Administration (EIA), "International Energy Outlook 2017 Overview," *International Energy Outlook 2017 IEO2017*, (2017). (https://www.eia.gov/).

[2] National Statistical Office (NSO), "Energy Statistics in India 2022," *Ministry of Statistics & Programme Implementation, Government of India*, (2022). (https://www.mospi.gov.in/publication/energy-statistics-india-2022).

[3] M. K. Anser, I. Hanif, M. Alharthi, I. S. Chaudhry, "Impact of fossil fuels, renewable energy consumption and industrial growth on carbon emissions in Latin American and Caribbean economies," *Atmosfera,* 33 (2020). https://doi.org/10.20937/ATM.52732.

[4] S. Chu, A. Majumdar, "Opportunities and challenges for a sustainable energy future," *Nature*, 488 (2012). https://doi.org/10.1038/nature11475.

[5] J. L. Holechek, H. M. E. Geli, M. N. Sawalhah, R. Valdez, "A Global Assessment: Can Renewable Energy Replace Fossil Fuels by 2050," *Sustainability*, 14 (2022). https://doi.org/10.3390/su14084792.

[6] A. Qazi, F. Hussain, N. A. B. D. Rahim, G. Hardaker, D. Alghazzawi, K. Shaban, K. Haruna, "Towards Sustainable Energy: A Systematic Review of Renewable Energy Sources, Technologies, and Public Opinions," *IEEE Access*, 7 (2019). https://doi.org/10.1109/ACCESS.2019.2906402.

[7] Z. S. Iro, C. Subramani, S. S. Dash, "A brief review on electrode materials for supercapacitor," *Int J Electrochem Sci.*, 11 (2016). https://doi.org/10.20964/2016.12.50.

[8] M. Vangari, T. Pryor, L. Jiang, "Supercapacitors: Review of Materials and Fabrication Methods," *Journal of Energy Engineering*, 139 (2013). https://doi.org/10.1061/(asce)ey.1943-7897.0000102.

[9] D. Majumdar, M. Mandal, S. K. Bhattacharya, "Journey from supercapacitors to supercapatteries: recent advancements in electrochemical energy storage systems," *Emergent Mater.*, 3 (2020). https://doi.org/10.1007/s42247-020-00090-5.

[10] M. I. A. Abdel Maksoud, R. A. Fahim, A. E. Shalan, M. Abd Elkodous, S. O. Olojede, A. I. Osman, C. Farrell, A. H. Al-Muhtaseb, A. S. Awed, A. H. Ashour, D. W. Rooney, "Advanced materials and technologies for supercapacitors used in energy conversion and storage: a review," *Environ Chem Lett.*, 19 (2021) 375–439. https://doi.org/10.1007/s10311-020-01075-w.

[11] P. Albertus, J. S. Manser, S. Litzelman, “Long-Duration Electricity Storage Applications, Economics, and Technologies,” *Joule*, 4 (2020). https://doi.org/10.1016/j.joule.2019.11.009.

[12] E. Pomerantseva, F. Bonaccorso, X. Feng, Y. Cui, Y. Gogotsi, “Energy storage: The future enabled by nanomaterials,” *Science*, 366 (2019). https://doi.org/10.1126/science.aan8285.

[13] I. Staffell, D. Scamman, A. Velazquez Abad, P. Balcombe, P. E. Dodds, P. Ekins, N. Shah, K. R. Ward, “The role of hydrogen and fuel cells in the global energy system,” *Energy Environ Sci.*, 12 (2019). https://doi.org/10.1039/c8ee01157e.

[14] V. Cigolotti, M. Genovese, P. Fragiacomo, “Comprehensive review on fuel cell technology for stationary applications as sustainable and efficient poly-generation energy systems,” *Energies (Basel)*, 14 (2021). https://doi.org/10.3390/en14164963.

[15] M. Winter, R. J. Brodd, “What are batteries, fuel cells, and supercapacitors,” *Chem Rev.*, 104 (2004). https://doi.org/10.1021/cr020730k.

[16] P. Simon, Y. Gogotsi, “Materials for electrochemical capacitors,” *Nat Mater.*, 7 (2008). https://doi.org/10.1038/nmat2297.

[17] C. Zhong, Y. Deng, W. Hu, J. Qiao, L. Zhang, J. Zhang, “A review of electrolyte materials and compositions for electrochemical supercapacitors,” *Chem Soc Rev.*, 44 (2015). https://doi.org/10.1039/c5cs00303b.

[18] J. Theerthagiri, G. Durai, K. Karuppasamy, P. Arunachalam, V. Elakkiya, P. Kuppusami, T. Maiyalagan, H.S. Kim, “Recent advances in 2-D nanostructured metal nitrides, carbides, and phosphides electrodes for electrochemical supercapacitors – A brief review,” *Journal of Industrial and Engineering Chemistry*, 67 (2018) 12–27. https://doi.org/10.1016/j.jiec.2018.06.038.

[19] Y. Liu, Q. Wu, L. Liu, P. Manasa, L. Kang, F. Ran, “Vanadium nitride for aqueous supercapacitors: a topic review,” *J Mater Chem A Mater.*, 8 (2020). https://doi.org/10.1039/d0ta01490g.

[20] P. J. Hall, M. Mirzaeian, S. I. Fletcher, F. B. Sillars, A. J. R. Rennie, G. O. Shitta-Bey, G. Wilson, A. Cruden, R. Carter, “Energy storage in electrochemical capacitors: Designing functional materials to improve performance,” *Energy Environ Sci.*, 3 (2010). https://doi.org/10.1039/c0ee00004c.

[21] G. Gopakumar, S. Anas, “Conventional Applications of Supercapacitors,” *Supercapacitors and Their Applications*, 2023. https://doi.org/10.1201/9781003258384-8.

[22] S. Banerjee, B. De, P. Sinha, J. Cherusseri, K. K. Kar, "Applications of supercapacitors," *Handbook of Nanocomposite Supercapacitor Materials I*, Springer Series in Materials Science, Springer International Publishing, (2020), 341–350.

[23] Poonam, K. Sharma, A. Arora, S. K. Tripathi, "Review of supercapacitors: Materials and devices," *J Energy Storage*, 21 (2019). https://doi.org/10.1016/j.est.2019.01.010.

[24] Y. Wang, Y. Song, Y. Xia, "Electrochemical capacitors: Mechanism, materials, systems, characterization and applications," *Chem Soc Rev.*, 45 (2016). https://doi.org/10.1039/c5cs00580a.

[25] T. Morimoto, K. Hiratsuka, Y. Sanada, K. Kurihara, "Electric double-layer capacitor using organic electrolyte," *J Power Sources*, 60 (1996). https://doi.org/10.1016/S0378-7753(96)80017-6.

[26] B. Lobato, "Carbon Materials as Electrodes of Electrochemical Double-Layer Capacitors: Textural and Electrochemical Characterization," *Carbon Related Materials*, (2021). https://doi.org/10.1007/978-981-15-7610-2_8.

[27] G. Wang, L. Zhang, J. Zhang, "A review of electrode materials for electrochemical supercapacitors," *Chem Soc Rev*, 41 (2012). https://doi.org/10.1039/c1cs15060j.

[28] B. Babakhani, D. G. Ivey, "Anodic deposition of manganese oxide electrodes with rod-like structures for application as electrochemical capacitors," *J Power Sources*, 195 (2009). https://doi.org/10.1016/j.jpowsour.2009.10.045.

[29] X. Chen, R. Paul, L. Dai, "Carbon-based supercapacitors for efficient energy storage," *Natl Sci Rev.*, 4 (2017). https://doi.org/10.1093/nsr/nwx009.

[30] A. Joseph, T. Thomas, "Pseudocapacitance: An Introduction," *Engineering Materials*, 2024. https://doi.org/10.1007/978-3-031-45430-1_1.

[31] A. Muzaffar, M. B. Ahamed, K. Deshmukh, J. Thirumalai, "A review on recent advances in hybrid supercapacitors: Design, fabrication and applications," *Renewable and Sustainable Energy Reviews*, 101 (2019). https://doi.org/10.1016/j.rser.2018.10.026.

[32] N. Choudhary, C. Li, J. Moore, N. Nagaiah, L. Zhai, Y. Jung, J. Thomas, "Asymmetric Supercapacitor Electrodes and Devices," *Advanced Materials*, 29 (2017). https://doi.org/10.1002/adma.201605336.

[33] N. Kumar, S. Bin Kim, S. Y. Lee, S. J. Park, "Recent Advanced Supercapacitor: A Review of Storage Mechanisms, Electrode Materials, Modification, and Perspectives," *Nanomaterials*, 12 (2022). https://doi.org/10.3390/nano12203708.

[34] P. A. Shinde, Y. Seo, S. Lee, H. Kim, Q. N. Pham, Y. Won, S. Chan Jun, “Layered manganese metal-organic framework with high specific and areal capacitance for hybrid supercapacitors,” *Chemical Engineering Journal*, 387 (2020). https://doi.org/10.1016/j.cej.2019.122982.

[35] Reenu, Sonia, L. Phor, A. Kumar, S. Chahal, “Electrode materials for supercapacitors: A comprehensive review of advancements and performance,” *J Energy Storage*, 84 (2024). https://doi.org/10.1016/j.est.2024.110698.

[36] Y. Kado, Y. Soneda, H. Hatori, M. Kodama, “Advanced carbon electrode for electrochemical capacitors,” *Journal of Solid State Electrochemistry*, 23 (2019). https://doi.org/10.1007/s10008-019-04211-x.

[37] Y. Zhai, Y. Dou, D. Zhao, P. F. Fulvio, R. T. Mayes, S. Dai, “Carbon Materials for Chemical Capacitive Energy Storage,” *Advanced Materials*, 23 (2011). https://doi.org/10.1002/adma.201100984.

[38] W. Gu, G. Yushin, “Review of nanostructured carbon materials for electrochemical capacitor applications: Advantages and limitations of activated carbon, carbide-derived carbon, zeolite-templated carbon, carbon aerogels, carbon nanotubes, onion-like carbon, and graphene,” *Wiley Interdiscip Rev Energy Environ.*, 3 (2014). https://doi.org/10.1002/wene.102.

[39] P. Forouzandeh, V. Kumaravel, S. C. Pillai, “Electrode materials for supercapacitors: A review of recent advances,” *Catalysts*, 10 (2020). https://doi.org/10.3390/catal10090969.

[40] P. Sengodu, A. D. Deshmukh, “Conducting polymers and their inorganic composites for advanced Li-ion batteries: A review,” *RSC Adv.*, 5 (2015). https://doi.org/10.1039/c4ra17254j.

[41] K. Namsheer, C. S. Rout, “Conducting polymers: a comprehensive review on recent advances in synthesis, properties and applications,” *RSC Adv.*, 11 (2021). https://doi.org/10.1039/d0ra07800j.

[42] C. D. Lokhande, D. P. Dubal, O. S. Joo, “Metal oxide thin film-based supercapacitors,” *Current Applied Physics*, 11 (2011). https://doi.org/10.1016/j.cap.2010.12.001.

[43] Y. Zeng, M. Yu, Y. Meng, P. Fang, X. Lu, Y. Tong, “Iron-Based Supercapacitor Electrodes: Advances and Challenges,” *Adv Energy Mater*, 6 (2016). https://doi.org/10.1002/aenm.201601053.

[44] V. C. Lokhande, A. C. Lokhande, C. D. Lokhande, J. H. Kim, T. Ji, “Supercapacitive composite metal oxide electrodes formed with carbon, metal oxides and conducting polymers,” *J Alloys Compd.*, 682 (2016). https://doi.org/10.1016/j.jallcom.2016.04.242.

[45] Y. Zhang, H. Feng, X. Wu, L. Wang, A. Zhang, T. Xia, H. Dong, X. Li, L. Zhang, “Progress of electrochemical capacitor electrode materials: A review,” *Int J Hydrogen Energy.*, 34 (2009). https://doi.org/10.1016/j.ijhydene.2009.04.005.

[46] S. Jayakumar, P. C. Santhosh, M. M. Mohideen, A. V. Radhamani, “A comprehensive review of metal oxides (RuO_2, Co_3O_4, MnO_2, and NiO) for supercapacitor applications and global market trends,” *J Alloys Compd.*, 976 (2024). https://doi.org/10.1016/j.jallcom.2023.173170.

[47] D. Majumdar, “An Overview on Ruthenium Oxide Composites – Challenging Material for Energy Storage Applications,” *Material Science Research India*, 15 (2018). https://doi.org/10.13005/msri/150104.

[48] Q. Abbas, M. Mirzaeian, M. R. C. Hunt, P. Hall, R. Raza, “Current state and future prospects for electrochemical energy storage and conversion systems,” *Energies (Basel)*, 13 (2020). https://doi.org/10.3390/en13215847.

[49] W. Wei, X. Cui, W. Chen, D. G. Ivey, “Manganese oxide-based materials as electrochemical supercapacitor electrodes,” *Chem Soc Rev.*, 40 (2011). https://doi.org/10.1039/c0cs00127a.

[50] R. Verma, “Applications of Hard Ferrites in Memory Devices,” *Materials Research Foundations*, (2023). https://doi.org/10.21741/9781644902318-7.

[51] M. M. Ahmed, N. Abu-Elsaad, “Exploring the Magnetic Behavior of Ferrites: From Diamagnetism to Superparamagnetism,” (2024). http://arxiv.org/abs/2406.10599.

[52] S. Arcaro, J. Venturini, “Modern Ferrites in Engineering: Synthesis, Processing and Cutting-Edge Applications,” *Springer*, (2021). http://doi.org/10.1007/978-3-030-78988-6.

[53] R. Valenzuela, “Novel applications of ferrites,” *Physics Research International*, (2012). https://doi.org/10.1155/2012/591839.

[54] S. F. Shaikh, M. Ubaidullah, R. S. Mane, A. M. Al-Enizi, “Types, Synthesis methods and applications of ferrites,” *Spinel Ferrite Nanostructures for Energy Storage Devices*, 2020. https://doi.org/10.1016/B978-0-12-819237-5.00004-3.

[55] A. Soam, “Application of Ferrites as Electrodes for Supercapacitor, Ferrites - Synthesis and Applications,” *IntechOpen*, Nov. 17, 2021. doi: 10.5772/intechopen.99381.

[56] A. Soufi, H. Hajjaoui, R. Elmoubarki, M. Abdennouri, S. Qourzal, N. Barka, “Spinel ferrites nanoparticles: Synthesis methods and application in heterogeneous Fenton oxidation of organic pollutants – A review,” *Applied Surface Science Advances*, 6 (2021). https://doi.org/10.1016/j.apsadv.2021.100145.

[57] B. B. Patil, “A review: Influence of divalent, trivalent, rare earth and additives ions on Ni–Cu–Zn ferrites,” *Journal of the Indian Chemical Society*, 100 (2023). https://doi.org/10.1016/j.jics.2022.100811.

[58] G. Abbas, A. U. Rehman, W. Gull, M. Afzaal, N. Amin, L. Ben Farhat, M. Amami, N. A. Morley, M. Akhtar, M. I. Arshad, A. Ghuffar, A. Mahmood, M. Ibrahim, “Impact of Co^{2+} on the spectral, optoelectrical, and dielectric properties of $Mg_{0.25}Ni_{0.25}Cu_{0.5-x}Co_xFe_{1.97}La_{0.03}O_4$ ferrites prepared via sol-gel auto-combustion route,” *J Solgel Sci Technol*, 101 (2022) 428-442. https://doi.org/10.1007/s10971-021-05713-9.

[59] O. Dehghani Dastjerdi, H. Shokrollahi, S. Mirshekari, “A review of synthesis, characterization, and magnetic properties of soft spinel ferrites,” *Inorg Chem Commun*, 153 (2023). https://doi.org/10.1016/j.inoche.2023.110797.

[60] A. Goldman, “Handbook of Modern Ferromagnetic Materials,” *New York: Springer*, (1999). https://doi.org/10.1007/978-1-4615-4917-8.

[61] S. J. Salih, W. M. Mahmood, “Review on magnetic spinel ferrite (MFe_2O_4) nanoparticles: From synthesis to application,” *Heliyon*, 9 (2023). https://doi.org/10.1016/j.heliyon.2023.e16601.

[62] A. P. G. Rodrigues, D. K. S. Gomes, J. H. Araújo, D. M. A. Melo, N. A. S. Oliveira, R. M. Braga, “Nanoferrites of nickel doped with cobalt: Influence of Co^{2+} on the structural and magnetic properties,” *J Magn Magn Mater.*, 374 (2015). https://doi.org/10.1016/j.jmmm.2014.09.045.

[63] L. I. Granone, A. C. Ulpe, L. Robben, S. Klimke, M. Jahns, F. Renz, T. M. Gesing, T. Bredow, R. Dillert, D. W. Bahnemann, “Effect of the degree of inversion on optical properties of spinel $ZnFe_2O_4$,” *Physical Chemistry Chemical Physics*, 20 (2018). https://doi.org/10.1039/c8cp05061a.

[64] D. S. Mathew, R. S. Juang, “An overview of the structure and magnetism of spinel ferrite nanoparticles and their synthesis in microemulsions,” *Chemical Engineering Journal*, 129 (2007) 51–65. https://doi.org/10.1016/j.cej.2006.11.001.

[65] S. Chandrasekaran, C. Bowen, P. Zhang, Z. Li, Q. Yuan, X. Ren, L. Deng, “Spinel photocatalysts for environmental remediation, hydrogen generation, CO_2 reduction and

photoelectrochemical water splitting," *J Mater Chem A* Mater, 6 (2018). https://doi.org/10.1039/c8ta03669a.

[66] A. Goldman, "Modern Ferrite Technology Second Edition," *Springer,* (2006). https://doi.org/10.1007/978-0-387-29166-7.

[67] V. V. Jadhav, R.S. Mane, P. V. Shinde, "Basics of Ferrites: Structures and Properties," *Springer Briefs in Materials*, (2020). https://doi.org/10.1007/978-3-030-16718-9_3.

[68] P. Garcia-Muñoz, F. Fresno, V. A. de la Peña O'Shea, N. Keller, "Ferrite Materials for Photo assisted Environmental and Solar Fuels Applications," *Top Curr Chem.*, 378 (2020). https://doi.org/10.1007/s41061-019-0270-3.

[69] H. H. Hegazy, J. Khan, N. Shakeel, E. A. Alabdullkarem, M. I. Saleem, H. Alrobei, I. S. Yahia, '2D-based electrode materials for supercapacitors – status, challenges, and prospects,' *RSC Adv*, 14 (2024) 32958–32977. https://doi.org/10.1039/D4RA05473C.

[70] M. Zeng, Y. Xiao, J. Liu, K. Yang, L. Fu, "Exploring Two-Dimensional Materials toward the Next-Generation Circuits: From Monomer Design to Assembly Control," *Chem Rev.*, 118 (2018) 6236–6296. https://doi.org/10.1021/acs.chemrev.7b00633.

[71] M. Gautam, S. Kanade, B. B. Kale, "Electrochemical Energy Storage and Conversion Applications of Graphene Oxide: A Review," *Energy and Fuels*, 37 (2023). https://doi.org/10.1021/acs.energyfuels.3c02933.

[72] R. Kumar, S. Sahoo, E. Joanni, R. K. Singh, R. M. Yadav, "Graphene-metal oxide hybrid materials with 2D and 3D morphologies for advanced supercapacitor electrodes: Status, challenges and prospects," *Mater Today Nano.*, 24 (2023). https://doi.org/10.1016/j.mtnano.2023.100399.

[73] A. K. Geim, K. S. Novoselov, "The rise of graphene," *Nat Mater.*, 6 (2007). https://doi.org/10.1038/nmat1849.

[74] R. Zhang, A. Palumbo, J. C. Kim, J. Ding, E. H. Yang, "Flexible Graphene-, Graphene-Oxide-, and Carbon-Nanotube-Based Supercapacitors and Batteries," *Ann Phys.*, 531 (2019). https://doi.org/10.1002/andp.201800507.

[75] S. V. Tkachev, E. Y. Buslaeva, S. P. Gubin, "Graphene: A novel carbon nanomaterial," *Inorganic Materials*, 47 (2011) 1–10. https://doi.org/10.1134/S0020168511010134.

[76] E. S. Agudosi, E. C. Abdullah, A. Numan, N. M. Mubarak, M. Khalid, N. Omar, "A Review of the Graphene Synthesis Routes and its Applications in Electrochemical Energy Storage," *Critical Reviews in Solid State and Materials Sciences*, 45 (2020). https://doi.org/10.1080/10408436.2019.1632793.

[77] J. Wu, H. Lin, D. J. Moss, K. P. Loh, B. Jia, “Graphene oxide for photonics, electronics and optoelectronics,” *Nat Rev Chem.*, **7**, 162–183 (2023). https://doi.org/10.1038/s41570-022-00458-7.

[78] X. Huang, F. Liu, P. Jiang, T. Tanaka, “Is graphene oxide an insulating material,” *Proceedings of IEEE International Conference on Solid Dielectrics, ICSD,* (2013). https://doi.org/10.1109/ICSD.2013.6619690.

[79] D. R. Dreyer, S. Park, C. W. Bielawski, R. S. Ruoff, “The chemistry of graphene oxide,” *Chem Soc Rev.*, 39 (2010). https://doi.org/10.1039/b917103g.

[80] M. U. Khan, M. A. Shaida, “Reduction mechanism of graphene oxide including various parameters affecting the C/O ratio,” *Mater Today Commun.*, 36 (2023). https://doi.org/10.1016/j.mtcomm.2023.106577.

[81] E. T. Mombeshora, E. Muchuweni, “Dynamics of reduced graphene oxide: synthesis and structural models,” *RSC Adv.*, 13 (2023). https://doi.org/10.1039/d3ra02098c.

[82] L. Drewniak, S. Drewniak, “The influence of the oxidation method on the size of reduced graphene oxide,” *Photonics Lett Pol.*, 14 (2022). https://doi.org/10.4302/plp.v14i3.1154.

[83] S. N. Alam, N. Sharma, L. Kumar, “Synthesis of Graphene Oxide (GO) by Modified Hummers Method and Its Thermal Reduction to Obtain Reduced Graphene Oxide (rGO),” *Graphene*, 06 (2017) 1–18. https://doi.org/10.4236/graphene.2017.61001.

[84] S. Kumar, S. Kumar, R. N. Rai, Y. Lee, T. Hong Chuong Nguyen, S. Young Kim, Q. Van Le, L. Singh, “Recent development in two-dimensional material-based advanced photoanodes for high-performance dye-sensitized solar cells,” *Solar Energy*, 249 (2023). https://doi.org/10.1016/j.solener.2022.12.013.

[85] L. Dong, J. Yang, M. Chhowalla, K. P. Loh, “Synthesis and reduction of large sized graphene oxide sheets,” *Chem Soc Rev.*, 46 (2017). https://doi.org/10.1039/c7cs00485k.

[86] S. Tamang, S. Rai, R. Bhujel, N. K. Bhattacharyya, B. P. Swain, J. Biswas, “A concise review on GO, rGO and metal oxide/rGO composites: Fabrication and their supercapacitor and catalytic applications,” *J Alloys Compd.*, 947 (2023). https://doi.org/10.1016/j.jallcom.2023.169588.

[87] G. Sriram, M. Arunpandian, K. Dhanabalan, V. R. Sarojamma, S. David, M. D. Kurkuri, T. H. Oh, “Recent Progress Using Graphene Oxide and Its Composites for Supercapacitor Applications: A Review,” *Inorganics (Basel)*, 12 (2024). https://doi.org/10.3390/inorganics12060145.

[88] J. Sun, B. Luo, H. Li, "A Review on the Conventional Capacitors, Supercapacitors, and Emerging Hybrid Ion Capacitors: Past, Present, and Future," *Advanced Energy and Sustainability Research*, 3 (2022). https://doi.org/10.1002/aesr.202100191.

[89] N. S. Shaikh, S. B. Ubale, V. J. Mane, J. S. Shaikh, V. C. Lokhande, S. Praserthdam, C. D. Lokhande, P. Kanjanaboos, "Novel electrodes for supercapacitor: Conducting polymers, metal oxides, chalcogenides, carbides, nitrides, MXenes, and their composites with graphene," *J Alloys Compd*., 893 (2022) 161998. https://doi.org/10.1016/J.JALLCOM.2021.161998.

[90] P. Kurzweil, "CAPACITORS | Electrochemical Double-Layer Capacitors," *Encyclopedia of Electrochemical Power Sources*, (2009), 607-633. https://doi.org/10.1016/B978-044452745-5.00353-1.

[91] E. Gongadze, S. Petersen, U. Beck, U. van Rienen, "Classical Models of the Interface between an Electrode and Electrolyte," *Comsol Conference*, (2009).

[92] H. I. Becker, "Low voltage electrolytic capacitor," *U.S. Patent Office, U.S. Patent*, 2,800,616, July 23, 1957.

[93] R. A. Rightmire, "Electrical energy storage apparatus, *U.S. Patent Office, U.S. Patent*, 3,288,641, Nov. 29, 1966.

[94] Y. J. Kim, M. Endo, T. Takeda, Y. J. Kim, K. Koshiba, K. Ishii, "High Power Electric Double Layer Capacitor (EDLC's); from Operating Principle to Pore Size Control in Advanced Activated Carbons," *Carbon Lett.*, 1 (2001).

[95] A. Yoshida, K. Imoto, H. Yoneda, A. Nishino, "An Electric Double-Layer Capacitor with High Capacitance and Low Resistance," *IEEE Transactions on Components, Hybrids, and Manufacturing Technology*, 15 (1992). https://doi.org/10.1109/33.124204.

[96] K. K. Kar, "Handbook of Nanocomposite Supercapacitor Materials II: Performance," vol. 302, *Springer Series in Materials Science, Springer,* (2020). https://doi.org/10.1007/978-3-030-52359-6.

[97] G. L. Bullard, H. B. Sierra-Alcazar, H. L. Lee, J. L. Morris, "Operating principles of the ultracapacitor," *IEEE Trans Magn.*, 25 (1989). https://doi.org/10.1109/20.22515.

[98] A. Namisnyk and J. Zhu, "A survey of electrochemical super-capacitor technology," *Proc. Australasian Universities Power Engineering Conf.*, (2003), pp. 51–56.

[99] P. Pattathil, N. Sivakumar, T. S. Sonia, "Capacitor to supercapacitor: An introduction," *Nanostructured Ceramic Oxides for Supercapacitor Applications*, (2014). https://doi.org/10.1201/b16522.

[100] J. Miller, “A brief history of supercapacitors,” *Batteries & Energy Storage Technology*, vol. 61, 2007.

[101] B. K. Kim, S. Sy, A. Yu, J. Zhang, “Electrochemical Supercapacitors for Energy Storage and Conversion,” *Handbook of Clean Energy Systems*, (2015). https://doi.org/10.1002/9781118991978.hces112.

[102] V. V. Jadhav, R. S. Mane, P. V. Shinde “Bismuth-Ferrite-Based Electrochemical Supercapacitors,” *Springer Briefs in Materials*, Springer (2020) http://www.springer.com/series/10111.

[103] A. Burke, “Ultracapacitors: Why, how, and where is the technology,” *J Power Sources,* 91 (2000). https://doi.org/10.1016/S0378-7753(00)00485-7.

[104] C. Atwell, “Supercapacitors: Past, Present, and Future,” *Power* Electronics, (2018). (https://www.powerelectronics.com/technologies/alternative-energy/article/21864122/supercapacitors-past-present-and-future)

[105] J. Shepard, “Maxwell Agrees to Acquire Montena Components,” *EE Power*, (2002). (https://eepower.com/news/maxwell-agrees-to-acquire-montena-components/)

[106] J. Ernst, “Maxwell Technologies ultracapacitors for energy storage applications,” presented at the *Supercapacitor Workshop*, ENEA, (2017). (https://www.afs.enea.it/lampasi/workshopsupercapacitors/JErnstMaxwell2017_publishversion.pdf.)

[107] A. Schneuwly, M. Bärtschi, V. Hermann, G. Sartorelli, R. Gallay, and R. Kötz, “BOOSTCAP double-layer capacitors for peak power automotive applications,” in *Proceedings of the 2nd International Advanced Automotive Battery Conference*, (2002).

[108] K. Naoi, “Electrochemical supercapacitors and hybrid systems,” *Encyclopedia of Sustainability Science and Technology*, R. A. Meyers, Ed. Springer, (2012). https://doi.org/10.1007/978-1-4419-0851-3_501.

[109] N. W. Stauffer, "Saying goodbye to batteries," *MIT Energy Initiative*, (2006). (https://energy.mit.edu/news/saying-goodbye-to-batteries/).

[110] P. K. Panda, A. Grigoriev, Y. K. Mishra, R. Ahuja, “Progress in supercapacitors: Roles of two dimensional nanotubular materials,” *Nanoscale Adv.*, 2 (2020). https://doi.org/10.1039/c9na00307j.

[111] A. Balakrishnan, K. R. V. Subramanian, “Nanostructured ceramic oxides for supercapacitor applications,” *CRC Press*, (2014). https://doi.org/10.1201/b16522.

[112] A. K. Samantara, S. Ratha, “Historical Background and Present Status of the Supercapacitors, in: *SpringerBriefs in Materials*, (2018). https://doi.org/10.1007/978-981-10-7263-5_2.

[113] E. Gerstner, “Nobel Prize 2010: Andre Geim & Konstantin Novoselov,” *Nat Phys*, 6 (2010). https://doi.org/10.1038/nphys1836.

[114] Y. Huang, J. Liang, Y. Chen, “An overview of the applications of graphene-based materials in supercapacitors,” *Small*, 8 (2012). https://doi.org/10.1002/smll.201102635.

[115] C. Liu, Z. Yu, D. Neff, A. Zhamu, B. Z. Jang, “Graphene-based supercapacitor with an ultrahigh energy density,” *Nano Lett.*, 10 (2010). https://doi.org/10.1021/nl102661q.

[116] Q. Ke, J. Wang, “Graphene-based materials for supercapacitor electrodes – A review,” *Journal of Materiomics*, 2 (2016). https://doi.org/10.1016/j.jmat.2016.01.001.

[117] S. Nagarani, G. Sasikala, K. Satheesh, Y. Manoharan, and R. Jayavel, “Synthesis and characterization of binary transition metal oxide/reduced graphene oxide nanocomposites and its enhanced electrochemical properties for supercapacitor applications,” *Journal of Materials Science: Materials in Electronics*, 29 (2018). https://doi.org/10.1007/s10854-018-9272-0.

[118] J. Kalidass, T. Sivasankar, A. Sambandam, “Time-Efficient Fabrication of Stable Core-Shell Spinel Ferrites on a Self-Assembled Nanoarchitectonic Graphene Matrix as a New-Gen Anode for Li-Ion Batteries,” *Ind Eng Chem Res.*, 63 (2024). https://doi.org/10.1021/acs.iecr.3c04223.

[119] S. Chai, R. Zheng, R. Guo, H. Luo, H. Cai, L. Liang, H. Huang, Z. Cheng, “Manganese ferrite/reduced graphene oxide composites as energy storage electrode materials for supercapacitors,” *Ionics (Kiel)*, (2024). https://doi.org/10.1007/s11581-024-05477-6.

[120] M. Ikram, A. Irshad, K. MohammedSaleh Katubi, Z. A. Alrowaili, M. S. Al-Buriahi, M. F. Warsi, “Enhanced electrochemical activity of chemically engineered rGO-decorated $NiO/CoFe_2O_4$ for supercapacitor applications,” *Ceram Int.*, 50 (2024) 19578–19591. https://doi.org/10.1016/J.CERAMINT.2024.03.075.

[121] A. Ahad, A. K. M. A. Hossain, “Enhancement of microstructural and magnetic properties of high spin Mn substituted nanocrystalline Ni–Mn–Cu–Zn ferrites,” *Heliyon*, (2024) e26050. https://doi.org/10.1016/j.heliyon.2024.e26050.

[122] T. Putjuso, S. Putjuso, A. Karaphun, P. Moontragoon, I. Kotutha, E. Swatsitang, “Influence of Co doping on phase, structure and electrochemical properties of hydrothermally obtained $Co_xZn_{1-x}Fe_2O_4$ (x = 0.0–0.4) nanoparticles,” *Sci Rep.*, 13 (2023). https://doi.org/10.1038/s41598-023-29830-3.

[123] T. T. H. Hoang, S. Le The, S. Maenosono, T. N. Van, H. G. Do Thi, S. E. Chun, T. T. Viet, N. T. Van, "Facile synthesis of spinel nickel–manganese cobaltite nanoparticles with high rate capability and excellent cycling performance for supercapacitor electrodes," *J Appl Electrochem.*, 53 (2023). https://doi.org/10.1007/s10800-023-01907-x.

[124] M. M. El-Masry, A. E. razek Mahmoud, H. Y. Morshidy, R. Ramadan, "Cu^{2+}- and Zn^{2+}-doped cobalt spinel ferrite: insights on structural, thermal conduction, electric, magnetic and elastic properties," *Journal of Materials Science: Materials in Electronics*, 34 (2023). https://doi.org/10.1007/s10854-022-09777-3.

[125] S. A. Habib, S. A. Saafan, T. M. Meaz, M. A. Darwish, D. Zhou, M. U. Khandaker, M. A. Islam, H. Mohafez, A. V. Trukhanov, S. V. Trukhanov, M. K. Omar, "Structural, Magnetic, and AC Measurements of Nanoferrites/Graphene Composites," *Nanomaterials*, 12 (2022). https://doi.org/10.3390/nano12060931.

[126] B. C. J. Mary, J. J. Vijaya, R. R. Nair, A. Mustafa, P. S. Selvamani, B. Saravanakumar, M. Bououdina, L. J. Kennedy, "Reduced Graphene Oxide-Tailored $CuFe_2O_4$ Nanoparticles as an Electrode Material for High-Performance Supercapacitors," *J Nanomater.*, 2022 (2022). https://doi.org/10.1155/2022/9861440.

[127] A. Aslam, N. A. Morley, N. Amin, M. I. Arshad, M. Ajaz un Nabi, A. Ali, K. Mahmood, A. Bibi, F. Iqbal, S. Hussain, Y. Jamil, "Study of structural, optical and electrical properties of La^{3+} doped $Mg_{0.25}Ni_{0.15}Cu_{0.25}Co_{0.35}Fe_{2-x}La_xO_4$ spinel ferrites," *Physica B Condens Matter.*, 602 (2021). https://doi.org/10.1016/j.physb.2020.412565.

[128] M. M. Roni, K. Hoque, T. C. Paul, M. N. I. Khan, M. E. Hossain, "Synthesis of La-doped $Mn_{0\cdot6}Zn_{0.4}La_xFe_{2-x}O_4$ and the study of its structural, electrical and magnetic properties for high frequency applications," *Results in Materials*, 11 (2021). https://doi.org/10.1016/j.rinma.2021.100215.

[129] M. A. Gabal, A. A. Al-Juaid, "Structural and electromagnetic studies of $Mg_{1-x}Zn_xFe_2O_4$ nanoparticles synthesized via a sucrose autocombustion route," *Journal of Materials Science: Materials in Electronics*, 31 (2020) 10055–10071. https://doi.org/10.1007/s10854-020-03551-z.

[130] L. Phor, S. Chahal, V. Kumar, "Zn^{2+} substituted superparamagnetic $MgFe_2O_4$ spinel-ferrites: Investigations on structural and spin-interactions," *Journal of Advanced Ceramics*, 9 (2020) 576–587. https://doi.org/10.1007/s40145-020-0396-3.

[131] R. Jasrotia, P. Puri, A. Verma, V. P. Singh, "Magnetic and electrical traits of sol-gel synthesized Ni-Cu-Zn nanosized spinel ferrites for multi-layer chip inductors

application," *J Solid State Chem.*, 289 (2020). https://doi.org/10.1016/j.jssc.2020.121462.

[132] A. Rajeshwari, I. Kartharinal Punithavthy, S. Johnson Jeyakumar, N. Lenin, B. Vigneshwaran, "Dependance of lanthanum ions on structural, magnetic and electrical of manganese based spinel nanoferrites," *Ceram Int.*, 46 (2020) 6860–6870. https://doi.org/10.1016/j.ceramint.2019.11.180.

[133] V. Verma, M. Kaur, J. M. Greneche, "Tailored structural, optical and magnetic properties of ternary nanohybrid $Mn_{0.4}Co_{0.6-x}Cu_xFe_2O_4$ (x= 0, 0.2, 0.4, 0.6) spinel ferrites," *Ceram Int.*, 45 (2019) 10865–10875. https://doi.org/10.1016/j.ceramint.2019.02.164.

[134] S. Suresh, A. Prakash, D. Bahadur, "The role of reduced graphene oxide on the electrochemical activity of MFe_2O_4 (M = Fe, Co, Ni and Zn) nanohybrids," *J Magn Magn Mater.*, 448 (2018) 43–51. https://doi.org/10.1016/j.jmmm.2017.08.034.

[135] N. Murali, S. J. Margarette, G. P. Kumar, B. Sailaja, S. Y. Mulushoa, P. Himakar, B. K. Babu, V. Veeraiah, "Effect of Al substitution on the structural and magnetic properties of Co-Zn ferrites," *Physica B Condens Matter*, 522 (2017) 1–6. https://doi.org/10.1016/j.physb.2017.07.043.

[136] K. Rajasekhar Babu, M. Purnachandra Rao, P. S. V. Subba Rao, K. Rama Rao, B. Kishore Babu, B. Rajesh Babu, "Structural and Magnetic Properties of Cu^{2+} Substituted Co–Zn Ferrite Nanoparticles, Synthesized by Sol–Gel Combustion Method," *J Inorg Organomet Polym Mater.*, 27 (2017) 612–621. https://doi.org/10.1007/s10904-017-0499-7.

[137] R. Sharma, P. Thakur, P. Sharma, V. Sharma, "Ferrimagnetic Ni^{2+} doped Mg-Zn spinel ferrite nanoparticles for high density information storage," *J Alloys Compd.*, 704 (2017) 7–17. https://doi.org/10.1016/j.jallcom.2017.02.021.

[138] J. Wang, Q. Deng, M. Li, K. Jiang, J. Zhang, Z. Hu, J. Chu, "Copper ferrites@reduced graphene oxide anode materials for advanced lithium storage applications," *Sci Rep.*, 7 (2017). https://doi.org/10.1038/s41598-017-09214-0.

[139] G. Chandra, R. C. Srivastava, V. R. Reddy, H. M. Agrawal, "Effect of sintering temperature on magnetization and Mössbauer parameters of cobalt ferrite nanoparticles," *J Magn Magn Mater.*, 427 (2017) 225–229. https://doi.org/10.1016/j.jmmm.2016.10.082.

[140] M. A. Mousa, M. Khairy, M. Shehab, “Nanostructured ferrite/graphene/polyaniline using for supercapacitor to enhance the capacitive behavior,” *Journal of Solid State Electrochemistry*, 21 (2017) 995–1005. https://doi.org/10.1007/s10008-016-3446-6.

[141] Q. Lin, G. Yuan, Y. He, L. Wang, J. Dong, Y. Yu, “The influence of La-substituted $Cu_{0.5}Co_{0.5}Fe_2O_4$ nanoparticles on its structural and magnetic properties,” *Mater Des.*, 78 (2015) 80–84. https://doi.org/10.1016/j.matdes.2015.04.029.

[142] R. Indhrajothi, I. Prakash, M. Venkateswarlu, N. Satyanarayana, “Lanthanum ion (La^{3+}) substituted $CoFe_2O_4$ anode material for lithium ion battery applications,” *New Journal of Chemistry*, 39 (2015) 4601–4610. https://doi.org/10.1039/c5nj00791g.

[143] Y. Wang, F. Xu, L. Li, H. Liu, H. Qiu, J. Jiang, “Magnetic properties of La-substituted Ni-Zn-Cr ferrites via rheological phase synthesis,” *Mater Chem Phys.*, 112 (2008) 769–773. https://doi.org/10.1016/j.matchemphys.2008.06.032.

[144] A. Sutka, G. Mezinskis, “Sol-gel auto-combustion synthesis of spinel-type ferrite nanomaterials,” *Front Mater Sci*, 6 (2012). https://doi.org/10.1007/s11706-012-0167-3.

[145] E .E. Ateia, A. A. Allah, R. Ramadan, “Impact of GO on Non-stoichiometric $Mg_{0.85}K_{0.3}Fe_2O_4$ Ferrite Nanoparticles,” *J Supercond Nov Magn.*, 35 (2022). https://doi.org/10.1007/s10948-022-06327-0.

[146] C. F. Holder, R. E. Schaak, “Tutorial on Powder X-ray Diffraction for Characterizing Nanoscale Materials,” *ACS Nano.*, 13 (2019). https://doi.org/10.1021/acsnano.9b05157.

[147] B. Cantor, "Bragg’s Law: Diffraction," *The Equations of Materials*, Oxford, (2020). https://doi.org/10.1093/oso/9780198851875.003.0002.

[148] A. Ali, Y. W. Chiang, R. M. Santos, “X-Ray Diffraction Techniques for Mineral Characterization: A Review for Engineers of the Fundamentals, Applications, and Research Directions,” *Minerals*, 12 (2022). https://doi.org/10.3390/min12020205.

[149] D. Alderton, “X-Ray Diffraction (XRD),” *Encyclopedia of Geology*, Vol. 1-6, Second Edition 1 (2021) 520–531. https://doi.org/10.1016/B978-0-08-102908-4.00178-8.

[150] C. V. Stan, C.M. Beavers, M. Kunz, N. Tamura, “X-ray diffraction under extreme conditions at the advanced light source,” *Quantum Beam Science*, 2 (2018). https://doi.org/10.3390/qubs2010004.

[151] O. A. Belyakova, Y. V. Zubavichus, I. S. Neretin, A. S. Golub, Y. N. Novikov, E. G. Mednikov, M. N. Vargaftik, I. I. Moiseev, Y. L. Slovokhotov, “Atomic structure of nanomaterials: Combined X-ray diffraction and EXAFS studies,” *J Alloys Compd.*, (2004). https://doi.org/10.1016/j.jallcom.2004.05.047.

[152] E. Almeida, M. Balmayore, T. Santos, “Some relevant aspects of the use of FTIR associated techniques in the study of surfaces and coatings,” *Prog Org Coat.*, 44 (2002). https://doi.org/10.1016/S0300-9440(02)00056-5.

[153] C. Berthomieu, R. Hienerwadel, “Fourier transform infrared (FTIR) spectroscopy,” *Photosynth Res.*, 101 (2009). https://doi.org/10.1007/s11120-009-9439-x.

[154] S. Rodin-Bercion, L. Lespade, D. Cavagnat, J. C. Cornut, “Spectroscopy of C-H stretching vibrations of gas-phase cyclohexene,” *J Mol Struct.*, 526 (2000). https://doi.org/10.1016/S0022-2860(00)00524-X.

[155] Y. Nishina, K. Sato, C. Setoyama, H. Tamaoki, R. Miura, K. Shiga, “Intramolecular and intermolecular perturbation on electronic state of FAD free in solution and bound to flavoproteins: FTIR spectroscopic study by using the C = O stretching vibrations as probes,” *J Biochem.*, 142 (2007). https://doi.org/10.1093/jb/mvm129.

[156] K. L. Andrew Chan, S. G. Kazarian, “Attenuated total reflection Fourier-transform infrared (ATR-FTIR) imaging of tissues and live cells,” *Chem Soc Rev.*, 45 (2016). https://doi.org/10.1039/c5cs00515a.

[157] A. C. S. Talari, M. A. G. Martinez, Z. Movasaghi, S. Rehman, I. U. Rehman, “Advances in Fourier transform infrared (FTIR) spectroscopy of biological tissues,” *Appl Spectrosc Rev.*, 52 (2017). https://doi.org/10.1080/05704928.2016.1230863.

[158] L. Liu, A. Mandelis, H. Huan, “Fourier-Transform Infrared Differential Photoacoustic Spectroscopy (FTIR-DPAS) for Simultaneous Monitoring of Multiple Air Contaminants/Trace Gases,” *Int J Thermophys.*, 39 (2018). https://doi.org/10.1007/s10765-018-2411-2.

[159] C. Petibois, B. Desbat, “Clinical application of FTIR imaging: New reasons for hope,” *Trends Biotechnol.*, 28 (2010). https://doi.org/10.1016/j.tibtech.2010.07.003.

[160] P. R. Griffiths, J. A. De Haseth, “Fourier Transform Infrared Spectrometry,” 2nd ed., *Wiley-Interscience*, (2006). https://doi.org/10.1002/047010631X.

[161] S. Prati, G. Sciutto, I. Bonacini, R. Mazzeo, “New Frontiers in Application of FTIR Microscopy for Characterization of Cultural Heritage Materials,” *Top Curr Chem.*, 374 (2016). https://doi.org/10.1007/s41061-016-0025-3.

[162] R. R. Jones, D. C. Hooper, L. Zhang, D. Wolverson, V. K. Valev, “Raman Techniques: Fundamentals and Frontiers,” *Nanoscale Res Lett.*, 14 (2019). https://doi.org/10.1186/s11671-019-3039-2.

[163] E. Smith, G. Dent, “Surface-enhanced Raman scattering and surface-enhanced resonance Raman scattering,” *Modern Raman spectroscopy: A practical approach*, Wiley (2004). https://doi.org/10.1002/0470011831.ch5.

[164] L. J. Bonales, J. M. Elorrieta, Á. Lobato, J. Cobos, “Raman Spectroscopy, a Useful Tool to Study Nuclear Materials,” *Applications of Molecular Spectroscopy to Current Research in the Chemical and Biological Sciences*, (2016). https://doi.org/10.5772/64436.

[165] T. Frosch, “Laser Raman spectroscopy for chemical and environmental analysis,” *Optics InfoBase Conference Papers*, *(*2016). http://dx.doi.org/10.1364/LACSEA.2016.LTh1G.1

[166] T. Vankeirsbilck, A. Vercauteren, W. Baeyens, G. Van der Weken, F. Verpoort, G. Vergote, J. P. Remon, “Applications of Raman spectroscopy in pharmaceutical analysis,” *TrAC - Trends in Analytical Chemistry*, 21 (2002). https://doi.org/10.1016/S0165-9936(02)01208-6.

[167] C. Cao, R. Gao, H. Shang, T. Peng, “Characterization of non-conductive materials using field emission scanning electron microscopy,” *Seventh International Symposium on Precision Mechanical Measurements*, (2016). https://doi.org/10.1117/12.2211862.

[168] M. Schreiner, M. Melcher, K. Uhlir, “Scanning electron microscopy and energy dispersive analysis: Applications in the field of cultural heritage,” *Anal Bioanal Chem.*, 387 (2007). https://doi.org/10.1007/s00216-006-0718-5.

[169] S. P. Kumar, D. Balaji, T. R. Mandlimath, “Characterization of flexible ceramics,” *Advanced Flexible Ceramics: Design, Properties, Manufacturing, and Emerging Applications*, (2023) 25–43. https://doi.org/10.1016/B978-0-323-98824-7.00003-8.

[170] H. Kohno, S. Takeda, T. Akita, “Tunneling electron transport of silicon nanochains studied by in situ scanning electron microscopy,” *Appl Phys Lett.*, 89 (2006). https://doi.org/10.1063/1.2403915.

[171] R. R. Cerchiara, P. E. Fischione, J. J. Gronsky, W. F. Hein, J. M. Matesa, M. P. McCarthy, A. C. Robins, D. W. Smith, “Recent developments in automated sample preparation for FESEM,” *Microscopy and Microanalysis*, (2003). https://doi.org/10.1017/s1431927603444024.

[172] M. Botifoll, I. Pinto-Huguet, J. Arbiol, “Machine learning in electron microscopy for advanced nanocharacterization: current developments, available tools and future outlook,” *Nanoscale Horiz.*, 7 (2022). https://doi.org/10.1039/d2nh00377e.

[173] W. Burgei, M. J. Pechan, H. Jaeger, “A simple vibrating sample magnetometer for use in a materials physics course,” *Am J Phys.*, 71 (2003). https://doi.org/10.1119/1.1572149.

[174] Z. Zhang, Z. Xu, J. He, J. Lu, “Wide-Range Calibration of Magnetic Moments for Vibrating Sample Magnetometers,” *IEEE Trans Instrum Meas.*, 71 (2022). https://doi.org/10.1109/TIM.2022.3196952.

[175] M. Rafique, “Study of the Magnetoelectric Properties of Multiferroic Thin Films and Composites for Device Applications,” *Ph.D. Dissertation*, (2014) https://doi.org/10.13140/RG.2.2.23827.94245.

[176] M. Frigura-Iliasa, L. Petrescu, E. Cazacu, F. M. Frigura-Iliasa, “Computer aided study of the hard-magnetic materials anisotropy,” *INES 2017 - IEEE 21st International Conference on Intelligent Engineering Systems, Proceedings*, (2017). https://doi.org/10.1109/INES.2017.8118538.

[177] M. F. de Campos, S. A. Romero, D. Rodrigues, “Estimate of the anisotropy field of strontium ferrite from powders using the stoner-wohlfarth model,” *Materials Science Forum*, (2017). https://doi.org/10.4028/www.scientific.net/MSF.881.128.

[178] S. P. John, J. Mathew M, “Determination of ferrimagnetic and superparamagnetic components of magnetization and the effect of particle size on structural, magnetic and hyperfine properties of $Mg_{0.5}Zn_{0.5}Fe_2O_4$ nanoparticles,” *J Alloys Compd.*, 869 (2021). https://doi.org/10.1016/j.jallcom.2021.159242.

[179] L. P. Carignan, C. Lacroix, A. Ouimet, M. Ciureanu, A. Yelon, D. Ménard, “Magnetic anisotropy in arrays of Ni, CoFeB, and Ni/Cu nanowires,” *J Appl Phys.*, 102 (2007). https://doi.org/10.1063/1.2756522.

[180] A. K. Katiyar, A. Prakash, A. Dangi, S. K. Dubey, “Development and validation of a low magnetic permeability measurement setup,” *Review of Scientific Instruments*, 93 (2022). https://doi.org/10.1063/5.0124348.

[181] B. Dodrill, J. R. Lindemuth, “Vibrating Sample Magnetometry,” *Magnetic Measurement Techniques for Materials Characterization*, (2021). https://doi.org/10.1007/978-3-030-70443-8_2.

[182] D. Barrettino, “A low-cost, low-power, 10MHz multifrequency impedance analyzer,” *I2MTC 2018 - 2018 IEEE International Instrumentation and Measurement Technology Conference: Discovering New Horizons in Instrumentation and Measurement Proceedings*, (2018). https://doi.org/10.1109/I2MTC.2018.8409789.

[183] E. Barsoukov, J. R. Macdonald, “Impedance Spectroscopy: Theory, Experiment, and Applications,” *Wiley*, (2005). https://doi.org/10.1002/0471716243.

[184] S. Doerner, T. Schneider, P. R. Hauptmann, “Wideband impedance spectrum analyzer for process automation applications,” *Review of Scientific Instruments*, 78 (2007). https://doi.org/10.1063/1.2785845.

[185] N. Elgrishi, K. J. Rountree, B. D. McCarthy, E. S. Rountree, T. T. Eisenhart, J. L. Dempsey, “A Practical Beginner’s Guide to Cyclic Voltammetry,” *J Chem Educ.*, 95 (2018). https://doi.org/10.1021/acs.jchemed.7b00361.

[186] A. J. Bard, L. R. Faulkner, “Electrochemical Methods: Fundamentals and Applications,” 2nd ed., *Wiley*, (2001).

[187] MTX Labs Team, “Cyclic Voltammetry,” *MTX Labs-Electrochemical Devices*, (2023). (https://mtxlabsglobal.com/resources/application-notes/).

[188] P. S. Nnamchi, C. S. Obayi, “Electrochemical characterization of nanomaterials,” *Characterization of Nanomaterials: Advances and Key Technologies*, (2018). https://doi.org/10.1016/B978-0-08-101973-3.00004-3.

[189] V. Climent, J. M. Feliu, “Cyclic voltammetry,” *Encyclopedia of Interfacial Chemistry: Surface Science and Electrochemistry*, Elsevier, (2018) pp. 48–74. https://doi.org/10.1016/B978-0-12-409547-2.10764-4.

[190] M. Shirzad Choubari, S. Rahmani, J. Mazloom, “Boosted electrochemical performance of magnetic caterpillar-like $Mg_{0.5}Ni_{0.5}Fe_2O_4$ nanospinels as a novel pseudocapacitive electrode material,” *Sci Rep.*, 13 (2023). https://doi.org/10.1038/s41598-023-35014-w.

[191] J. P. S., D.S. Sutrave, “A Brief Study of Cyclic Voltammetry and Electrochemical Analysis,” *Int J Chemtech Res.*, 11 (2018). https://doi.org/10.20902/ijctr.2018.110911.

[192] M. Gaire, K. Liang, S. Luo, B. Subedi, S. Adireddy, K. Schroder, S. Farnsworth, D. B. Chrisey, “Nanostructured manganese oxides electrode with ultra-long lifetime for electrochemical capacitors,” *RSC Adv.*, 10 (2020). https://doi.org/10.1039/d0ra01081b.

[193] S. Ban, J. Zhang, L. Zhang, K. Tsay, D. Song, X. Zou, “Charging and discharging electrochemical supercapacitors in the presence of both parallel leakage process and electrochemical decomposition of solvent,” *Electrochim Acta.*, 90 (2013). https://doi.org/10.1016/j.electacta.2012.12.056.

[194] S. Sharma, P. Chand, “Supercapacitor and electrochemical techniques: A brief review,” *Results Chem.*, 5 (2023). https://doi.org/10.1016/j.rechem.2023.100885.

[195] A. Lasia, “Electrochemical impedance spectroscopy and its applications,” (2014). https://doi.org/10.1007/978-1-4614-8933-7.

[196] H. Herrera Hernández, A. M. Ruiz Reynoso, J. C. Trinidad González, C. O. González Morán, J. G. Miranda Hernández, A. Mandujano Ruiz, J. Morales Hernández, R. Orozco Cruz, "Electrochemical Impedance Spectroscopy (EIS): A Review Study of Basic Aspects of the Corrosion Mechanism Applied to Steels," *Electrochemical Impedance Spectroscopy*, (2020). https://doi.org/10.5772/intechopen.94470.

[197] B. A. Mei, O. Munteshari, J. Lau, B. Dunn, L. Pilon, "Physical Interpretations of Nyquist Plots for EDLC Electrodes and Devices," *Journal of Physical Chemistry*, C 122 (2018). https://doi.org/10.1021/acs.jpcc.7b10582.

[198] A. U. Rehman, N. A. Morley, N. Amin, M. I. Arshad, M. A. un Nabi, K. Mahmood, A. Ali, A. Aslam, A. Bibi, M. Z. Iqbal, F. Iqbal, N. Bano, M. Alzaid, "Controllable synthesis of La^{3+} doped $Zn_{0.5}Co_{0.25}Cu_{0.25}Fe_{2-x}La_xO_4$ (x = 0.0, 0.0125, 0.025, 0.0375, 0.05) nano-ferrites by sol-gel auto-combustion route," *Ceram Int.*, 46 (2020) 29297–29308. https://doi.org/10.1016/j.ceramint.2020.08.106.

[199] Y. K. Dasan, B. H. Guan, M. H. Zahari, L. K. Chuan, "Influence of La^{3+} substitution on structure, morphology and magnetic properties of nanocrystalline Ni-Zn ferrite," *PLoS One*, 12 (2017). https://doi.org/10.1371/journal.pone.0170075.

[200] K. A. Ganure, L. A. Dhale, S. E. Shirsat, K. S. Lohar, "Morphological Study of Lanthanum-Doped Nano Spinel Ferrite via Normal Micelles Method," *J Inorg Organomet Polym Mater.*, 28 (2018) 1821–1828. https://doi.org/10.1007/s10904-018-0825-8.

[201] V. Chaudhari, S. E. Shirsath, M. L. Mane, R. H. Kadam, S. B. Shelke, D. R. Mane, "Crystallographic, magnetic and electrical properties of $Ni_{0.5}Cu_{0.25}Zn_{0.25}La_xFe_{2-x}O_4$ nanoparticles fabricated by sol-gel method," *J Alloys Compd.*, 549 (2013) 213–220. https://doi.org/10.1016/j.jallcom.2012.09.060.

[202] S. Liu, K. Wei, Y. Cheng, S. Yan, L. He, L. Deng, "Structural, magnetic and microwave electromagnetic properties in La-substituted quaternary ferrite," *J Alloys Compd.*, 791 (2019) 469–476. https://doi.org/10.1016/j.jallcom.2019.03.227.

[203] W. S. Mohamed, A. M. Abu-Dief, "Impact of rare earth europium (RE-Eu^{3+}) ions substitution on microstructural, optical and magnetic properties of $CoFe_{2-x}Eu_xO_4$ nanosystems, *Ceram Int.*, 46 (2020) 16196–16209. https://doi.org/10.1016/j.ceramint.2020.03.175.

[204] W. Zhang, A. Sun, X. Zhao, N. Suo, L. Yu, Z. Zuo, "Structural and magnetic properties of La^{3+} ion doped Ni–Cu–Co nano ferrites prepared by sol–gel auto-combustion

method," *J Solgel Sci Technol.*, 90 (2019) 599–610. https://doi.org/10.1007/s10971-019-04941-4.

[205] H. Mahajan, S. Kumar, A. Sharma, I. Mohammed, M. Thakur, A. Kaur, A. K. Srivastava, "Effect of sintering temperature on structural, morphological, magnetic, and electrochemical properties of $Mn_{0.3}Co_{0.2}Zn_{0.5}Fe_2O_4$ Ferrite," *J Solgel Sci Technol.*, (2022). https://doi.org/10.1007/s10971-022-06022-5.

[206] S. Ikram, J. Jacob, M. I. Arshad, K. Mahmood, A. Ali, N. Sabir, N. Amin, S. Hussain, "Tailoring the structural, magnetic and dielectric properties of Ni-Zn-$CdFe_2O_4$ spinel ferrites by the substitution of lanthanum ions," *Ceram Int.*, 45 (2019) 3563–3569. https://doi.org/10.1016/j.ceramint.2018.11.015.

[207] A. Kompa, D. Kekuda, K. Mohan Rao, "A comparative study on the structural, optical, and electrical properties of titania films grown by spin-coating method," *Appl Phys A Mater Sci Process*, 126 (2020). https://doi.org/10.1007/s00339-020-3405-z.

[208] A. Aslam, A. U. Rehman, N. Amin, M. Ajaz un Nabi, Q. ul ain Abdullah, N. A. Morley, M. I. Arshad, H. T. Ali, M. Yusuf, Z. Latif, K. Mehmood, "Lanthanum doped $Zn_{0.5}Co_{0.5}La_xFe_{2-x}O_4$ spinel ferrites synthesized via co-precipitation route to evaluate structural, vibrational, electrical, optical, dielectric, and thermoelectric properties," *Journal of Physics and Chemistry of Solids*, 154 (2021). https://doi.org/10.1016/j.jpcs.2021.110080.

[209] F. Ahmed Sheikh, M. Khalid, M. Shahzad Shifa, H. M. Noor Ul Huda Khan Asghar, S. Aslam, A. Perveen, J. Ur Rehman, M. Azhar Khan, Z. Abbas Gilani, "Effects of bismuth on structural and dielectric properties of cobalt-cadmium spinel ferrites fabricated via micro-emulsion route," *Chinese Physics B*, 28 (2019). https://doi.org/10.1088/1674-1056/28/8/088701.

[210] Y. Liu, X. G. Zhu, L. Zhang, F. F. Min, M. X. Zhang, "Microstructure and magnetic properties of nanocrystalline $Co_{1-x}Zn_xFe_2O_4$ ferrites," *Mater Res Bull.*, 47 (2012) 4174–4180. https://doi.org/10.1016/j.materresbull.2012.08.076.

[211] A. Sinha, A. Dutta, "Structural, optical, and electrical transport properties of some rare-earth-doped nickel ferrites: A study on effect of ionic radii of dopants," *Journal of Physics and Chemistry of Solids*, 145 (2020). https://doi.org/10.1016/j.jpcs.2020.109534.

[212] S. K. Godara, V. Kaur, K. Chuchra, S. B. Narang, G. Singh, M. Singh, A. Chawla, S. Verma, G. R. Bhadu, J. C. Chaudhari, P. D. Babu, A. K. Sood, "Impact of Zn^{2+}-Zr^{4+} substitution on M-type Barium Strontium Hexaferrite's structural, surface morphology,

dielectric and magnetic properties," *Results Phys.*, 22 (2021). https://doi.org/10.1016/j.rinp.2021.103892.

[213] R. D. Waldron, M. M. Stimson, and M. J. O'Donnell, "Infrared Spectra of Ferrites," *Physical Review*, vol. 97, no. 5, pp. 1514–1515, 1955.

[214] R. Sagayaraj, S. Aravazhi, C. Selva Kumar, S. Senthil Kumar, G. Chandrasekaran, "Tuning of ferrites ($Co_xFe_{3-x}O_4$) nanoparticles by co-precipitation technique," *SN Appl Sci.*, 1 (2019). https://doi.org/10.1007/s42452-019-0244-7.

[215] K. Shahzadi, A. D. Chandio, G. Mustafa, M. Khalid, J. K. Khan, M. S. Akhtar, Z. A. Gilani, H. M. N. ul H. K. Asgar, "Impact of aluminum substitution on the structural and dielectric properties of Ni–Cu spinel ferrite nanoparticles synthesized via sol–gel route," *Opt Quantum Electron*, 52 (2020). https://doi.org/10.1007/s11082-020-02304-w.

[216] N. R. Rethi, J. Johnson, A. Murugeswari, R. Sankaranarayanan, "Role of Al^{3+} and Cr^{3+} Ions on Structural, Optical, Magnetic, and Impedance Properties of $Al_yCr_xZn_{(0.4-y)}Ni_{(0.6-x)}Fe_2O_4$ Nanoparticles," *J Supercond Nov Magn.*, 36 (2023) 1443–1454. https://doi.org/10.1007/s10948-023-06579-4.

[217] Z. Javed, R. T. Rasool, H. Alhummiany, A. Majeed, S. Gulbadan, G. A. Ashraf, M. mana Al-Anazy, M. Irfan, E. S. Yousef, M. N. Akhtar, M. Arshad, M. A. Khan, "Structural, morphological, dielectric, and spectral properties of Sr-Mg-Ho X-type magnetic nano materials suitable for microwave absorption application," *Vacuum*, 222 (2024) 112965. https://doi.org/10.1016/j.vacuum.2024.112965.

[218] M. N. Akhtar, M. Babar, S. Qamar, Z. ur Rehman, M. A. Khan, "Structural Rietveld refinement and magnetic features of prosademium (Pr) doped Cu nanocrystalline spinel ferrites," *Ceram Int.*, 45 (2019) 10187–10195. https://doi.org/10.1016/j.ceramint.2019.02.069.

[219] G. Mustafa, M. Khalid, J. K. Khan, Z. Uddin, M. G. B. Ashiq, H. H. Somaily, "Lanthanum doped Manganese-Zinc spinel ferrite nanoparticles for microwave and soft magnet applications," *Journal of Materials Science: Materials in Electronics*, 34 (2023). https://doi.org/10.1007/s10854-022-09700-w.

[220] M. A. Almessiere, A. Demir Korkmaz, Y. Slimani, M. Nawaz, S. Ali, A. Baykal, "Magneto-optical properties of rare earth metals substituted Co-Zn spinel nanoferrites," *Ceram Int.*, 45 (2019) 3449–3458. https://doi.org/10.1016/j.ceramint.2018.10.260.

[221] I. Kartharinal Punithavathy, A. Rajeshwari, S. Johnson Jeyakumar, N. Lenin, B. Vigneshwaran, M. Jothibas, B. Arunkumar, "Impact of lanthanum ions on magnetic and

dielectric properties of cobalt nanoferrites," *Journal of Materials Science: Materials in Electronics*, 31 (2020) 9783–9795. https://doi.org/10.1007/s10854-020-03523-3.

[222] S. Qamar, M. N. Akhtar, K. M. Batoo, E. H. Raslan, "Structural and magnetic features of Ce doped Co-Cu-Zn spinel nanoferrites prepared using sol gel self-ignition method," *Ceram Int.* , 46 (2020) 14481–14487. https://doi.org/10.1016/j.ceramint.2020.02.246.

[223] J. K. Khan, M. Khalid, G. Mustafa, Z. Uddin, M. Saleem, A. A. Azam, "Study of lanthanum ions (La^{3+}) doped Manganese-Cobalt (Mn-Co) based spinel ferrite nanoparticles for technological applications," *Appl Phys A Mater Sci Process*, 128 (2022). https://doi.org/10.1007/s00339-022-06106-7.

[224] S. K. Gore, R. S. Mane, M. Naushad, S. S. Jadhav, M. K. Zate, Z. A. Alothman, B. K. N. Hui, "Influence of Bi^{3+}-doping on the magnetic and Mössbauer properties of spinel cobalt ferrite," *Dalton Transactions*, 44 (2015) 6384–6390. https://doi.org/10.1039/c5dt00156k.

[225] C. Barathiraja, A. Manikandan, A. M. Uduman Mohideen, S. Jayasree, S. A. Antony, "Magnetically Recyclable Spinel $Mn_xNi_{1-x}Fe_2O_4$ (x= 0.0–0.5) Nano-photocatalysts: Structural, Morphological and Opto-magnetic Properties," *J Supercond Nov Magn.*, 29 (2016) 477–486. https://doi.org/10.1007/s10948-015-3312-2.

[226] P. Kumar, S. K. Sharma, M. Knobel, J. Chand, M. Singh, "Investigations of lanthanum doping on magnetic properties of nano cobalt ferrites," *J Electroceram.*, 27 (2011) 51–55. https://doi.org/10.1007/s10832-011-9649-4.

[227] G. M. Alzoubi, "The Effect of Co-Doping on the Structural and Magnetic Properties of Single-Domain Crystalline Copper Ferrite Nanoparticles," *Magnetochemistry*, 8 (2022). https://doi.org/10.3390/magnetochemistry8120164.

[228] D. N. Dipesh, L. Wang, H. Adhikari, J. Alam, S. R. Mishra, "Influence of Al^{3+} doping on structural and magnetic properties of $CoFe_{2-x}Al_xO_4$ Ferrite nanoparticles," *J Alloys Compd.*, 688 (2016) 413–421. https://doi.org/10.1016/j.jallcom.2016.07.030.

[229] N. Suo, A. Sun, L. Yu, Z. Zuo, X. Zhao, W. Zhang, Y. Zhang, L. Shao, Z. Dang, "Effect of Al^{3+} ion-substituted Ni–Mg–Co ferrite prepared by sol–gel auto-combustion on lattice structure and magnetic properties," *Appl Phys A Mater Sci Process*, 126 (2020). https://doi.org/10.1007/s00339-020-3361-7.

[230] N. A. Algarou, Y. Slimani, M. A. Almessiere, F. S. Alahmari, M. G. Vakhitov, D. S. Klygach, S. V. Trukhanov, A. V. Trukhanov, A. Baykal, "Magnetic and microwave properties of $SrFe_{12}O_{19}/MCe_{0.04}Fe_{1.96}O_4$ (M = Cu, Ni, Mn, Co and Zn) hard/soft

nanocomposites," *Journal of Materials Research and Technology*, 9 (2020) 5858–5870. https://doi.org/10.1016/j.jmrt.2020.03.113.

[231] A. Ur Rehman, N. Amin, M. B. Tahir, M. A. un Nabi, N. A. Morley, M. Alzaid, M. Amami, M. I. Arshad, "Evaluation of spectral, optoelectrical, dielectric, magnetic, and morphological properties of RE^{3+} (La^{3+}, and Ce^{3+}) and Co^{2+} co-doped $Zn_{0.75}Cu_{0.25}$ Fe_2O_4 ferrites," *Mater. Chem. Phys.*, 275, 125301, (2022). https://doi.org/10.1016/j.matchemphys.2021.125301.

[232] A. Saleem, Y. Zhang, H. Gong, M. K. Majeed, J. Jing, X. Lin, J. Mao, M. Zeeshan Ashfaq, "Structural, magnetic and dielectric properties of nano-crystalline spinel $Ni_xCu_{1-x}Fe_2O_4$," *J. Alloys Compd.*, 825, 154017, (2020). https://doi.org/10.1016/j.jallcom.2020.154017.

[233] D. M. Jnaneshwara, D. N. Avadhani, B. Daruka Prasad, H. Nagabhushana, B. M. Nagabhushana, S. C. Sharma, S. C. Prashantha, C. Shivakumara, "Role of Cu^{2+} ions substitution in magnetic and conductivity behavior of nano-$CoFe_2O_4$," *Spectrochim Acta A Mol Biomol Spectrosc.*, 132 (2014) 256–262. https://doi.org/10.1016/j.saa.2014.04.179.

[234] P. Kumar, S. K. Sharma, M. Knobel, M. Singh, "Effect of La^{3+} doping on the electric, dielectric and magnetic properties of cobalt ferrite processed by co-precipitation technique," *J Alloys Compd.*, 508 (2010) 115–118. https://doi.org/10.1016/j.jallcom.2010.08.007.

[235] T. Şaşmaz Kuru, "Frequency Dependence of Dielectric, Conductivity, Impedance and Electrical Modulus Properties of La^{3+} Substituted in Cobalt- Magnesium Ferrites," *J. Inst. Sci. and Tech.*, 11 (2021) 240–257. https://doi.org/10.21597/jist.792023.

[236] M. M. N. Ansari, S. Khan, N. Ahmad, "Influence of Dy^{3+} and Cu substitution on the structural, electrical and dielectric properties of $CoFe_2O_4$ nanoferrites," *Journal of Materials Science: Materials in Electronics*, 30 (2019) 17630–17642. https://doi.org/10.1007/s10854-019-02112-3.

[237] H. M. Zaki, "AC conductivity and frequency dependence of the dielectric properties for copper doped magnetite," *Physica B Condens Matter.*, 363 (2005) 232–244. https://doi.org/10.1016/j.physb.2005.03.026.

[238] M. A. Ahmed, S. F. Mansour, M. A. Abdo, "Electrical properties of Cu substituted Co nano ferrite," *Phys Scr.*, 86 (2012). https://doi.org/10.1088/0031-8949/86/02/025705.

[239] J. C. Maxwell, "A Treatise on Electricity and Magnetism," *Cambridge: Cambridge University Press*, (2010). https://doi.org/10.1017/CBO9780511709333.

[240] K. W. Wagner, “The Distribution of Relaxation Times in Typical Dielectrics,” *Ann. Phys.*, 40, (1913) 817-819.

[241] C. G. Koops, “On the Dispersion of Resistivity and Dielectric Constant of Some Semiconductors at Audiofrequencies,” *Phys. Rev.*, 83, 1, (1951) 121–124. https://link.aps.org/doi/10.1103/PhysRev.83.121.

[242] K. Deshmukh, S. Sankaran, B. Ahamed, K. K. Sadasivuni, K. S. K. Pasha, D. Ponnamma, P. S. Rama Sreekanth, K. Chidambaram, “Dielectric Spectroscopy,” *Spectroscopic Methods for Nanomaterials Characterization*, *Elsevier*, (2017), 237–299. https://doi.org/10.1016/B978-0-323-46140-5.00010-8.

[243] M. M. Hossen, M. B. Hossen, “Structural, electrical and magnetic properties of $Ni_{0.5}Cu_{0.2}Cd_{0.3}La_xFe_{2-x}O_4$ nano-ferrites due to lanthanum doping in the place of trivalent iron,” *Physica B Condens Matter*, 585 (2020). https://doi.org/10.1016/j.physb.2020.412116.

[244] S. Ikram, M. I. Arshad, K. Mahmood, A. Ali, N. Amin, N. Ali, “Structural, magnetic and dielectric study of La^{3+} substituted $Cu_{0.8}Cd_{0.2}Fe_2O_4$ ferrite nanoparticles synthesized by the co-precipitation method,” *J Alloys Compd.*, 769 (2018). https://doi.org/10.1016/j.jallcom.2018.08.065.

[245] S. Atiq, M. Majeed, A. Ahmad, S. K. Abbas, M. Saleem, S. Riaz, S. Naseem, “Synthesis and investigation of structural, morphological, magnetic, dielectric and impedance spectroscopic characteristics of Ni-Zn ferrite nanoparticles,” *Ceram Int.*, 43 (2017). https://doi.org/10.1016/j.ceramint.2016.11.046.

[246] M. Hashim, Alimuddin, S. E. Shirsath, S. Kumar, R. Kumar, A. S. Roy, J. Shah, R. K. Kotnala, “Preparation and characterization chemistry of nano-crystalline Ni-Cu-Zn ferrite,” *J Alloys Compd.*, 549 (2013). https://doi.org/10.1016/j.jallcom.2012.08.039.

[247] K. Jalaiah, K. Vijaya Babu, “Structural, magnetic and electrical properties of nickel doped Mn-Zn spinel ferrite synthesized by sol-gel method,” *J Magn Magn Mater.*, 423 (2017). https://doi.org/10.1016/j.jmmm.2016.09.114.

[248] B. Bhujun, M. T. T. Tan, A. S. Shanmugam, “Study of mixed ternary transition metal ferrites as potential electrodes for supercapacitor applications,” *Results Phys.*, 7 (2017) 345–353. https://doi.org/10.1016/j.rinp.2016.04.010.

[249] G. Singh, S. Chandra, “Electrochemical performance of $MnFe_2O_4$ nano-ferrites synthesized using thermal decomposition method,” *Int J Hydrogen Energy*, 43 (2018) 4058–4066. https://doi.org/10.1016/j.ijhydene.2017.08.181.

[250] U. Wongpratat, P. Tipsawat, J. Khajonrit, E. Swatsitang, S. Maensiri, "Effects of Nickel and Magnesium on electrochemical performances of partial substitution in spinel ferrite," *J Alloys Compd.*, 831 (2020). https://doi.org/10.1016/j.jallcom.2020.154718.

[251] W. Gul, H. Alrobei, "Effect of graphene oxide nanoparticles on the physical and mechanical properties of medium density fiberboard," *Polymers (Basel)*, 13 (2021). https://doi.org/10.3390/polym13111818.

[252] N. Q. Man, N. T. T. Tu, N. T. V. Hoan, H. X. A. Vu, L. L. Son, N. D. V. Quyen, D. N. Nhiem, N. H. Phong, V. T. Nguyen, T. N. Tuyen, D. Q. Khieu, "Electrochemical determination of clenbuterol with nickel-ferrite/reduced-graphene-oxide-modified electrode," *Journal of Nanoparticle Research*, 25 (2023). https://doi.org/10.1007/s11051-023-05679-5.

[253] Q. T. Ain, S. H. Haq, A. Alshammari, M. A. Al-Mutlaq, M. N. Anjum, "The systemic effect of PEG-nGO-induced oxidative stress in vivo in a rodent model," *Beilstein Journal of Nanotechnology*, 10 (2019) 901–911. https://doi.org/10.3762/BJNANO.10.91.

[254] M. Zong, Y. Huang, N. Zhang, H. Wu, "Influence of (RGO)/(ferrite) ratios and graphene reduction degree on microwave absorption properties of graphene composites," *J Alloys Compd*., 644 (2015). https://doi.org/10.1016/j.jallcom.2015.05.073.

[255] S. Ramesh, B. Dhanalakshmi, B. Chandra Sekhar, P. S. V. Subba Rao, B. Parvatheeswara Rao, "Structural and magnetic studies on Mn-doped Ni–Zn ferrite nanoparticles," *Appl Phys A Mater Sci Process*, 122 (2016). https://doi.org/10.1007/s00339-016-0517-6.

[256] R. Lakra, C. Mahender, B. K. Singh, R. Kumar, S. Kumar, P. K. Sahoo, D. Thatoi, A. Soam, "$ZnFe_2O_4$ Nanoparticles Supported on Graphene Nanosheets for High-Performance Supercapacitor," *J Electron Mater.*, 52 (2023) 2676–2684. https://doi.org/10.1007/s11664-023-10230-2.

[257] M. I. A. Abdel Maksoud, G. S. El-Sayyad, A. Abokhadra, L. I. Soliman, H. H. El-Bahnasawy, A. H. Ashour, "Influence of Mg^{2+} substitution on structural, optical, magnetic, and antimicrobial properties of Mn–Zn ferrite nanoparticles," *Journal of Materials Science: Materials in Electronics*, 31 (2020). https://doi.org/10.1007/s10854-019-02799-4.

[258] K. Madi, D. Chebli, H. Ait Youcef, H. Tahraoui, A. Bouguettoucha, M. Kebir, J. Zhang, A. Amrane, "Green Fabrication of ZnO Nanoparticles and ZnO/rGO Nanocomposites from Algerian Date Syrup Extract: Synthesis, Characterization, and Augmented

Photocatalytic Efficiency in Methylene Blue Degradation," *Catalysts*, 14 (2024). https://doi.org/10.3390/catal14010062.

[259] W. Shen, B. Ren, K. Cai, Y. fei Song, W. Wang, "Synthesis of nonstoichiometric $Co_{0.8}Fe_{2.2}O_4$/reduced graphene oxide (rGO) nanocomposites and their excellent electromagnetic wave absorption property," *J Alloys Compd.*, 774 (2019). https://doi.org/10.1016/j.jallcom.2018.09.361.

[260] M. L. Baynosa, A. H. Mady, V. Q. Nguyen, D. R. Kumar, M. S. Sayed, D. Tuma, J. J. Shim, "Eco-friendly synthesis of recyclable mesoporous zinc ferrite@reduced graphene oxide nanocomposite for efficient photocatalytic dye degradation under solar radiation," *J Colloid Interface Sci.*, 561 (2020). https://doi.org/10.1016/j.jcis.2019.11.018.

[261] H. Javed, A. Rehman, S. Mussadiq, M. Shahid, M. A. Khan, I. Shakir, P. O. Agboola, M. F. A. Aboud, M. F. Warsi, "Reduced graphene oxide-spinel ferrite nano-hybrids as magnetically separable and recyclable visible light driven photocatalyst," *Synth Met.*, 254 (2019) 1–9. https://doi.org/10.1016/j.synthmet.2019.05.013.

[262] D. Selvakumar, H. Sivaram, A. Alsalme, A. Alghamdi, R. Jayavel, "Freestanding flexible, pure and composite form of reduced graphene oxide paper for ammonia vapor sensing," *Sci Rep.*, 9 (2019). https://doi.org/10.1038/s41598-019-45408-4.

[263] W. E. Ghann, H. Kang, J. Uddin, F. A. Chowdhury, S. I. Khondaker, M. Moniruzzaman, M. H. Kabir, M. M. Rahman, "Synthesis and characterization of reduced graphene oxide and their application in dye-sensitized solar cells," *ChemEngineering*, 3 (2019). https://doi.org/10.3390/chemengineering3010007.

[264] R. D. Waldron, M. M. Stimson, and M. J. O'Donnell, "Infrared Spectra of Ferrites," *Physical Review*, vol. 97, no. 5, pp. 1514–1515, 1955.

[265] T. Ma, Y. Cui, Y. Sha, L. Liu, J. Ge, F. Meng, F. Wang, "Facile synthesis of hierarchically porous rGO/MnZn ferrite composites for enhanced microwave absorption performance," *Synth Met.*, 265 (2020). https://doi.org/10.1016/j.synthmet.2020.116407.

[266] B. Babukutty, N. Kalarikkal, S.S. Nair, "Studies on structural, optical and magnetic properties of cobalt substituted magnetite fluids ($Co_xFe_{1-x}Fe_2O_4$)," *Mater Res Express*, 4 (2017). https://doi.org/10.1088/2053-1591/aa628b.

[267] K. Kacem, S. Ameur, J. Casanova-Chafer, M. F. Nsib, E. Llobet, "Bio-reduction of graphene oxide using pomegranate peels for NO_2 sensing and photocatalysis applications," *Journal of Materials Science: Materials in Electronics*, 33 (2022). https://doi.org/10.1007/s10854-022-08501-5.

[268] P. E. Saranya, S. Selladurai, “Efficient electrochemical performance of $ZnMn_2O_4$ nanoparticles with rGO nanosheets for electrodes in supercapacitor applications,” *Journal of Materials Science: Materials in Electronics*, 29 (2018). https://doi.org/10.1007/s10854-017-8268-5.

[269] T. Ravindran Madhura, P. Viswanathan, G. Gnana kumar, R. Ramaraj, “Nanosheet-like manganese ferrite grown on reduced graphene oxide for non-enzymatic electrochemical sensing of hydrogen peroxide,” *Journal of Electroanalytical Chemistry*, 792 (2017). https://doi.org/10.1016/j.jelechem.2017.03.014.

[270] F. T. Johra, W. G. Jung, “Hydrothermally reduced graphene oxide as a supercapacitor,” *Appl Surf Sci*., 357 (2015). https://doi.org/10.1016/j.apsusc.2015.09.128.

[271] M. R. Khan, H. Mahajan, A. K. Srivastava, “Investigation of Crystallographic, Morphological, Magnetic and Electrochemical Properties of La-Doped Cu-$CoFe_2O_4$ Spinel Ferrites,” *Crystal Research and Technology*, 59, (2024). https://doi.org/10.1002/crat.202300356.

[272] H. J. Bae, T. H. Yoo, S. Kim, W. Choi, Y. S. Song, D. K. Kwon, B. J. Cho, W. S. Hwang, “Enhanced photocatalytic degradation of 2-butanone using hybrid nanostructures of gallium oxide and reduced graphene oxide under ultraviolet-C irradiation,” *Catalysts*, 9 (2019). https://doi.org/10.3390/catal9050449.

[273] A. Zamani, M. S. Sadjadi, A. Mahjoub, M. Yousefi, N. Farhadyar, “Synthesis, characterization and investigation of photocatalytic activity of $ZnFe_2O_4$@MnO–GO and $ZnFe_2O_4$@MnO–rGO nanocomposites for degradation of dye Congo red from wastewater under visible light irradiation,” *Research on Chemical Intermediates*, 46 (2020). https://doi.org/10.1007/s11164-019-03934-w.

[274] M. Kooti, A. N. Sedeh, K. Gheisari, A. Figuerola, “Synthesis, characterization, and performance of nanocomposites containing reduced graphene oxide, polyaniline, and cobalt ferrite,” *Physica B Condens Matter*, 612 (2021). https://doi.org/10.1016/j.physb.2021.412974.

[275] B. Bashir, W. Shaheen, M. Asghar, M. F. Warsi, M. A. Khan, S. Haider, I. Shakir, M. Shahid, “Copper doped manganese ferrites nanoparticles anchored on graphene nano-sheets for high performance energy storage applications,” *J Alloys Compd*., 695 (2017) 881–887. https://doi.org/10.1016/j.jallcom.2016.10.183.

[276] A. Rahman, M. F. Warsi, I. Shakir, M. Shahid, S. Zulfiqar, “Fabrication of Ce^{3+} substituted nickel ferrite-reduced graphene oxide heterojunction with high

photocatalytic activity under visible light irradiation," *J Hazard Mater.*, 394 (2020). https://doi.org/10.1016/j.jhazmat.2020.122593.

[277] H. Ren, C. Gu, S. W. Joo, J. Zhao, Y. Sun, J. Huang, "Effective hydrogen gas sensor based on NiO@rGO nanocomposite," *Sens Actuators B Chem.*, 266 (2018). https://doi.org/10.1016/j.snb.2018.03.130.

[278] A. N. Yadav, A. K. Singh, P. Kumar, K. Singh, "Graphene-Induced Room Temperature Ferromagnetism in Cobalt Nanoparticles Decorated Graphene Nanohybrid," *Nanoscale Res Lett.*, 15 (2020). https://doi.org/10.1186/s11671-020-03398-7.

[279] J. Liu, D. Xu, P. Chen, Q. Yu, H. Qiu, X. Xiong, "Solvothermal synthesis of porous superparamagnetic RGO@Fe_3O_4 nanocomposites for microwave absorption," *Journal of Materials Science: Materials in Electronics*, 30 (2019). https://doi.org/10.1007/s10854-019-02057-7.

[280] Q. Yu, Y. Wang, P. Chen, W. Nie, H. Chen, J. Zhou, "Reduced graphene oxide-wrapped super dense Fe_3O_4 nanoparticles with enhanced electromagnetic wave absorption properties," *Nanomaterials*, 9 (2019). https://doi.org/10.3390/nano9060845.

[281] Z. Li, X. Li, Y. Zong, G. Tan, Y. Sun, Y. Lan, M. He, Z. Ren, X. Zheng, "Solvothermal synthesis of nitrogen-doped graphene decorated by superparamagnetic Fe_3O_4 nanoparticles and their applications as enhanced synergistic microwave absorbers," *Carbon*, 115 (2017). https://doi.org/10.1016/j.carbon.2017.01.036.

[282] M. Zong, Y. Huang, Y. Zhao, X. Sun, C. Qu, D. Luo, J. Zheng, "Facile preparation, high microwave absorption and microwave absorbing mechanism of RGO-Fe_3O_4 composites," *RSC Adv*., 3 (2013). https://doi.org/10.1039/c3ra43359e.

[283] C. Caizer, "Nanoparticle size effect on some magnetic properties," *Handbook of Nanoparticles,* (2015). https://doi.org/10.1007/978-3-319-15338-4_24.

[284] M. A. Almessiere, Y. Slimani, A. Baykal, "Exchange spring magnetic behavior of $Sr_{0.3}Ba_{0.4}Pb_{0.3}Fe_{12}O_{19}$/($CuFe_2O_4$) nanocomposites fabricated by a one-pot citrate sol-gel combustion method," *J Alloys Compd*., 762 (2018). https://doi.org/10.1016/j.jallcom.2018.05.232.

[285] E. H. El-Khawas, A. A. Azab, "Synergetic implementation of magnetic and electrical characteristics of rGO/$Cu_{0.3}Mn_{0.7}Fe_2O_4$ nanocomposites," *Appl Phys A Mater Sci Process*, 125 (2019). https://doi.org/10.1007/s00339-019-3095-6.

[286] L. Kumar, M. Kar, "Effect of La^{3+} substitution on the structural and magnetocrystalline anisotropy of nanocrystalline cobalt ferrite ($CoFe_{2-x}La_xO_4$)," *Ceram Int.*, 38 (2012) 4771–4782. https://doi.org/10.1016/j.ceramint.2012.02.065.

[287] E. C. Stoner, E. P. Wohlfarth, “A mechanism of magnetic hysteresis in heterogeneous alloys,” *IEEE Trans Magn*., 27 (1991). https://doi.org/10.1109/TMAG.1991.1183750.

[288] M. A. Almessiere, Y. Slimani, A. D. Korkmaz, S. Guner, M. Sertkol, S. E. Shirsath, A. Baykal, “Structural, optical and magnetic properties of Tm^{3+} substituted cobalt spinel ferrites synthesized via sonochemical approach,” *Ultrason Sonochem*., 54 (2019). https://doi.org/10.1016/j.ultsonch.2019.02.022.

[289] A. Goldman, “Soft Magnetic Materials for EMI Suppression,” *Handbook of Modern Ferromagnetic Materials*, 1999. https://doi.org/10.1007/978-1-4615-4917-8_16.

[290] N. Singh, J. R. Ansari, M. Pal, N. T. K. Thanh, T. Le, A. Datta, “Synthesis and magnetic properties of stable cobalt nanoparticles decorated reduced graphene oxide sheets in the aqueous medium,” *Journal of Materials Science: Materials in Electronics*, 31 (2020). https://doi.org/10.1007/s10854-020-04075-2.

[291] N. N. Malinga, A. L. L. Jarvis, “Synthesis, characterization and magnetic properties of Ni, Co and FeCo nanoparticles on reduced graphene oxide for removal of Cr(VI),” *J Nanostructure Chem*., 10 (2020). https://doi.org/10.1007/s40097-019-00328-7.

[292] K. Malaie, M. R. Ganjali, “Spinel nano-ferrites for aqueous supercapacitors; linking abundant resources and low-cost processes for sustainable energy storage,” *J Energy Storage*, 33 (2021). https://doi.org/10.1016/j.est.2020.102097.

[293] S. Chella, P. Kollu, E. V. P. R. Komarala, S. Doshi, M. Saranya, S. Felix, R. Ramachandran, P. Saravanan, V. L. Koneru, V. Venugopal, S. K. Jeong, A. N. Grace, “Solvothermal synthesis of $MnFe_2O_4$-graphene composite-Investigation of its adsorption and antimicrobial properties,” *Appl Surf Sci*., 327 (2015). https://doi.org/10.1016/j.apsusc.2014.11.096.

[294] H. Pfeiffer, “Determination of anisotropy field distribution in particle assemblies taking into account thermal fluctuations,” *Physica Status Solidi*., (a) 118 (1990). https://doi.org/10.1002/pssa.2211180133.

[295] A. Yadav, M. Fahad, P. M. Sarun, “Frequency dependent studies of dielectric and impedance properties of $NaNb_{0.92}V_{0.08}O_3$ ceramics,” *Mater Today Proc*., 46 (2021) 6286–6289. https://doi.org/10.1016/J.MATPR.2020.05.151.

[296] V. Senthil, T. Badapanda, A. Chithambararaj, A. Chandra Bose, A. K. Mohapatra, S. Panigrahi, “Dielectric relaxation behavior and electrical conduction mechanism in polymer-ceramic composites based on Sr modified Barium Zirconium Titanate ceramic,” *Journal of Polymer Research*, 19 (2012). https://doi.org/10.1007/s10965-012-9898-1.

[297] D. R. Smith, N. Kroll, “Negative refractive index in left-handed materials,” *Phys Rev Lett*., 85 (2000). https://doi.org/10.1103/PhysRevLett.85.2933.

[298] H. He, M. Dyck, “Application of Multiphase Dielectric Mixing Models for Understanding the Effective Dielectric Permittivity of Frozen Soils,” *Vadose Zone Journal*, 12 (2013). https://doi.org/10.2136/vzj2012.0060.

[299] A. Sihvola, “Electromagnetic Mixing Formulas and Applications,” London, U.K.: IET, (1999). https://doi.org/10.1049/pbew047e.

[300] T. I. Yang, P. Kofinas, “Dielectric properties of polymer nanoparticle composites,” *Polymer (Guildf)*, 48 (2007). https://doi.org/10.1016/j.polymer.2006.12.030.

[301] J. S. Brooks, R. Vasic, A. Kismarahardja, E. Steven, T. Tokumoto, P. Schlottmann, S. Kelly, “Debye relaxation in high magnetic fields,” *Phys. Rev. B,* 78, (2008). https://doi.org/10.1103/PhysRevB.78.045205.

[302] A. K. Jonscher, “The “universal” dielectric response,” *Nature*, 267 (1977). https://doi.org/10.1038/267673a0.

[303] A. Kumar, V. Saraswat, A. Dahshan, H. I. Elsaeedy, N. Mehta, “Exploring dielectric and AC conduction characteristics in elemental selenium glass modified with silver halides,” *RSC Adv*., 14 (2024) 20933–20950. https://doi.org/10.1039/d4ra02999b.

[304] V. A. Markel, “Introduction to the Maxwell Garnett approximation: tutorial,” *Journal of the Optical Society of America A*, 33 (2016). https://doi.org/10.1364/josaa.33.001244.

[305] S. Sahoo, J. J. Shim, “Facile Synthesis of Three-Dimensional Ternary $ZnCo_2O_4$/Reduced Graphene Oxide/NiO Composite Film on Nickel Foam for Next Generation Supercapacitor Electrodes,” *ACS Sustain Chem Eng.*, 5 (2017). https://doi.org/10.1021/acssuschemeng.6b01367.

[306] J. Jayachandiran, J. Yesuraj, M. Arivanandhan, A. Raja, S. A. Suthanthiraraj, R. Jayavel, D. Nedumaran, “Synthesis and Electrochemical Studies of rGO/ZnO Nanocomposite for Supercapacitor Application,” *J Inorg Organomet Polym Mater*, 28 (2018). https://doi.org/10.1007/s10904-018-0873-0.

[307] D. Ghosh, S. Giri, C. K. Das, “Preparation of CTAB-assisted hexagonal platelet $Co(OH)_2$/graphene hybrid composite as efficient supercapacitor electrode material,” *ACS Sustain Chem Eng.,* 1 (2013). https://doi.org/10.1021/sc400055z.

[308] Z. Lei, N. Christov, X. S. Zhao, “Intercalation of mesoporous carbon spheres between reduced graphene oxide sheets for preparing high-rate supercapacitor electrodes,” *Energy Environ Sci*., 4 (2011). https://doi.org/10.1039/c1ee01094h.

[309] Y. Gong, D. Li, Q. Fu, C. Pan, “Influence of graphene microstructures on electrochemical performance for supercapacitors,” *Progress in Natural Science: Materials International*, 25 (2015). https://doi. org/10.1016/j.pnsc.2015.10.004.

[310] S. Ishaq, M. Moussa, F. Kanwal, M. Ehsan, M. Saleem, T. N. Van, D. Losic, “Facile synthesis of ternary graphene nanocomposites with doped metal oxide and conductive polymers as electrode materials for high performance supercapacitors,” *Sci Rep*., 9 (2019). https://doi.org/10.1038/s41598-019-41939-y.

[311] M. Ghosh, A. Ray, G. M. Rao, “Performance dependence of electrochemical capacitor on surface morphology for vertically aligned graphene nanosheets,” *Ionics (Kiel)*, 26 (2020). https://doi.org/10.1007/s11581-019-03254-4.

[312] A. Mondal, S. Maiti, S. Mahanty, A. Baran Panda, “Large-scale synthesis of porous $NiCo_2O_4$ and rGO-$NiCo_2O_4$ hollow-spheres with superior electrochemical performance as a faradaic electrode,” *J Mater Chem A Mater.*, 5 (2017). https://doi.org/10.1039/c7ta03491a.

[313] S. Saha, A. Roy, A. Ray, T. Das, M. Nandi, B. Ghosh, S. Das, “Effect of particle morphology on the electrochemical performance of hydrothermally synthesized $NiMn_2O_4$,” *Electrochim Acta.,* 353 (2020). https://doi.org/10.1016/j.electacta.2020.136515.

[314] Y. Wu, Ed. “Metal Oxides in Energy Technologies,” *Elsevier*, (2018). https://doi.org/10.1016/c2015-0-06082-8.

[315] S. Chaudhary, L.S. James, A. B. V. Kiran Kumar, C. V. V. Ramana, D. K. Mishra, S. Thomas, D. Kim, “Reduced Graphene Oxide/ZnO Nanorods Nanocomposite: Structural, Electrical and Electrochemical Properties,” *J Inorg Organomet Polym Mater.*, 29 (2019). https://doi.org/10.1007/s10904-019-01172-6.

[316] M. M. Vadiyar, S. C. Bhise, S. K. Patil, S. A. Patil, D. K. Pawar, A. V. Ghule, P. S. Patil, S. S. Kolekar, “Mechanochemical growth of a porous $ZnFe_2O_4$ nano-flake thin film as an electrode for supercapacitor application,” *RSC Adv*., 5 (2015). https://doi.org/10.1039/c5ra07588b.

[317] M. Zhu, X. Zhang, Y. Zhou, C. Zhuo, J. Huang, S. Li, “Facile solvothermal synthesis of porous $ZnFe_2O_4$ microspheres for capacitive pseudocapacitors,” *RSC Adv.*, 5 (2015). https://doi.org/10.1039/c5ra00447k.

[318] Y. Z. Cai, W. Q. Cao, P. He, Y. L. Zhang, M. S. Cao, “$NiFe_2O_4$ nanoparticles on reduced graphene oxide for supercapacitor electrodes with improved capacitance,” *Mater Res Express*, 6 (2019). https://doi.org/10.1088/2053-1591/ab3fff.

[319] F. Meng, M. Yang, L. Zhao, Y. Zhang, X. Shang, P. Jin, W. Zhang, "A comparative study of the structural, magnetic and electrochemical properties of Al^{3+} and Cu^{2+} substituted NiZn ferrite/reduced graphene oxide nanocomposites," *Ceram Int.,* 43 (2017). https://doi.org/10.1016/j.ceramint.2017.08.179.

[320] V. Vignesh, K. Subramani, M. Sathish, R. Navamathavan, "Electrochemical investigation of manganese ferrites prepared via a facile synthesis route for supercapacitor applications," *Colloids Surf A Physicochem Eng Asp.*, 538 (2018) 668–677. https://doi.org/10.1016/j.colsurfa.2017.11.045.

[321] B. Li, Y. Fu, H. Xia, X. Wang, "High-performance asymmetric supercapacitors based on $MnFe_2O_4$/graphene nanocomposite as anode material," *Mater Lett*., 122 (2014). https://doi.org/10.1016/j.matlet.2014.02.046.

[322] M. Buldu-Akturk, M. Toufani, A. Tufani, E. Erdem, "ZnO and reduced graphene oxide electrodes for all-in-one supercapacitor devices," *Nanoscale*, 14 (2022) 3269–3278. https://doi.org/10.1039/d2nr00018k.

[323] M. Aadil, S. Zulfiqar, H. Sabeeh, M. F. Warsi, M. Shahid, I. A. Alsafari, I. Shakir, "Enhanced electrochemical energy storage properties of carbon coated Co_3O_4 nanoparticles-reduced graphene oxide ternary nano-hybrids," *Ceram Int.*, 46 (2020). https://doi.org/10.1016/j.ceramint.2020.04.090.

Research Publications

- **Mohd Rouf Khan**, Hamnesh Mahajan, Ajeet Kumar Srivastava, "Investigation of Crystallographic, Morphological, Magnetic and Electrochemical Properties of La-Doped Cu-$CoFe_2O_4$ Spinel Ferrites" ***Cryst. Res. Technol***. 2024, 59, 2300356. https://doi.org/10.1002/crat.202300356
- Din, L.M.U., **Khan, M.R.,** Lone, G.A. et al. *Structural and Morphological Analysis of Copper-Doped Zirconia Thin Films Cast on Silicon Substrates*. J. Electron. Mater. 54, 6780–6792 (2025). https://doi.org/10.1007/s11664-025-12100-5

Communicated Papers

- **Mohd Rouf Khan,** Latief Mohi Ud din, Ajeet Kumar Srivastava, "Fabrication and Analysis of Zinc-Doped Mn-$NiFe_2O_4$/rGO Nanocomposite Electrodes for High-Performance Supercapacitors, **Ceramics International** (Submission ID: CERI-D-25-12139)

Oral Presentations

- **Mohd Rouf Khan,** Ajeet Kumar Srivastava, "Impact on Energy Storage Properties by Analysing the Structural and Magnetic Properties of Rare-Earth Doped Cu-Co Spinel Ferrites" ***International Conclave on Materials, Energy & Climate (ICMEC-A6066),*** 12 - 14 December 2022, Indira Gandhi Delhi Technical University for Women, Delhi, India.
- **Mohd Rouf Khan**, Ajeet Kumar Srivastava, "Investigation of Crystallographic, and Magnetic Properties of La-Doped Cu-$CoFe_2O_4$ Spinel Ferrites" ***International Conference on Futuristic Materials in Science and Technology (ICFMST-2022),*** 21-22 December 2022, Department of Chemistry, Bannari Amman Institute of Technology, Sathyamangalam, Erode, Tamil Nadu, India.

Paper Award

- **"Best Paper Award"** for the paper entitled Investigation of Crystallographic, and Magnetic Properties of La-Doped Cu-$CoFe_2O_4$ Spinel Ferrites in the ***International Conference on Futuristic Materials in Science and Technology (ICFMST-2022),*** 21-22 December 2022, at Department of Chemistry, Bannari Amman Institute of Technology, Sathyamangalam, Erode, Tamil Nadu, India.

Course Awards and Participation Certificates

- Attended IIRS-ISRO Distance Learning Programme and received the certificate of participation on ***"Geodata Processing using Python"*** held from 15-19 January 2024, organized by Indian Space Research Organisation (ISRO) in collaboration with Indian Institute of Remote Sensing (IIRS), Dept. of Space, Govt. of India, Dehradun.
- Received a certificate of participation at the Advanced Materials World Congress (AMWC), held from 11-14, October 2022, organized by the International Association of Advanced Materials, Stockholm, Sweden.

Professional Certifications

- Attended a One Week Training Program on ***"Material Characterization Techniques"*** under the Synergistic Training Program Utilizing the Scientific and Technological Infrastructure (STUTI), held from 28 June - 4 July 2022, organized by NIT Srinagar in collaboration with Aligarh Muslim University (AMU), supported by Department of Science and Technology (DST), Govt. of India.
- Attended a Workshop on ***"Advanced Material Characterization Techniques"*** held from 19-20 December 2022, organized by Lovely Professional University, Punjab, and secured an **"O"** Grade.